TESIS DE LA UNIVERSIDAD DE ZARAGOZA

2013

56

Pablo Sáez Viñas

Theoretical and computational study of the mechano-biology in hypertension disease

Departamento
Ingeniería Mecánica

Director/es
Peña Baquedano, Estefanía
Martínez Barca, Miguel Ángel

ISSN 2254-7606

Prensas de la Universidad
Universidad Zaragoza

Universidad Zaragoza
1542

Tesis Doctoral

THEORETICAL AND COMPUTATIONAL STUDY OF THE MECHANO-BIOLOGY IN HYPERTENSION DISEASE

Autor

Pablo Sáez Viñas

Director/es

Peña Baquedano, Estefanía
Martínez Barca, Miguel Ángel

UNIVERSIDAD DE ZARAGOZA

Ingeniería Mecánica

2013

Theoretical and computational study of the mechano-biology in hypertension disease

Thesis by

Pablo Saez

For the Degree of

Doctor in Philosophy

University of Zaragoza

Zaragoza, Spain

Universidad Zaragoza

Theoretical and computational study of the mechano-biology in hypertension disease

Thesis by

Pablo Sáez

For the Degree of

Doctor in Philosophy

Faculty advisors:

Prof. Miguel Ángel Martínez Barca

Dr. Estefanía Peña Baquedano

University of Zaragoza

Zaragoza, Spain

Acknoweldge

The work of this PhD thesis was carried out at the department of Mechanical Engineering of the University of Zaragoza, first at the GEMM and later in the AMB lab, both group being part of the I3A, a broader cluster of research institutes. We were quite bunch of people back on these days so this first acknowledge go to all of those how are or were part of them and that we share time together.

I would like to thanks my supervisors, Dr. Estefania Peña and Prof. Miguel Ángel Martínez for the opportunity I had to be part of this great group. I will also like to thanks them for the freedom that they gave me and their confidence in my research during my thesis and all the time they spent on my work. I would also like to acknowledge to Prof. Manuel Doblaré which was the PI of my graduate grant, BES-2009-028593, which made me able to accomplish this thesis.

I want to thanks also some professors that have been and will be a reference and that I had the pleasure to work with. Prof. Andreas Menzel with who I had the opportunity to work in its group at TU Dormund. To Prof. Ellen Kuhl from Stanford University. She has been a fundamental part of this work and I will always be in debt for the six months I spent at her lab. I would also like to thank Prof. John M.Tarbell, from the City College of New York, for the opportunity to work in his lab. Finally, I always will be in debt with Prof. Micheal Ortiz, who accept me to spend three months in his group. In was astonishing to spend that time in one of the most amazing computational solid mechanics group in the world.

And above all, I would like to remember firstly to all my class colleges: Myriam Cilla, Belen Hernandez, Carlos Borau, Fares El Halabi and Sergio Gabarre. It was amazing to share all this time with you guys and I will miss you all!! Hopefully we will end up somewhere close enough to hang out together again!

I would also like to thank Mauro. You were a great friend here and a great travel mate. Also to JF that helps, not only me but everyone else, in the lab to anything we ask him for. I hope your new life in the boot-shaped country goes

great. Sarita for her positiveness and happiness and for being a great person. Marina and Raquel!!...They both are making me to wish never leave the lab, at least during they stay in. I was really great all the useless time we spend taking coffee, getting a nice tone or just hanging out!! And many others: Noelia, Mar, Jorge, Jamal, Clara, Carlos, Enrique, Berto, V. Alastrue., V. Acosta, Galavis, Olfa, Libardo, Horacio, Mena, Tobias, Claudia, Sonja, Ronny, Alex, Manuel, Jon, Adrian, Nick... I sure I will miss you guys wherever I end up!

Abstract

The present work deals with the development of a theoretical and computational framework of the mechano-biology happening in the arterial tissue during hypertension disease. Biological tissue adapts actively to different mechanical and chemical stimuli where the underlying mechanical properties of the tissue play an important role. The mechanical stimuli that trigger these changes is the increase of blood pressure experienced in hypertensive patient. There are also changes in the blood flow. This work is divided in four aspects of the adaptation of different components of the tissue to hypertension. Firsts, we focus on the mechanical properties of the arterial tissue and we particularly look at the behavior of a real human carotid artery. We obtain a finite element model of the carotid artery to apply all the models developed during this work. Two of them are related with the growth and remodeling of the collagen and smooth muscle cells within the arterial wall. Its thermodynamic description fall into the description of open systems where mass is allowed to gain or loss via changes of volume, density of both. The characteristic thickening of the arterial wall is describe by means of a volumetric growth model. The stiffening of the arterial tissue, which is due to the increase of the collagen content, is formulated within a density growth model. Both of these approaches are described theoretically and are later included computationally in a finite element framework. The last part of this dissertation aims at deriving a model of endothelial cell orientation and morphological adaptation to the blood flow.

Index

List of Figures

List of Tables

1 Motivation

This thesis studies some of the biological processes found in hypertensive diseases to, after that, present some mathematical models within a continuum mechanics framework. We focus on the the adaptation of the arterial wall by volumetric growth of the SMC and the collagen turnover. We also look at the endothelial cell adaptation to changes in the blood flow. The final goal is to apply the developed models to a real patient geometry of carotid where, by means of numerical techniques (Finite Element Method in particular) be able to reproduce the mechanical and structural changes happening in it. The next section of this chapter gives a brief description of the biological tissue and processes studied in this work.

Nowadays, the mathematical and computational study of biomechanics and biology have gained a huge significance in the research community. There has been an important increase in the number of scientific forums devote to them, while some years or decades ago bioengineering works were doomed to be presented in general continuum mechanics and computational journals. This outbreak in bioengineering, both from the continuum and computational points of view, have other interesting counterparts. Many of the research laboratories and institutes from all over the world, which were working extensively and successfully in classical continuum and computational problems, moved forward, or may

be backward, into the biological field. There could be different reasons for such a change.

The study of plasticity, damage, viscoelasticity, etc., have been key points of development in continuum mechanics for decades. Up today many important progresses have been achieved and the amount of knowledge about these topics is quite high. No mention that many of the most important continuum and computational researchers have been focusing their efforts in those topics. However, the biological point of view of continuum mechanics and computational methods have not been so well exploited and probably many researchers felt the necessity of moving to this close area of research in order to set off for this new challenge. It is relevant to point out that those theories and methods used for the study of these classical topics have been used with good success in dealing with the study of biological tissue. However, biological tissues are, at some extend, much more complicated materials than those usually studied in the field of continuum mechanics, such as steel, rubbers, etc., basically due to its "living" nature. A huge amount of adaptation processes undergo and not only due to mechanical stimuli but also to chemical unbalance and cellular behavior.

There are probably other reasons for that change, such as an economical one. Laboratories and departments saw that the amount of funding devoted to bioengineering by public and private organizations was starting to growth while to classical topics was getting stuck or even decreased.

Bioengineers have the goal of bringing together some research fields of biology and mathematics. The basic idea is to study and understand what biologists or engineers found in its experimental studies. They have to create mathematical models that qualitatively and quantitatively describe the phenomena saw in those experiments and at the end apply to different practical goals, such as, e.g., create artificial tissues to substitute natural ones, develop clinical equipment or computational models that recreate the behavior of different tissues. The big deal of mathematical and computational models, compared with experimentation, is that once the model is correctly characterized, a fast and cheap reproducibility of different cases of study can be achieved as, e.g., different load cases, chemical environments or cellular disorders, etc.

Therefore, it is not surprising that in 2009 The Wall Street Journal placed Mathematicians and Biologists in the first and fourth most valued jobs in the world (Needleman, 2009). In 2010 the USnews pointed out that bioengineer was the job with fastest-growing occupation, a 72%, far from the 10% average. USnews described them as "Biomedical engineers help develop the equipment and devices that improve or enable the preservation of health. They're working to grow cardiac tissue or develop tomorrow's MRI machines, asthma inhalers, and artificial hearts." (Wolgemuth, 2009). There is an enormous demand of better medical devices, biomedical materials, etc., and there is an estimation of 12000 new jobs through 2018 in the USA.

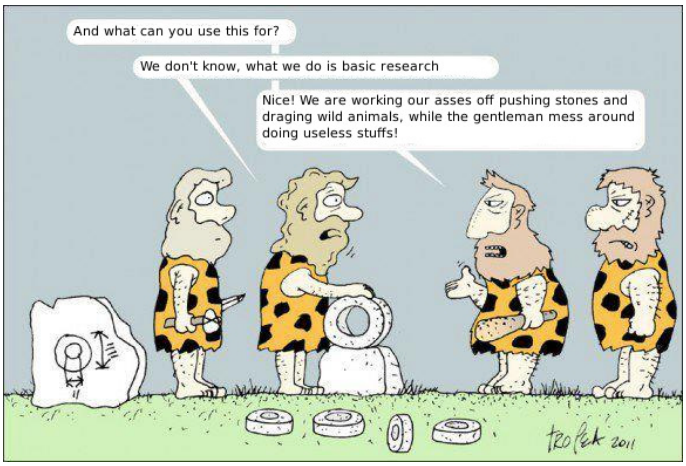

Figure 1.1: A widespread idea of basic science (Tropea, 2011).

However, this great perspective of the bioengineering sector and its achievements in particular, are sometimes far away from providing society non only of economical profit but also wealthiness and sometimes sinks to the so called basic science. Or more precisely, there is a lack of translation of the basic research achievements into society. Fig. 1.1 represents this issue quite well. There is now a doubt that basic research is a key milestone in the evolution of societies. However it is important to allow to translate as much as of these works into productive market, which seems to be a problem in the field of bioengineering. According

to a publication of a committee of the UK parliament there is a clear difficulty of translating such knowledge into an clear and fast economical profit. They concluded that private funding should help out basic research to be, in somehow, a pushing force to get and orient research into what industry and society need. They also recognized that public funds are essential to grant researchers to accomplish those works that may not have a clear profit today but probably will have in the future. We cannot also forget the pure basic research, which probably will be never use for anything in particular but for our better understanding of what surround us.

1.1 The cardiovascular system

The cardiovascular system (Topol et al., 2006) is one of the most important systems in mammalians. It is composed of the heart, the blood and the blood vessels and it has the main goal of transporting oxygen and nutrients to the rest of the body. The blood has a total volume of 4.7 to 5.7 liters and between its more important substances there are plasma, red blood cells, white blood cells and platelets. The heart is the engine of this system pumping oxygenated blood to the body and desoxygenated blood to the lungs.

There are three main circulatory systems in mammals. The *pulmonary circulatory system* (see Fig. 1.2(a)) is the network in which poor oxygenated blood is pumped out from the heart to the lungs via the pulmonary artery and return to the heart through the pulmonary vein with a high oxygen content. Poor-oxygenated blood coming from the vena cava, enters the right atrium and goes through the tricuspid valve into the right ventricle, from where it is pumped into the pulmonary artery to the lungs. Thanks to the a CO2-oxigen exchange in the lungs blood becomes oxygenated and goes back to the heart through the pulmonary vein. The high-content oxygen blood is used by the systemic system to provide oxygen to all the cells in the body. *Systemic circulation* (see Fig. 1.2(b)) is the circulation network which transports oxygenated blood from the heart to the rest of the body and returns oxygen-depleted blood to the heart due to the consumption of oxygen by cells all over the way of the arterial tree. Systemic

circulation transports blood to every part of the body via diffusion of oxygen and nutrients across the vessel wall to feed cells and they return carbon dioxide and wastes into the blood torrent. Blood gets out the left ventricle to the aorta, the largest artery in the body, moving toward the aorta arches and branches into arteries to the upper body, passing through the diaphragm after that, where it branches further into arteries which supply the lower parts of the body, these into arterioles and finally capillaries. The waste and non-oxygenated blood is then collected in the vein capillaries going up to the vena cava from where the blood enters the heart at the right atrium where the pulmonary system starts over again. The *coronary circulatory system* (see Fig. 1.2(c) by PHOTOSCIENCE) injects oxygenated blood into the heart. Although it could be considered as part of the systemic circulation system is usually taken apart from it because blood motion occurs at diastole movement instead of systole as does in pulmonary and systemic system.

1.1.1 Cardiovascular disorders

This well organized and synchronized system presents a important number of diseases which are main target of research all over the world and over different research fields. According to the World Health Organization, chronic diseases are responsible for 63% of all deaths in the world, with cardiovascular diseases as the leading cause of death (WHO, 2009). Cardiovascular disease is any disease that affects the heart itself and/or the blood vessel system, especially the veins and arteries.

Between the most important cardiovascular diseases (Leonard, 2008), we find the rupture of atherome plaque within the artery wall, which consist in the occlusion of the blood conduct by the growth of fat tissue. One of the worst consequences is ischemic heart disease, characterized by reduced blood supply to the cardiac muscles, i.e. myocardium.

Hypertensive heart disease, another important disease, is caused by high blood pressure. Valvular heart disease is a disease process that affects one or more valves of the heart. There are four major heart valves which may be affected,

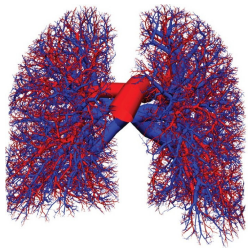

(a) Pulmonary circulation Burrowes et al. (2005).

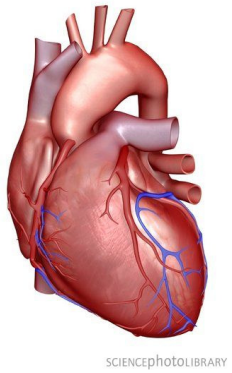

(b) Coronary circulation Zygote Media Group (2011).

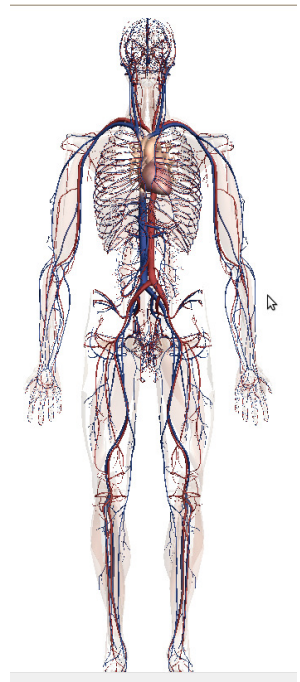

(c) Systemic circulation.

Figure 1.2: Representation of the different circulatory system.

including the tricuspid, aortic, mitral and pulmonary valves. Angina pectoris (chest pain) and myocardial infarction (heart attack) are symptoms or conditions caused by coronary heart disease. Over 459,000 Americans die of coronary heart disease every year (Association, 2012). Cardiomyopathy is the deterioration of the function of the myocardium for any reason. People with cardiomyopathy are often at risk of arrhythmia and/or sudden cardiac death.

Multiple explanations have been proposed to explain why age increases the risk of cardiovascular diseases (Bridget, 2010). One of them is related to serum cholesterol level. In most populations, the serum total cholesterol level increases

as age increases. In men, this increase levels off around age 45 to 50 years. In women, the increase continues sharply until age 60 to 65 years (Jousilahti et al., 1999). One of the proposed explanations for the gender difference in cardiovascular disease is hormonal difference. Among women, estrogen is the predominant sex hormone. Estrogen may have protective effects through glucose metabolism and hemostatic system, and it may have a direct effect on improving endothelial cell function. The production of estrogen decreases after menopause, and may change the female lipid metabolism toward a more atherogenic form by decreasing the HDL cholesterol level and by increasing LDL and total cholesterol levels. Aging (Jani and Rajkumar, 2006) is also associated with changes in the mechanical and structural properties of the vascular wall, which leads to the loss of arterial elasticity and reduced arterial compliance and may subsequently lead to coronary artery disease. In this thesis, we are going to focus in hypertension. In the next section we discuss briefly the main aspects of hypertension, from causes to consequences.

1.1.2 Hypertension

Hypertension is a chronic medical condition in which the blood pressure is elevated. This makes the heart to work harder than normal to pump out blood through the blood vessels. Blood pressure involves two measurements, systolic and diastolic, which depend on whether the heart muscle is contracting (systole) or relaxed between beats (diastole). JNC7 (the Seventh Report of the Joint National Committee on Prevention of Detection, Evaluation and Treatment of High Blood Pressure) (Chobanian et al., 2003) classification set normal pressures below 140 mmHg systolic and 90 mmHg diastolic. High blood pressure is considered when it is at or above 140/90 mmHg for long time based on JNC7 classification. Recent international hypertension guidelines have range values to indicate a continuum of risk with higher blood pressures in the normal range. JNC7 uses the term prehypertension for blood pressure in the range 120-139 mmHg systolic and/or 80-89 mmHg diastolic. There is also a classification for different hypertension stages. Isolated systolic hypertension refers to elevated systolic pressure

with normal diastolic pressure and is common in the elderly. A first stages refers to blood pressure between 140 and 159 or diastolic pressure between 90 and 99. A second stage for people with systolic blood pressure exceeding 160 mmHg systolic or a diastolic pressure over 100 mmHg.

Hypertension is classified as either primary (essential) hypertension or secondary hypertension; about $90 - 95$ of cases are categorized as "primary hypertension" which means that blood pressure increases with no obvious underlying medical cause (Carretero and Oparil, 2000). The remaining $5 - 10$ of cases (secondary hypertension) are caused by other conditions that affect the kidneys, arteries, heart or endocrine system.

Primary hypertension is the most common form of hypertension, accounting for 90 - 95 of all cases of hypertension (Carretero and Oparil, 2000). Blood pressure rises with aging and the risk of becoming hypertensive in later life is considerable (Narayan et al., 2003). Hypertension results from a complex interaction of genes and environmental factors. Numerous common genes with small effects on blood pressure have been identified as well as some rare genes with large effects on blood pressure but the genetic basis of hypertension is still poorly understood (Lifton et al., 2001). Several environmental factors influence blood pressure. The possible role of other factors such as stress, caffeine consumption, and vitamin D deficiency are less clear cut (Chobanian et al., 2003).

Many mechanisms have been proposed to account for the rise in peripheral resistance in hypertension. Most evidences implicates either disturbances in renal salt and water handling, particularly abnormalities in the intrarenal renin-angiotensin system and/or abnormalities of the sympathetic nervous system (Anderson et al., 1989). These mechanisms are not mutually exclusive and it is likely that both contribute to some extent in most cases of essential hypertension. It has also been suggested that endothelial dysfunction and vascular inflammation may also contribute to increase peripheral resistance and vascular damage in hypertension (Brunner et al., 2005)

In most people with established essential (primary) hypertension, the increased resistance to blood flow (total peripheral resistance) trigger a high pres-

sure output while cardiac outflow remains normal (Conway, 1984). There is evidence that some younger people with prehypertension or 'borderline hypertension' have high cardiac output, an elevated heart rate and normal peripheral resistance, termed hyperkinetic borderline hypertension. These individuals develop the typical features of established essential hypertension in later life as their cardiac output falls and peripheral resistance rises with age.

The increased peripheral resistance in established hypertension is mainly attributable to structural narrowing of small arteries and arterioles, although a reduction in the number or density of capillaries may also contribute (Folkow, 1982). Hypertension is also associated with decreased peripheral venous compliance which may increase venous return, increase cardiac preload and, ultimately, cause diastolic dysfunction (Safar and London, 1987). Whether increased active vasoconstriction plays a role in established essential hypertension is unclear (Schiffrin et al., 2000).

Secondary hypertension results from an identifiable cause. Renal disease is the most common secondary cause of hypertension (O'Brien et al., 2007). Hypertension can also be caused by endocrine conditions, such as Cushing's syndrome, hyperthyroidism, hypothyroidism, acromegaly, Conn's syndrome or hyperaldosteronism, hyperparathyroidism and pheochromocytoma. Other causes of secondary hypertension include obesity, sleep apnea, pregnancy, coarctation of the aorta, excessive liquorice consumption and certain prescription medicines, herbal remedies and illegal drugs.

The World Health Organization has identified hypertension, or high blood pressure, as the leading cause of cardiovascular mortality. Last data available shows that around one billion people all over the world, close to the 26% of the total adult population in the world suffer of hypertension. The World Hypertension League (WHL) recognized that over the 50% of the hypertensive population worldwide do not know their condition. Hypertension does not represent a danger by itself, but is a major risk factor for stroke, myocardial infarction, heart failure, aneurysms, peripheral arterial disease among many others and it is closely related to a shorten of time life. Contrarily, hypertension is the most important

preventable disease for early death worldwide.

USA leads many of the survays and studies about hypertension as they do for suffering of hypertension and it is the most common chronic medical problem, prompting visits to primary health care providers in USA (Association, 2012). The American Heart Association estimated the direct and indirect costs of high blood pressure in 2010 as 76.6 billion. 34% of the US population (over the world mean) and African American adults have among the highest rates of hypertension in the world, being lower in whites and mexican americans. What change in US, as in other developed countries, is that 80% of people are aware of their condition while just 71% take some medication or are adequately controlled. Inadequate management of hypertension could be boosted by inadequacies in the diagnosis, treatment, and/or control of high blood pressure.

Hypertension is rarely accompanied by any symptoms, and its identification is usually through screening, or when seeking healthcare for an unrelated problem. A proportion of people with high blood pressure reports headaches, as well as lightheadedness, vertigo, tinnitus (buzzing or hissing in the ears), altered vision or fainting episodes. A "hypertensive emergency" is diagnosed when there is evidence of direct damage to one or more organs as a result of the severely elevated blood pressure. This may include hypertensive encephalopathy, caused by brain swelling and dysfunction, and characterized by headaches and an altered level of consciousness (confusion or drowsiness). Breathlessness, cough, and the expectoration of blood-stained sputum are characteristic signs of pulmonary edema, the swelling of lung tissue due to left ventricular failure, an inability of the left ventricle of the heart to adequately pump blood from the lungs into the arterial system.

The first line of treatment for hypertension is identical to the recommended preventative lifestyle changes and includes: dietary changes, physical exercise, and weight loss (Chobanian et al., 2003). These have all been shown to significantly reduce blood pressure in people with hypertension. If hypertension is high enough to justify immediate use of medications, lifestyle changes are still recommended in conjunction with medication. Different programs aimed to reduce psychological stress such as biofeedback, relaxation or meditation are advertised

to reduce hypertension. However, in general claims of efficacy are not supported by scientific studies, which have been in general of low quality.

With the aim of studying the hypertension disease in the arterial tissue within a computational mechanics framework we have to look at some aspects of the arterial wall to characterize the biological process. We assume two behaviors of this tissue, a passive and an active one.

1.2 Passive behavior of the vessel wall

Among the most important features of the cardiovascular tissue we find a highly non-linear and anisotropic material with a nearly incompressible response due to the high water content. They area made up of different components as collagen, elastin, smooth muscle cells and fibroblast, turning them into heterogeneous composite-like materials. We devote Chapter 3 to describe the actual passive behavior of the arterial tissue and the carotid artery in particular.

1.3 Active behavior of the vessel wall

In contrast with other materials, traditionally studied in the field of continuum mechanics, biological tissue is a very active matter. It does not only bear mechanical load. They exhibit a very optimized and advanced auto-regulatory mechanisms under mechanical and chemical stimuli. The cardiovascular system in particular undergoes a constant evolution over mammalian life. Moreover, these changes can be dramatically speed up in some diseases such a hypertension, atheroesclerosis, etc. The experimental and computational study of such processes are a very important research field. In the following section we will address those changes observed in hypertension disease.

1.3.1 Role of smooth muscle cells

Smooth Muscle Cells (SMC) play an important role in both the passive and active behavior of the arterial tissue. However, it is in the active and evolution

aspects where SMC play a differentiate role. After a mechanical stimulus has occurred, up-regulating or down-regulating the homeostatic state, we can give a time-line description of its behavior. Focusing the problem on the hypertensive disease, an increase in blood pressure, and changes in blood flow the arterial wall experience an increase in the stretches and therefore stresses. The first active response to such changes is the contraction of the SMC in order to reestablish both normal stresses over the arterial thickness and normal values of the wall shear stress on the endothelial layer. The change of the basal tone is described usually as a short-term response and depends on the type and health of the artery. While important in all arteries, the active behavior of the SMC are known to have a primarily role on peripheral or resistance arteries. They are the ones that control the cardiovascular resistance to fulfill the requirements of the cardiovascular network. However, large and medium size arteries have lower contraction capabilities. SMC also boost the release of many different substances which have the main goal of acting on other cells and on the Extracellular Matrix (ECM) to adapt the internal structure to the new mechanical environment. Among the most important substances are the Transforming Growth Factors (TGF), such as TGF-β, Metalloproteinases enzymes (MMP) and Tissue Inhibitors of Metalloproteinases (TIMP).

In the long-term response SMC experience a change in volume which have been well documented in terms of thickening of the arterial wall. Chronically, SMC start to growth, via hypertrophy, hyperplasia or both (Owens et al., 1981; Owens, 1989), to restore the homeostatic stress state. This chronic adaptation leads to the well-documented thickening of the vessel wall. These changes are also more pronounced in small or resistance vessels (Folkow et al., 1958; Mulvany and Aalkjaer, 1990). Bishop and Lindahl (1999) showed that the increase in extracellular matrix (ECM) deposition can be caused by hyperplasia or by the increase in cell synthesis, while Owens et al. (1981) identified hypertrophy to be the main origin of SMC growth.

1.3.2 Role of endothelial cells

Endothelial cells (EC) are cells of the selectin family (E-Selectin) which conform the inner layer of blood vessels. They are distributed along the lumen in a monocell layer and are in charge, jointly with the SMC and fibroblast, of the regulatory system of the peripheral cardiovascular system. While SMC sense and react to changes of the blood vessel, EC do to variations of the shear stress, transforming mechanical stimulus into intracellular signals leading to functional, mechanical and chemical variations of the cell. Concerning the mechano-sensing receptors, several hypothesis have been investigated and established as sensors of shear stress. Ion channels represent one of the most important receptors, in particular by increasing K^+ permeability, increasing Ca^{2+} influx and activation of NonSelective Cation channels (NSC) and Cl^- channels. Integrins are known to play an important role in mechanosensing of EC. They are placed on the cell membrane and represent an interface between the ECM, fibronectin and collagen, and the cell. They and their glycoproteins content are sensitive to displacement due to strain or shear stress. Platelet endothelial cell adhesion molecule-1 (PECAM-1) bind adjacent endothelial cells and have been also observed to increase due to shear strees. They play a role in abgeogenesis and cell adhesions. G-Proteins-Coupled receptors (GPCRs) and G-Proteins also have been reported to activate due to shear stress. Glycocalyx covers the surface of some cells, like in the EC, and plays a fundamental role in the mechonosensing and transduction of the shear stress, see Weinbaum et al. (2007); Tarbell and Shi (2012) for more details. All these receptors activate other huge cascade of signaling intracellular pathways. Among the most identified molecules involved we can point out Protein Kinase C (PKC), Rho family GTPases, PI3K and MAPKs. All this machinery effects and leads to changes on several aspects of EC. Shear stress have shown increase of gene expression in of Platelet-Derived Growth Factor (PDGF)-A and -B, Transforming Growth Factors ($TGF-\beta$), Intercellular Adhesion Molecule-1 (ICAM-1) and vasodilators NO and decreasing of Vascular Cell Adhesion Molecule-1 (VCAM-1) and the expression of the vasoconstrictor ET-1.

1.4 Computational models

The mathematical modeling of natural processes is a nice path to a better knowledge of what is happening in them. In particular the modeling of biomechanics and mechanobiology is a enterprising area of research (Humphrey, 2003; Holzapfel, 2004). Moreover, the inclusion of such models in a computational framework, the finite element method for example, allows researchers to study real patient specific geometries. Note that one of the main goals of computational and theoretical studies of biomechanics and mechonobiology related problems is the application of these studies to improve current diagnostic tool and drugs as well as a new research field in building synthetic organs (see an interesting New York Times article by Fountain (2012)). These two issues brought together are a wonderful tools to study many different topics within the biological and computational mechanics community. Among many of the topics to study in biomechanics, researchers have been focusing more strongly on the modeling of different kinds of tissue as the heart (McCulloch et al., 1998), bones (Rice et al., 1988; Weinbaum et al., 1994), vessels (Holzapfel et al., 2000), tendoms (Peña et al., 2006), eye (Pandolfi and Manganiello, 2006; Alastrué et al., 2006), etc. Many efforts have been also invested to model the electrical behavior of the heart (Heidenreich et al., 2010; Wong et al., 2011) and arteries (Murtada et al., 2010). There are also a high amount of works about the evolution of biological tissue over time like remodeling and growth, see e.g. the review in Humphrey (2009) and Ambrosi et al. (2011). Molecular dynamics is other useful tool for the simulation of movement of atoms and molecules (Rapaport, 2002).

In terms of the **mechanical behavior**, a large number of constitutive laws have been recently proposed for modeling the mechanical behavior of soft biological tissues and blood vessel in particular. In general, this kind of tissues are made up of an extra-cellular matrix, composed of an isotropic ground substance with a high water content in which a network of fiber composed of elastin, different kinds of collagen and proteoglycans are embedded. The combined contribution of these constituents determines the mechanical response of the tissue, which turns out to be highly non-lineal. Those fibers are also responsible for the anisotropic

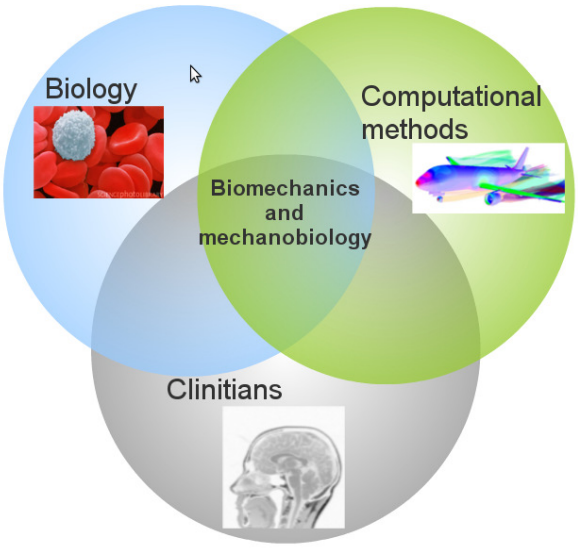

Figure 1.3: Workflow in current biomechanics research field.

response of the tissue due to the existence of clear preferential orientations of the fibre bundles (Rhodin, 1980; Landuyt, 2006). They are commonly incorporated to the constitutive models as discrete anisotropy directions by means of, e.g., additional structural tensors (Gasser et al., 2006). Nevertheless, histological studies have shown that it does exist some fiber dispersion around the preferential orientation, which varies as a function of many variables as the vessel layer, the vessel type or even the position along the vessel length (O'Connell et al., 2008; Gasser et al., 2012). Thus, the incorporation of anisotropy considering fiber dispersion is one of the challenges for modeling the mechanical behavior of soft tissues. There exist also many models considering damage, viscoelastic and plastic effects (see e.g. the monographs of Fung (1990) and Humphrey (2002)).

Firstly developed anisotropic constitutive models for blood vessels were purely phenomenological. Fung et al. (1979) proposed an exponential law of the deformations in the principal cylindrical directions in order to account for the anisotropic behaviour of the tissue. Later, directional fibre dispersion was introduced in the

models by means of different methodologies. In Holzapfel et al. (2005), a phenomenological parameter served to account for dispersion, whereas Gasser et al. (2006) used the von Mises Orientation Density Function (ODF) (Fisher, 1953) to determine a structural tensor representing the fibre distribution. More recently, models including fiber dispersion from a micro-structurally-based approach have been proposed (Alastrué et al., 2009).

Hemodynamics is also an important topic in computational mechanics. FSI has been applied to cardiovascular problems. Coupling medical images with computing resources made possible the study of the blood flow in human arteries through Computational Fuid Dynamics (CFD) simulations and, in more recent years, through Fluid Structure Interaction (FSI) simulations with the aim to evaluate the influence of vessel properties (e.g., geometrical properties and wall compliance) on arterial pathologies. Steinman et al. (2002) proposed a novel approach for non-invasively reconstructing artery wall thickness and local hemodynamics at the human carotid bifurcation, and reported the first direct comparison of hemodynamic variables and wall thickness. On FSI analysis, Perktold and Rappitsch (1995) investigated the effect of a distensible artery wall on the local flow field and determined the mechanical stresses in the artery wall where incrementally linearly elastic behavior was assumed. Tang et al. (2001, 2003, 2004, 2005, 2008) conducted extensive research on stress analysis in plaque MRI-based models. Gao et al. (2009) compared the differences in stress distribution on plaque locations, between different diseased carotid bifurcations and analyzed the impacts of the specific combination of fibrous cap thickness and lipid core volume to the stress distribution (Gao and Long, 2008).

Besides the fluid dynamics involved in the blood through the vessel there is an important fluid contribution within the arterial wall. Plasma, the fluid component of blood, comprises around 55% of the blood volume and it is part of the fluid that goes through the endothelial layer. However what is really important to be considered is the mass transfer happening in the arterial wall which makes many biochemical substances to react over time. They are usually taken into account by diffusion and convection equations. Mathematical models and computational schemes have been widely used to account for it. Given such

a complex microstructure as the one described above, it is seem natural to think that many of those models have been focused on how molecules, e.g. LDL, go through this porous-like tissue.

Remodeling has been also studied from a computational and theoretical point of view. It is well known that biological tissue remodels itself when exposed to a given stimulus, e.g. mechanical loads such as an increase in blood pressure, and changes in the chemical environment that controls the signaling processes and the overall evolution of the tissue. Biological remodeling can occurs in any kind of biological tissue (see e.g. remodeling in a tendon-like structure in Fig. 1.4). In particular, the study of collagen as the most important tissue to be remodeled, in all its types (preferentially Type I and III), has been given considerable attention in the last few years (Driessen et al., 2003; Kuhl et al., 2005; Driessen et al., 2008). The reorientation of this kind of structures can be assumed to be the consequence of the reorientation of the fibrils or filaments that make them up. This phenomenon leads to changes in the micro-structural orientation, fiber shape and fiber properties, due to the reorientation of the fibrils (see e.g. Stopak and Harris (1982); Rubbens et al. (2009); Sander et al. (2009)). Several remodeling models have been proposed in the recent years. Some of them analyze the reorientation of unidimensional fibers driven by different stimuli such as Menzel (2007), Himpel et al. (2008) or Karsaj et al. (2009). In Himpel et al. (2008), a complete consistent linearization of the equations in an implicit finite element framework was performed. Garikipati et al. (2006) presented an elegant energetic and stationary study of the remodeling problem from a thermodynamical point of view.

The computational study of growth has gained increasing attention in the theoretical and computational mechanics community as well (see e.g. the reviews in Taber (1995); Humphrey (2009); Ambrosi et al. (2011)). In particular, the works of Skalak et al. (1982) and Rodriguez et al. (1994) were pioneered in the underlying kinematic description of volumetric growth. Mechanical treatment of growth has been dealt in different ways. Usually, growing and swelling of biological tissues are considered as open systems. Their different configurational settings and their numerical treatments in a finite element method (FEM) framework are

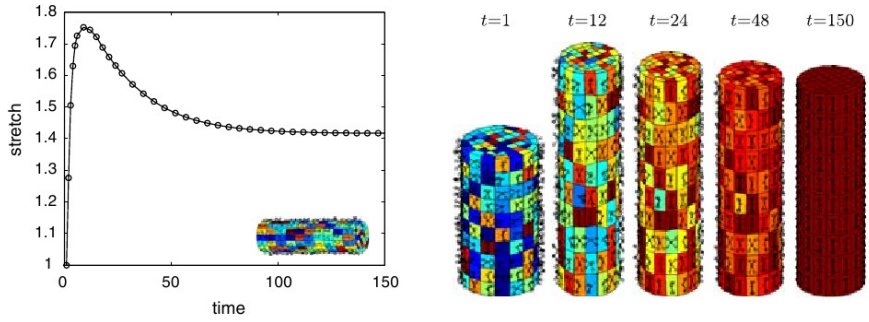

Figure 1.4: Computational model of remodeling of fibers in a tendon-like structure (Kuhl and Holzapfel, 2007).

discussed in Kuhl and Steinmann (2003). Typically, two fundamentally different forms of growth can be distinguished: volumetric growth and density growth, where a change of mass occurs in both of them. The first one allows for changes in volume while keeping the density constant whereas the second one maintains a constant volume while the density is allowed to change, see e.g. the works of Himpel et al. (2005) in isotropic growth, Menzel (2004, 2007) for anisotropic growth and Waffenschmidt et al. (2012) in the context of the micro-sphere model (see Fig. 1.5). An alternative approach towards growth is the one presented by Humphrey and Rajagopal (2002, 2003) based on constrained mixture theory, where several constituents of a tissue are allowed to growth in an independent way. In this context other works have been presented (Gleason and Humphrey, 2004, 2005; Klisch et al., 2005) and extended to reactive mixtures (Ateshian, 2007). Other interesting approaches are reported by Imatani and Maugin (2002); Ganghoffer (2010) in the context of volumetric material growth. It is also worth noting the early work of Fung and Liu (1989), which demonstrates that the growth of blood vessels induces a change in the natural configuration of the tissue, associated with the notion of a stress free configuration.

Another important biological structure able to remodel itself is **cell cytoskeleton**. Cytoskekleton is composed of microtubules, microfilaments and

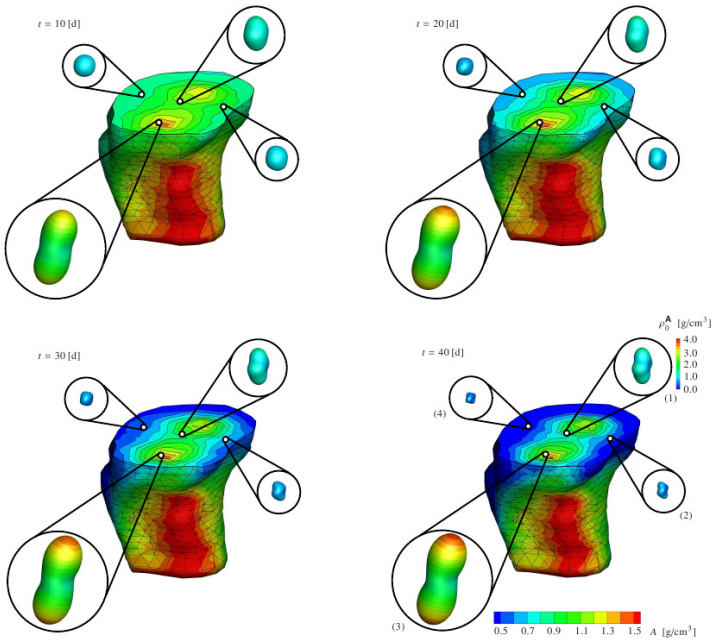

Figure 1.5: A computational model of density growth for bone (Waffenschmidt et al., 2012).

a network of actin filaments among many other elements (see e.g the review of Mofrad and Kamm (2006) and references therein for details). In terms of mechanical models there have been an increase of the number of works, see e.g. Ingber (2003); Maurin et al. (2008); Kardas et al. (2012) (see Fig. 1.6).

Cells move and reorient their inner structure depending on the stiffness and strain of the substrate (Discher et al., 2005; De et al., 2007). Cytoskeleton shape can change due to the adaptation of the microtubules and filaments to a specific external mechano-chemical stimulus (Saez et al., 2005; De et al., 2008). There are several experimental tests in the literature showing morphological changes of the cell due to mechanical stimulation of the matrix where cells are located. There exists two main procedures to induce cell morphological changes, static and cyclic loading (De et al., 2007; De and Safran, 2008; Goli-Malekabadi et al., 2011).

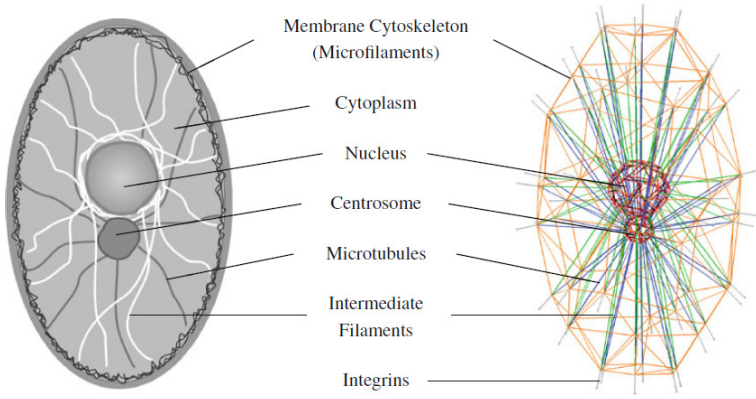

Figure 1.6: Computational tensegrity-type model of a cell (Kardas et al., 2012).

While static and low-frequency loading leads to a reorientation and remodeling of the cellular structure parallel to the stretching direction (Collinsworth et al., 2000; Bischofs and Schwarz, 2003), high-frequency cyclic loading does in nearly perpendicular (Hayakawa et al., 2001; Hsu et al., 2009; Faust et al., 2011). In high-frequency stimulus, the feeling agents of external environment, e.g. focal adhesions, are not able to follow such changes so no stress fibers and miosin motors are activated. However in static and low-frequency load states, focal adhesions react to such changes by means of an active internal tension of the stress fibers leading to changes in its morphology. These works mentioned above usually present the evolution from a random distribution of the micro-structure of the cells to be aligned with a particular direction. These experimental results are characterized by a gradual reorientation of the principal direction of the cell followed by a progressive remodeling of the micro-structural element leading to more pointed shape, see e.g., the experimental work of Dai et al. (2004) and references therein. In Fig. 1.7 we show some results presented by Hayakawa et al. (2001) where this behavior is shown. In many cases this change of shape, unlike changes in orientation, is measured by a shape-index in the biomedical community. The underlying biological processes are more in number and complexity. Some of them, like dynamics of focal adhesions, the tension exerted by molecular motors over actin stress fibers are among the most important aspect to be con-

sidered (see e.g. Mofrad and Kamm (2006) for an overall understanding of cell behavior).

In reference to models capturing these features not much have been done, while in terms of the orientation of the preferential direction of the cell, some of the most accepted models are those presented in De et al. (2007); De and Safran (2008), where the reorientation is assumed to be controlled by the matrix behavior and the forces that arise from the active regulation of the cell in a dipole-like manner. In terms of modeling changes on the morphology of cell shape due to external stimuli no many models exist in the literature, see e.g. Levesque et al. (1986); Ingber (2003); Ohashi and Sato (2005).

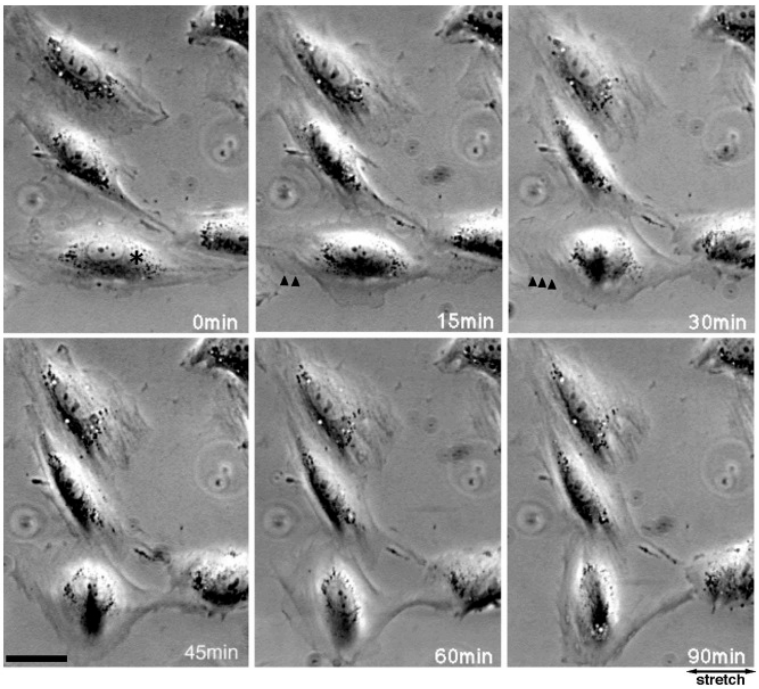

Figure 1.7: Experimental results of vascular smooth muscle cell cyclically loaded (Hayakawa et al., 2001)

1.5 Objectives and Thesis outline

The thesis is organized in 6 chapters, describing four different aspects of the arterial behavior and its response to hypertension. Each individual chapter is conceived to pursue an individual goal within the overall view of the computational modeling of hypertension disease. Every chapter contains a brief conclusion of each issue and a final conclusion chapter is addressed to bring a global conclusion. The chapters organization is as follows.

- Chapter 2 describes the passive behavior of the arterial wall. The general kinematics and constitutive relations used are reviewed. A general continuum approach is used and described through the Chapter and results from homeostatic and hypertensive states are presented. The results are based on the constitutive relations of every component of the layered material. Some experimental findings from literature are also reviewed. Those results presented here are based in a fluid structure interaction simulation whose basic characteristics will be also commented.

- Chapter 3 describes a model of volumetric growth of the SMC due to its over-stretching and to a long-term control of the lumen diameter. Its mathematical and computational aspects are described and results of the thickening of the arterial wall are presented.

- Chapter 4 describes the process by which collagen density change in hypertension. The chapter starts describing the trigger factor, SMC over-stretch due to the increase of pressure found in hypertension. Given this stretching difference, a model of SMC synthesis of TGF$-\beta$ and TIMP and the regulation of MMP is exploited. A computational model of diffusion-convection is used to study the transport of these substances through the arterial wall. After that, a computational model of the turnover of collagen is described which, at the end, leads to an increase in the stiffness of the arterial wall.

- Chapter 5 deals with the response of endothelial cells to changes of the wall shear stress found in hypertension. These changes are given by FSI simulations in the carotid artery. Endothelial cells adapt both their microstructure

and its genetics expression. We address a model for reorganization of the endothelial cytoskeleton based on its mechanical environment. The model is exploited in a computational way and the results of such simulation are presented. The model is also applied to the real carotid geometry. We also present a simple model of the synthesis and diffusion of the NO through the vessel wall.

- Chapter 6 discusses the most important conclusions as a whole and outlines future lines of research in the different topics studied in this thesis.

2

Continuum mechanics framework

The chapter outlines the basic notions of continuum mechanics that our models are based on. It describe the mapping configurations, kinematics, master balance, balance of mass, balance of momentum,, balance of mechanical energy and enthropy inequality. At the end we will provide some particularization used in the constitutive modeling of arterial tissue. The goal of this chapter is to provide a minimum framework in the context of solid mechanics that allow us to exploit later developments. This is not a complete review of solid mechanics and many important topics are omitted. Readers with a background in solid mechanics will see it very basic. This chapter would be more focus on give to the more biological oriented reader a basic notion of solid mechanics. Marsden and Hughes (1994); Ogden (1996); Bonet and Wood (1997) and Truesdell and Noll (2004), among many others, are monographs that the interested readers should not avoid for more comprehensive view of continuum mechanics.

2.1 Configuration and associated manifolds

Let's star by considering a body of interest $\mathcal{MP} \subset \mathbb{R}^3$ and let's consider a point $\mathcal{P}$. We need to provide him with a reference or a configuration. Let's consider a configuration for $\mathcal{MP}$ called $\mathcal{B}$. A configuration, $\mathcal{B}$, is a smooth, so differentiable,

manifold, such that $\mathcal{B} : \mathcal{MP} \to \mathbb{R}^3$. In other words, any particular point of $\mathcal{MP}$ in the configuration$\mathcal{B}$, e.g. $\mathbf{X} \in \mathbb{R}^3$, is a funtion that associated points of our body in euclidean reference system, that is

$$\mathcal{B}_0 \colon \mathcal{MP} \to \mathcal{B}_0(\mathcal{MP}) \subset \mathbb{R}^3 \qquad \mathcal{B}_0(\mathcal{P}) = \mathbf{X}. \tag{2.1}$$

Let's take the a point $\mathcal{P}$ contained in a chart. A chart is a portion of the manifold from where we can define a reference coordinates for the manifold. We can define the tangent space $\mathcal{TB}_0$ of $\mathcal{MP}$ at $\mathcal{P}$. A tangent space is a vector space $\mathbb{R}^3$ containing all the possible tangent vector from $\mathcal{P}$.

We have given $\mathcal{MP}$, and therefore to $\mathcal{P}$, a place and a reference system. Let's now consider the configuration at time t $\mathcal{B}$ such that

$$\mathcal{B} \colon \mathcal{MP} \to \mathcal{B}(\mathcal{MP}) \subset \mathbb{R}^3 \qquad \mathcal{B}(\mathcal{P}) = \mathbf{x}. \tag{2.2}$$

At this point we have set not only the initial configuration of our body but also a the final configuration, and the reference system associated to that configuration. We adopt in the entire work a Euclidean reference system. This issue have important implication in the description of continuum mechanics and differential geometry in general. The material and spatial metrics called in literature $\mathbf{G}$ and $\mathbf{g}$ renders the second order identity tensor δ_{ij}. As consequence Christtoffel symbols vanish so the covariant derivative correspond to the derivative of a quantity in the direction of $\{\circ\}$ (vector or tensor) for any scalar, vector or tensor.

$$\nabla_{\{\circ\}}\{\bullet\} = \nabla\{\bullet\}[\{\circ\}]. \tag{2.3}$$

And finally, we need to give to our body of a path or a way to move from the initial to the final configuration. We allow to that motion to be reversible, that is invertible at any time. We do that by the so called, material and spatial motion respectively from now on, as

$$\begin{aligned} \varphi : \quad & \mathcal{B}_0(\mathcal{MP}) \to \quad \mathcal{B}(\mathcal{MP}), \phi(\mathbf{x}) = \mathbf{X}(\mathbf{x}, t), \\ \phi : \quad & \mathcal{B}(\mathcal{MP}) \to \quad \mathcal{B}_0(\mathcal{MP}), \varphi(\mathbf{X}, t) = \mathbf{x}(\mathbf{X}, t). \end{aligned} \tag{2.4}$$

It is usual to write, given a composition of function as

$$\begin{aligned} \varphi \circ \mathcal{B}_0(\mathcal{MP}) = &\quad \mathcal{B}(\mathcal{MP}) \\ \phi \circ \mathcal{B}(\mathcal{MP}) = &\quad \mathcal{B}_0(\mathcal{MP}) \end{aligned} \tag{2.5}$$

Remark 1 ***Time derivatives*** *The derivation of a given quantitity with respect to time t have some parcularirties dependending on the features of the configuration frame we are working on. Let's consider a quantity* $\{\bullet\}$ *as a function of material points* $\mathcal{X}$ *and time t. Let's also define other quatity* $\{\circ\}$ *in terms of spatial point* § *and time t. We define the following called material derivatives that representent the time derivatives of material and spatial quantities respectively as*

$$\begin{aligned} D_t\{\bullet\} = &\quad \partial_t\{\bullet\}|_{\mathbf{X}} && \textit{we call it material local derivative} \\ D_t\{\circ\} = &\quad \partial_t\{\circ\}|_{\mathbf{X}} = \partial_t\{\circ\}|_{\mathbf{x}} + \nabla_{\mathbf{x}}\{\circ\} \cdot \mathbf{v} && \textit{we call it material derivative of a spatial quantity} \end{aligned} \tag{2.6}$$

Let's consider that we fixed the spatial position § *and derivate with respect to time, called spatial derivatives.*

$$\begin{aligned} d_t\{\circ\} = &\quad \partial_t\{\circ\}|_{\mathbf{x}} && \textit{we call it material local spatial derivative} \\ d_t\{\bullet\} = &\quad \partial_t\{\bullet\}|_{\mathbf{x}} = \partial_t\{\bullet\}|_{\mathbf{X}} + \nabla_{\mathbf{x}}\{\bullet\} \cdot \mathbf{v} && \textit{for points in the spatial configuration} \end{aligned} \tag{2.7}$$

Let's define two important time derivatives, the velocities of the motion and the inverse of the motion. We call them material and spatial velocity of the motion and are defined (see Remark 1) as

$$\boldsymbol{V}(\mathbf{X}) = \mathrm{D}_t\varphi(\mathbf{X}, t) \quad \text{and} \quad \boldsymbol{v}(\mathbf{x}, t) = \boldsymbol{V}(\mathbf{X}) \circ \phi(\mathbf{x}, t). \tag{2.8}$$

The convective velocity can be obtained by the pull-back of the spatial velocity as $\boldsymbol{\mathcal{V}} = \mathbf{F}^{-1}\boldsymbol{v}$. The $\varphi^*(\bullet)$ define the pull-back and $\varphi_*(\bullet)$ the push-forward operator.

And finally, the acceleration in the different configuration can be expressed as

$$\begin{aligned} \mathbf{A}(\mathbf{X}) = &\quad \mathrm{D}_t \mathbf{V}(\mathbf{X}, t), \\ \mathbf{a}(\mathbf{x}) = &\quad \mathrm{d}_t \mathbf{v}(\mathbf{X}, t) = \nabla_{\mathbf{x}} \mathbf{v} \cdot \mathbf{v} \quad \text{and} \\ \boldsymbol{\mathcal{A}}(\mathbf{x}) = &\quad \mathrm{d}_t \boldsymbol{v}(\mathbf{X}, t) = \nabla_{\mathbf{x}} \boldsymbol{v}, \end{aligned} \tag{2.9}$$

.

2.2 Kinematics

We want to start by recalling some basic notions of the kinematic assumption. The deformation gradient is the tangent of the motion and represents a two-point linear map over the reference configuration. Based on the motion φ we defined the deformation gradient

$$\begin{aligned} \boldsymbol{F}(\boldsymbol{X}, t) &: \mathcal{T}\mathcal{B}_0 \to \mathcal{T}\mathcal{B} \\ \boldsymbol{F}(\boldsymbol{X}, t) &= \nabla_{\boldsymbol{X}} \boldsymbol{\varphi}(\boldsymbol{X}, t) \end{aligned} \tag{2.10}$$

between the tangent spaces $\mathcal{T}\mathcal{B}_0$ and $\mathcal{T}\mathcal{B}$ of $\mathcal{B}_0$ and $\mathcal{B}$ respectively. The Jacobian of the deformation gradient will be denoted as $J = \det(\boldsymbol{F}) > 0$.

Assuming $\boldsymbol{X}$, $\boldsymbol{Y} \in \mathcal{B}_0$ being neighbouring points the material length element

$$\mathrm{d}\boldsymbol{X} \;=\; \boldsymbol{Y} - \boldsymbol{X} \;=\; \mathrm{d}\epsilon = \|\boldsymbol{Y} - \boldsymbol{X}\| \, \boldsymbol{n}_0, \tag{2.11}$$

where the $\boldsymbol{n}_0$ is associated to the material configuration $\mathcal{B}_0$ fulfilling $\|\boldsymbol{n}_0\| = 1$, describing the direction of a material line element at the point $\boldsymbol{X}$.

The deformation gradient $\mathbf{F}$ can be used to express the material line element in its spatial counterpart as $\mathrm{d}\boldsymbol{x} = (\boldsymbol{y} - \boldsymbol{x})$ as

$$\mathrm{d}\boldsymbol{x} \;=\; \boldsymbol{F} \cdot \mathrm{d}\boldsymbol{X} \;=\; \boldsymbol{F} \cdot [\boldsymbol{Y} - \boldsymbol{X}] \,. \tag{2.12}$$

And similarly the vector $\boldsymbol{n}_0$can be transformed into

$$\boldsymbol{n}(\boldsymbol{X},\, t) \,=\, \boldsymbol{F}(\boldsymbol{X},\, t) \cdot \boldsymbol{n}_0. \tag{2.13}$$

$\lambda = \|\boldsymbol{n}\|$ represents the stretch in the direction of $\boldsymbol{n}$.

We also introduce the right and left Cauchy-Green strain tensors

$$\boldsymbol{C} \,=\, \boldsymbol{F}^{\mathrm{t}} \cdot \boldsymbol{F} \quad \text{and} \quad \boldsymbol{b} \,=\, \boldsymbol{F} \cdot \boldsymbol{F}^{\mathrm{t}}, \tag{2.14}$$

which are symmetric and positive-definite tensors.

It is also interesting to represent the polar decomposition of the deformation gradient tensor as

$$\boldsymbol{F} \,=\, \boldsymbol{R} \cdot \boldsymbol{U} \,=\, \mathbf{v} \cdot \boldsymbol{R}, \tag{2.15}$$

$\boldsymbol{R}$ satisfies the relation $\boldsymbol{R}^{\mathrm{t}} \,=\, \boldsymbol{R}^{-1}$, and the stretch tensors $\boldsymbol{U}$ and ,v are unique positive definite symmetric tensors defined in the material and spatial configurations respectively.

The material $\boldsymbol{L}$ and spatial velocity gradient $\boldsymbol{l}$ then takes the following multiplicative representation

$$\boldsymbol{l} = \dot{\boldsymbol{F}} \cdot \boldsymbol{F}^{-1} \qquad \text{with} \qquad \boldsymbol{l} = \nabla_x \boldsymbol{v}, \tag{2.16}$$

and

$$\boldsymbol{L} = \dot{\boldsymbol{F}} \qquad \text{with} \qquad \boldsymbol{L} = \nabla_X \boldsymbol{V}, \tag{2.17}$$

The symmetric part of the spatial velocity gradient defines the spatial rate of deformation tensor $\boldsymbol{d} = \boldsymbol{l}^{\mathrm{sym}}$. Among other quantities, we can also express the material deformation rate tensor as $\dot{\boldsymbol{E}} = \boldsymbol{F}^t \boldsymbol{d} \boldsymbol{F}$. To conclude, the time rate of the Jacobian of the deformation gradient is given by

$$\dot{J} = J \boldsymbol{F}^{-t} : \dot{\boldsymbol{f}} = J \mathrm{div} \mathbf{V}. \tag{2.18}$$

In connection with the modeling of biological tissue the mechanical response

of nearly incompressible material can be multiplicative split as

$$\boldsymbol{F} = J^{\frac{1}{3}}\boldsymbol{I}\cdot\bar{\boldsymbol{F}}. \tag{2.19}$$

where $J^{\frac{1}{3}}\boldsymbol{I}$ is associated to the volumetric part and $\bar{\boldsymbol{F}}$ with the isochoric contribution, so that $\det(\bar{\boldsymbol{F}}) = 1$. And the right and left Cauchy-Green strain tensors transform into

$$\bar{\boldsymbol{C}} = \bar{\boldsymbol{F}}^{\mathrm{t}}\cdot\bar{\boldsymbol{F}} = J^{-\frac{2}{3}}\boldsymbol{C}, \qquad \bar{\boldsymbol{b}} = \bar{\boldsymbol{F}}\cdot\bar{\boldsymbol{F}}^{\mathrm{t}} = J^{-\frac{2}{3}}\boldsymbol{b}. \tag{2.20}$$

and

$$\bar{\boldsymbol{n}} = \bar{\boldsymbol{F}}\cdot\boldsymbol{n}_0 = J^{-\frac{1}{3}}\boldsymbol{n}, \quad \text{and} \quad \bar{\lambda} = \|\bar{\boldsymbol{n}}\| = J^{-\frac{1}{3}}\|\boldsymbol{n}\|. \tag{2.21}$$

Remark 2 ***Objectivity.*** *One of the most important principles of mechanics is the notion of objectivity. This principle comes up from the idea that any quantity describing the behavior of a body remains unchanged when an observer attached to and rotating with the body remain unchanged. Although the nature of such quantity remain unchanged, its description can be altered. This time dependent rotation* $\mathbf{Q}(t) \in SO(3)$ *is a proper orthogonal transformation in the proper orthogonal group. For example, the superimposition of a rigid body motion of two any points preserve distances, so the motion is said to be rigid or isometric. However, there are some tensorial forms that do not transform in this same objectively manner. The velocity gradient tensor* $\mathbf{l} = \dot{\mathbf{F}}\cdot\mathbf{F}^{-1}$ *is one of this non-objective tensor. Stress tensors in spatial configuration are also important tensorial forms that do not transform objectively. This particular quantity will be reviewed later as well as the principle of material frame invariance for hyperelastic description.*

2.3 Stress

Given some forces acting both on the surface of the body and we assumed that this body is cut by a plane passing though a spatial point $\boldsymbol{x} \in \mathcal{B}_t$. A differential surface element $\mathrm{d}s$ in the cutting plane around $\boldsymbol{x}$, characterized by its outward oriented normal $\boldsymbol{n}$. The resultant of the internal forces are $\mathrm{d}\boldsymbol{f} = \boldsymbol{t}\,\mathrm{d}s$, where

$\boldsymbol{t}$ represents the Cauchy traction vector exerted on $\mathrm{d}s$ with outward normal $\boldsymbol{n}$. The counterpart surface element $\mathrm{d}S$ (associated to the $\boldsymbol{X} \in \mathcal{B}_0$ point), and first Piola-Kirchhoff traction vector $\boldsymbol{T}$, defined in the reference configuration as

$$\mathrm{d}\boldsymbol{f} = \boldsymbol{t}\,\mathrm{d}s = \boldsymbol{T}\mathrm{d}S, \tag{2.22}$$

$$\boldsymbol{t} = \boldsymbol{t}(\boldsymbol{x}, t, \boldsymbol{n}) \quad \text{and} \qquad \boldsymbol{T} = \boldsymbol{T}(\boldsymbol{X}, t, \boldsymbol{N}), \tag{2.23}$$

where $\boldsymbol{t}$ and $\boldsymbol{T}$ are usually defined as surface traction.

Cauchy's theorem assumed the existence of unique second-order tensor fields so that

$$\boldsymbol{t}(\boldsymbol{x}, t, \boldsymbol{n}) = \boldsymbol{\sigma}(\boldsymbol{x}, t) \cdot \boldsymbol{n} \quad \text{and} \quad \boldsymbol{T}(\boldsymbol{X}, t, \boldsymbol{N}) = \boldsymbol{P}(\boldsymbol{X}, t) \cdot \boldsymbol{N}, \tag{2.24}$$

where $\boldsymbol{\sigma}$ denotes the symmetric spatial Cauchy stress tensor, while $\boldsymbol{P}$ characterizes the two-point first Piola-Kirchhoff stress tensor.

Given that force does not depend on the body geometry, a relation between the Cauchy stress and the first Piola-Kirchhoff stress tensor must exist, we write

$$\boldsymbol{\sigma}(\boldsymbol{x}, t) \cdot \boldsymbol{n}\,\mathrm{d}s = \boldsymbol{P}(\boldsymbol{X}, t) \cdot \boldsymbol{N}\,\mathrm{d}S, \tag{2.25}$$

Using the Nanson's formula $\mathrm{d}s = J\boldsymbol{F}^{-\mathrm{t}}\mathrm{d}V$, which relates elements in the reference and deformed configurations by making use of the volume ratio, then $\boldsymbol{P}$ and $\boldsymbol{\sigma}$ can be related by

$$\boldsymbol{P} = J\boldsymbol{\sigma} \cdot \boldsymbol{F}^{-\mathrm{t}}. \tag{2.26}$$

In addition to these two measures of stress, other definitions of stress tensors can be described. The spatial Kirchhoff stress tensor, e.g., can be expressed as $\boldsymbol{\tau} = J\boldsymbol{\sigma}$, the second Piola-Kirchhoff tensor, convinient for the definition of constitutive theories is given by $\boldsymbol{S} = \boldsymbol{F}^{-1} \cdot \boldsymbol{\tau} \cdot \boldsymbol{F}^{-\mathrm{t}}$.

We give in the following sections a brief description of the balance equations. Nevertheless, we can move between configuration with push-backs and pull-forward operation in a fashion way.

2.4 Balance of mass

Although biological tissue undergo a huge amount of mass production and transport it is quite usual to treat them as closed system. A closed system it is that one that do not allow mass to cross over the boundary $\partial\mathcal{B}_0$. A closed system is, therefore, characterized by a fixed mass in the system. We call system a collection of matter in space. Let's define a mass density function $\rho(\mathbf{x}, t)$, such that $\mathrm{dm} = \rho(\mathbf{x}, t)\mathrm{dv}$. For the material description the desnsity is given by $\rho_0(\mathbf{X}, t) = \rho(\mathbf{x}, t) \circ \varphi$ and the convective as $\varrho(\mathbf{X}, t) = \rho(\mathbf{X}, t)$. The mass balance laws give, in its spatial, material and convective description respectively,

$$\partial_t \rho + div(\rho \mathbf{v}) = 0 \tag{2.27}$$

$$J\rho_0 = \rho \tag{2.28}$$

$$\partial_t \varrho + Div(\varrho \boldsymbol{\mathcal{V}}) = 0 \tag{2.29}$$

2.5 Balance of linear momentum

To obtain the balance of momentum we identify our three classical terms. The variation with respect to time of the lineal momentum have to be balanced by the external volume specific momentun sources $\rho\mathbf{b}$ and the spatial momentum fluxes σ in the spatial configuration. And as usual with standard transformation we can get the spatial, material and convected terms as

$$\rho\mathbf{a} = \mathrm{div}(\sigma) + \rho\mathbf{b}, \tag{2.30}$$

$$\rho_0\mathbf{A} = \mathrm{Div}(\mathbf{P}) + \rho_0\mathbf{B} \quad \text{and} \tag{2.31}$$

$$\varrho\boldsymbol{\mathcal{A}} = \mathrm{DIV}(J^{-1}\mathbf{S}) + \varrho\mathcal{B}. \tag{2.32}$$

2.6 Balance of angular momentum

The balance of linear momentum required that the time derivative of the moment of linear momentum balance the sum of the moments of the forces acting in the same body. The most important conclusion from this principle is that

$$\boldsymbol{\tau} = \boldsymbol{\tau}^t, \qquad \mathbf{P}\mathbf{F}^t = \mathbf{F}\mathbf{P}^t \quad \text{and} \quad \mathbf{S} = \mathbf{S}^t \tag{2.33}$$

which demonstrate the symmetry of the Kirchhoff and second Piola-Kirhhoff stress tensors.

2.7 Balance of mechanical energy

The balance of the total energy of a system, or a body in this case, is seen as the rate of the volumen specific internal energy V and the cinetic energy of the system T which have to be balanced with the external mechanical work W plus a non-mechanical, usually heat, term Q. In a sketchy way we can see this as

$$d_t(T+E) = W + Q, \qquad \text{where} \tag{2.34}$$

$$\begin{aligned} T+E = &\int_{\mathcal{B}} \frac{1}{2}\rho \mathbf{v}\cdot\mathbf{v} dv + \int_{\mathcal{B}} \rho e dv \\ W = &\int_{\mathcal{B}} \rho \mathbf{b}\cdot\mathbf{v} dv + \int_{\partial\mathcal{B}} \mathbf{t}\cdot\mathbf{v} da \\ Q = &\int_{\mathcal{B}} \rho r dv - \int_{\mathcal{B}} \mathbf{q}_n \cdot \mathbf{n} da \end{aligned} \tag{2.35}$$

From now on any heat source is neglected so $Q = 0$. After some algebra we can get the following localized form

$$\rho d_t e = \sigma : \mathbf{d}, \quad \rho_0 D_t E = \mathbf{P} : \dot{\mathbf{F}} \quad \text{and} \quad \varrho D_t E = J^{-1}\mathbf{S} : \mathbf{D} \tag{2.36}$$

.

2.8 Enthropy inequality

Let's following with the assumption that we do not have any heat source in or into our system, this is an adiabatic system. We also consider that our system is isothemic, so there are not variation of temperature in the system. The enthropy inequality, also known as the Second Law of Thermodynamics or as Clausius-Duhen inequality, set that

$$\frac{d}{dt}\int_{\varphi} \rho\eta dv \geq 0, \tag{2.37}$$

where $\eta(\mathbf{x}, t)$ is the mass-specific entrophy. We can define the production rate of entrophy, as

$$\rho\dot{\eta} \geq 0. \tag{2.38}$$

In terms of the strain energy density function (SEDF) ψ and the internal energy as a Legendre transformation such that $\psi = e - \theta\eta$ and recalling the energy balance law, we get the so called reduced production inequalities, in the different descriptions, as

$$\rho\dot{\psi} - \sigma : \mathbf{d} \geq 0, \qquad \rho_0\dot{\Psi} - \mathbf{P} : \dot{\mathbf{F}} \geq 0 \qquad \text{and} \qquad \varrho\dot{\Psi} - J^{-1}\mathbf{S} : \mathbf{D} \geq 0 \tag{2.39}$$

Remark 3 ***Principle of frame invariance***
The principle of objectivity have to be also required to the strain energy of the body. It is assumed that the SEDF in terms of the deformation gradient $\boldsymbol{F}$ *to be objective or frame indifferent if for a arbitrary motion and a superimposed rigid body motion* $\tilde{\mathbf{F}} = \mathbf{Q} \cdot \mathbf{F}$, $\Psi(\mathbf{F}) = \hat{\Psi}(\tilde{\mathbf{F}}) = \check{\Psi}(\mathbf{U})$ *apply. And it can be demonstrated that choosing* $\mathbf{Q}$ *the right polar decomposition of* $\boldsymbol{F}$, $\Psi(\mathbf{F}) = \tilde{\Psi}(\mathbf{C})$ *directly satisfies the conditions of objectivity. Constitutive equations are usually describe in terms of* $\Psi(\mathbf{C})$ *to avoid objectivity problems.*

2.9 Constitutive equations

A constitutive law is said to be hyperelastic if its strain energy density function per reference volume unit, is a solely function of the deformation, that is, $\Psi(\boldsymbol{F})$. Since neither thermal effects nor entropy variations are considered, the strain energy function must coincide with the free energy variation in these conditions. Based on the Clausius-Planck inequality described in Eq. 2.39, it yields the definition of the second Piola-Kirchhoff stress tensor defined as

$$\mathbf{S} = \partial_{\mathbf{C}} \Psi(\mathbf{C}). \tag{2.40}$$

Any other stress measure in the different configuration can be gathered by the other inequalities in Eq. 2.39 or by means of pull-back or push-forwards operation over the different quantities.

For convenience, it is commonly required that the strain energy function vanishes in the reference configuration, i.e. where $\boldsymbol{F} = \boldsymbol{I}$. This normalization condition implies that no energy is stored in the body in the undeformed state, and therefore

$$\Psi \; = \; \Psi(\boldsymbol{I}) \; = \; 0. \tag{2.41}$$

Since, from physical observations, it has been observed that the strain energy increases with deformation it will be required, in addition to Equation 2.41, that

$$\Psi \; = \; \Psi(\boldsymbol{F}) \; > \; 0. \tag{2.42}$$

Moreover, it will be assumed that the strain energy density function has no other stationary point in the strain space. Note that relations of Equations 2.41 and 2.42 ensure that the residual stress in the reference configuration, namely the residual stress, is zero and, therefore, the reference configuration is stress-free.

Another requirement, for behaviour at finite deformations, is related to the changes of local volume, whose ratio is represented by the Jacobian determinant J. This implies that $\Psi \mapsto +\infty$ if $J = \det(\boldsymbol{F})$ approximates to $+\infty$ or $+0$, which is physically means that an infinite amount of energy is required to expand a

material volume to the infinite range or to compress until vanishing it.

Since most problems involving hyperelastic materials undergoing finite strains are non-linear, the computation of the tangent operator is frequently required in computational mechanics methods in order to solve the problem implicitly. The relation between the directional derivative of $\mathbf{S}$ and $\mathbf{C}$ can be expressed as $2\mathrm{d}\mathbf{S} = \partial_{\mathbf{C}}\mathbf{S} : \mathrm{d}\mathbf{C}$. The term $\partial_{\mathbf{C}}\mathbf{S}$ is usually referred as material elastic tensor $\mathbf{C}$ and its counterparts in other configuration can be obtained by push-forward and pull-back considerations. This linealised version can be solved by means of iterative schemes, which provide an approximate solution of the original problem. The tangent operator, which is basically the derivative of the stress with respect to the strain, is of crucial importance in order to optimize the convergence of those numerical procedures. The number of independent components is reduced to 36 due to the symmetries of $\boldsymbol{S}$ and $\boldsymbol{C}$ and $\mathbf{C}$ has minor symmetries, i.e. $C_{ABCD} = C_{BACD} = C_{ABDC}$. And if a scalar-valued strain energy Ψ function is assumed, $\boldsymbol{S}$ can be derived from Ψ the elasticity tensor can be expressed

$$\mathbf{C} = 4\,\partial^2_{\mathbf{C}}\Psi(\boldsymbol{C}), \tag{2.43}$$

which implies that $\mathbf{C}$ posses major symmetries, i.e. $C_{ABCD} = C_{CDAB}$ so there are only 21 independent components.

As we argued above, constitutive theories in the context of hyperlasticity rely on the definition of a SEDF. Given a SEDF in its material description $\Psi(\mathbf{C})$, and based on the dissipation inequality from classical thermodynamics we can write, neglecting heat sources and thermal effects given the constant temperature of living organs,

$$\Psi(J, \bar{\mathbf{C}}) = \Psi_{\mathrm{vol}}(J) + \Psi_{\mathrm{ich}}(\bar{\mathbf{C}}) \tag{2.44}$$

Ψ_{vol} is related with water content in the cardiovascular tissue. The second term Ψ_{ich} is associated with the isochoric contribution of the deformation gradients. As we describe in deep in next chapter, this later term can be again split in for recover isotropic behavior, related with the elastin and the anisotropic behavior, with the collagen fibers (see remarks 4 and 5). The above decomposition of

the SEDF naturally affects the decomposition of the stresses and the elastic moduli tensor. Following Eq. 2.39 we are able to obtain the stress tensors for every configuration presented above by derivation the Helmholzt free energy by its associated strain measure. We can obtain the second Piola-Kirchhoff stress tensor as

$$\mathbf{S} = \mathbf{S}_{\text{vol}} + \mathbf{S}_{\text{ich}} \quad \text{where} \tag{2.45}$$

$$\mathbf{S}_{\text{vol}} = 2\partial_{\mathbf{C}}\Psi_{\text{vol}} \quad \text{and} \tag{2.46}$$

$$\mathbf{S}_{\text{ich}} = 2\partial_{\mathbf{C}}\Psi(\bar{\mathbf{C}}) = 2\partial_{\bar{\mathbf{C}}}\Psi(\bar{\mathbf{C}}) : \partial_{\mathbf{C}}\bar{\mathbf{C}} = \mathrm{J}^{-2/3}\mathbf{P} : \bar{\mathbf{S}}_{\text{ich}}. \tag{2.47}$$

$\bar{\mathbf{S}} = \partial_{\bar{\mathbf{C}}}\Psi(\bar{\mathbf{C}})$ is the fictitious second Piola-Kirchhoff stress and $\mathbf{P}$ is the fourth order projection tensor in the material reference defined as $\mathbf{P} = \mathbf{I} - 1/3\mathbf{C}^{-1} \otimes \mathbf{C}$ where $\mathbf{I}_{ijkl} = \delta_{ik}\delta_{jl}$ the fourth order identity tensor.

Remark 4 ***Isotropic constitutive laws*** *Isotropy is based on the idea that the stress-strain response of a body have the same behavior in all directions. A SEDF is said to be isotropic if* $\Psi(\boldsymbol{C}) = \Psi(\boldsymbol{F} \cdot \boldsymbol{Q}^t)$ *or* $\Psi(\boldsymbol{C}) = \Psi(\boldsymbol{Q} \cdot \boldsymbol{C} \cdot \boldsymbol{Q}^t)$, $\forall \boldsymbol{Q}^3_+$.

The strain energy function can be expressed in terms of the principal invariants of the isochoric right Cauchy-Green tensor $\bar{\boldsymbol{C}}$ *as*

$$\Psi(\bar{\boldsymbol{C}}) = \Psi(I_1(\bar{\boldsymbol{C}}), I_2(\bar{\boldsymbol{C}}), I_3(\bar{\boldsymbol{C}})), \tag{2.48}$$

and expressed in terms of invariants (Spencer, 1971)

$$I_1(\bar{\boldsymbol{C}}) = tr(\bar{\boldsymbol{C}}),\ I_2(\bar{\boldsymbol{C}}) = \frac{1}{2}\left[\left[tr(\bar{\boldsymbol{C}})\right]^2 - tr(\bar{\boldsymbol{C}}^2)\right] \quad \textit{and} \quad I_3(\bar{\boldsymbol{C}}) = \det(\bar{\boldsymbol{C}}). \tag{2.49}$$

Remark 5 ***Anisotropic constitutive laws***

Anisotropic material are those with different stress-strain behavior depending at the direction of body. The use of structural tensors to introduce anisotropy in material models is one of the most used techniques. The anisotropy is introduced

by unit vectors in the reference configuration and the strain energy density function of material with n directions of anisotropy reads, given that anisotropy is usually included in the isochoric part, as

$$\Psi = \Psi_{ich}(\bar{\boldsymbol{C}}\, \boldsymbol{A}_1, \cdots, \boldsymbol{A}_n), \tag{2.50}$$

where $\boldsymbol{A}_i$, are structural tensor characterizing the anisotropic response of the material associated to the referential unit vector $\boldsymbol{a}_i$ as $\boldsymbol{A}_i = \boldsymbol{a}_i \otimes \boldsymbol{a}_i$.

As well as for the isotropic case, the modeling of incompressible and compressible materials render different expression for the stress and elastic tensor quantities. Based on the kinematic assumption of Equation 2.19, together with the additive split of the strain energy density function, it is possible to express the strain energy function for anisotropic materials as

$$\Psi = \Psi_{vol}(J) + \Psi_{ich}(\bar{\boldsymbol{C}},\, \boldsymbol{A}_1, \cdots,\, \boldsymbol{A}_n). \tag{2.51}$$

And it can be also expressed in terms of invariants. It is usual to take into account

$$\bar{I}_4(\bar{\boldsymbol{C}},\, \boldsymbol{a}_1) = \boldsymbol{a}_1 \cdot \bar{\boldsymbol{C}} \cdot \boldsymbol{a}_1 \tag{2.52}$$

$$\bar{I}_5(\bar{\boldsymbol{C}},\, \boldsymbol{a}_1) = \boldsymbol{a}_1 \cdot \bar{\boldsymbol{C}}^2 \cdot \boldsymbol{a}_1 \tag{2.53}$$

$$\bar{I}_6(\bar{\boldsymbol{C}},\, \boldsymbol{a}_2) = \boldsymbol{a}_2 \cdot \bar{\boldsymbol{C}} \cdot \boldsymbol{a}_2 \tag{2.54}$$

$$\bar{I}_7(\bar{\boldsymbol{C}},\, \boldsymbol{a}_2) = \boldsymbol{a}_2 \cdot \bar{\boldsymbol{C}}^2 \cdot \boldsymbol{a}_2 \tag{2.55}$$

$$\tag{2.56}$$

Then the strain energy function can be expressed as

$$\Psi = \Psi_{vol}(J) + \Psi_{ich}(\bar{I}_1,\, \bar{I}_2,\, \bar{I}_4,\, \bar{I}_5,\, \bar{I}_6). \tag{2.57}$$

To obtain the tangent moduli, quantity that relate momentum fluxes and strains, is essential for a consistent finite element implementation. We can evaluate the total derivative of the **S** with respect to **C** as a direct definition, and

split again into volumetrixc-isochoric terms

$$\mathbf{C} = 2\partial_{\mathbf{C}}\mathbf{S} = 2\partial_{\mathbf{C}}\mathbf{S}_{vol} + 2\partial_{\mathbf{C}}\mathbf{S}_{ich} = \mathbf{C}_{vol} + \mathbf{C}_{ich}. \tag{2.58}$$

The volumetric contribution to the elastic tensor end up as

$$\mathbf{C}_{vol} = 2J[p + J\partial_J p]\mathbf{C}^{-1} \otimes \mathbf{C}^{-1} - 2Jp\mathbf{C}^{-1} \odot \mathbf{C}^{-1}, \tag{2.59}$$

.

And the isochoric contribution does as

$$\mathbf{C}_{\text{ich}} = \mathbf{P} : \overline{\mathbf{C}} : \mathbf{P}^t - 2/3\text{Tr}(J^{-2/3}\mathbf{S}_{\text{ich}})\tilde{\mathbf{P}} - 2/3[\overline{\mathbf{S}} \otimes \mathbf{C}^{-1} + \mathbf{C}^{-1} \otimes \overline{\mathbf{S}}], \tag{2.60}$$

where $\tilde{\mathbf{P}} = \mathbf{C}^{-1} \odot \mathbf{C}^{-1} - 1/3\mathbf{C}^{-1} \otimes \mathbf{C}^{-1}$ and $\bar{\mathbf{C}} = 2\, J^{-4/3}\partial_{\bar{\mathbf{C}}}\bar{\boldsymbol{S}}$.

Remark 6 ***Identity tensors and diadic products.*** *For the use in the entire work we summarize some notations. We use the fourth order identity tensor and fourth order symmetric tensor as*

$$\mathbf{I}_{ijkl} = \delta_{ik}\delta_{jl} \quad \textit{and} \quad \mathbf{I}^{sym}_{ijkl} = \frac{1}{2}[\delta_{ik}\delta_{jl} + \delta_{il}\delta_{kj}]. \tag{2.61}$$

In connection with this expression we define the standard and two non-standard diadic product as

$$\begin{aligned}
(\{\bullet\} \otimes \{\circ\})_{ijkl} &= \{\bullet\}_{ij}\{\bullet\}_{kl}, \\
(\{\bullet\} \bar{\otimes} \{\circ\})_{ijkl} &= \{\bullet\}_{ik}\{\bullet\}_{jl} \quad \textit{and} \\
(\{\bullet\} \underline{\otimes} \{\circ\})_{ijkl} &= \{\bullet\}_{il}\{\bullet\}_{jk} \quad \textit{and} \\
(\{\bullet\} \odot \{\bullet\})_{ijkl} &= 1/2[\{\bullet\}_{ik}\{\bullet\}_{jl} + \{\bullet\}_{il}\{\bullet\}_{jk}].
\end{aligned} \tag{2.62}$$

Remark 7 ***Objectives stress rates*** *To properly define the constitutive equation in the updated lagrangian approach that it is followed in this work a proper definition of the stress rate is needed. In contrast with the objective nature of the stress tensor, its material derivative is not objective. In the spirit of getting the hyperelastic rate constitutive equation the variation of the Kirchhoff stress tensor*

have to be derived properly. The Lie derivative of a spatial quantity is defined as the push-forward of the material time derivative of its pull-back, provide the needed tool, expressed as

$$\mathcal{L}(\bullet) = \varphi_*(D_t\varphi^*(\bullet)). \tag{2.63}$$

The known as Jaumann rate, given by the Lie derivative of the Kirchhoff stress tensor, neglecting the stretch components of $\boldsymbol{F}$*, can be expressed*

$$\mathcal{L}_v(\boldsymbol{\tau})|_{\mathbf{l}=\mathbf{w}} = \overset{\circ}{\boldsymbol{\tau}} = D_t\boldsymbol{\tau} + \boldsymbol{\tau}\cdot\mathbf{w} + \mathbf{w}\cdot\boldsymbol{\tau}, \tag{2.64}$$

with $\mathbf{w} = \dot{\mathbf{R}}\mathbf{R}^T$.

3

Structure and Passive Behavior of the arterial tissue

The artery wall has been object of research since a long time ago. The vessel wall is the conduit responsible for driving the blood flow from the heart all over the body. It is, together with the heart, key factors in terms of feeling and supplying the extra pressure needed to transport nutrients to the organs and tissue. Arteries can suffer from different diseases as we pointed out in the Introduction chapter. Any of these diseases can modify or cancel the normal work of the organism. This is the reason why the study of the arteries, whether from a biological or a mechanical point of view, has gained so much attention. What we could call normal behavior of materials, as a purely mechanical response to stimulus, is only a small part of the biological tissue behavior. They do underlie damage, plastic and viscoelastic behavior, as many conventional materials (rubbers, steel, aluminum etc.). But they also present a very active component where chemical reactions, cell synthesis and apoptosis, electrical signaling etc., are involved in its response.

In this Chapter we focus on the mechanical response of the arterial wall, where no other chemical, active or any other kind of response is assumed. The vessel wall is a very complex, heterogeneous material. Arteries show a bunch of characteristic mechanical properties. They present a high level of incompressibility due to a high

water content ($\approx 70\%$), a high non-linear response primarily due to the collagen fibers that made up this tissue and they also show a complex microstructure where different layers and structural organization of its components can be found. We focus on these features over the next sections as we review some experimental data found in literature and provide a constitutive model to characterize them. Finally we reconstruct a patient specific carotid artery geometry in a finite element model, which is used over the entire work to check the performance of our models in a real artery geometry.

3.1 Structural organization

Arteries are made up of three main components and have a clear composite-like **structure** (Fung, 1990). The arterial wall has three differentiated layers called intima, media and adventitia (Clark and Glagov, 1985). The *intima* layer is a thin sheet of endothelial cells (Fig. 3.2(a)) and is the one in contact with the blood flow and taking care of the mechanotransduction due to fluid dynamic changes (Runanyi et al., 1990). We study some aspects of this phenomenon in Chapter 6. The *media*, the next layer in radial direction, is made of sheets of elastin fibers randomly packed. In most of the arteries SMC are placed in a preferential circumferential direction and bundles of collagen fibers are placed along the SMC. Arteries are also classified by muscular and elastic arteries depending on the percentage of each constituent. Elastic arteries have a high content of elastin and collagen and they are the vessels in a closer distance from the heart and usually called large and medium size arteries. Muscular arteries have a higher percentage of SMC and they are further away form the heart constituting medium and small size arteries. The *adventitia* is made of collagen in a more random fashion. Fibroblast are also an important component of adventitia and are mainly the responsible of the synthesis of collagen (Bell et al., 1979). O'Connell et al. (2008) shows a nice reconstruction of a pig aorta artery (see Fig. 3.1) where we can observed all these properties.

In terms of its **components**, elastic fibers, collagen and smooth muscle cells (SMC) are the responsible to accomplish structural purposes.

Elastic fibers (Fig. 3.2(b)) are bundles of elastin proteins, secreted mainly by fibroblast and SMC, and fibrillin-microfibrils, secreted by fibroblast and which are essential for the correct formation of the elastic fibers (Rosenbloom et al., 1993). Fibrillin is secreted into the ECM forming microfibrils which have been seen to provide a scaffold-like structure for elastin deposition and play a key role in deposition of tropoelastin (Kielty et al., 2002).

*[Confocal laser scanning microscopy reconstruction. In (a) the elastin (green), SMC (blue) and collagen fibers (red). (b) represent the elastin, (c) SMC and (d) the collagen bundles.]

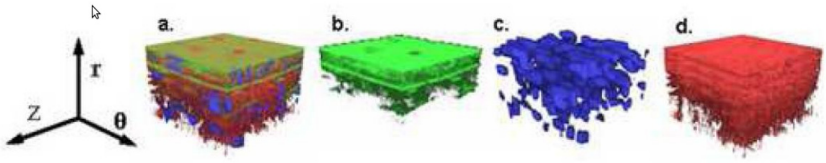

*[Scanning electron microscopy reconstruction.]

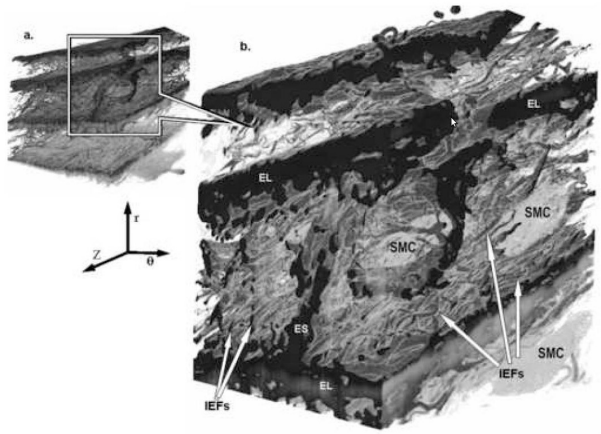

Figure 3.1: Microstrutural representation of rat aorta (O'Connell et al., 2008).

These components have different elastic properties. Sherratt et al. (2003) investigate the stiffness of fibrillin micro-fibrils. They reported Young's modulus values of 78-96 [MPa]. They suggested that these elements behave as reinforcement of the elastin fibers. Lillie et al. (1998) also showed that removal of fibrillin

within the arterial tissue decreased the Young's modulus at low strain while slightly increasing at higher strains also suggesting the stiffening role of fibrillin micro-fibrils. However, how they interact to increase the overall stiffness of the tissue is not yet well understood. Mechanical characterization of elastic fibers have been reported in the literature for bovine ligament in the order of 0.4-1.2 [MPa] (Aaron and Gosline, 1981), in equine ligament (Koenders et al., 2009) from to 0.3-1.5 [kPa] and 0.56-0.74 [MPa] for the fibrillin-microfibrils. These authors stated that microfibrils are not essential in the mechanical behavior of elastic fibers in vertebrates. Sherebrin (1983) reported values for the elastic fibers in dog and sheep aorta in the rage of 0.13-0.65 [MPa], which are in accordance with other experimental findings.

Elastin has important flexibility and extensibility features for blood vessels and endows the ECM with resilience during the loading of the cardiac cycle. The elastic fibers are randomly packed forming sheets. During pathological conditions (Kielty, 2006), e.g. cardiovascular diseases, there exist remodeling and turnover of elastin which lead to the modification of the mechanical properties of the arterial wall.

Structurally, *collagen* (Fig. 3.2(c)) is the most important protein found in many connective and fibrous tissues. The extracellular collagen molecule, procollagen, is made up of three left-handed helix polypeptides, the so-called α-chains, coiled-up in a right-handed helical structure, about 300 nm long and 1.5 nm in diameter (Bella et al., 1994; Orgel et al., 2001; Bhattacharjee and Bansal, 2005). Collagen molecules assemble along a given direction through covalent bonds to form collagen microfibrils, constituting the basic building block of collagen fibrils (Baselt et al., 1993; Hulmes et al., 1995; Orgel et al., 2006, 2011). Collagen fibrils are gathered in the extracellular matrix to form bundles of collagen fibers. Fig.3.2(c) shows a representation of such structure.

Collagen bears the major part of the load transmitted through the tissue, and a lot of research has been devoted to understand its hierarchical microstructure at and across the different scales (see Fratzl (2008) for a review). Its highly non-linear behavior makes the arterial wall to "block" under too large deformation preventing the tissue to damage. Strain of collagen fibers is achieved by stretching

of collagen molecules and fibril sliding.

Mechanical properties of the different scales of collagen, in molecules (Bozec and Horton, 2005), fibrils (Wenger et al., 2007) and fibers (Silver et al., 2003) have been well studied. We encourage the reader with the thesis works of van der Rijt (2004) and Yang (2008) who did an extensive experimental work characterizing collagen fibrils. Although the mechanical properties of the different collagen hierarchical constituents is well understood, the mechanisms by which all the levels interplays represents a more complicated process and the connections from different scales is more poorly known. A complete understanding of these mechanisms would allow to predict the macroscopic behavior of collagen fibers by means of the behavior of its smaller structures. It is known, however, that in a first strain regime, molecular stretching predominates and beyond that point slipping of fibrils take place (Sasaki and Odajima, 1996). Sasaki and Odajima (1996) show how as we move from smaller (molecule) to higher scale stiffness of the structure decreases due to the different cross-liking mechanism between scales. Moreover, the waving at which collagen fibrils ensemble into the ECM to form collagen bundles also modifies the behavior of the tissue.

As in elastin, collagen also experiences a very important turnover both in healthy and different pathologies. We address some of these issues in Chapter 5.

Smooth Muscle Cells (SMC) (Fig. 3.2(d)) are a very important part of the puzzle in terms of its active response. SMC accomplish the so called myogenic tone. SMC react mechanically to external stimuli by contraction or dilating the vessel. SMC also have the important role of synthesizing different kind of biological substances which make the arterial tissue to remodel.

Finally, we would like to point out an important feature of arterial tissue related to the SMC, the myogenic tone. As we barely described above, myogenic tone is an active force exterted by SMC during the cardiac circle. This force is used to accomodate the arterial tissue to the pressure load to maintain normal values of stress and strain in the arterial wall. Normal myogenic tone can be changed, and exert larges forces, when blood pressure increases, e.g. in hypertensive disease. Myogenic tone is also an key factor in small arteries and arterioles which, due to neurological mechanisms, contract and increase the blood

(a) Endothelial layer (SCIENCEphotoLIBRARY, 2013).

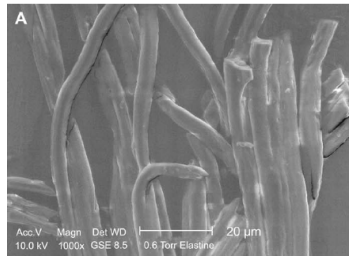

(b) Elastic fibers (Koenders et al., 2009).

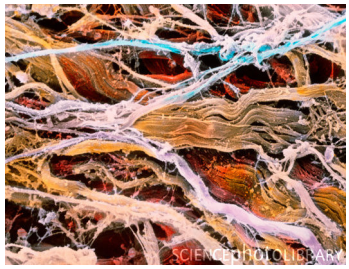

(c) Collagen fibrils packed in fibers (SCIENCEphotoLIBRARY, 2013).

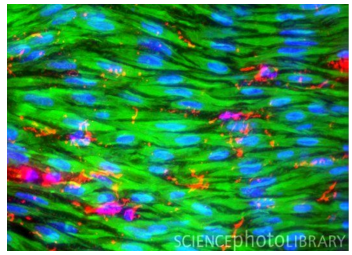

(d) Smooth muscle cells (SCIENCEphotoLIBRARY, 2013).

Figure 3.2: Microstrutural components of arterial tissue.

pressure gradient between the heart and capillaries. This process is one the main mechanisms by which essential hypertension occurs. There are come attemps in literature to model this behavior, see e.g. (Zulliger et al., 2004; Murtada et al., 2010). In the first one the authors propose a SEDF to incorporate the active contraction and relaxation of the SMC while the second relies on a kinematic model of the cells based on Ca^{+} and K concentrations.

All these material features are important in order to properly characterize the arterial wall. During the next Sections we particularize to different models to capture the carotid artery behavior.

3.2 The carotid artery: Previous studies and models

The carotid artery have been widely studied in literature because of it is prone to develop atherosclerosis, stenosis, remodeling, etc. Experimental results in carotid artery are wide in literature but they used to be focused on a specific issue of the tissue, using different species on human, pig, dog, etc. Some of them rely on the mechanical properties of the wall using uniaxial or inflation test. Others also present values of the pre-stretch of the carotid or micro-structural features of the material. However there are few of them where a complete characterization of the tissue is performed for a specific study, therefore the researcher have to rely on different studies from different samples, species, etc. Here, we review two studies (Garcia et al., 2011; Sommer and Holzapfel, 2012) that, for our understanding, present the most completed set of experimental tests.

First, it is convenient to present the constitutive modeling, which is the same for both studies. They were interested in the mechanical properties of the mechanical behavior of the tissue. These authors used a hyperelastic framework (see Chapter 2) to characterize the tissue and used the same constitutive model use to fit the experimental findings. The elastin, which is usually described with a isotropic behavior, was described with a Neo-Hookean model as

$$\Psi_{\text{elas}}(\overline{I}_1) = C_{10}[\overline{I}_1 - 3] \tag{3.1}$$

where μ is a stress-like parameter and $\overline{I}_1 = \text{tr}(\overline{\mathbf{C}})$ is the first invariant of the isochoric part of the deformation. The isochoric Piola-Kirchhoff stress reads as in Eq. 3.2 while the isochoric elastic tensor $\partial^2_{\overline{\mathbf{C}}}\Psi_{\text{elas}}(\overline{I}_1)$ nulls in this case.

$$\mathbf{S}_{iso} = \partial_{\overline{\mathbf{C}}}\Psi_{\text{elas}}(\overline{I}_1) = \partial_{\overline{I}_1}\Psi_{\text{elas}}(\overline{I}_1)\partial_{\overline{\mathbf{C}}}\overline{I}_1 = C_{10}I_1\mathbf{I} \tag{3.2}$$

For the description of the collagen fibers, they adopted the exponential-type

model presented by Holzapfel et al. (2005), which is given as follows.

$$\Psi_{\text{coll}}(\overline{I}_1, \overline{I}_4) = \begin{cases} 0, & \text{if } \overline{\lambda} < 1 \\ \dfrac{k_1}{2k_2}[\exp(k_2[(1-\rho)[\overline{I}_1 - 3]^2 + \rho[\overline{I}_4 - 1]^2) - 1] & \text{if } \overline{\lambda} \geq 1 \end{cases} \tag{3.3}$$

where $k_1 \in \mathbb{R}^+$ represents a stress-like parameter, $k_2 \in \mathbb{R}^+$ measures the exponential behavior of the response, $\rho \in \mathbb{R}, \rho \subset [0, 1]$ represents a measure of the dispersion of collagen. $\overline{I}_4 = \overline{\mathbf{C}} : \mathbf{N}$ is the isochoric anisotropic invariant with $\mathbf{N} = \mathbf{n} \otimes \mathbf{n}$, being $\mathbf{n}$ the direction of the fibers. This model represents a symmetric helicoidal distribution of the fiber within the vessel thickness. For more information of this model, as well as a with other constitutive models, we address to Holzapfel et al. (2005).

Other important issue when studying arterial tissue is the residual stresses within the arterial wall. Residual stresses were shown for the first time in Fung and Liu (1989) to be an important feature of arterial tissue. It has been hypothesized that they play a role to maintain physiological stresses in the arterial wall. The modeling of pre-stress have been described from a kinematic point of view. The usual way to characterized residual stresses is to cut the artery up in rings and then longitudinal to release those stresses in the circumferential direction. The final geometry of the ring once cut is taken to describe the stress-free state of the tissue. Further discussion is addressed in following section.

Remark 8 ***Pre-stress in biological tissue.*** *It has been also pointed out the importance of pres-stress in the behavior of arterial tissue. It is not clear if this feature is associated to the elastin, collagen or SMC. Moreover, if this is associated to collagen or elastin fibers is neither clear if these elements achieve this residual stress by generating an active force by themselves, which seem awkward, or if it comes from the state at which collagen and elastin is deposited. It could be suggested that not incorporating the residual stresses do not reflect the actual behavior of the artery. At some extend we could agree with that statement. However, given the phenomenological models of arterial tissue this argument seems also arguable since the fitting experimental results in samples with residual stresses*

are, in somehow, taking into account the pre-stress behavior.

Remark 9 ***Pre-stress and layered arteries.*** *Delfino et al. (1997) presented a well known example in literature. In that work they investigate they influence of residual stresses in a carotid artery. One should point out that they do not consider media and adventitia layers in that model, which have been reported to have very different mechanical properties. They asses that, after imposing a deformation from a stress-free cut configuration to achieve a no loading state and applying the physiological pressure, the stress over the thickness is more uniform in the model with residual stress than in the model without. The initial point of such a statement is somehow not accurate since they are starting from a wrong hypothesis, considering that stress over the arterial wall is homogeneous which given the different behavior of the arterial layers is not possible. Moreover we can argue about how those results were achieved. They took material parameters from a pressure-radio test. Those material parameters were obtained in a non residual stress free configuration so in somehow those material parameters gather the features of the the pres-stress state. In fact, we would argue that imposing a deformation to achieve a non loaded with residual stress material parameters should be collected from a stress free state, otherwise those effects are considered twice. The most correct way to proceed would be to asses the material parameters of stress free tissue and after that apply some technique to deal with the residual stresses. If that tissue would be tested in a stress free state those material parameters would be different. Moreover they did not include layered specific properties, setting an averaged material parameter over the thickness. In short, we want to state that, even known the residual stress state of arteries, the phenomenological approach of mechanical models allow to incorporate information of the pre-stress within the material parameters although a kinematic description, when available, provides a more accurate approach. In any case, although a well described in literature we are not considering pre-stress in our models in a kinematical description.*

3.2.1 Pig carotid artery experiments and fitting

The first of the two works was done by Garcia et al. (2011) using pig carotid arteries in their studies. They performed uniaxial tests in both longitudinal and circumferential directions of the vessel to find the material parameters. They focused on the proximal and distal sides of the common carotid artery. In this case, they cut the arterial wall into circumferential and longitudinal strips which were after tested in uniaxial tests. The fitting problem relies on minimizing the following objective function

$$\mathrm{E}^2 = \sum_{j=1}^{n} \left[\left[\sigma_c^j - \hat{\sigma}_c^j \right]^2 + \left[\sigma_l^j - \hat{\sigma}_l^j \right]^2 \right] \tag{3.4}$$

where j represents every experimental data point, σ_l^j is the Cauchy stress in longitudinal direction achieved by the constitutive model and $\hat{\sigma}_l^j$ the stress obtained from the experimental test. σ_c represents circumferential stresses as depicted in Fig. 3.3. The goodness of the fitting was measured by computing the coefficient of determination R^2, defined as $R^2 = 1 - \frac{\Sigma_{j=1}^{n}(\sigma - \hat{\sigma})_j^2}{\Sigma_{j=1}^{n}(\sigma - \mu)_j^2}$ where σ^j and $\hat{\sigma}^j$ represent the measured and the fitted stress values for the jth point respectively and μ the mean value of the measured stresses $\mu = \frac{\Sigma_{j=1}^{n}\sigma^j}{n}$. Also the normalized mean square root error ε was computed for each fitting $\varepsilon = \frac{\sqrt{\frac{\chi^2}{n-q}}}{\mu}$. In this equation q is the number of parameters of the SEF, so $n - q$ is the number of degrees of freedom, and μ the mean stress already defined above. θ is the angle of the fibers with respect to the longitudinal direction (see Fig. 3.3). The material parameter results are shown in Tables 3.1 and 3.2 for the proximal and distal specimens respectively.

Remark 10 ***The fitting problem.*** *Usually, fitting of material parameters of a constitutive model gives a set of values that can or can not have an actual biological meaning. A non-constraint minimization problem is prone to such non-uniqueness of the results. To this end, some limitation to the optimization problem should be provided. Information of the micro-strutural organization of the constituent, layer specific test, material content of every constituent, etc., can*

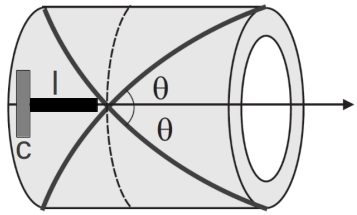

Figure 3.3: Representation of the longitudinal (l) and circumferential (c) strips and the angle of the fibers.

Specimen	C_{10} [MPa]	k_1 [MPa]	k_2 [-]	$\theta[^o]$	ρ [-]	ε [-]
- *I*	0.019	0.003	4.020	88.798	0.210	0.097
II	0.010	0.027	5.299	89.609	0.652	0.125
III	0.010	0.016	2.675	61.228	0.672	0.059
IV	0.011	0.006	1.468	89.469	0.625	0.103
V	0.0120	0.018	8.562	89.439	0.846	0.039
VI	0.007	0.019	1.246	89.999	0.618	0.081
VII	0.015	0.003	1.535	89.984	0.605	0.051
VIII	0.017	0.001	2.231	86.186	0.285	0.028
IX	0.0106	0.024	2.948	89.937	0.873	0.067
X	0.013	0.004	2.364	52.797	0.465	0.099
XI	0.019	0.016	2.390	84.605	0.049	0.062
XII	0.011	0.013	1.839	89.953	0.514	0.077
XII	0.013	0.011	1.564	89.999	0.543	0.050
XIV	0.018	0.008	0.784	89.923	0.675	0.033
Mean	0.013	0.012	2.780	84.423	0.545	0.069
SD	0.003	0.008	2.037	11.839	0.230	0.028
Mean curve	0.010	0.013	1.664	73.963	0.575	0.052

Table 3.1: Material constants obtained for the proximal curves obtained from Garcia et al. (2011).

help to minimize the ill-possesness of the problem.

In an attempt to get extra information, Garcia (2012) also performed polarized light microscopy studies in order to find the preferential direction of the collagen fibers as well as a statistical dispersion of those fibers with respect to the mean preferential direction as represented in Fig. 3.4. For the visualization of the collagen fibers, picrosirius red staining with the polarization method enhances the light intensity due to the birefringence of the collagen, (Borges et al., 2007; Junqueira et al., 1979). Picrosirius red is not a selective stain for collagen fibers

Specimen	C_{10} [MPa]	k_1 [MPa]	k_2 [-]	$\theta[^o]$	ρ [-]	ε [-]
I	0.010	0.022	7.457	89.934	0.696	0.068
II	0.010	0.023	12.324	89.819	0.795	0.095
III	0.010	0.025	6.495	59.233	0.857	0.100
IV	0.010	0.218	0.826	72.928	0.925	0.194
V	0.010	0.070	3.405	89.999	0.818	0.085
VI	0.002	0.066	1.466	89.999	0.869	0.109
VII	0.010	0.024	7.269	55.848	0.933	0.082
VIII	0.010	0.013	2.353	89.193	0.759	0.061
IX	0.010	0.041	4.825	89.062	0.915	0.117
X	0.010	0.024	2.384	89.867	0.770	0.089
XI	0.010	0.013	2.198	89.999	0.686	0.074
XII	0.010	0.048	5.447	58.550	0.903	0.079
XII	0.010	0.016	2.232	68.086	0.614	0.062
XIV	0.010	0.044	2.194	86.606	0.810	0.062
Mean	0.009	0.046	4.348	79.937	0.811	0.091
SD	0.002	0.052	3.174	13.781	0.098	0.034
Mean curve	0.010	0.025	3.278644	85.363	0.765	0.071

Table 3.2: Material constants obtained for distal curves obtained from Garcia et al. (2011).

although it provides a minimum amount of optical dispersion. The optical dispersion is the variation of refractive index with changing wavelength. By means of this technique it is possible to better recognize the zones of collagen due to the low dispersion. Picrosirius polarization method shows a different color when compared with regions that present collagen type III (Junqueira et al., 1979) sites containing collagen type I. This approach represents a feasible method for the study of collagen turnover under pathological conditions because the birefringence property shows different pattern in comparison with collagen fibers in a normal tissue (Borges et al., 2007).

Garcia (2012) found that collagen fibers are mainly located in a circumferential direction for both the distal, Fig. 3.4(a), and proximal location, Fig. 3.4(b), and for all the specimens, Fig. 3.4(c). These experimental results also showed a markedly concentrated distribution of the fibers. They used this information to feed the optimization problem providing the orientation and distribution of the collagen fiber bundles, so these parameters were kept fixed while varying the rest of parameters. When they included these values in the optimization problem to obtain the set of parameters that best fit the mechanical behavior, found out that

it was not possible to obtain a good enough set of parameters. The orientation of the fibers obtained from the polarization, as we said, was markedly oriented in circumferential direction which means that the behavior of the circumferential and longitudinal direction differ further than a structure with helicoidal fibers. The problem was only possible to fit when considering the angle of the fibers variable although this would go against the experimental findings. Therefore there should be something in the approach that the authors used. This could be because the chosen constitutive model was not appropriate to fit this material.

Finally, and to the same end of collecting as much information as possible to feed the modeling problem Garcia (2012) studied the composition content of the three main constituents of the artery, elastin, collagen and SMC. They performed histological studies for both pig and human carotids, reporting the results in Table 6.1.

Pig			
	ϕ_{col}	ϕ_{elas}	ϕ_{SMC}
Proximal	$14.9 \pm 2.3\%$	$52.6 \pm 6.7\%$	$31.0 \pm 3.3\%$
	ϕ_{col}	ϕ_{elas}	ϕ_{SMC}
Dismal	$23.5 \pm 3.9\%$	$19.6 \pm 4.1\%$	$44.3 \pm 4.2\%$
Human			
	ϕ_{col}	ϕ_{elas}	ϕ_{SMC}
Proximal	$24.8 \pm 5.4\%$	$41.1 \pm 5.4\%$	$27.1 \pm 3.2\%$
	ϕ_{col}	ϕ_{elas}	ϕ_{SMC}
Dismal	$29.5 \pm 1.1\%$	$21.9 \pm 8.7\%$	$39.8 \pm 4.0\%$

Table 3.3: Composition of pig carotid artery of elastin, collagen and SMC measured by Garcia (2012).

Remark 11 ***Variability of material parameters.*** *One of the most odd aspects about these studies dealing with biological tissues are the large variability of the material parameters. At some extent it could look like unusual how these parameters can differ so much. There are important differences in the content reported in the literature. Material parameters, describing both elastin and collagen also differ, which should indicate that elastin and collagen are very different from species, from same species and even within close spots of the some tissue. We do not know from any report that state that collagen or elastin molecules and fibrils have different properties based on the type of artery or even species.*

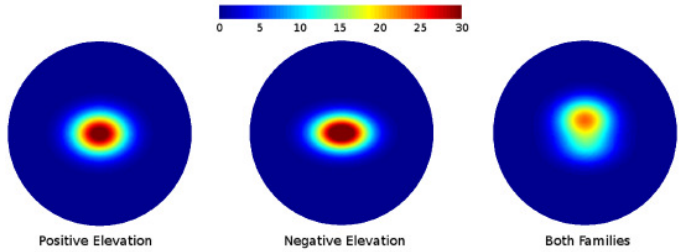

(a) Proximal specimens

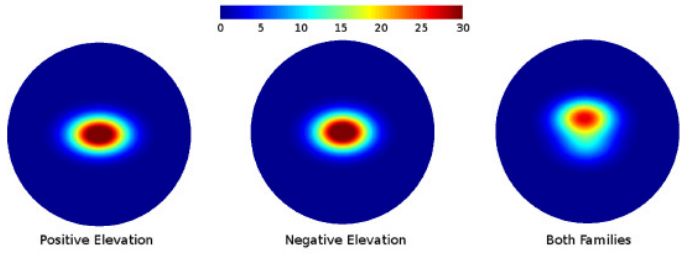

(b) Distal specimens

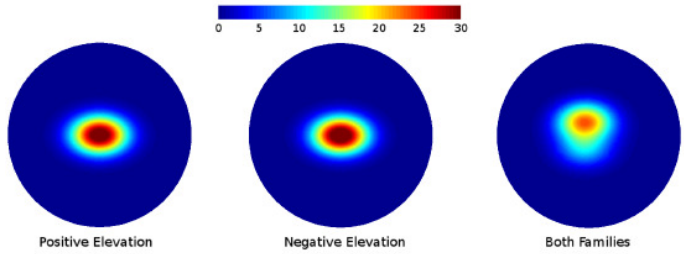

(c) All specimens

Figure 3.4: Bingham fitted functions for the micro structural organization of collagen by Garcia (2012). It represented the probability of finding a collagen fibrils in a given direction of space.

Therefore, the material parameters should have some kind of relation between the actual mechanical behavior of the material and the amount of that material.

However, the main concern about this study was the lack of information about the mechanical properties of the two differentiated layers, which have been shown

to have a very different behavior. And although some residual stresses information was collected, it was not incorpareted later in the constitutive relation.

3.2.2 Human carotid artery

Sommer and Holzapfel (2012) provided data from human carotid arteries tested by inflation test. A general strategy to fit these material parameters is to consider an analytical thick wall problem under pression and axial stretch. We refer to Holzapfel et al. (2000) for the complete developed equations. They presented a bunch of experimental results of pressurized vessels and stretch imposed in axial direction. In a series of papers they provide both residual stresses and mechanical behavior of human carotid arteries. At the end, the problem relies on finding a set of material parameters that best fit a pressure-stretch test for the particular expression of σ_{tt}, σ_{rr} and σ_{zz} see, e.g., Holzapfel et al. (2000).

The material parameters are obtained by means of a non-linear least-square optimization by minimizing the following objective function.

$$\mathrm{E}^2 = \sum_{j=1}^{n} \left[\left[p_j - p_j^{\psi} \right]^2 + \left[F_j - F_j^{\psi} \right]^2 \right] \tag{3.5}$$

with

$$p = \int_{r_i}^{r_0} (\sigma_{rr} - \sigma_{tt} \frac{\mathrm{dr}}{\mathrm{r}}) \qquad \text{and} \tag{3.6}$$

$$F_z = \int_{r_i}^{r_0} (2\sigma_z - \sigma_{rr} - \sigma_{tt}) \mathrm{rdr} \tag{3.7}$$

The results achieved in this work for the common carotid artery (CCA) and the internal carotid artery (ICA), where pres-stress was included, is summarized in Table 3.4. For more specific data we refer to Sommer and Holzapfel (2012) where some data for the different specimens are provided.

Remark 12 ***Age-related data.*** *Looking at the results and the specimens used by Sommer and Holzapfel (2012) one could argue that the sample represents a old sample field. As it is explained in that work, the carotid arteries were extracted from a mean 74 years old humans. It is well known that arterial wall stiffens*

	$C_{10}[kPa]$	k_1 $[kPa]$	k_2 $[-]$	$\theta[^o]$	$\rho[-]$
CCA adv Mean	59.6	180.9	109.8	30.1	0.8
CCA adv SD	33.8	316.6	104.4	10.6	0.1
CCA media Mean	122.3	24.7	16.5	6.9	0.8
CCA media SD	12.2	10.7	9.3	2.4	0.2
ICA adv Mean	28.3	112.1	100.6	31.8	0.9
ICA adv SD	59.5	179.1	101.1	11.2	0.1
ICA media Mean	17.6	21.3	17.3	9.8	0.8
ICA media SD	17.8	10.3	9.5	2.9	0.2

Table 3.4: Results of material parameters fitted for inflation test for the CCA and ICA for the adventitia and media layers provided by Sommer and Holzapfel (2012).

during the lifetime. In this study they also reported material content and gave the results shown in Table 3.5. As it can be seen the value of elastin, and mainly of collagen seems too high compared to previous values and other data (see Table 3.6) in literature (Humphrey and Rajagopal, 2003). This could be related to the old age of samples and therefore to the stiff response of those samples.

ϕ_{col}	ϕ_{elas}	ϕ_{SMC}
$59 \pm 8\%$	$31 \pm 6\%$	$10 \pm 3\%$

Table 3.5: Percentage of the material constituents, elastin, collagen and SMC given by Sommer and Holzapfel (2012).

In connection with Remark 8 we also performed the material fitting including the residual stresses as an example of the residual stresses role on phenomenological models. We have fixed the angle of the fibers to reduce variability. In the following figure we present the fitting curves by Sommer and Holzapfel (2012) with and without pretension. The pre-stress is introduced by kinematical consideration as is described in, e.g., Holzapfel et al. (2000). Results of the fitting procedure were almost identical for the C_{10} and k_1 and the angle of the fibers, only k_2 increase $\approx 10\%$. This results indicate that pre-stress provide a higher stiffness at higher strain values. However, it can not be concluded further details of the actual pre-stress disposition of the fibers and how this phenomenon occurs by means of this kind of data.

However the biggest problem we deal with in this fitting problem is the non-

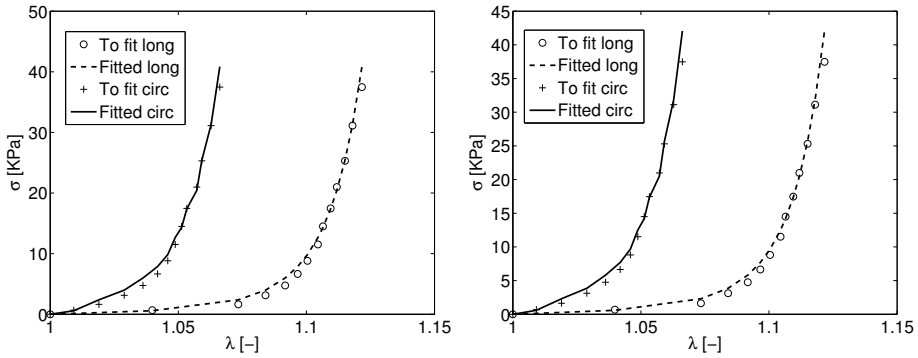

(a) Fitting without considering pre-stress.

(b) Fitting considering pre-stress.

Figure 3.5: Numerical fitting with and without considering residual stresses using data from Sommer and Holzapfel (2012).

uniqueness of solution. In fact, we can gather a good fitting with different set of parameters. In the next section we will try to reduce these drawbacks.

3.3 A new approach toward microstructural fitting

In this section we want to include different aspects of the arterial tissue to fit again those tests shown before to, our understanding, better describe the microstructural behavior described by, e.g., Garcia (2012) and O'Connell et al. (2008), and reduce the ill-possenes of the optimization problem.

Beginning from the biggest to the smallest scale in our model, our first attempt is to obtain values of the *material content* of SMC, elastin and collagen. The SEDF is used to be described in terms of energy per mass unit or, equivalently, in terms of the Helmholtz free energy per volume unit, which give us stress units for those quantities. This is usually done to avoid scale problems in the definition of the constitutive models. When splitting the SEDF into different parts one should take into account the percentage of substance for each one of the splitting quantities. Usually these measures are into the mechanical parameters,

ϕ_{col}	ϕ_{elas}	ϕ_{SMC}
50%	20%	30%

Table 3.6: Weight percentage of each component respect to fry weight in human carotid arteries obtained by Humphrey and Rajagopal (2003).

but it should be more correct to state them explicitly. A Helmholtz free energy function $\mathrm{U} = \rho\Psi$ is introduced with Ψ the SEDF, reorganizing to have them in its volume and mass functions we get $\mathrm{U/m} = \Psi/\mathrm{V}$. Therefore we can write the splitting of both forms of the energy as

$$\frac{\mathrm{U}}{\mathrm{m}} = \frac{\Psi}{\mathrm{V}} = \phi_w \Psi_{\mathrm{vol}}(J) + \phi_{elas}\Psi_{\mathrm{iso}}(\overline{I}_1) + \phi_{col}\Psi_{\mathrm{ani}}(\overline{I}_4,) + \phi_{SMC}\Psi_{\mathrm{SMC}}(\overline{I}_4). \quad (3.8)$$

where ϕ_w, ϕ_{elas}, ϕ_{col} and ϕ_{SMC} represent the relative amount of water, elastin, collagen and SMC respectively. Note that we are not considering the mechanical contribution of the SMC from now on since collagen and elastin are supossed to bear the major part of the mechanical load. Also note that $\sum_{i\geq 1}\phi_i = 1$ with ϕ_i the percentage in volume of each constituent (Humphrey and Rajagopal, 2003). Water content is usually measured to be a 70% of the material, while the remaining correspond to the dry part, that can be related to the isochoric part of the SEDF. Out the 30% remaining, the percentages are split based on the elastin, collagen and SMC contect described in previous sections. This approach is the base of the Mixture-theory. We refer to Humphrey and Rajagopal (2003) for a complete development of this theory with application to arterial tissue. Values of material content are provided by Humphrey and Rajagopal (2003) in human carotids.

Regarding the *collagen behavior*, as we pointed out in the introduction of this section, collagen fibers are made up of collagen fibrils which gain into the extracellular matrix achieving some degree of pretension and are organized following a preferential direction. The mechanical behavior of the different components in the hierarchical structure are quite different. However the mechanical properties of the collagen molecules and the collagen fibrils maintain a similar behavior be-

tween different tissues and different species. What change from one to another is the degree of link and the deposition state of the fibrils within the ECM, which give also the pre-stress behavior. In Fig. 3.6 we fit the mechanical properties of a collagen fibril from a tensile test by Yang (2008). We use a SEDF initially proposed by Holzapfel et al. (2000),

$$\Psi_{\text{fib}}(\overline{I}_4) = \frac{k_1}{2k_2}[\exp(k_2[\overline{I}_4 - 1]^2) - 1] \tag{3.9}$$

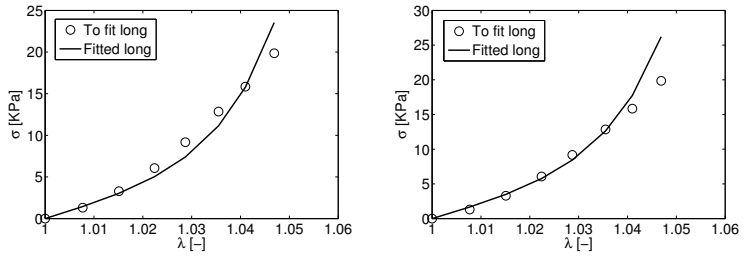

(a) Experimental test by Yang (2008) (b) Experimental test by van der Rijt et al. (2006)

Figure 3.6: Fitting results of the mechanical behavior of individual collagen fibrils from data presented in the literature.

However, this behavior only takes into account the collagen fibril. The behavior of a collagen fiber is softer than the fibrils due to the cross-links so an upper bound can be stated in the mechanical values of the fibrils. This model does not account for high strain states where breaks of cross-linking between fibril are important.

Once we know the individual mechanical behavior of the collagen fibrils and material parameters are fitted we want to describe the *structural organization* of the arterial layers. O'Connell et al. (2008) have shown that arterial fibers distribution follows a helicoidal distribution from the outer to the inner layer. As they stated, collagen fibers are bundled around the SMC with some collagen fibrils linking the main fiber in a predominant perpendicular direction. Adventitia layer is known to have a random distribution of collagen with almost any SMC and

some fibroblast. In the media layer there are several sublayers, every one with a preferential direction of the SMC and therefore of collagen fibers, and elastin sheets separating these sublayers. In the case of the media layer of carotid arteries previous studies report that SMC keep a very circumferential direction (Garcia, 2012). Having in mind these works we modified the SEDF in Eq. 3.3 to recover these features, sketchy drawn in Fig. 3.7.

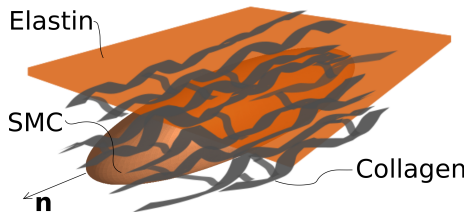

Figure 3.7: Schematic representation of the structural organization in the media of the carotid artery, being **n** the preferential direction.

Following Sommer and Holzapfel (2012), Garcia et al. (2011) and O'Connell et al. (2008) observations we can consider that the preferential direction of the fibers are in circumferential direction. The collagen fibers are linked each other by other collagen fibers, cross-linking fibrils, that we consider isotropic and perpendicular to the main one, representing the amount of cross-linking between main fibers. This contribution is multiplied by a factor α to measure the amount of these cross-links. Given that the cross-linking are isotropically connecting to the main fibers we propose an isotropic contribution of it, taking out the contribution of the main fibers. We can write this as

$$\begin{aligned}\Psi_{\text{coll}}(\overline{I}_1, \overline{I}_4) &= \sum_{i=1}^{N}[1-\alpha]\Psi^i_{fib} + \alpha\left[\frac{k_1}{2k_2}[\exp(k_2[\overline{I}_1-3]^2)-1] - \Psi^i_{fib}\right] \\ &= \sum_{i=1}^{N}[1-2\alpha]\Psi^i_{fib} + \alpha\frac{k_1}{2k_2}[\exp(k_2[\overline{I}_1-3]^2)-1]\end{aligned} \tag{3.10}$$

where α represents the amount of cross-links being $\alpha \leq 0.5$. $\alpha = 0$ represents no cross-links and $\alpha = 0.5$ that the degree of links is high enough to consider an isotropic distribution of the fibers.

Our approach consists on a preferential direction of the main fiber, which, in the present case is in the circumferential direction for the carotid artery. So we set N= 1 as we consider a unique family of fibers in the circumferential direction. For shake of scouting possible values of α we use some experimental tests performed in a pig aorta artery in our laboratory. Fig. 3.8 shows the fitting of such uniaxial tests. As we could predict, values for the adventitia layer are higher than values in the media layer since orientation of the collagen fibers is much randomly packed in adventitia layer than in the media one.

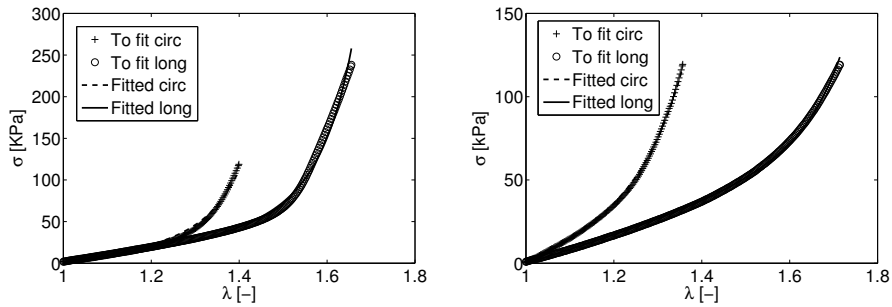

(a) Adventitia fitting results. $C_{10} = 11.2$ kPa, $k_1 = 18.72$ kPa, $k_2 = 1.84$ and α=0.41.

(b) Media fitting results. $C_{10} = 13.59$ kPa, $k_1 = 15.93$ kPa, $k_2 = 1.20$ and α=0.13

Figure 3.8: Uniaxial test in longitudinal and circumferential direction in a pig aorta artery.

3.3.1 Results of pig carotid

The proposed workflow is initially applied to the experimental result in Garcia et al. (2011). There are some evidences of non-isotropic behavior of the elastin in arterial walls, however we will ignore the anisotropic contribution in this work. As pointed out by Zou and Zhang (2009), the behavior of the first part of the stress-strain curve of the arterial wall is due to the compliance of the elastin. Therefore, we initiate our optimization problem (Eq. 3.11) with the minimization

function $\mathcal{F}$ to fit the material parameter corresponding with the first part of test up to $3-4\%$ of strain.

$$\text{(OP1) For } p \text{ given minimize}$$
$$\mathcal{F}(p, C_{10}) = \sum_{j=1}^{N_{OP1}} \left[\left[\sigma_{lj} - \sigma_{lj}^{\psi} \right]^2 + \left[\sigma_{cl} - \sigma_{cj}^{\psi} \right]^2 \right], \tag{3.11}$$

where $N_{OP1} \in \mathbb{N}^+$ is the number of points in the strain interval [1-1.04]. σ_{lj} and σ_{cj} represents the longitudinal and circumferential stress at the sample point j. Applying OP1, fitting only the elastin part, we obtain the results in Table 3.7

				$\phi_{elast} C_{10}[kPa]$			Mean	SD
Distal	24.43	21.65	14.72	21.81	33.39	19.81		
Specimen I-XIV	19.66	20.58	18.24	22.68	21.34	22.94	21.81	4.25
Proximal	22.84	24.42	22.23	19.21	21.79	26.77		
Specimen I-XIV	20.98	19.02	21.96	18.72	29.78	27.06	22.89	3.49

Table 3.7: Results of the OP1, solving for the Neo-Hookean parameter C_{10}, for pig carotid specimens (Garcia et al., 2011). First and second line are the I-VI and VII-XIII specimens of the distal and proximal part respectively while third and fourth are the I-VI and VII-XIII specimens of the distal and proximal samples respectively.

Now we focus on each artery constituent to get as much information as possible. Concerning the *elastin behavior* of the material which, as we said before, is usually modeled by means of a Neo-hooken law. The Young modulus of elastin fibrils has been measured to 560-740 kPa (Koenders et al., 2009) although, as we discussed previously, the value of the elastic modulus for the elastic fibrils depend on the fibrillin and cross-linking degree. In a low strain regime $C_{10} = E/6$ is usually approached, so we get a $C_{10} \approx 100kPa$. Interestingly, if we apply the content values of elastin in carotid arteries of an rough averaged of $20-30\%$ we get the C_{10} values for our fitting of $\approx 20-30$ kPa. Note that this is an upper bound, since there will be some collagen working in the strain regime. Note also that the values presented by Koenders et al. (2009) are for individual elastin fibers, the elastin lamelae we are dealing with have other cross-linking that probably stiffen

the material at some level (Lillie et al., 1998; Sherratt et al., 2003).

As we can see this approach gives a very similar values for all the specimens, as we highlight in the introduction of this chapter.

Now we apply OP2 to extract the rest of the material parameters.

(OP2) For p given minimize

$$\mathcal{F}(P, \mathbf{Mat}) = \sum_{j=1}^{N_{OP2}} \left[\left[\sigma_{l_j} - \sigma_{l_j}^{\psi} \right]^2 + \left[\sigma_{cl} - \sigma_{c_j}^{\psi} \right]^2 \right]. \tag{3.12}$$

where $\mathbf{Mat}$=$[k_1\ k_2\ \alpha]$ subject to $\alpha \leq 0.5$.

The experimental and fitted curves are presented in Fig. 3.9 and 3.10 for the proximal and distal place respectively. In Table 3.8 and 3.9 we resume the material parameters for such fittings. Values of C_{10} are allowed to change with respect to those obtained previously for a better fitting result.

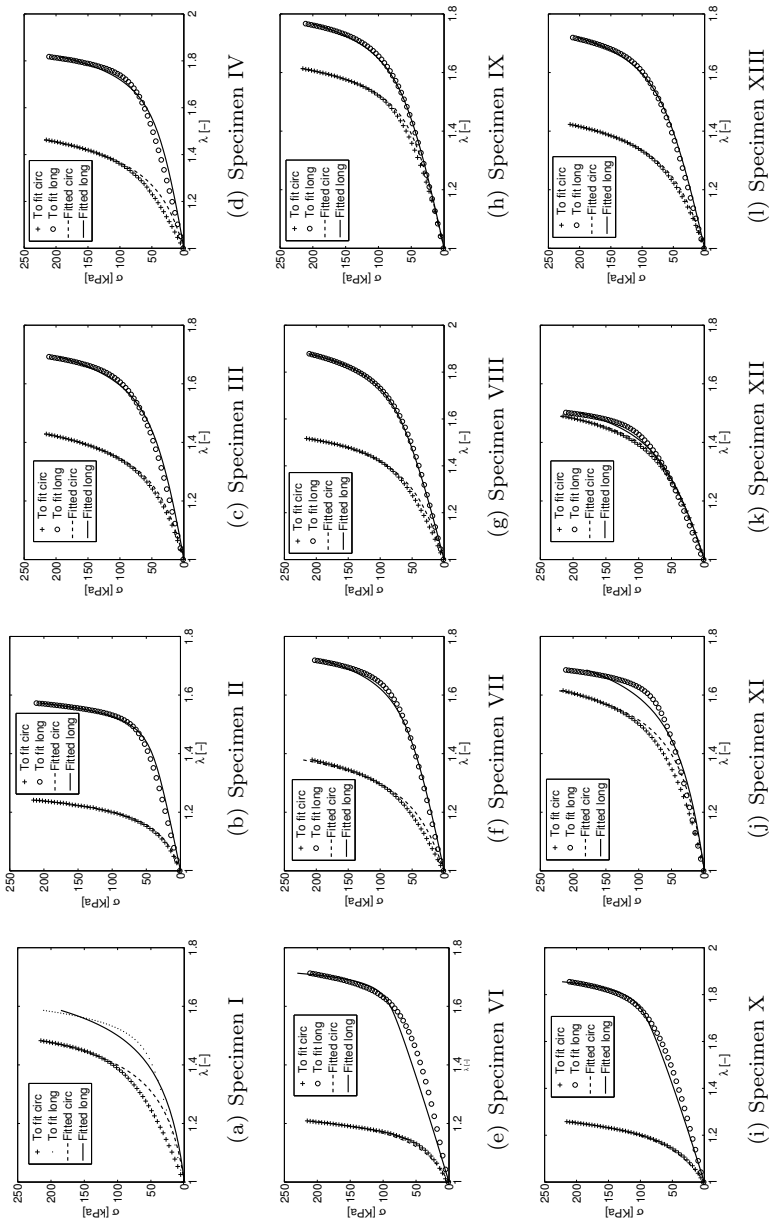

(a) Specimen I (b) Specimen II (c) Specimen III (d) Specimen IV

(e) Specimen VI (f) Specimen VII (g) Specimen VIII (h) Specimen IX

(i) Specimen X (j) Specimen XI (k) Specimen XII (l) Specimen XIII

Figure 3.9: Experimental and fitted curves of the uniaxial test of the proximal pig CCA.

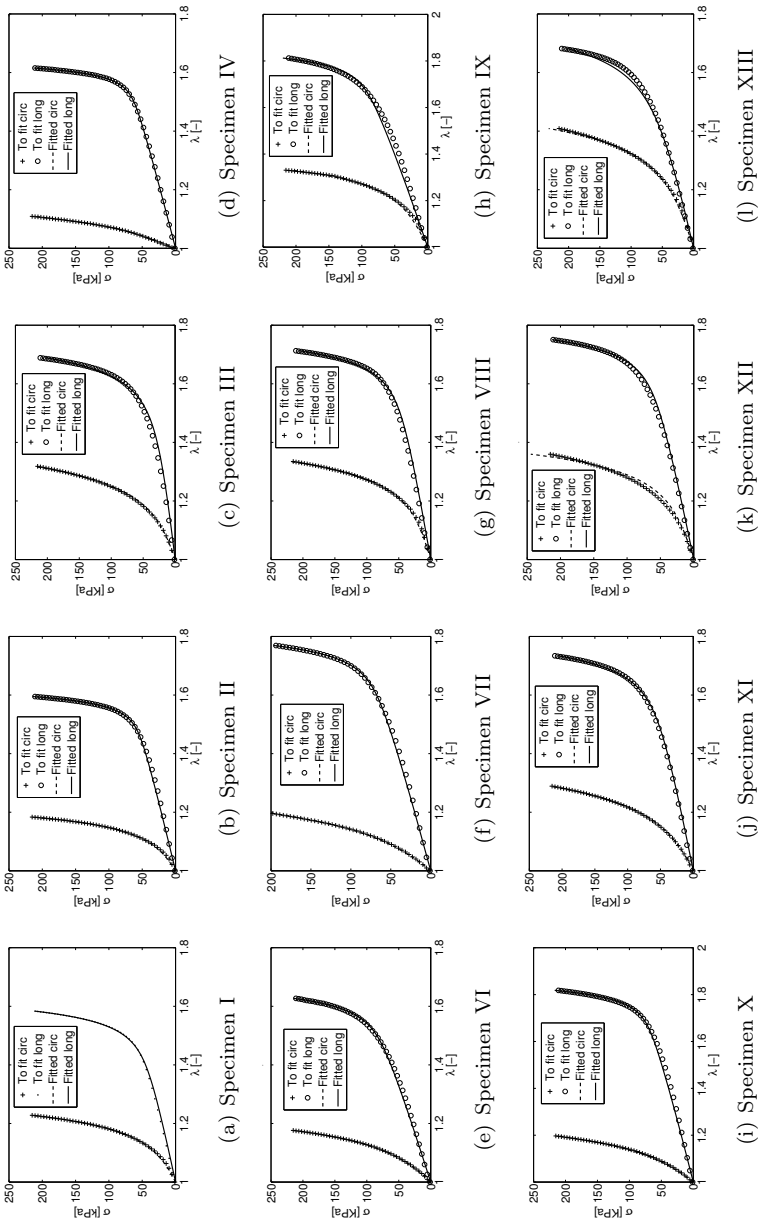

(a) Specimen I (b) Specimen II (c) Specimen III (d) Specimen IV

(e) Specimen VI (f) Specimen VII (g) Specimen VIII (h) Specimen IX

(i) Specimen X (j) Specimen XI (k) Specimen XII (l) Specimen XIII

Figure 3.10: Experimental and fitted curves of the uniaxial test of the distal pig CCA.

Specimen	$C_{10}[kPa]$	k_1 [kPa]	k_2 [-]	α [-]	ϵ
I	39.753	1.366	1.292	0.454	0.111
II	14.489	21.899	6.143	0.063	0.032
III	13.330	18.876	1.388	0.263	0.044
IV	10.407	15.984	0.926	0.149	0.069
V	22.393	34.284	6.369	0.000	0.075
VI	13.414	22.822	1.395	0.144	0.057
VII	15.760	7.609	0.909	0.138	0.023
VIII	16.045	5.162	1.219	0.434	0.032
IX	19.223	35.516	2.965	0.000	0.046
X	10.357	17.887	0.945	0.469	0.106
XI	23.596	28.765	3.241	0.499	0.061
XII	17.834	15.689	1.366	0.205	0.031
XIII	24.190	8.860	0.932	0.071	0.021
mean	17.199	19.560	2.424	0.241	0.059
stnd.Dev	4.304	4.249	1.496	0.471	0.234

Table 3.8: Results of the OP2 for proximal pig carotid specimens.

Specimen	C_{10} [kPa]	k_1 [kPa]	k_2 [-]	α [-]	ϵ
I	15.77	35.28	5.32	4.70E-002	1.30E-002
II	17.66	42.15	8.81	3.13E-003	1.19E-002
III	9.04	28.58	2.21	8.90E-002	3.20E-002
IV	18.91	219.37	9.18	1.90E-004	1.38E-002
V	24.41	82.27	5.23	5.40E-003	1.51E-002
VI	16.53	84.04	2.96	1.52E-003	1.40E-002
VII	13.33	14.96	2.69	5.65E-002	2.59E-002
VIII	20.16	12.01	2.74	5.06E-003	4.18E-002
IX	15.48	90.62	2.88	5.27E-004	2.59E-002
X	14.93	34.65	2.23	2.73E-002	1.71E-002
XI	13.14	12.03	2.49	4.03E-002	0.0648916
XII	14.45	20.05	1.50	2.40E-001	4.36E-002
XIII	22.60	54.33	2.74	1.15E-002	2.06E-002
mean	15.46	52.17	3.64	3.77E-002	2.43E-002
stnd. Dev	4.55	53.09	2.41	6.37E-002	0.00E+000

Table 3.9: results of the OP2 for distal pig carotid specimens.

In Table 3.10 we show a comparative of the material parameters obtained with the model fitted in Garcia et al. (2011) and the fitting proposed here. Our results shows lower errors and lower standard deviations. The elastin-related parameters are comparable although our results show lower deviation between distal and proximal locations. k_1, a collagen-related parameter presents a very similar tendency. In terms of the k_2, the parameter that establish the exponential-type behavior of the collagen, our results produce very similar values between distal

and proximal location while values from Garcia et al. (2011) differ in one order of magnitude. The collagen distribution differs from one model to the other in magnitude but also keeps a similar tendency. Our results indicate, by means of the parameter α, that collagen fibers are very aligned with the circumferential direction (and low degree of cross-links) for the distal samples while this degree of links goes up to 25 for the proximal positions. Garcia et al. (2011) showed angles of the fibers orientation of 75 and 80 which represent a relatively low variability between distal and proximal samples.

Specimen	$C_{10}[kPa]$	k_1 [kPa]	k_2 [-]	α [-]	ϵ [-]	
mean Prox	17.19	19.56	2.42	0.24	0.05	
stnd.Dev	4.30	4.24	1.49	0.47	0.23	
mean Distal	15.46	52.17	3.64	0.03	0.02	
stnd. Dev	4.55	53.09	2.41	0.06	0.00	
Specimen	$C_{10}[kPa]$	k_1 [kPa]	k_2 [-]	$\theta[^o]$	ρ [-]	ϵ [-]
mean Prox	13.6	12.4	2.78	84.4	0.54	0.07
stnd. Dev	3.94	8.11	2.03	11.83	0.23	0.02
mean Distal	9.54	46.61	44.34	79.93	0.81	0.09
stnd. Dev	2.01	52.62	3.17	13.78	0.09	0.03

Table 3.10: Comparison of the fitting results presented in Garcia et al. (2011) and the fitting proposed in previous sections.

3.3.2 Results in human carotid

Although data in Sommer and Holzapfel (2012) are extensive, its actual reproduction in that work, in order to be able to use their data, is quite reduced. We fit our model with the experimental data avaible in that work. Moreover, they showed plots of $P - \lambda_\theta$ and $P - \lambda_z$ while the other main control variable of the test it is not showed, so a proper inflation fitting procedure is not possible. We have to restrict ourself to $P - \lambda_\theta$, so we obtain the material parameters by means of the procedures

$$\text{(OP1) For } p \text{ given minimize}$$
$$\mathcal{F}(p, C_{10}) = \sum_{j=1}^{N_{OP1}} \left[\left[p_j - p_j^{\psi} \right]^2 \right], \tag{3.13}$$

Specimen	C_{10} [kPa]	k_1 kPa	k_2 [-]	α	ϵ
CCA media	4.31	2.19	4.15	0.13	0.05
CCA adv	0.04	7.32	66.81	0.41	0.05
ICA media	11.01	2.14	20.72	0.13	0.01
ICA adv	0.04	15.97	51.01	0.41	0.04

Table 3.11: Material parameters of the OP2 procedure for human carotid specimens in Sommer and Holzapfel (2012).

where p_j represents the pressure at the sample point j and

$$\text{(OP2) For } p \text{ given minimize}$$
$$\mathcal{F}(P, \mathbf{Mat}) = \sum_{j=1}^{N_{OP2}} \left[\left[p_j - p_j^{\psi} \right]^2 \right]. \tag{3.14}$$

where $\mathbf{Mat}$=[k_1 k_2 α] subject to $\alpha \leq 0.5$.

In Fig. 3.11 we show the fitting results which shows a good agreement with experimental response. Table 3.11 shows the numerical values of the fitting problem. The Neo-Hook part give higher values for the media layer since it is known that elastin is mainly in the media layer. Values related with the anisotropic part (k_1 and k_2) are much higher in the adventitia layer since collagen is the main component in the adventitia while the percentage of collagen in the media is lower. The higher value of the α parameter in the adventitia layer reflects a more random organization of the fibers in that layer. From these results we can also observe that the behavior of the tissue in a low strain regime is stiffer in the ICA than in the CCA.

3.4 Patient specific human carotid artery modeling

In order to apply all the above models and the ones that are coming in the following sections in clinical interest situations, we have built a geometrical model of a patient specific carotid artery (Fig. 3.12). The geometry obtained in Alastrue

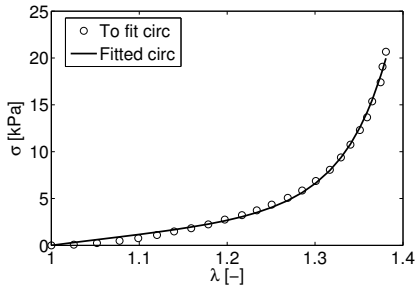

(a) Results of inflation test in the media layer of the CCA.

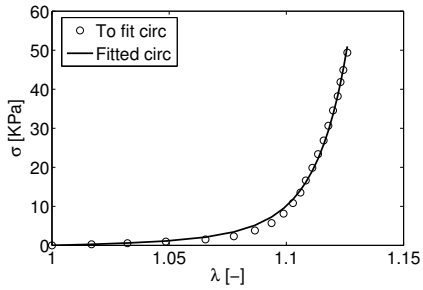

(b) Results of inflation test in the adventitia layer of the CCA.

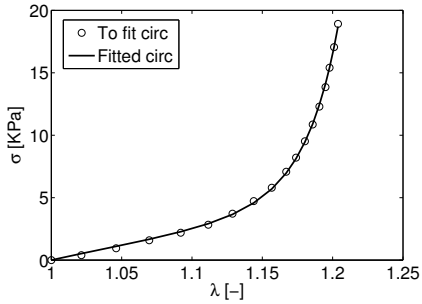

(c) Results of inflation test in the media layer of the ICA.

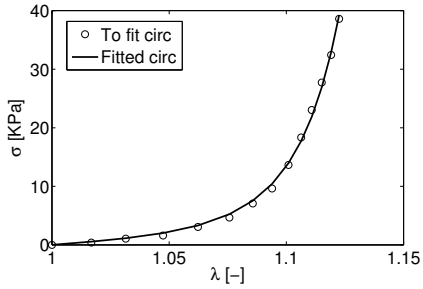

(d) Results of inflation test in the adventitia layer of the ICA.

Figure 3.11: Experimental data presented by Sommer and Holzapfel (2012) and fitted curves using the model presented in Eq. 3.10.

et al. (2010a) using computed tomography (CT). This model is used in following chapters to apply the evolution models of hypertensive disease as density and volumetric growth in a real human carotid geometry.

3.4.1 Geometrical reconstruction

As the modern imaging techniques such as computed tomography (CT), magnetic resonance imaging (MRI), or positron emission tomography (PET), among others, provide a huge amount of customized information about the geometrical description of the tissues and organs, their use in medical diagnosis has increased in the last years. The combination of these medical imaging acquisition techniques with advanced numerical methods has allowed developing personalized models for preoperative planning, virtual surgery, or implant-design. However, prior to the development of a numerical model, it is necessary to deal with the medical imaging data in order to extract the useful information. Image segmentation, generation of the computational mesh, and the extraction of particular material information (i.e. fibre directions) are the required steps prior to performing a numerical simulation. The objective of image segmentation is to find and to identify objects with certain characteristics from the rest of the image. Data segmentation will allow to visualize and to extract the part of the volume of interest. As this task is actually a standard process and in many cases the image acquisition equipments provide this semi-automatic software no further details are discussed in this section.

3.4.2 Finite Element Model

The reconstructed carotid geometry was obtained from CT image (Alastrue et al., 2010a) to simulate it in a finite element framework. In this context we first discretize the model in a finite element mesh (Fig. 3.13). The resulting mesh contains 128008 standard bricks with linear interpolation, resulting in a total of 434,484 degrees of freedom. The meshing process results in a very homogeneous undistorted elements. As CT data do not fill us in with information about the internal composition and structure of the arterial wall, so we make use of the

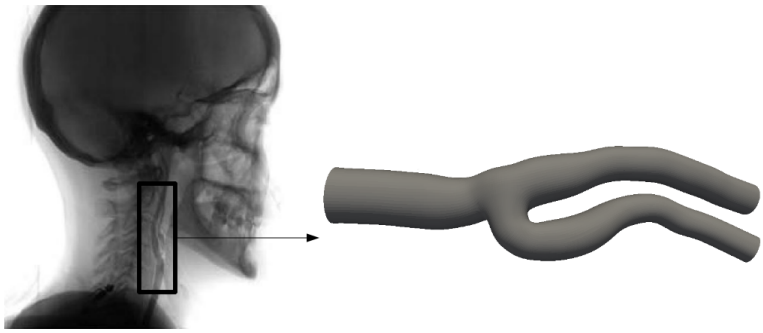

Figure 3.12: Reconstruction of the carotid artery from human carotid CT image (Alastrue et al., 2010a).

experimental data in Sommer et al. (2010) to describe the thickness for the different layers of the arterial wall. They provide thickness values of the media and adventitia layer in the CCA and ICA. We apply a linear transition of the thickness over the arterial wall from the CCA and the ICA. Therefore, the finite element mesh has two different and important groups. The first group consists of 5 elements in radial direction and a total of 104,005 elements, representing the media layer of the carotid artery. The other group, representing the adventitia layer, contains three element in thickness and a total of 62.403 elements. Fig. 3.13 shows some details of the final finite element mesh.

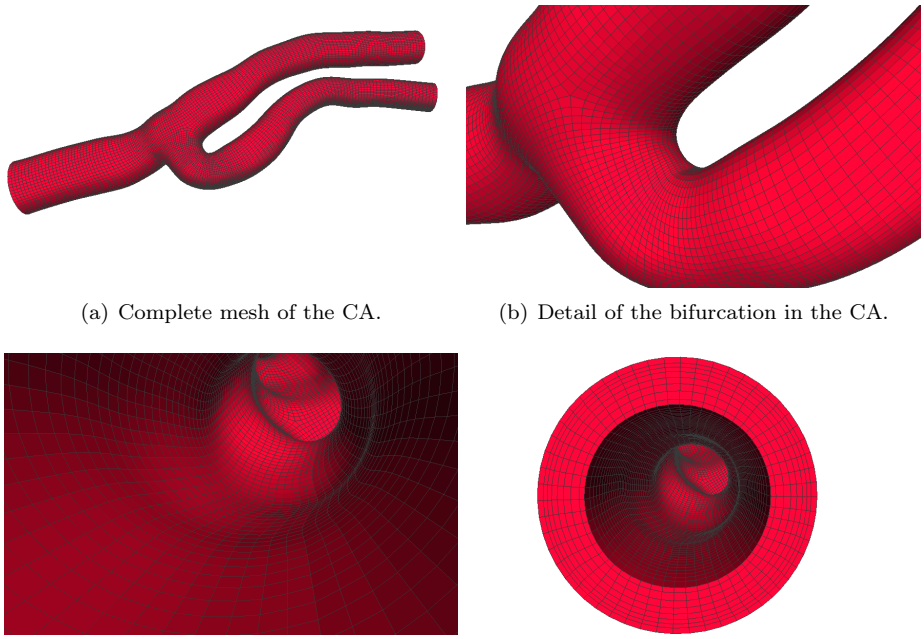

(a) Complete mesh of the CA.

(b) Detail of the bifurcation in the CA.

(c) Detail of the lumen in the CA.

(d) Detail of the front side of the CA.

Figure 3.13: Finite element mesh of a human carotid artery.

Unlike usually in computational model of blood vessels, besides the linear variable distribution of the thickness, we adopt a variable distribution of the mechanical parameters. In a very same fashion, we linearly interpolate the values of the mechanical properties obtained in Table 3.11 at both parts of the artery to describe in a more realistic way the mechanical properties along the artery length. The results of the three mechanical constants are plotted in Fig. 3.14.

An important issue in this kind of finite element models is the imposition of boundary conditions reproducing the actual *in-situ* conditions of the vessel. These arteries, and carotid artery in particular, are surrounded by connective tissue, therefore we have included a set of spring elements all over the surface of the carotid model to simulate then and avoid solid rigid motions. These springs block rigid solid motion but allow deformation of the arterial wall. The mechanical properties of these springs have been chosen so that this condition is fulfilled.

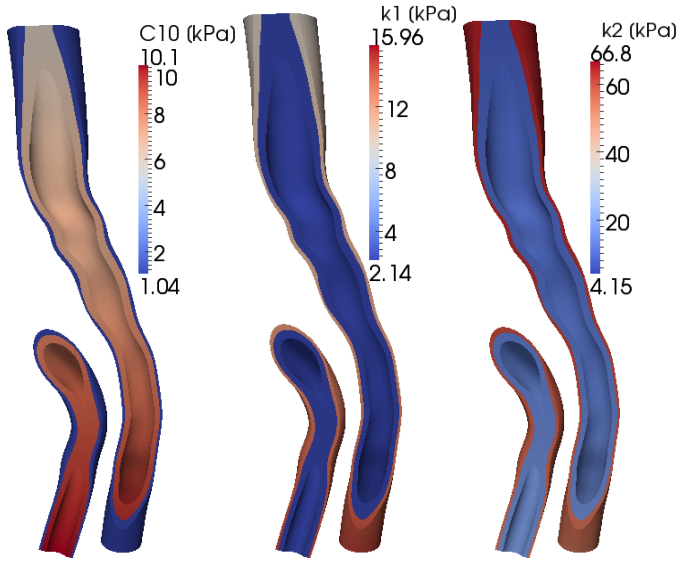

Figure 3.14: Spatial distribution of the mechanical material parameters along the carotid artery.

The differences of the element face have to be also taken into account to avoid mesh-related issues.

To close-up the mechanical and structural description of the model at hand, we left to describe the structural organization of the constituents. As we discuss before, we assume an isotropic distribution of the elastin component. The collagen and SMC follow the same organization and they are preferentially oriented in circumferential direction. The differences in collagen distribution between the media and adventitia layer are considered by means of the cross-link-related parameter α but the preferential direction stays circumferential. Fig.3.15 shows details of the fiber distribution in some representative places. The orientation of the fibers is gathered by means of the principal stresses directions of the carotid modeled with an isotropic model, under internal pressure and the displacement of the external face constrained (Alastrue et al., 2010a). Maximal principal stress appears in the circumferential direction from where we can get the unitary vectors $\mathbf{n}$ which can be associated with the orientation of the fibers. This slice is

used in the following for fitting and visualization purposes.

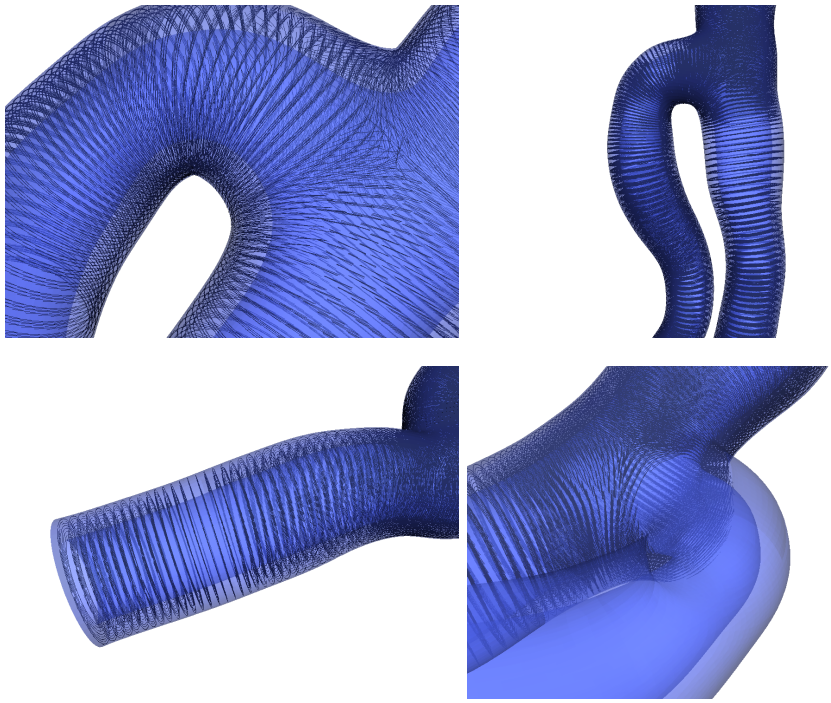

Figure 3.15: Some details of the fiber distribution defined along the carotid artery.

3.4.3 Results in carotid artery

In this section we present the finite element results of the carotid artery geometry shown in the previous section at different slices (Fig. 3.16). In Fig. 3.17 we shown the maximum principal stresses for the whole artery and the three slices of the CCA, ICA and external carotid artery (ECA) for the normotensive at 13.3 [kPa] and Fig. 3.18 does for the hypertensive sate at 16 [kPa]. As we can see, due to the mechanical properties of the carotid, stresses in the ICA and ECA are higher than those in the CCA. We can also appreciate the increase of stress due to the overpressure in hypertensive case and the transition of the media and adventitia layer.

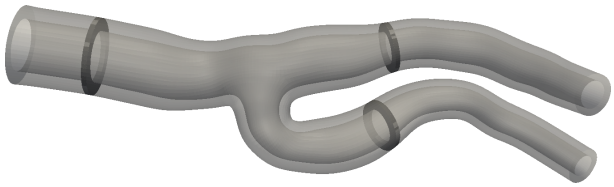

Figure 3.16: Representative slice of the CCA, ICA and ECA from the carotid model.

In Fig. 3.17 and 3.18 we show results in the homeostatic and hypertensive cases respectively and for the whole artery and in different longitudinal cuts. Besides the stresses difference in the CCA and ICA and ECA is also appreciable similar stress concentration in a ring just before the bifurcation and a ring at the bifurcation part of the ICA.

To close up the results section we present in Fig. 3.19 the maximum principal stretch at normotensive and hypertensive conditions and the ratio between hypertensive and normotensive. This variable will be the mechanical stimulus that will trigger different adaptation processes developed in the following chapters.

3.5 Conclusions

The study of arterial tissue from its structural organization and its mechanical behavior have been widely researched over the last decades. The most important features of the material structure from a load bearing point of view are that they are made up of collagen, elastin, SMC and water, that collagen and SMCs are distributed mainly in a preferential circumferential direction and that collagen has highly non-linear behavior. Based on these observations, researches have investigated different phenomenological models to capture the behavior of arterial tissue (see e.g. Fung et al. (1979); Demiray et al. (1988); Holzapfel et al. (2000), among others). Usually, elastin is modeled as a Neo-Hookean material while collagen has been object of further investigation, where it is common the use of exponential-type expressions, given the uniaxial response of collagen fibers.

Although these phenomenological models reproduce very nicely some type of

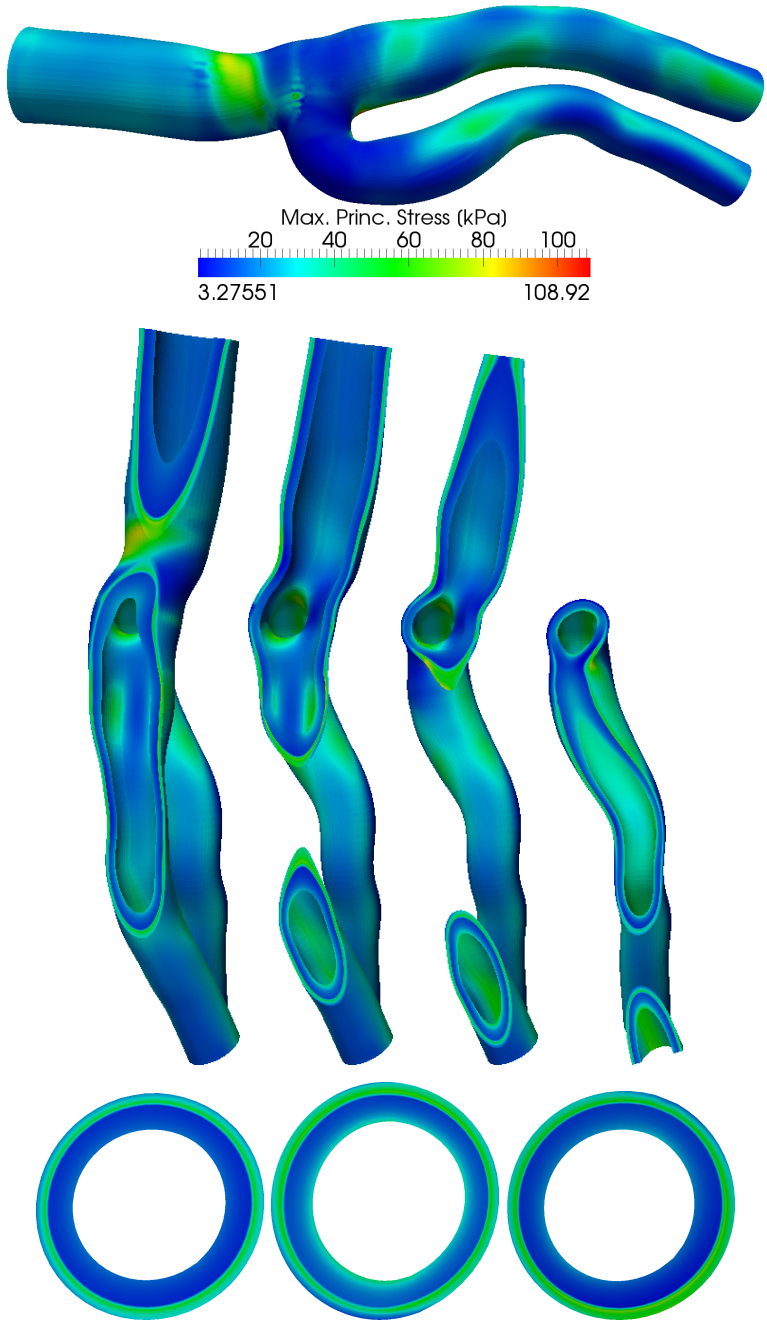

Figure 3.17: Maximum principal stress at different cuts in the whole CA for the homeostatic loads.

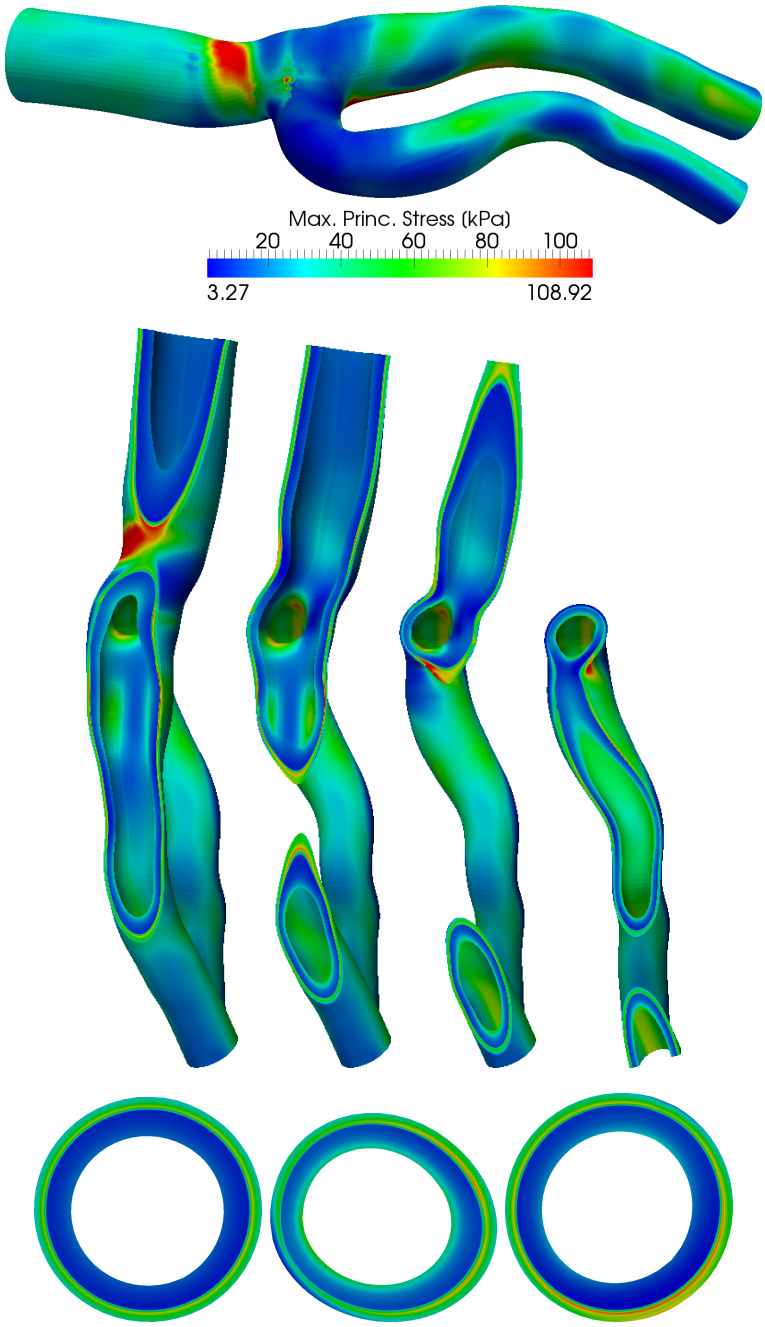

Figure 3.18: Maximum principal stress at different cuts in the whole CA for the hypertensive loads.

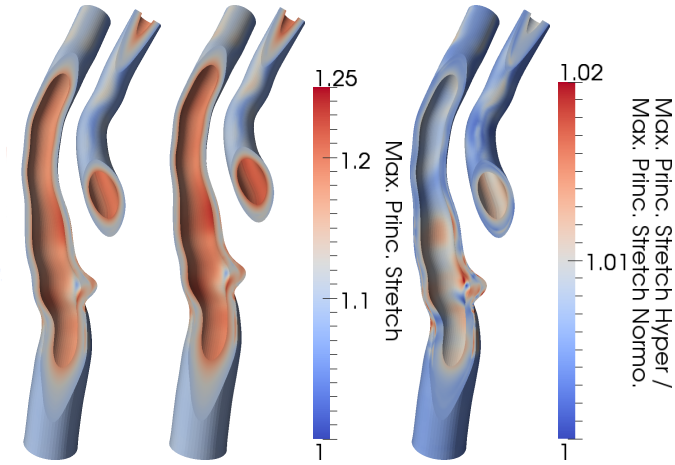

Figure 3.19: Maximum principal stretch at homeostatic and hypertensive and ratio at hypertensive and homeostatic state from left to right.

tissues or arteries others do not fit so well. In other situations, although they fit, the fitted parameters do not have a physical meaning or they do not match with some experimental observations. This is usually because of the lack of a particular feature of the tissue in the model or because of the ill-possess of the fitting problem. The aims in constitutive modeling of soft tissue should go towards the micro-structural characterization of its components, both its organization and its mechanical behavior. In any case, there are much efford to be done in the modeling of soft tissue, e.g., from more micro-structural oriented models to a multiscale model, which for some reason there have not been introduced in mechanics of soft tissue.

In this chapter we have looked into several structural data of the arterial wall and the mechanical behavior of the elastin (Lillie et al., 1998; Koenders et al., 2009) and the collagen fibers (van der Rijt et al., 2006; Yang, 2008), which are known to be the most important constituents in terms of mechanical behavior. In this direction, we have modified a well known and widely used SEDF to describe some features that this previous model did not include. For example, Garcia (2012) and O'Connell et al. (2008) showed that some arteries have a preferentially

circumferential direction. Based on this previous model, the experimental finding could not be fitted, in our opinion, because they do not consider small amount of collagen fibrils that link the main fibers, conferring a non negligible stiffness in the transversal direction of the fibers. To this end, we have introduced a cross-linked-related parameter. We have also looked into the particular behavior of elastin and collagen fibers in order to reduce the variability of the results in the fitting problem. We have been able to overcome the limitations that we found with previous models and our results in different carotid arteries were improved with respect to previous models.

Our final goal in this work was to apply this mechanical model, and others that we will show in the following chapters, to real patient specific carotid arteries to be able to simulate it computationally in a finite element framework. We obtained a geometrical model from CT images of a human carotid artery. We also obtained a circumferential distribution of the fibers over the arterial thickness which correlated well with experimental data (Garcia et al., 2011; Garcia, 2012; O'Connell et al., 2008). Latter, we gather information in literature to create a variable distribution of the mechanical properties along the carotid artery. Our results showed a good agreement with experimental findings of uniaxial and inflation tests. In terms of other FE simulations, our results showed similar (Alastrue et al., 2010a) or slightly lower stress values than other models (Delfino et al., 1997). Usually the external face of the artery is a free face which does not reflect the physiological conditions of the artery, surrounded by other connective tissue. The direct inclusion of this tissue or spring elements in the external face, as in our case, describe the physiology of the arterial tissue, in our opinion, in a more realistic way.

There are also important limitations in the current model. Firstly, we did not consider the pre-stress of the arterial wall and, although we show that it can be recovered by means of constitutive models that do not include implicitly the pre-stress, it can not be omitted if an accurate model of arterial tissue wants to be performed. Pre-stress have been extensively studied in analytical models (Holzapfel et al., 2000; Rachev and Greenwald, 2003) and simple FE models (Alastrué et al., 2007) but an approach for general geometries is more singular

task. There are also a lack of pre-stress models where the background meaning of these phenomena is described (what do create it, how is the mechanism?) since there used to be purely phenomenological models. This is, by far, the most important limitation of our model. They would be also interesting to consider the myogenic tone of SMC (Zulliger et al., 2004; Murtada et al., 2010; Stalhand et al., 2011) since this active force can modify completely the stress field over the arterial wall.

In summary, we have extended previous SEDF by means of a cross-link-related parameter that allow to gather mechanical features that previous models did not. With this approach we have been able to fit a set of mechanical tests of carotid arteries that produced better results than with previous models. This information, together with a geometrical reconstruction of a human carotid artery, leads to a finite element model of this geometry, with variable properties over the arterial length and a micro-structural description of the wall components based on experimental data.

4

Computational modeling of hypertension-induced anisotropic growth.

A computational model for smooth muscle growth due to changes of blood pressure is presented in this work. It is well known that geometry and properties of blood vessels adapt in response to alterations in blood pressure, for example in hypertension. This work is focused on the underlying volumetric growth which is mainly attributed to the smooth muscle cells. Smooth muscles cells adapt to new mechanical environments by means of an active response acutely, i.e., in a short scale of time, and increase their volume chronically, i.e., in long-term to deactivate contraction. This methodology uses a decoupled form of the deformation gradient, introducing a growth tensor, which characterizes smooth muscle growth. Based on clinical observations, we define a growth tensor for the smooth muscle cells driven by the strain that these cells undergo. The resulting changes are also computed to illustrate their temporal evolution. Our model is solved computationally by means of the finite element method, where the growth is solved implicitly using a local Newton-Raphson scheme. We solve an ideal cylindrical slice of a vessel to demonstrate the chracteristic features of the presented model to, finally, solve a human carotid geometry to investigate the effects of hypertension in the growth of the arterial wall.

4.1 Introduction

Hypertension is characterized through a substantial elevation of blood pressure which initiate the adaptation of vascular tissue. The first change, on a short-term scale, is the adaptation of SMC contractile forces discussed above, which can reduce the lumen diameter compensating extra stresses for a short-term. In addition, we can observe two long-term adaptation processes. The first long-term change is related to the secretion of collagen in the extracellular matrix. The second one consists of the increase of the number and volume of SMC in order to reestablish the homeostatic tone. This phenomenon manifests itself experimentally in an increasing thickness of the vessel wall. In this chapter we will focus on the growth of SMC in hypertension.

SMC seems to be, by themselves, liable for a sustained contraction, known as myogenic tone (Brayden and Nelson, 1992; Schubert and Mulvany, 1999), which is directly related to the intracellular calcium concentration and to the ion channels of the cell (Davis and Hill, 1999). This force attempts to compensate the over-stress in the wall in order to maintain the same vessel diameter. See, e.g., Osol (1995); Haga et al. (2007) for a review of the molecular and biochemical aspects of SMC.

SMCs grow via hypertrophy, hyperplasia or both (Owens et al., 1981; Owens, 1989), to restore the homeostatic stress state and this micro-structural change leads to the well-documented thickening of the vessel wall (Fig. 4.1). These changes are more pronounced in small or resistance vessels (Folkow et al., 1958; Mulvany and Aalkjaer, 1990). There are multitude of experimental findings related with hypertension thickening of the arterial wall, many of them related to drugs performance, genetic expression of multitude of substances and some of them deal with the plain case of thickening. Some of these studies look at essential hypertension while other asses hypertension by means of hypoxic states or ligands of some particular arteries.

Wiener et al. (1977) studied aortic arteries of rats obtaining a decrease of the lumen diameter of $\sim$9% while the thickness went from 182.5μm in normotensive state to 215.5μm in hypertension ($\uparrow$ 18%). Owens et al. (1981) reported an

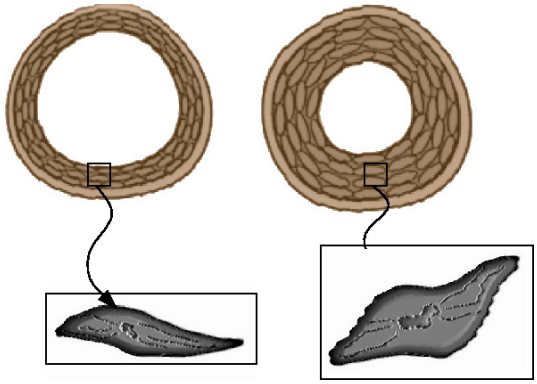

(a) Schematic process of growth.

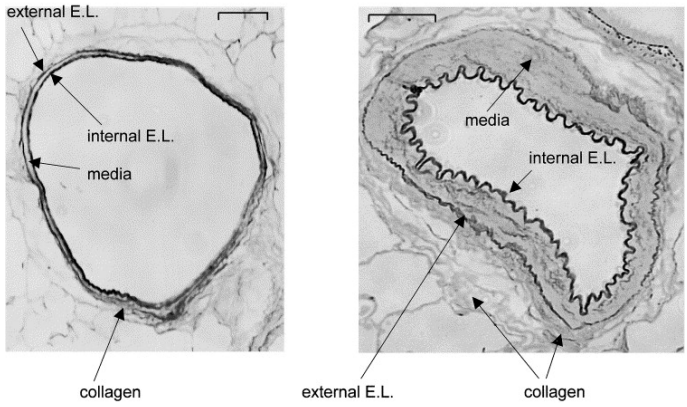

(b) Media thickening in a pulmoary artery of hypoxic rat.

Figure 4.1: (a) represents a sketch of the SMCs growth via hypertrophy and (b) a pulmonary artery of a hypertensive rat (Jeffery and Wanstall, 2001).

increase of 35% in SMC size due to hyperplasia also in aortic artery of rat. The same authors (Owens and Schwartz, 1983) showed an increase of 39.67% and a 21.16% in SMC mass in different type of rats. Schofield et al. (2002) looked at the evolution of small human arteries and found out that internal diameter went down from 140μm to 118μm, while thickness underwent a high 46.39%. Note that small arteries have a more important contractile response and such a decrease could be caused by that phenomena. In fact these authors were also interested on study the miogenic response during that procedure. Tian et al. (2011) worked on right and main pulmonary arteries for calfs and rats. While Mean pulmonary Artery (MPA) showed the same tendency (increase of internal radios and thickness of 1.02% - 1.22% and 1.17% - 1.53% respectively) however for the Right Pulmonary Artery (RPA) the animals showed a different behavior. The internal diameter of the artery calf keeps equal while the rat increase a 1.71% and the thickness of calf decrease a 52.1% and the rat increases a 1.25%.

Boutouyrie et al. (1999) reported a rise of the internal diameter in human carotids from 5.25 mm to 5.66 mm and an increase in thickness from 0.487 to 0.572 mm ($\uparrow$ 27.27%). However the same work showed a decrease in the lumen diameter from 2.33 to 2.32 mm in the radial artery and an increase of 21.98% in the thickness. Fridez et al. (2002) worked on the influence of hypertension in carotid arteries of rats. They showed that internal radius increase in hypertensive rats but it did it at lower rate than the control group. The thicnkness rise from 142 μm to 225 μm ($\uparrow$ 58.4%) although it represented just a 30% increase with respect to control group. They also saw that thickness of outer lammelar units grow more than inner units do. Eberth et al. (2010) also studied the morphological changes in carotid of rats. They reported an increase in the internal radius from 531μm to 592μm while the thickness increase from 23.1 μm to 85.7 μm after 56 weeks.

These results show how the data differ, not only between species and arteries but also from the same artery of the same species. Variation from specimen to specimen, different degree of SMC activation, genetic disorders not considered, ages, life styles and many more, can be a cause of this variability. To point out a last example, Feihl et al. (2008) collected data from different authors studying

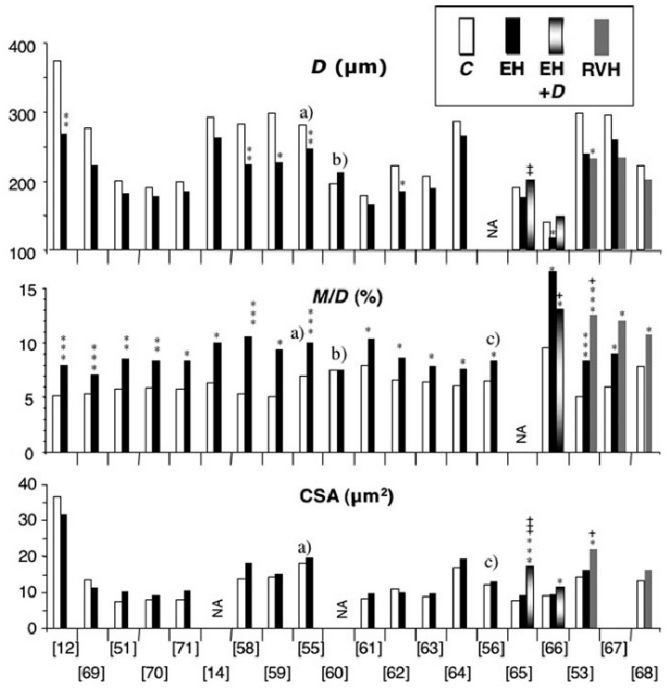

Figure 4.2: Data collected in Feihl et al. (2008) showing the variability of the diameter (D), ration media thickness to internal diameter (M/D) and cross-sectional area (CSA). Bars indicate control group (C), essential hypertension (EH), essential hypertension and diabetes (EH+D) and renovascular hypertension (RVH).

small subcutaneous human arteries (see table below and paper for references) showing this variability of the results although keeping always the same tendency.

The computational study of growth has gained increasing attention in the theoretical and computational mechanics community, see, e.g, the reviews in Taber (1995); Humphrey (2009); Ambrosi et al. (2011). Mechanical treatment of growth has been dealt with in different ways. Usually, growing biological tissues are considered as open systems. Their different configurational setting and their numerical treatment in a finite element method (FEM) framework is discussed in Kuhl and Steinmann (2003). Typically, two fundamentally different

forms of growth can be distinguished: volumetric growth and density growth. The first one allows for changes in volume while keeping the density constant whereas the second one maintains a constant volume while the density is allowed to change, see e.g. the works of Himpel et al. (2005) in the context of isotropic growth and Menzel (2004, 2007) for anisotropic growth. The works of Skalak et al. (1982) and Rodriguez et al. (1994) pioneered the underlying kinematic description of volumetric growth. An alternative approach towards growth is the one presented by Humphrey and Rajagopal (2002, 2003) based on the constrained mixture theory, where several constituents of a tissue are allowed to growth in a independent way. In this context other works have been presented (Gleason and Humphrey, 2004, 2005; Klisch et al., 2005) and extended to reactive mixtures (Ateshian, 2007). Other interesting approaches are reported by Imatani and Maugin (2002); Goriely and Amar (2007); Ganghoffer (2010). It is also worth noting the early work of Fung and Liu (1989), which demonstrates that the growth of blood vessels induces a change in the natural configuration of the tissue, associated with the notion of a stress free configuration.

The goal of this work is to present a computational model of volumetric growth for SMC based on the anisotropic structure of the tissue. We will adapt well-established consistent numerical procedures. The SMC are the main constituents, which are responsible for volumetric changes of blood vessels. We focus on SMC growth due to hypertension disease and the thickening of the arterial wall due to that growth. First, we will state the general mechanical background of soft tissue and growth mechanics that it is used in this work. Later, based on experimental data, we will compute a simple case of hypertension from where we will be able to obtain the material parameters of our model. We compute the growth of the SMC driven by the stretch of the SMC in the over pressure state. The growth will be calculated implicitly be means of a Newton-Raphson scheme. Finally, we will present a real human carotid geometry where our model will be applied.

4.2 Kinematics of finite growth

Within the framework of finite growth, the key kinematic assumption is the multiplicative decomposition of the deformation gradient $\boldsymbol{F}$ into an elastic part $\boldsymbol{F}_{\mathrm{e}}$ and a growth part $\boldsymbol{F}_{\mathrm{g}}$ (Rodriguez et al., 1994),

$$\boldsymbol{F} = \boldsymbol{F}_{\mathrm{e}} \cdot \boldsymbol{F}_{\mathrm{g}} \qquad \text{with} \qquad \boldsymbol{F} = \nabla_{\boldsymbol{X}} \boldsymbol{\varphi}, \tag{4.1}$$

adapting a concept first proposed in the context of finite elasto-plasticity (Lee, 1969). During this Chapter, we consider the growth part of the deformation gradient to be, at least, function of a growth tensor $\boldsymbol{\vartheta}$. From now on we consider this variable as a scalar quantity, ϑ. The Jacobians of the deformation gradient and its elastic and growth counterparts will be denoted as $J = \det(\boldsymbol{F})$, $J_{\mathrm{e}} = \det(\boldsymbol{F}_{\mathbf{e}})$, and $J_{\mathrm{g}} = \det(\boldsymbol{F}_{\mathbf{g}})$, respectively, such that $J = J_{\mathrm{e}}\, J_{\mathrm{g}}$. We can then introduce the right Cauchy Green tensor $\boldsymbol{C}$, and, in complete analogy, the elastic right Cauchy Green tensor $\boldsymbol{C}_{\mathrm{e}}$.

$$\boldsymbol{C} = \boldsymbol{F}^{\mathrm{t}} \cdot \boldsymbol{F} \qquad\qquad \boldsymbol{C}^{\mathrm{e}} = \boldsymbol{F}_{\mathrm{e}}^{\mathrm{t}} \cdot \boldsymbol{F}_{\mathrm{e}} = \boldsymbol{F}_{\mathrm{g}}^{-\mathrm{t}} \cdot \boldsymbol{C} \cdot \boldsymbol{F}_{\mathrm{g}}^{-1}. \tag{4.2}$$

Recall that the pull back of the spatial velocity gradient to the intermediate configuration

$$\boldsymbol{F}_{\mathrm{e}}^{-1} \cdot \boldsymbol{l} \cdot \boldsymbol{F}_{\mathrm{e}} = \boldsymbol{L}_{\mathrm{e}} + \boldsymbol{L}_{\mathrm{g}} \tag{4.3}$$

results in its additive decomposition into the elastic velocity gradient $\boldsymbol{L}_{\mathrm{e}}$ and the growth velocity gradient $\boldsymbol{L}_{\mathrm{g}}$

$$\boldsymbol{L}_{\mathrm{e}} = \boldsymbol{F}_{\mathrm{e}}^{-1} \cdot \dot{\boldsymbol{F}}_{\mathrm{e}} = \dot{\boldsymbol{F}}_{\mathrm{e}} \cdot \boldsymbol{F}_{\mathrm{e}}^{-1} \qquad \text{and} \qquad \boldsymbol{L}_{\mathrm{g}} = \dot{\boldsymbol{F}}_{\mathrm{g}} \cdot \boldsymbol{F}_{\mathrm{g}}^{-1}, \tag{4.4}$$

such that the rate of deformation tensor of the intermediate configuration can be expressed as $\boldsymbol{d}_{\mathrm{g}} = \boldsymbol{l}_{\mathrm{g}}^{\mathrm{sym}}$ with $\boldsymbol{l}_{\mathrm{g}} = \boldsymbol{F}_{\mathrm{e}} \cdot \boldsymbol{L}_{\mathrm{g}} \cdot \boldsymbol{F}_{\mathrm{e}}^{-1}$. Figure 4.3 illustrates the kinematics of finite growth, the deformation tensors $\boldsymbol{C}$ and $\boldsymbol{C}_{\mathrm{e}}$, and the mappings $\boldsymbol{F} = \boldsymbol{F}_{\mathrm{e}} \cdot \boldsymbol{F}_{\mathrm{g}}$ and $\boldsymbol{F}^{-\mathrm{t}} = \boldsymbol{F}_{\mathrm{e}}^{-\mathrm{t}} \cdot \boldsymbol{F}_{\mathrm{g}}^{-\mathrm{t}}$ between tangent spaces $T\mathcal{B}$, $T\mathcal{B}_g$ and $T\mathcal{B}_0$ in the material configuration, the intermediate configuration, and the spatial configuration.

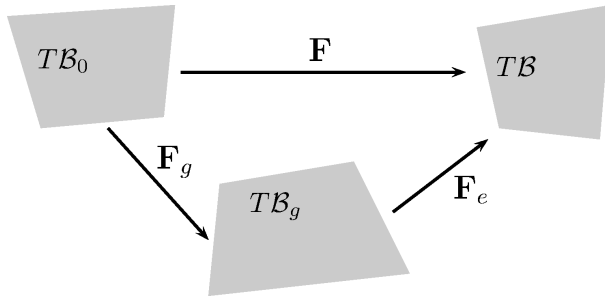

Figure 4.3: Kinematics of growth. Composition of a elastic deformation gradient $\boldsymbol{F}_e$ and a growth tensor $\boldsymbol{F}_g$.

Remark 13 (Growth of arterial tissue) *For the particular problem of growth in arterial tissue, we adopt the formulation proposed by Himpel et al. (2005) and Goektepe et al. (2010). To account for experimental observations of SMC growth (Owens et al., 1981; Owens and Schwartz, 1983; Owens, 1989), we define the growth tensor as*

$$\mathbf{F}_{\mathrm{g}} = \mathbf{I} + [\,\vartheta - 1\,]\,\mathbf{n}_{\mathrm{r}} \otimes \mathbf{n}_{\mathrm{r}}$$

where ϑ is the scalar-valued growth multiplier that defines the level of growth and $\mathbf{n}_{\mathrm{r}}$ characterizes the radial direction (Rausch et al., 2011). This particular format of the growth tensor characterizes smooth muscle cell thickening in the radial direction $\mathbf{n}_{\mathrm{r}}$ while the ellipsoidal muscle cells maintain the same length, see Figure 4.4. Acutely, SMC maintain their original length by contracting. Chronically SMC grow in the radial direction to reduce elevated wall stresses Some experiments indicate that SMC may also contract in the axial direction, to decrease the lumen diameter. However, for simplicity, here we assume that the axial dimension remains constant.

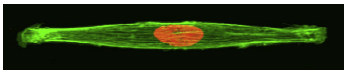

(a) Nuclei and actin staining of a SMC (Thakar et al., 2009)

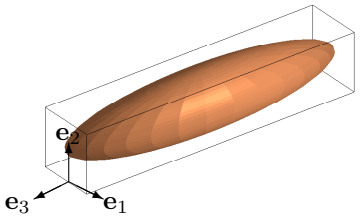

(b) Sketch representation of a SMC.

Figure 4.4: Representation of a SMC based on experimental data from (Thakar et al., 2009).

4.3 Hyperelastic model of growth

We consider a hyperelastic framework for soft tissue, motivated by their highly nonlinear behavior and the finite strains they are subjected to *in-vivo*. Given a Helmmholtz strain energy density function (SEDF) in its material description $\Psi(\mathbf{C}, \mathbf{F}_g)$, and based on the dissipation inequality from classical thermodynamics we can write, neglecting heat sources and thermal effects given the constant temperature in living organs,

$$-\dot{\Psi} = -\partial_{\mathbf{C}}\Psi : \dot{\mathbf{C}} - \partial_{\mathbf{F}_g}\Psi : \dot{\mathbf{F}}_{\mathbf{g}}, \tag{4.5}$$

$$\mathbf{S} = 2\partial_{\mathbf{C}}\Psi = 2\partial_{\mathbf{C}_e}\Psi : \partial_{\mathbf{C}}\mathbf{C}_e = \mathbf{F}_g^{-1} \cdot 2\partial_{\mathbf{C}_e}\Psi\mathbf{F}_g^t = \mathbf{F}_g^{-1} \cdot \mathbf{S}_e \cdot \mathbf{F}_g^{-t}. \tag{4.6}$$

To obtain the tangent moduli, essential for a consistent finite element implementation, we evaluate the total derivative of the $\mathbf{S}$ with respect to $\mathbf{C}$.

$$\mathbf{C} = 2\mathrm{d}_{\mathbf{C}}\mathbf{S} = 2\partial_{\mathbf{C}}\mathbf{S}\big|_{\mathbf{F}_g} + 2\partial_{\mathbf{C}}\mathbf{S}\big|_{\mathbf{F}} = 2\partial_{\mathbf{C}}\mathbf{S}\big|_{\mathbf{F}_g} + 2\left[\partial_{\mathbf{F}_g}\mathbf{S} : \partial_{\vartheta}\mathbf{F}_g\right] \otimes \partial_{\mathbf{C}}\vartheta\big|_{\mathbf{F}} \tag{4.7}$$

The first term reads the classical tangent modulus and which is no more that a pull-back of the $\mathbf{C}_e$ with $\mathbf{F}_g$. We will call $\mathbf{C}_e$ the elastic tangent modulus in the intermediate configuration, $\hat{\mathbf{C}}_e$ the same tensor in the initial, stress-free

configuration and $\mathbf{c}_e$ the elastic modulus in the actual configuration.

$$\hat{\mathbf{C}}_e = \mathbf{F}_g^{-1} \cdot \mathbf{F}_g^{-1} \cdot 2\partial^2_{\mathbf{C}_e} \Psi \cdot \mathbf{F}_g^{-t} \cdot \mathbf{F}_g^{-t} = \mathbf{F}_g^{-1} \cdot \mathbf{F}_g^{-1} \cdot \mathbf{C}_e \cdot \mathbf{F}_g^{-t} \cdot \mathbf{F}_g^{-t}. \tag{4.8}$$

The second sum term is related with the linearization of the stresses for the growth model. $\partial_\vartheta \mathbf{F}_g$ and $\partial_{\mathbf{F}} \vartheta$ are specific of the $\mathbf{F}_g$ chosen and is provided in following sections. Finally, $\partial_{\mathbf{F}_g} \mathbf{S}$ reads

$$\partial_{\mathbf{F}_g} \mathbf{S} = -\left[\mathbf{F}_g^{-1} \overline{\otimes} \mathbf{S} + \mathbf{S} \underline{\otimes} \mathbf{F}_g^{-1}\right] - \left[\mathbf{F}_g^{-1} \overline{\otimes} \mathbf{F}_g^{-1}\right] : \frac{\hat{\mathbf{C}}^e}{2} : \left[\mathbf{F}_g^{-t} \overline{\otimes} \mathbf{C}_e + \mathbf{C}_e \underline{\otimes} \mathbf{F}_g^{-t}\right] \tag{4.9}$$

with $(\{\bullet\} \bar{\otimes} \{\circ\})_{ijkl} = \{\bullet\}_{ik}\{\bullet\}_{jl}$ and $(\{\bullet\} \underline{\otimes} \{\circ\})_{ijkl} = \{\bullet\}_{il}\{\bullet\}_{jk}$.

Last, we need to define the evolution of the growth multiplier ϑ. We adopt the assumption of stress-driven growth described in Goektepe et al. (2010) $\dot{\vartheta} = \kappa(\vartheta)\phi(\boldsymbol{\Xi})$ where $\boldsymbol{\Xi}$ represents a given stimuli. $\kappa(\vartheta)$ is a function ensuring that the tissue does not grow over a threshold limit and $\phi(\boldsymbol{\Xi})$ represents the growth criteria. In the next two sections, we discuss two different approaches to the description of the growth evolution. The first one is a Mandel-based driven evolution and the second one is based on a strain measure.

4.3.1 Numerical implementation

For the numerical implementation of the growth evolution law, we adopt an implicit Euler backward scheme

$$\dot{\vartheta} = [\vartheta^{n+1} - \vartheta^{n}]/\Delta t \tag{4.10}$$

We introduce the discrete residual

$$\mathcal{R} = \vartheta^{n+1} - \vartheta^{n} - \kappa(\vartheta)\phi(\boldsymbol{\Xi})\Delta t. \tag{4.11}$$

To solve the non-linear equation we expand the residual form up to the first order term. This allows us to solve the problem within a Newton iterative scheme as

$$\mathcal{R}(\vartheta)^n + \partial_\vartheta \mathcal{R}(\vartheta)^n\big|_{\vartheta^n}[\vartheta - \vartheta^n] = 0. \tag{4.12}$$

The tangent of the residual form reads then

$$\mathcal{K} = \mathrm{d}_\vartheta \mathcal{R} = 1 - [\kappa \partial_\vartheta \phi + \vartheta \partial_\vartheta \kappa]\, \Delta t, \tag{4.13}$$

and the local update of the growth variable can be updated as $\vartheta^{\mathrm{n}} - \mathcal{R}/\mathcal{K} \to \vartheta^{\mathrm{n}+1}$ to evaluate the growth parameter determined by the current stress state and the loading history. Table 4.1 shows the algorithm used to compute the growth model.

It remains to establish the function $\kappa(\vartheta)$ and the growth criteria $\phi(\boldsymbol{\Xi})$. In the following we use

$$\kappa(\vartheta) = \frac{1}{\tau}\left[\frac{\vartheta^{max} - \vartheta}{\vartheta^{max} - 1}\right]^{\gamma} \qquad \partial_\vartheta \kappa(\vartheta) = -\frac{\gamma}{\vartheta^{max} - \vartheta}\kappa(\vartheta), \tag{4.17}$$

ϑ^{max} sets the threshold value of growth. τ and γ represent parameters that control the speed and the non-linearity of the growth respectively. The particular expression for $\phi(\boldsymbol{\Xi})$ is established in the next two sections.

4.3.2 Stress-type anisotropic growth

Last, we need to define the evolution of the growth multiplier ϑ. We adopt the assumption of stress-driven growth described in Goektepe et al. (2010) $\dot{\vartheta} = \kappa(\vartheta)\phi(\mathbf{M}_e)$ with

$$\phi(\mathbf{M}_e) = \mathrm{tr}(\mathbf{M}_e) - \mathrm{M}_e^{crit}. \tag{4.18}$$

Note that $\mathbf{M}_e = \mathbf{C}_e \cdot \mathbf{S}_e$ and M_e^{crit} represent the growth criteria value above which growth occurs. The derivative of the growth criteria with respect to the growth variable reads

$$\partial_\vartheta \phi = -\partial_\vartheta \mathbf{C}^e : \mathbf{S}^e + \mathbf{C}^e : \partial_\vartheta \mathbf{S}^e, \quad \text{with} \tag{4.19}$$

Input: $\mathbf{F}^{t+1}, \vartheta^t$

1. Compute different kinematic variables: $\mathbf{C}^{t+1}, \mathbf{F}_e^{t+1} = \mathbf{F}^{t+1} \cdot \mathbf{F}_g^t$ and consitutive variables $\mathbf{S}^{t+1}, \mathbf{S}_e^{t+1}$.

2. Check state of tissues IF ($\lambda_{\text{SMC}} > \lambda_{\text{crit}}$) THEN
   Apply local newton iteration
   ELSE
   GO TO 4

3. Local newton iteration WHILE $\mathcal{R} > Tol$ DO

$$\mathcal{R} = \vartheta^{\text{n}+1} - \vartheta^{\text{n}} - \kappa(\vartheta)\phi(\boldsymbol{\Xi})\Delta t, \tag{4.14}$$

$$\mathcal{K} = 1 - \left[\kappa \partial_\vartheta \phi + \vartheta \partial_\vartheta \kappa\right] \Delta t, \tag{4.15}$$

$$\vartheta^{\text{n}+1} \leftarrow \vartheta^{\text{n}} - \mathcal{K}^{-1} \cdot \mathcal{R}. \tag{4.16}$$

4. Compute Cauchy stresses σ^{t+1}.

5. Compute tangent operator related to the Jaumann rate that ABAQUS uses as $\overset{\nabla}{\mathbf{c}}{}^{t+1} = [\mathbf{c}^{t+1} + 1/2[\boldsymbol{\delta}\boldsymbol{\tau}^{t+1} + \boldsymbol{\tau}^{t+1}\boldsymbol{\delta} + \boldsymbol{\delta}\boldsymbol{\tau}^{t+1} + \tau^{t+1}\boldsymbol{\delta}]]/J$.

Output: $\boldsymbol{\sigma}^{t+1}, \overset{\nabla}{\mathbf{c}}, \vartheta^{n+1}$

Table 4.1: Algorithm for an implicit Euler scheme of volumetric growth

$$\partial_\vartheta \mathbf{C}_e = -\mathbf{F}_g^{-t} \cdot \partial_\vartheta \mathbf{F}_g^t \cdot \mathbf{C}_e - \mathbf{C}_e \cdot \partial_\vartheta \mathbf{F}_g \cdot \mathbf{F}_g^{-1} \quad \text{and} \quad \partial_\vartheta \mathbf{S}_e = \frac{1}{2} \mathsf{C}_e : \partial_\vartheta \mathbf{C}_e. \tag{4.20}$$

Finally, to completely define Eq. 4.7, the derivative of the growth variable with respect to the Cauchy-Green strain tensor lead to

$$\partial_{\mathbf{C}} \vartheta = \partial_{\mathbf{C}_e} \vartheta : \partial_{\mathbf{C}} \mathbf{C}_e = \frac{k^g \Delta t}{\mathcal{K}} \left[\frac{1}{2} \mathbf{C}_e : \mathsf{C}_e + \mathbf{S}_e \right]. \tag{4.21}$$

4.3.3 Strain-driven anisotropic growth

And the evolution of the growth multiplier ϑ for the strain-driven growth based on the description given in Goektepe et al. (2010) as

$$\phi(\lambda) = \lambda - \lambda_{\text{crit}} \quad \text{and} \quad \frac{\partial \phi}{\partial \vartheta} = -\lambda / \lambda_g^2. \tag{4.22}$$

Note that λ_{SMC} can be expressed as $\lambda = \mathbf{F}_e : [\mathbf{n}_z \otimes \mathbf{n}_z]$, this is the elastic stretches in the longitudinal direction of the SMC.

It remains to state the sensitivities of the scaling function κ, the growth law ϕ, and the SMC stress with respect to the growth multiplier.

4.4 A growth model problem in hypertension

In this section we present some results of the two approaches described above and we discuss about its applicability to modeling volumetric growth in arterial tissue due to hypertensive conditions.

4.4.1 Preliminary results

The aim of this first subsection is making a first approach to the volumetric growth in the arterial wall to analyze some growth features, e.g. what driven quantity is more suitable for hypertension-induced growth. The procedure is as follow:

- Apply internal pressure up to normotensive state, this is an internal pressure of 13.3 kPa. At this point, the critic stretch or stress values are calculated

and saved to trigger the growth evolution.

- Apply elevated pressure to simulate a hypertensive pressure at 16.0 kPa.
- Allow the tissue to growth to compensate the extra deformation of the SMC.

First, we apply this methodology to an idealized artery slice, made up of media and adventitia layer. Mechanical parameters are taken from the values of the CCA which were described in chapter 3. The growth parameters were chosen as $\vartheta_{max} = 2$, $\gamma = 2$ and $\tau = 1$.

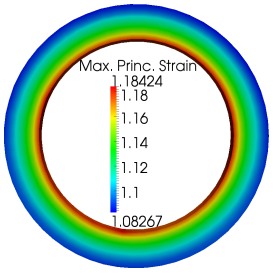

(a) Maximun principal strain at normotensive conditions.

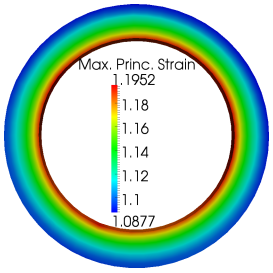

(b) Maximun principal strain at hypertensive conditions.

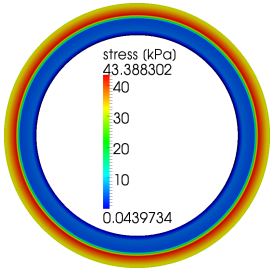

(c) Maximun principal Piola-Kircchoff stress at normotensive conditions.

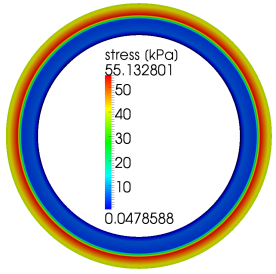

(d) Maximun principal Piola-Kircchoff stress at hypertensive conditions.

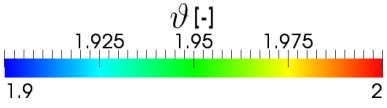

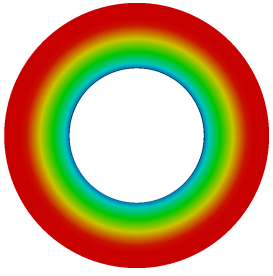

(f) Growth for the strain-driven problem.

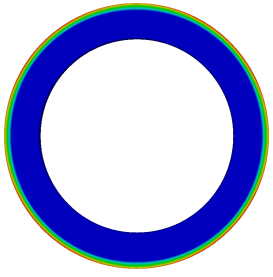

(g) Growth for the stress-driven problem.

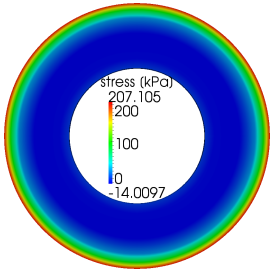

(h) Maximun principal Piola-Kircchoff stress for the strain-driven problem.

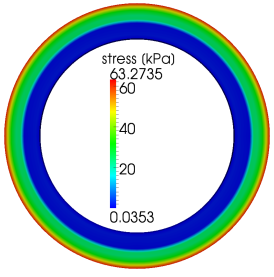

(i) Maximun principal Piola-Kircchoff stress for the stress-driven problem.

Figure 4.5: Growth variable and stress evolution.

In Fig. 4.5(a-b) we picture the maximum strain field in the slice of the CCA for the normotensive and hypertensive load state. In Fig. 4.5(f-g) we show the evolution the growth variable at two different time steps for the two driven cases while 4.5(h-i) shows the maximum principal stress. Result are quite different. In the *Mandel case* the volumetric growth goes outward to inwards and in a very marked way. As we discuss in previous section, mechanical properties of the adventitia layer are much stiffer than properties of the media layer, these higher stresses in the adventitia layer makes the material of this layer to growth much faster. Moreover, given the higher rate of growth in adventitia, the expansion of the material in the perpendicular direction toward the center of the slice makes the internal material, corresponding to the media layer, to decrease its circumferential direction. In this simulation we have adopted a growth model that applies all over the thickness. Himpel et al. (2005); Rodriguez et al. (2007) also relied on computational models that do not consider the separation of the media and adventitia layers. Our results show that taking into account different layers, growth occurs in the adventitia layer when imposing a Mandel-driven stimulus. Experimental findings, as we discuss in the introduction, show that thickening occurs meanly in the media layer due to the hypertrophy and hyperplasia of the SMC, which are located in the media layer.

In the case of the *strain driven* problem (Fig. 4.5(f-g)), the growth shows a more uniform distribution over the thickness. Since the circumferential stretch is more uniform than the stress distribution growth occurs in a more spread way with higher growth in the outer than in the inner layer. There is an open debate about what is the actual quantity that better describes different processes in cells, as differentiation, migration, etc., and in this direction the choice of a strain or stress based approach to describe the actual volumetric growth due to hypertension is also not clear.

From these results we can conclude that mechanical stimuli for growth in arterial tissue is an important issue. In the particular case of growth in arteries is also known that growth occurs basically in the media layer since there is where the SMC are placed. In order to better describe the actual behavior of the arterial wall we focus on a model where growth is allowed to occur only in the media layer.

Moreover, we consider that stretch of the SMC is the mechanical variable that stimulates the SMC to trigger the growing process.

4.4.2 Growth in a human carotid artery

Based on the aspects discussed before, this sections deals with the particularization of the strain-based approach to volumetric growth in the previous section to the case of a human carotid artery. The mechanical stimulus that triggers the growth process is the stretch of the SMC. SMCs are attached to the ECM and it is reasonable to assume an affine deformation of the ECM and SMC, so $\lambda_{col} \approx \lambda_{SMC}$ with λ_{SMC} as $\lambda_{\text{SMC}} = \mathbf{F}_e : [\mathbf{n}_z \otimes \mathbf{n}_z]$. The growth criterion can be then expressed as

$$\phi(\lambda_{\text{SMC}}) = \lambda_{\text{SMC}} - \lambda_{\text{crit}} \tag{4.23}$$

and the rest of the model as discussed in Section 4.3.3. And as we pointed out growth is considered to take place only in the media layer, where the SMC are located.

To illustrate the features of the proposed approach, we analize the finite element-based growth model to characterize some experimental findings (Fridez et al., 2002). We study first the growing process in the carotid slice showed in Fig. 4.6 corresponding to a section of the CCA. Mechanical properties and boundary conditions are the same as in Chapter 3.

Fig. 4.7 shows the growth in the CCA slice at different times giving a final growth ratio close to an increase of 50%. Fig. 4.8 shows the evolution of individual SMC presenting an increase of the radial direction while keeping longitudinal constant. In Fig. 4.9 we present the evolution of the growth rate over 100 days, for the experimental results in Fridez et al. (2002) and the numerical results of our model. Results show a very similar tendency in the growing process. Our results overrate the growth rate during the first days while slightly underrate at long time. We also present in Fig. 4.10(a) the evolution of the growth rate at four different points of the medial layer, from outwards (see Fig. 4.6). Results slightly shows a higher growth rate in the outer layer of the media layer.

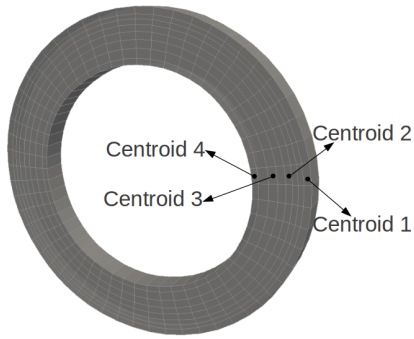

Figure 4.6: Slice of the CCA presented in chapter 3.

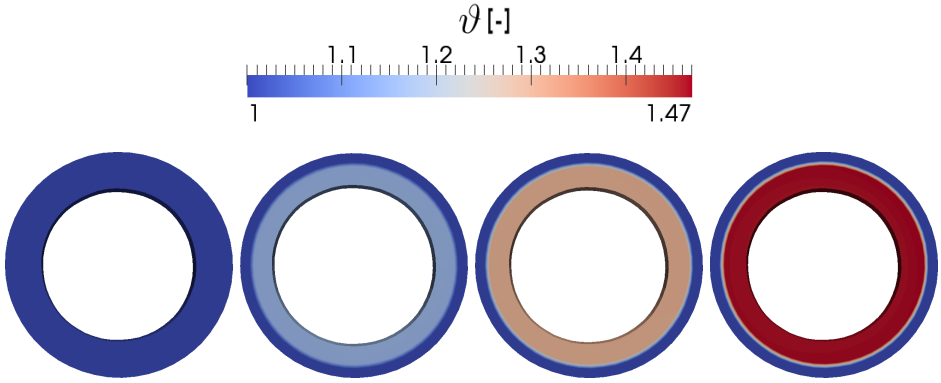

(b) Growth of the CCA slice at t=1 days

(c) Growth of the CCA slice at t=33 days

(d) Growth of the CCA slice at t=66 days

(e) Growth of the CCA slice at t=100 days

Figure 4.7: Growth evolution in CCA section at different time steps. (b-e) shows the evolution of the the CCA carotid section at four time steps.

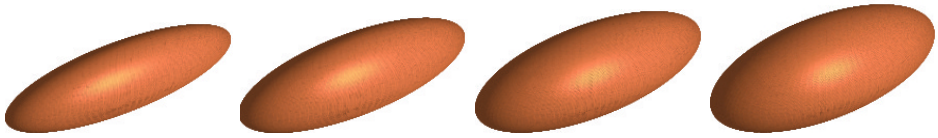

(a) Step t=1 days

(b) Step t=33 days

(c) Step t=66 days

(d) Step t=100 days

Figure 4.8: Evolution of the SMC in the middle section of the media layer at different time steps.

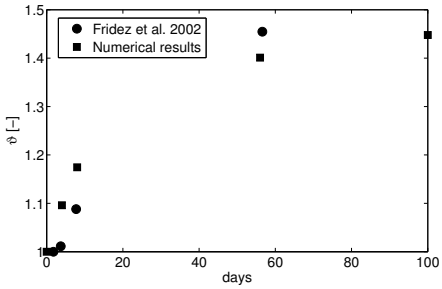

Figure 4.9: Comparison of the evolution of growth for experimental findings (Fridez et al., 2002) and numerical study.

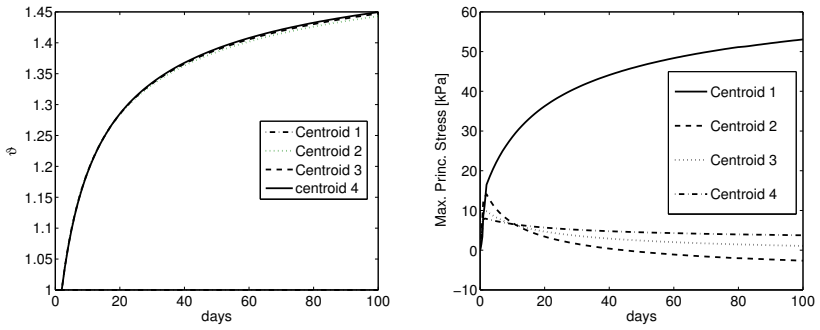

(a) Evolution of J. (b) Evolution of stress in radial direction.

Figure 4.10: Growth variable and stress evolution.

The evolution of the maximum principal stress over the entire process is shown in Fig. 4.10(b) for the four different points. Stress evolution in the media layer decrease due to the effect of the SMC growth. SMC growth, myogenic tone and others physiological processes have as goal to reduce the increase of stress due to the over pressure and go back to values close to those in the normotensive situation. The effect of the growth part of the deformation gradient of the model makes the elastic stress to decrease to compensate the deformation induce by the growth. However, stresses in the adventitia layer undergo a high increase. This fact is due to the expansion that the growth of the SMC exerts over the adventitia layer, having in mind that small deformation gradients induce high stress variation due to the highly nonlinear exponential type shape of the constitutive model of this layer.

To close up this Chapter we show the results in the carotid geometry of the model presented in this Section. Fig. 4.11 shows the growth at the end of the simulation for different longitudinal and transversal cuts. Results show a very homogeneous growth over the media as we already discussed above. Slightly lower values can be seen at the inner layer and higher at the bifurcation.

Moreover, we present the growth evolution as well as the stress in the media and adventitia in the three slices that we highlighted in chapter 3.

In Fig. 4.12, 4.13 and 4.14 we show the evolution of growth and maximal principal stresses at four different time steps. Evolution of growth and stress describe a very similar trend between the three parts of the carotid artery. The growth evolution follows a very similar behavior in the three slices, as we saw in the previous figure. This is in agreement with the smooth difference in the stretches between the normotensive and the hypertensive states. Adventitia layer undergoes a 20% increase in the stress level while the stresses in the media layer decrease in a 25%, 13% and a 7% in the CCA, ECA and ICA respectively.

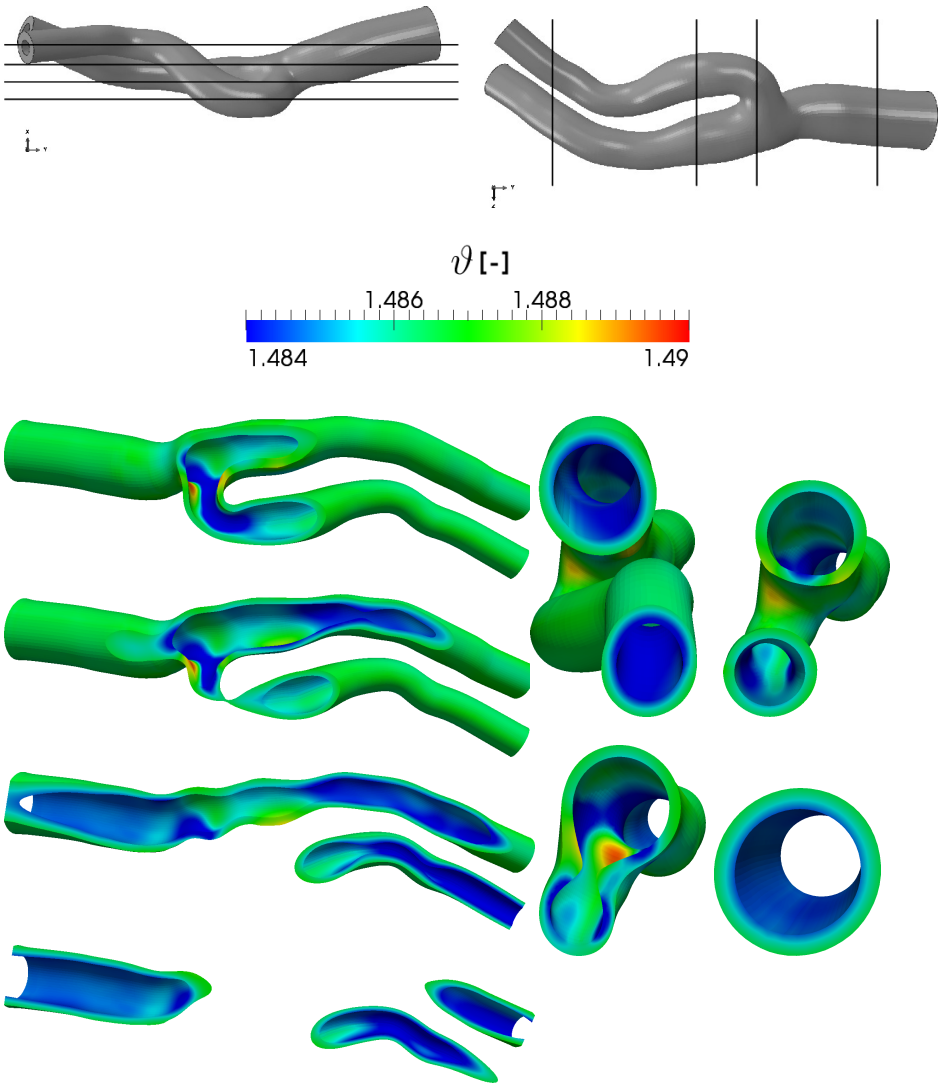

Figure 4.11: Growth for the carotid geometry at t= 100 days for different longitudinal and transversal cuts

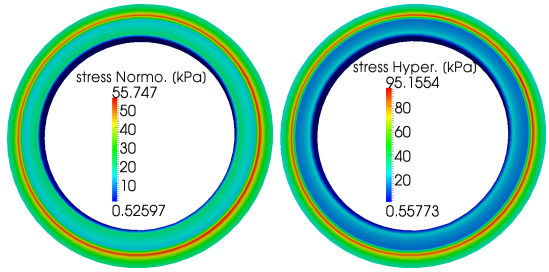

(a) Homeostatic state (b) Hypertensive state

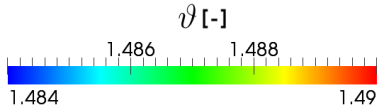

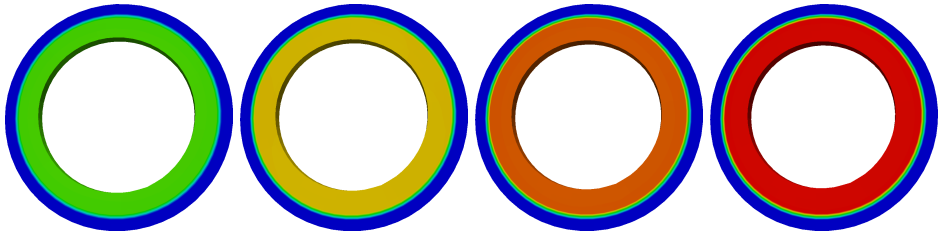

(d) Time t=5 days (e) Time t=15 days (f) Time t=40 days (g) Time t=100 days

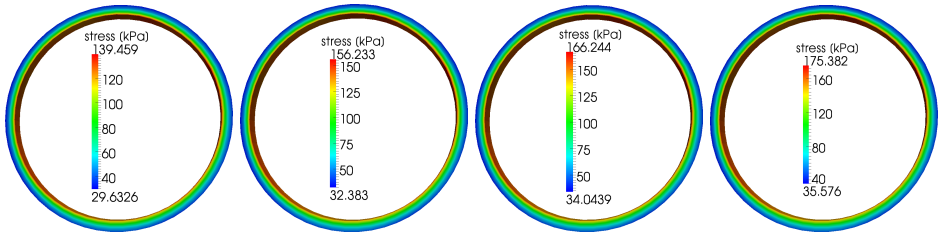

(h) Time t=5 days (i) Time t=15 days (j) Time t=40 days (k) Time t=100 days

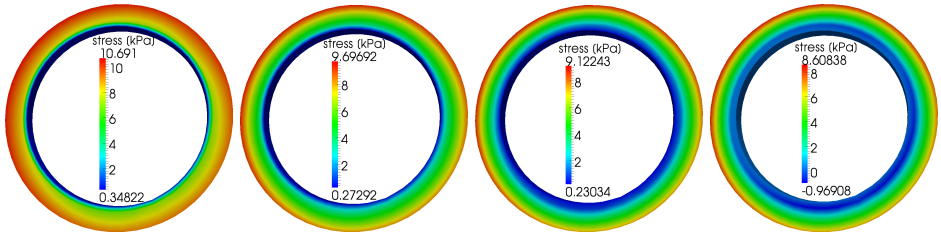

(l) Time t=5 days (m) Time t=15 days (n) Time t=40 days (o) Time t=100 days

Figure 4.12: Evolution of the growth (d-g) and maximal principal stresses in the adventitia (h-k) media (l-o)layer at different times steps in the slice of the CCA.

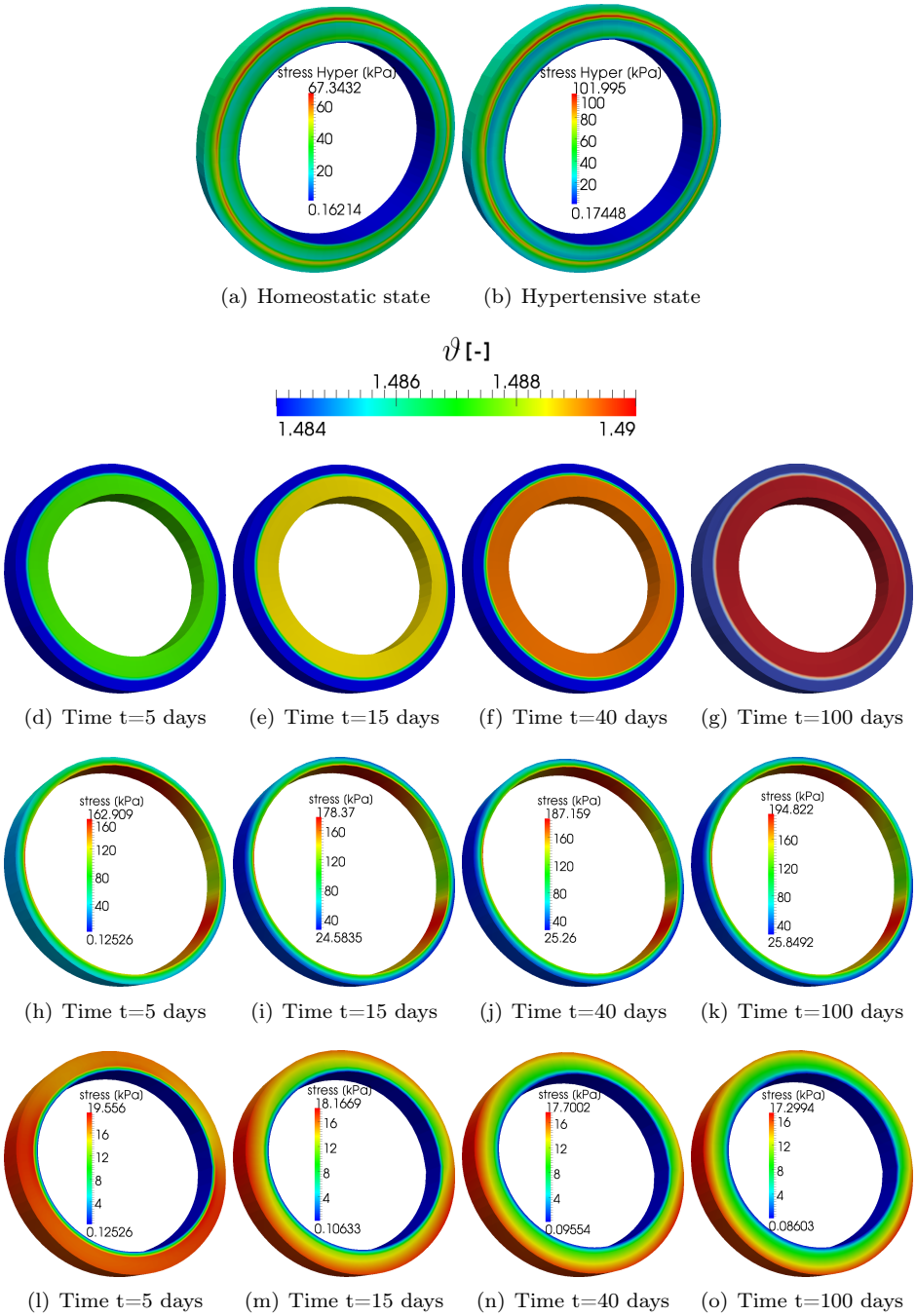

(a) Homeostatic state (b) Hypertensive state

(d) Time t=5 days (e) Time t=15 days (f) Time t=40 days (g) Time t=100 days

(h) Time t=5 days (i) Time t=15 days (j) Time t=40 days (k) Time t=100 days

(l) Time t=5 days (m) Time t=15 days (n) Time t=40 days (o) Time t=100 days

Figure 4.13: Evolution of the growth (d-g) and maximal principal stresses in the adventitia (h-k) media (l-o)layer at different times steps in the slice of the ICA.

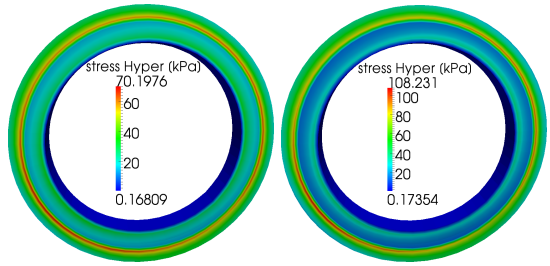

(a) Homeostatic state (b) Hypertensive state

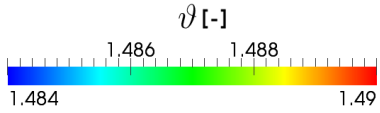

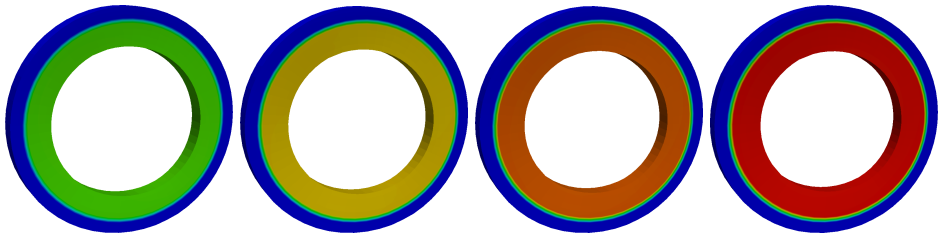

(d) Time t=5 days (e) Time t=15 days (f) Time t=40 days (g) Time t=100 days

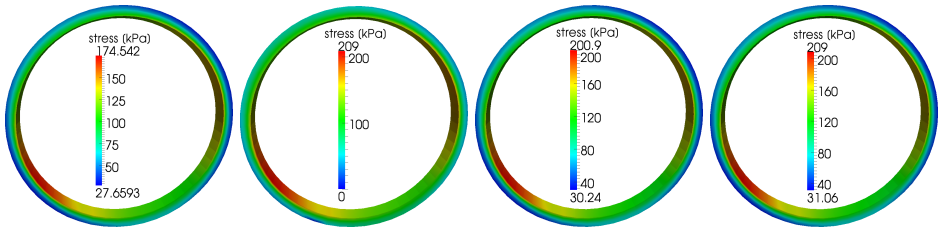

(h) Time t=5 days (i) Time t=15 days (j) Time t=40 days (k) Time t=100 days

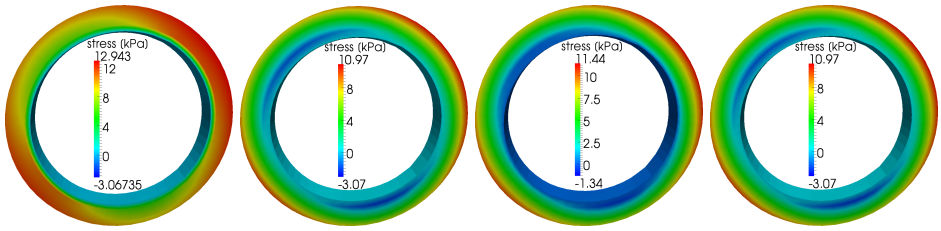

(l) Time t=5 days (m) Time t=15 days (n) Time t=40 days (o) Time t=100 days

Figure 4.14: Evolution of the growth (d-g) and maximal principal stresses in the adventitia (h-k) media (l-o)layer at different times steps in the slice of the ECA

4.5 Conclusions

The study of remodeling and growth of biological tissue have been an extensive research field over the last decades (Ambrosi et al., 2011). Researchers deal with different kinematics formulations, approaches to balance equations, define appropiate evolution equations and identification of suitable stimuli to drive the growth process. In this Chapter we have focused on a classical kinematics decomposition of the deformation gradient (Lee, 1969; Rodriguez et al., 1994) into an elastic and a growth part. Moreover, this formulation was consistently linealized and it was embedded into a finite element framework. Our model looks into the volumetric growth process of the arterial tissue. This growth, or arterial thickening, is due to the hypertrophy of the SMC. We studied how the growth of a micro-structural component, the SMCs, undergo a macroscopically thickening of the arterial wall. Our approach establishes that stretch of the SMC is the stimulus that triggers the SMC growth. We also consider that SMC thicken only along its radial direction.

Our results show a good agreement in terms of thickening and growth rates in comparison with experimental findings. We also showed the FE simulation of a real patient-specific carotid geometry. Our numerical results showed a very homogeneous growth over the medial layer all over the carotid length and only small portions of the carotid bifurcation showed slight variations. Our simulations also raise an interesting aspect of the stress distribution. Stresses in the media layer decrease due to the effect of the SMC cell. This is a classical assumption in adaptation of biological tissue, it reacts to compensate the over stimuli and goes back to a physiological situation. Cells are responsible for this sensing task and SMCs, in particular, are for sensing strains in the arterial wall. However, stresses in the adventitia layer rise up in a 20-30% (note the highly non-linear behavior pointed out in chapter 3). SMC growth in the media layer induces strains in the adventitia and these, in turn, make the stresses to increase. These results also meet the well accepted idea that the adventitia layer acts as a protection layer.

There are also not few limitations. Our model is based on purely passive underlying elasticity. SMC have a very important active component, the myogenic

tone, which makes the arterial wall to contract or expand to maintain a similar lumen radio. The arterial model could improved by the inclusion of this feature, althought, up to date, only a few computational models of myogenic tone are available in literature. The growth stimuli could be better characterized based on this basal tone. Note, however, that the myogenic tone is a response to the over stretch of the SMC, which are the stimuli that we are considering and results should not differ markedly from our present results. It is also important to note that the evolution equation for growth pre-imposes both the growth level and its rate. Rate-related parameters can be experimentally fitted to describe specific arteries and specimens. This leads other two important limitations. Experimental results are usually studied at normotensive and at the final stage of hypertension, which do not allow to fit rate-dependent parameters. Although some of them do, none of them make and extensive study of different spots of an artery, which neither allow to stablish more accurate growth models. Moreover, experimental results are amazingly different from arteries, specimens and even some arteries of the same species. There are, therefore, drawbacks in the experimental part of the study that turn to induce limitations of the computational model.

In summary, we have adopted a well established computational model for volumetric growth and we have adapted it to describe the thickening of a human carotid artery. Our model takes a generic approach of growth and bases the actual thickening of the arterial wall on the microstructural growth of the SMC. This and the consideration of variables related to the micro-structure, nicely establish a multiscale view of the problem. In this way we can simulate arterial thickening of any kind of artery in hypertension. This thickening is a very common complication in hypertensive patients because it leads to a decrease in the blood flow and other related complications. Computational models like the one presented here can, and do, help to understand the underlying mechano-chemical processes and to provide a frame work for biologists and clinicians to develop drugs and devices to prevent and deal with this kind of complications.

5

Computational model of collagen density-growth.

The goal of this chapter is the study of the turnover of collagen content in arterial tissue in hypertensive patients. This process can be divided in three different stages. The flowchart begins studying the SMC synthesis of different biological substances. As we described in chapter 3, SMC are located mainly in the media layer. The trigger stimulus of this mass production is assumed to be the over-stretching of the SMC due to the increase of pressure reported in hypertensive patients. The next step is the mass-transport simulation through the arterial wall up to the adventitia layer of the substances previously released into the extracelullar matrix. The third, and last step, is to compute the turnover of collagen based on the amount of substances in the arterial wall, which interact each other and also trigger other cells, like fibroblast, to modify the turnover rate of collagen. The overall change in the collagen density can be attributed to the perturbation of the deposition/degradation rate of collagen in the ECM.

5.1 Mass production of biological substances

5.1.1 Introduction

In this section we study the mass production of different substances of interest within the context of collagen turnover in arterial tissue. Classical close-systems in continuum mechanics keep mass changes constant; however, this is not the case of biological tissues. For this reason we consider the thermodynamic theory of open systems in this work. This assumes a non-vanishing term, called source term $\mathcal{R}$, that fulfill mass balance equation. Next we will discuss some particular substances and processes of interest in hypertensive disease.

In terms of collagen deposition, which is our final goal, fibrogenic cytokine proteins such as the transforming growth factor TGF-β are the most important regulators of collagen synthesis (see e.g. Border and Noble (1994); Wrana et al. (1994)) by vascular fibroblasts (Burke and Ross, 1979; Roberts et al., 1986). TGF-β is a protein that influences cellular functions as proliferation or differentiation and plays a key role in numerous cardiovascular diseases (Massague et al., 2000) and cancer (Massague, 2008). The activation pathway (Massague, 2000) of the TGF-β family, which is part of a superfamily of proteins, is still not completely understood. They also play a prominent role in SMC proliferation (Owens, 1995; Raines, 2004). Butt et al. (1995) reported that SMC release TGF-β growth factor associated with an increase of procollagen deposition and a decrease of collagen degradation. They also showed that both SMC and endothelial cells are the source of platelet-derived growth factor PDGF, another important growth factor. The molecular structure of TGF-β is shown in Fig. 5.1(a), presenting a 25 [kDa] molecular weight and an equivalent external radius of around $3.8 \cdot 10^{-9}$[m].

In terms of degradation, Metalloproteinases Enzymes (MMP) (Nagase and Woessner, 1999) and Tissue Inhibitors of Metalloproteinase (TIMP) (WojtowiczPraga et al., 1997), and in particular their aspect ratio MMP/TIMP (Visse and Nagase, 2003), might be the most important metric to quantify the evolution of collagen degradation (Galis and Khatri, 2002). MMP (Galis et al., 1994), in addition to other regulatory mechanisms such as differentiation and apoptosis of cells,

are responsible for extracellular matrix degradation in general, and for collagen degradation in particular. TIMPs are a type of inhibitor of metalloproteinase. In hypertension, TIMP have been reported to increase, decreasing the total MMP, which, in turn, decreases the rate of collagen degradation. O'Callaghan and Williams (2000) have shown that the amount of collagen turnover increases with the magnitude of the strain imposed to SMC in *in-vitro* experiments. They also reported the production of MMP-2, a gelatinase-degrading enzyme and TGF-β (see also Sarzani et al. (1989); Hamet et al. (1991)), which could be stimulated by cyclic stretching. It acts as an important regulator of ECM production, mainly by inhibition of MMP-1 and by increasing the activity of MMP-2. The molecular structure of MMP-1 and TIMP-1 is shown in Fig. 5.1(b) and (c), presenting a 52 [kDa] and 28 [kDa] molecular weight and an equivalent external radius of around $4 \cdot 10^{-9}$[m] and $7 \cdot 10^{-9}$[m] respectively. MMP-1 is known as one of the most important collagenase and will be the form used here as well as its inhibitor TIMP-1.

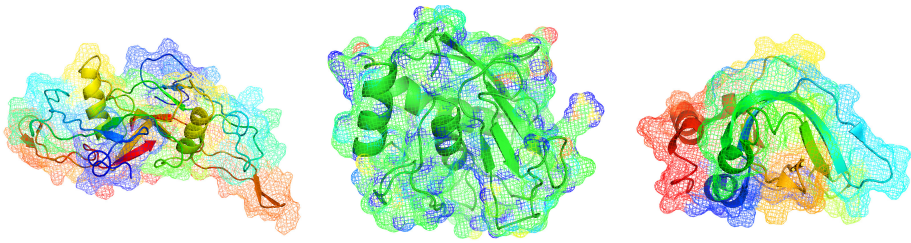

(a) TGF $-\beta$ molecule (b) MMP-1 molecule (c) TIMP-1 molecule

Figure 5.1: Molecule representation (PDBe, 2013).

5.1.2 Model

In this section a model for synthesis and degradation of TGF-β, MMP and TIMP is presented. We allow the material density to evolve in time according to the balance of mass for open system thermodynamics, and adopt a source term, $\mathcal{R}$, similar to the one described by Harrigan and Hamilton (1992); Kuhl and

Steinmann (2003), as

$$\dot{\rho} = \mathcal{R} \qquad \text{with} \qquad \mathcal{R} = \left[\frac{\rho}{\rho^*}\right]^{-m} \lambda - \lambda^*, \tag{5.1}$$

where the exponent m typically vary between two and three, λ^* is the stretch of the homeostatic equilibrium state and $\lambda = [\mathbf{r} \cdot \mathbf{C} \cdot \mathbf{r}]^{1/2}$ the stretch of a fiber with orientation $\mathbf{r}$. ρ is the density of the substance at hand, ρ^* is the initial density and $\dot{\rho}$ the material time derivative of ρ.

Depending on the stretch of the SMC λ_{smc}, which we understand to be the main driving force for these processes, the substance density will increase or decrease. In particular, we hypothesize that an increase in the stretch will increase growth factors such as TGF-β, responsible for collagen deposition.

$$\mathcal{R}_{\text{TGF}-\beta} = \dot{\rho}_{\text{TGF}-\beta} = \gamma_{\text{TGF}-\beta} \left[\left[\frac{\rho_{\text{TGF}-\beta}}{\rho^*_{\text{TGF}-\beta}}\right]^{-m_{\text{TGF}-\beta}} \lambda_{\text{smc}} - \lambda^*_{\text{TGF}-\beta}\right] \tag{5.2}$$

Both deposition and degradation can occur at the intracellular (collagen molecules) or extracellular (tropocollagen) levels. There have been several *in-vitro* and *in-vivo* experiments studying these processes in detail, as we discussed in the introduction. There is a strong agreement that the TGF $-$ β plays a fundamental role in the turnover of collagen. This implies that TGF-β will be upregulated, $\mathcal{R}_{\text{TGF}-\beta} > 0$, for blood pressures above a characteristic threshold level, $\left[\rho_{\text{TGF}-\beta}/\rho^*_{\text{TGF}-\beta}\right]^{-m_{\text{TGF}-\beta}} \lambda_{\text{smc}} > \lambda^*_{\text{TGF}-\beta}$, downregulated, $\mathcal{R}_{\text{TGF}-\beta} < 0$, for blood pressures below, $\left[\rho_{\text{TGF}-\beta}/\rho^*_{\text{TGF}-\beta}\right]^{-m_{\text{TGF}-\beta}} \lambda_{\text{smc}} < \lambda^*_{\text{TGF}-\beta}$, and otherwise remain constant, $\mathcal{R}_{\text{TGF}-\beta} = 0$. We further hypothesize that an increase in blood pressure will increase tissue inhibitors of metalloproteinase, TIMP, causing a decrease in metalloproteinase, responsible for collagen degradation. The mass production of TIMP is also expressed as

$$\mathcal{R}_{\text{TIMP}} = \dot{\rho}_{\text{TIMP}} = \gamma_{\text{TIMP}} \left[\left[\frac{\rho_{\text{TIMP}}}{\rho^*_{\text{TIMP}}}\right]^{-m_{\text{TIMP}}} \lambda_{\text{smc}} - \lambda^*_{\text{TIMP}}\right] \tag{5.3}$$

This implies that TIMP will be upregulated, $\mathcal{R}_{\text{TIMP}} > 0$, for blood pressures above a characteristic threshold, $[\rho_{\text{TIMP}}/\rho^*_{\text{TIMP}}]^{-m_{\text{TIMP}}}\,\lambda_{\text{smc}} > \lambda^*_{\text{TIMP}}$, downregulated $\mathcal{R}_{\text{TIMP}} < 0$, for blood pressures below, $[\rho_{\text{TIMP}}/\rho^*_{\text{TIMP}}]^{-m_{\text{TIMP}}}\,\lambda_{\text{smc}} > \lambda^*_{\text{TIMP}}$, and otherwise remain constant, $\mathcal{R}_{\text{TIMP}} = 0$. Basically, we consider the changes of TGF-β and TIMP as the primary variables, assuming that the up- and downregulation of TGF-β and TIMP is driven by the local SMC state. The material parameters $m_{\text{TGF}-\beta}, m_{\text{TIMP}} \in \mathbb{R}^+$ govern the evolution of TGF-β and TIMP respectively, while $\gamma_{\text{TGF}-\beta}, \gamma_{\text{TIMP}} \in \mathbb{R}^+$ set the sensibility of these substances to changes of the SMC stretch.

Finally, we define the source term of the MMP, which directly change the rate of absorption of collagen. For the sake of simplicity, we hypothesize that it directly correlated to the source term of TIMP as

$$\mathcal{R}_{\text{MMP}} = \gamma_{\text{MMP}}\,\mathcal{R}_{\text{TIMP}} \tag{5.4}$$

where $\gamma_{\text{MMP}} \in \mathbb{R}^-$ defines the sensitivity of MMP to changes in TIMP.

5.1.3 Computational treatment

To solve the non-linear differential equations of collagen deposition and absorption (Eqs. 5.2 and 5.3) we adopt a standard Euler backward scheme,

$$\dot{\rho}_0 = [\,\rho_0^{j+1} - \rho_0^j\,]/\Delta t \tag{5.5}$$

for given initial conditions $\rho_0|_{t_0=0} = \rho_0^*$. The temporal discretization is given by dividing the time interval $\mathcal{T}$ into s discrete subintervals, $\mathcal{T} = \bigcup_{j=0}^{s-1}[t^j, t^{j+1}]$, with a time increment $\Delta t = t^{j+1} - t^j \geq 0$. We transform the evolution equations Eqns. 5.2 and 5.3 for TGF-β and TIMP into their residual formats,

$$\begin{array}{lcccccl} \mathsf{R}_{\text{TGF}-\beta} & = & \rho^{j+1}_{\text{TGF}-\beta} & - & \rho^{j}_{\text{TGF}-\beta} & - & \mathcal{R}_{\text{TGF}-\beta}\quad \Delta t = 0 \\ \mathsf{R}_{\text{TIMP}} & = & \rho^{j+1}_{\text{TIMP}} & - & \rho^{j}_{\text{TIMP}} & - & \mathcal{R}_{\text{TIMP}}\quad \Delta t = 0. \end{array} \tag{5.6}$$

We solve these equations by applying a local Newton-Raphson iteration, based on a Taylor expansion at $\rho^k_{\text{TGF}-\beta}$ and ρ^k_{TIMP} up to terms of first order, see e.g

Kuhl et al. (2003a); Kuhl and Steinmann (2003) for more details. To this end, we calculate the derivative of the residuals with respect to the current TGF-β and TIMP concentrations.

$$\begin{aligned}
\frac{\partial \mathsf{R}_{\mathrm{TGF}-\beta}}{\partial \rho_{\mathrm{TGF}-\beta}}\Big|^{-1}_{\rho^k_{\mathrm{TGF}-\beta}} &= 1 - \frac{\partial \dot{\rho}^k_{\mathrm{TGF}-\beta}}{\partial \rho^k_{\mathrm{TGF}-\beta}}\,\Delta t \;=\; 1 + \frac{m_{\mathrm{TGF}-\beta}}{\rho^k_{\mathrm{TGF}-\beta}}\left[\frac{\rho^k_{\mathrm{TGF}-\beta}}{\rho^*_{\mathrm{TGF}-\beta}}\right]^{-m_{\mathrm{TGF}-\beta}} \lambda_{\mathrm{smc}}\,\Delta t \\
\frac{\partial \mathsf{R}_{\mathrm{TIMP}}}{\partial \rho_{\mathrm{TIMP}}}\Big|^{-1}_{\rho^k_{\mathrm{TIMP}}} &= 1 - \frac{\partial \dot{\rho}^k_{\mathrm{TIMP}}}{\partial \rho^k_{\mathrm{TIMP}}}\,\Delta t \;=\; 1 + \frac{m_{\mathrm{TIMP}}}{\rho^k_{\mathrm{TIMP}}}\left[\frac{\rho^k_{\mathrm{TIMP}}}{\rho^*_{\mathrm{TIMP}}}\right]^{-m_{\mathrm{TIMP}}} \lambda_{\mathrm{smc}}\,\Delta t
\end{aligned} \tag{5.7}$$

We can then calculate the discrete changes in the TGF-β and TIMP concentrations,

$$\begin{aligned}
\Delta\rho_{\mathrm{TGF}-\beta} &= -\;\frac{\partial \mathsf{R}_{\text{TGF-}\beta}}{\partial \rho_{\mathrm{TGF}-\beta}}\Big|^{-1}_{\rho^k_{\mathrm{TGF}-\beta}} \mathsf{R}_{\mathrm{TGF}-\beta}(\rho^k_{\mathrm{TGF}-\beta}) \\
\Delta\rho_{\mathrm{TIMP}} &= -\;\frac{\partial \mathsf{R}_{\mathrm{TIMP}}}{\partial \rho_{\mathrm{TIMP}}}\Big|^{-1}_{\rho^k_{\mathrm{TIMP}}} \mathsf{R}_{\mathrm{TIMP}}(\rho^k_{\mathrm{TIMP}})
\end{aligned} \tag{5.8}$$

and update the current concentration values.

$$\begin{aligned}
\rho^{k+1}_{\text{TGF-}\beta} &= \rho^k_{\text{TGF-}\beta} + \Delta\rho_{\mathrm{TGF}-\beta} \\
\rho^{k+1}_{\mathrm{TIMP}} &= \rho^k_{\mathrm{TIMP}} + \Delta\rho_{\mathrm{TIMP}}
\end{aligned} \tag{5.9}$$

Once the local Newton iteration is converged, we can calculate the MMP concentration

$$\rho^{j+1}_{\mathrm{MMP}} = \gamma_{\mathrm{MMP}}\,\rho^{j+1}_{\mathrm{TIMP}} \tag{5.10}$$

Table 5.1 summarizes the algorithm to compute the update of the local collagen content.

5.1.4 Sensitivity anaylisis

In Fig. 5.2 we present a sensitivity analysis of the material parameters involved in the evolution of the TGF$-\beta$ content for baseline values of $m = 1$, $\rho^*_{\mathrm{TGF}-\beta} = 1.0$, $\gamma_{\mathrm{TGF}-\beta} = 1.0$ and $\lambda^*_{\mathrm{TGF}-\beta} = 1.1$. We impose a $\lambda_{SMC} = 1.2$ in this case. We study the problem for $s = 100$ discrete time steps of $\Delta t = 1$. We illustrate in Fig. 5.2(a) the sensitivity of the TGF$-\beta$ concentration when we vary the $\gamma_{\text{TGF-}\beta}$

Table 5.1: Algorithm to compute the local main substances content using an implicit Euler backward scheme.

Input: $\mathbf{F}^{j+1}$, **internal variables at time** j

I Evaluate kinematics $\mathbf{C}^{j+1}$ and constitutive equations λ^{j+1}

II Check state of SMC
IF $(\lambda_{\text{smc}}^{j+1} \neq \lambda^{*})$ THEN GO TO III
ELSE GO TO IV

III Local Newton iteration. WHILE $\mathsf{R}_{\rho_{\text{TGF}-\beta}} > \text{tol}$ or $\mathsf{R}_{\rho_{\text{TIMP}}} > \text{tol}$

Calculate local TGF-β and TIMP residuals

$$\begin{aligned} \mathsf{R}_{\text{TGF}-\beta} &= -\ \rho_{\text{TGF}-\beta}^{j+1} + \rho_{\text{TGF}-\beta}^{j} + \mathcal{R}_{\text{TGF}-\beta}\ \Delta t = 0 \\ \mathsf{R}_{\text{TIMP}} &= -\ \rho_{\text{TIMP}}^{j+1} + \rho_{\text{TIMP}}^{j} + \mathcal{R}_{\text{TIMP}}\ \Delta t = 0 \end{aligned}$$

Calculate local TGF-β and TIMP tangents

$$\begin{aligned} \mathsf{K}_{\text{TGF}-\beta} &= 1 + \frac{m_{\text{TGF}-\beta}}{\rho_{\text{TGF}-\beta}^{k}} \left[\frac{\rho_{\text{TGF}-\beta}^{k}}{\rho_{\text{TGF}-\beta}^{*}}\right]^{-m_{\text{TGF}-\beta}} \lambda_{\text{smc}}\ \Delta t \\ \mathsf{K}_{\text{TIMP}} &= 1 + \frac{m_{\text{TIMP}}}{\rho_{\text{TIMP}}^{k}} \left[\frac{\rho_{\text{TIMP}}^{k}}{\rho_{\text{TIMP}}^{*}}\right]^{-m_{\text{TIMP}}} \lambda_{\text{smc}}\ \Delta t \end{aligned}$$

Update TGF-β and TIMP concentrations

$$\begin{aligned} \rho_{\text{TGF}-\beta}^{\text{j+1}} &\leftarrow \rho_{\text{TGF}-\beta}^{\text{j+1}} - \mathsf{R}_{\rho_{\text{TGF}-\beta}} \,/\, \mathsf{K}_{\rho_{\text{TGF}-\beta}} \\ \rho_{\text{TIMP}}^{\text{j+1}} &\leftarrow \rho_{\text{TIMP}}^{\text{j+1}} - \mathsf{R}_{\rho_{\text{TIMP}}} \,/\, \mathsf{K}_{\rho_{\text{TIMP}}} \end{aligned}$$

IV Update MMP concentration

$$\rho_{\text{MMP}}^{j+1} = \gamma_{\text{MMP}}\, \rho_{\text{TIMP}}^{j+1}$$

Output: $\rho_{\text{TGF}-\beta}^{t+1}, \rho_{\text{TIMP}}^{t+1}$ and ρ_{MMP}^{t+1}

parameter, variations of the exponent $m_{\text{TGF-}\beta}$ in Fig.5.2(b), $\rho_{\text{TGF-}\beta}^{*}$ in Fig 5.2(c), and for different saturation values $\lambda_{\text{TGF-}\beta}^{*}$ in Fig 5.2(d).

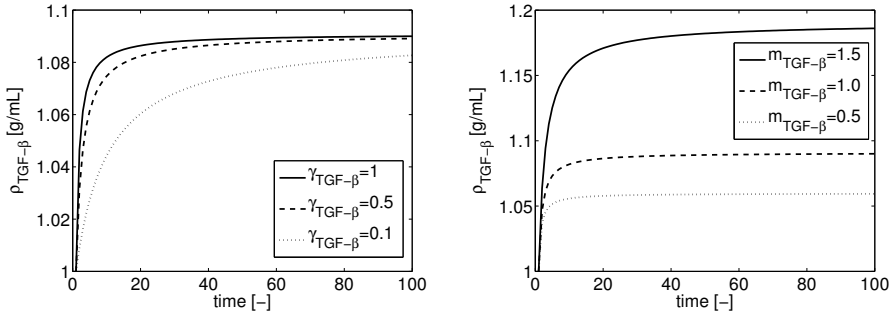

(a) Variation of $\gamma_{\mathrm{TGF}-\beta}$

(b) Variation of $m_{\mathrm{TGF}-\beta}$

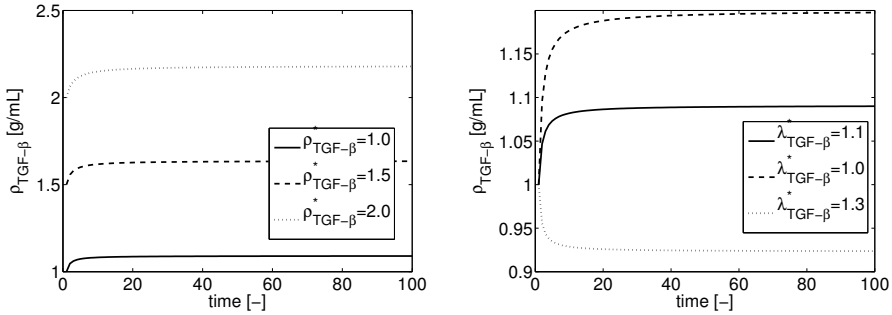

(c) Variation of $\rho^*_{\mathrm{TGF}-\beta}$

(d) Variation of $\lambda^*_{\mathrm{TGF}-\beta}$

Figure 5.2: Sensitivity of TGF $-$ β content, $\rho_{\mathrm{TGF}-\beta}$, with respect to sensitivity parameter $\gamma_{\mathrm{TGF}-\beta}$, evolution exponent $m_{\mathrm{TGF}-\beta}$, initial value $\rho^*_{\mathrm{TGF}-\beta}$, and saturation value $\lambda^*_{\mathrm{TGF\text{-}}\beta}$.

5.1.5 Material fitting in hypertension-induced collagen deposition and absorption

As discussed in the introductory section, the turnover of collagen in disease conditions can be related to changes in the rates of deposition and absorption of MMP and TGF-β. However, the net result of collagen production and removal highly depends on the type of tissue and on the level of hypertension as well as the cell response. In this section we fit our model with experiments (see Laviades et al. (1998)), who investigated alterations in collagen type I, matrix

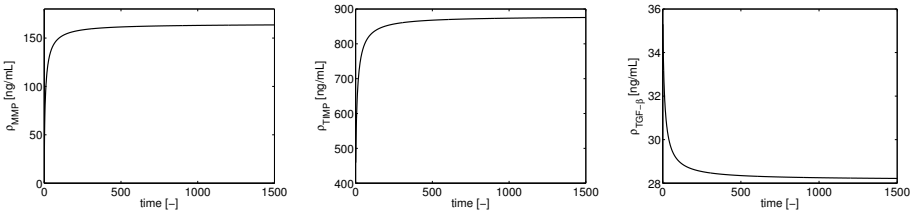

(a) Evolution of TGF-β (b) Evolution of TIMP (c) Evolution of MMP

Figure 5.3: Evolution of TGF-β, TIMP, and MMP concentrations involved in progressive collagen turnover.

metalloproteinase, and inhibitors of matrix metalloproteinase. This experimental study found an increase of 178.9%, from 641±31 ng/mL to 1147±55, in total TIMP-1 and a decrease in total MMP-1 density of 18.07%, from 56±2 ng/mL to 47±1 ng/mL. The authors point out that both TGF-β and collagen content are upregulated in hypertensive patients. Motivated by normal baseline TGF-β concentration of 35ng/mL (Schaan et al., 2007), and its 4.2-fold increase in hypertensive patients (Porreca et al., 1997), we can compute increase in collagen due to the upregulation of TGF-β.

Table 5.2: Collagen turnover model. Material parameters for hypertensive case study.

material parameter	value	units
$\rho^*_{\mathrm{TGF}-\beta}$	0.035	[μg/mL]
ρ^*_{TIMP}	0.0459	[μg/mL]
ρ^*_{MMP}	0.0353	[μg/mL]
$m_{\mathrm{TGF}-\beta}$	0.007	[$-$]
m_{TIMP}	0.016	[$-$]
$\gamma_{\mathrm{TGF}-\beta}$	40	[$-$]
γ_{TIMP}	80	[$-$]

In Fig. 5.3, we summarize the evolution of the (a) TGF-β, b) TIMP and (c) MMP contents in response to hypertension. Results were achieved with the material paramters presented in Table 5.2. Values of λ_{SMC} and λ^*_{SMC} were collected from averaged values of the SMC stretches of homeostatic and hypertensive

states, as it was discussed in chapter 3. Results show a good agreement with the numerical values obtained from experiments for a time frame of 4 years. We do not have, however, information of how these substance evolve over time.

5.1.6 Results in carotid artery

In this section we present the results of the mass production in the real carotid artery (see chapter 3) based on the model and material parameters presented above. The results are shown in two longitudinal cuts. In Figs. 5.4 and 5.5 we show the evolution of the TGF-β production in the media layer for different times and both cuts. Figs. 5.6, 5.7, and, 5.8 and 5.9 present the evolution of TIMP-1 and MMP-1 respectively. The results correlate well with the range of values presented in the experimental findings reported in Section 5.1.5. Distribution of the the mass production of each substance match with the field of increase of stretches showed in the previous chapter. Mass production is higher at the beginning of the carotid bifurcation while the section of the CCA before the bifurcation present lower rates of production. The rest of the carotid shows very similar production rate values due to the uniform stretch field.

In Fig. 5.10 we present the evolution of every substances in six points of interest of the carotid artery. They also follow a saturation-like behavior as the one shown in the analytic results of the previous section. Values of these points, as in the whole artery, stay in among the values that we showed in the previous section and the mass production in the carotid artery do not show any important variation of any of the substances.

5.2 Diffusion through the vessel wall

5.2.1 Introduction

Mass transport phenomena, as the movement of particles or molecules, have been studied for a long time. The pioneers works of Fick (1855) about diffusion

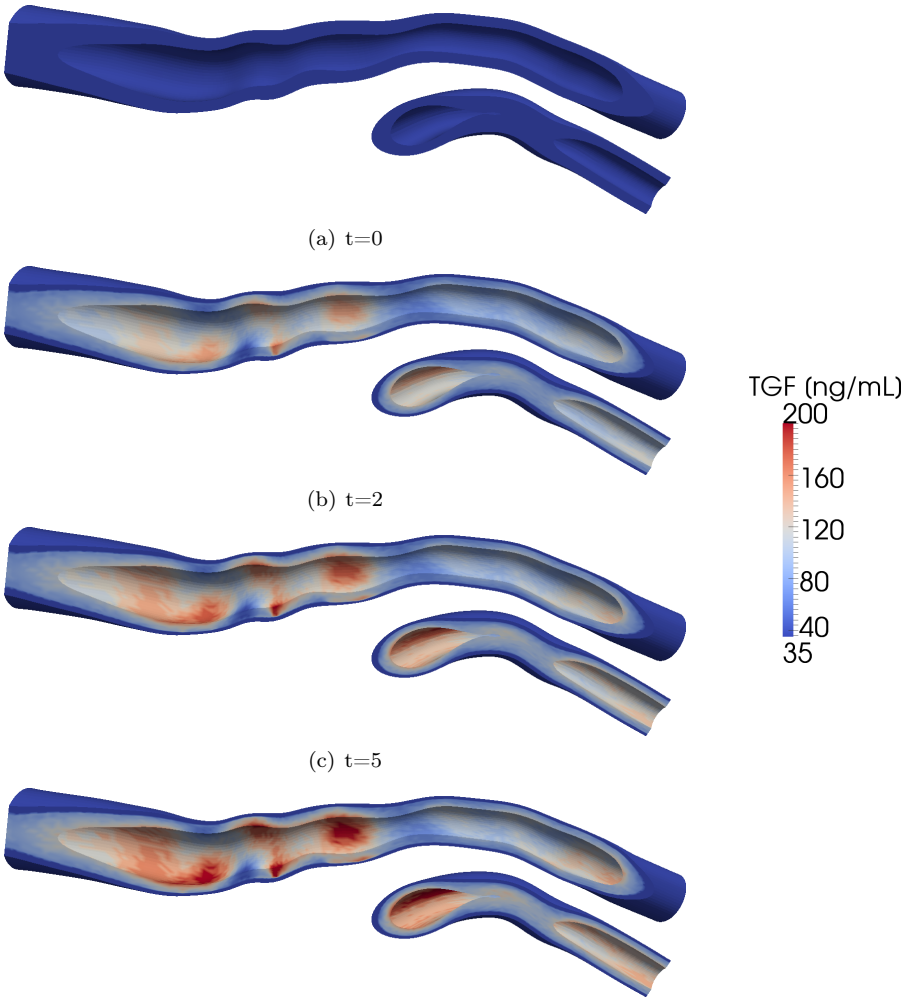

(a) t=0

(b) t=2

(c) t=5

(d) t=19

Figure 5.4: Evolution of the mass production of TGF-β due to SMC activity in different depth cuts.

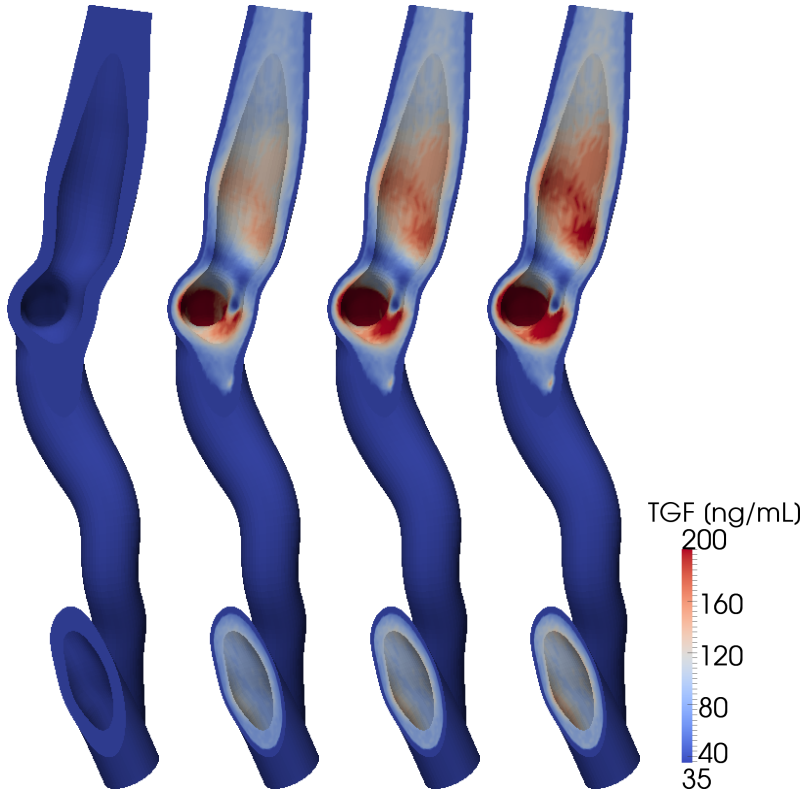

(a) t=0 (b) t=2 (c) t=5 (d) t=19

Figure 5.5: Evolution of the mass production of TGF-β due to SMC activity in different transversal cuts.

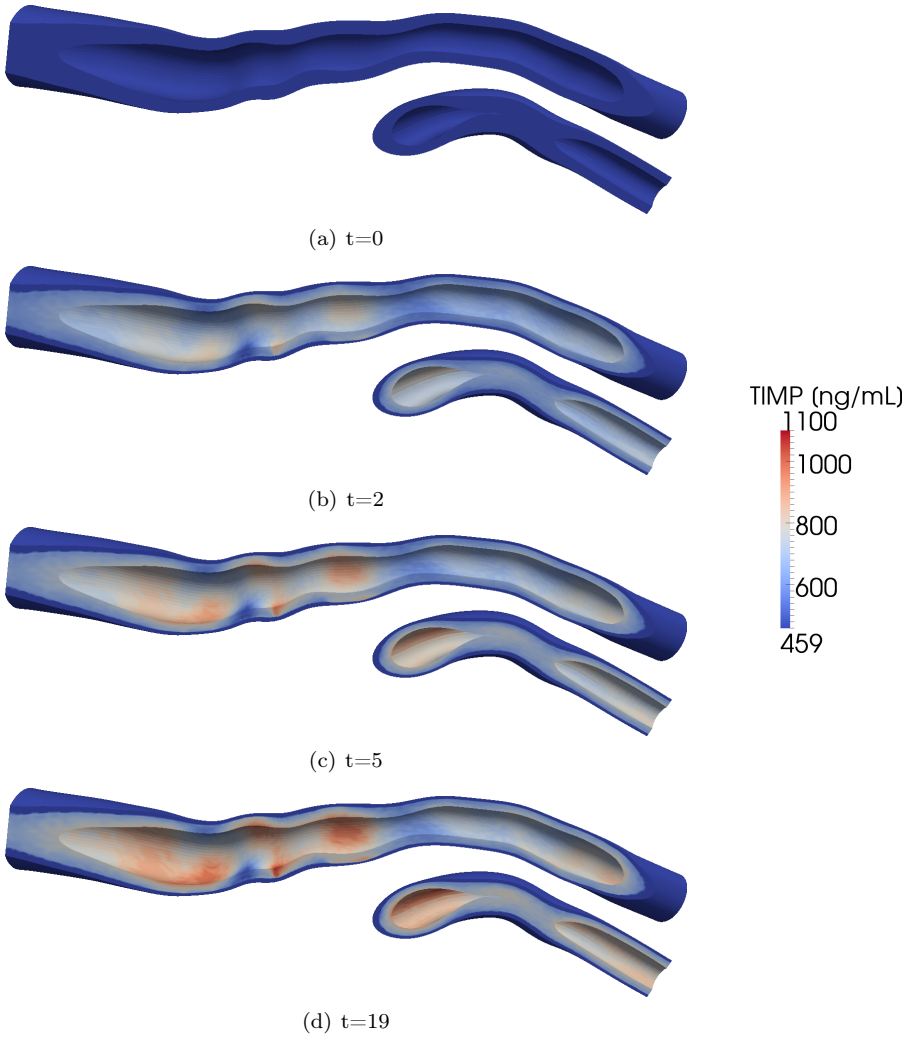

(a) t=0

(b) t=2

(c) t=5

(d) t=19

Figure 5.6: Evolution of the mass production of TIMP due to SMC activity in different depth cuts.

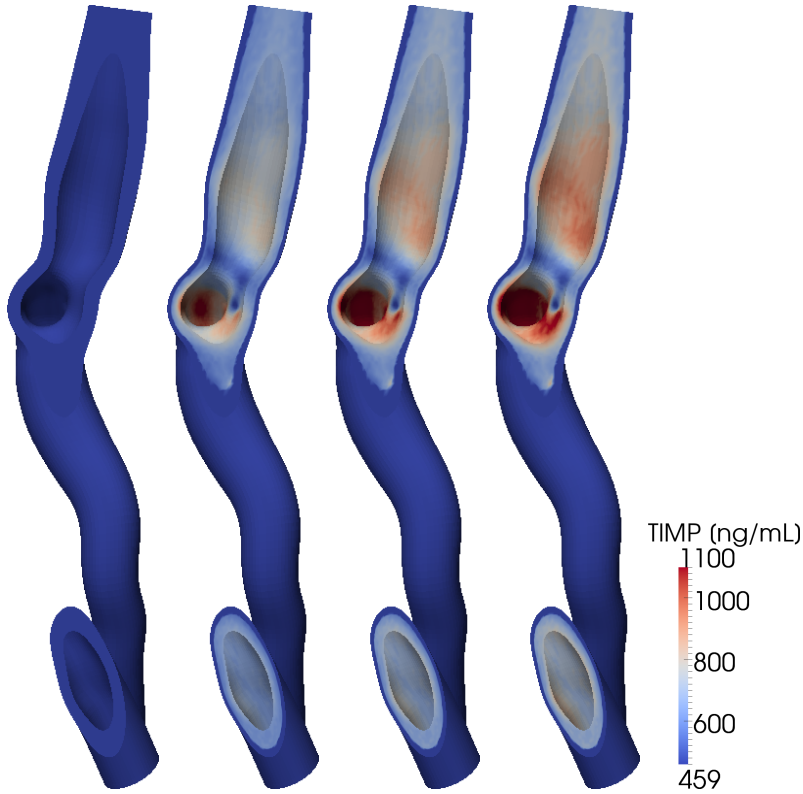

(a) t=0 (b) t=2 (c) t=5 (d) t=19

Figure 5.7: Evolution of the mass production of TIMP due to SMC activity in different transversal cuts.

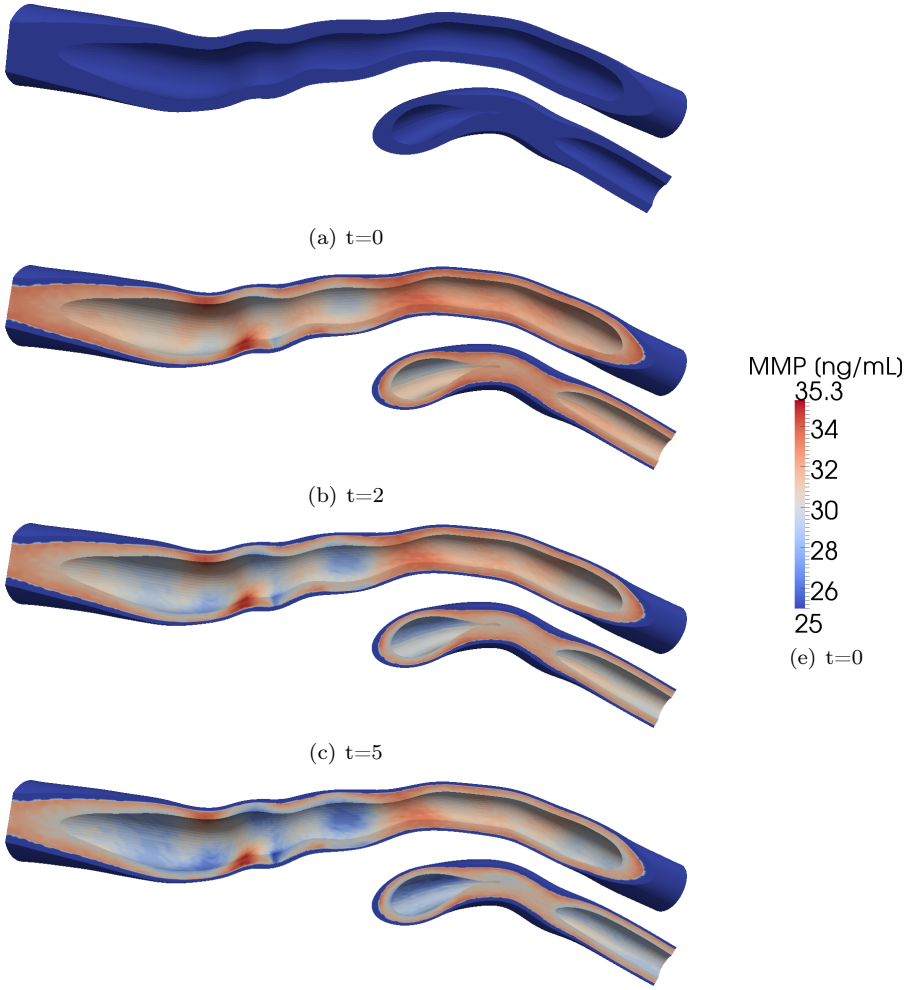

(a) t=0

(b) t=2

(c) t=5

(d) t=19

(e) t=0

Figure 5.8: Evolution of the mass production of MMP due to SMC activity in different depth cuts.

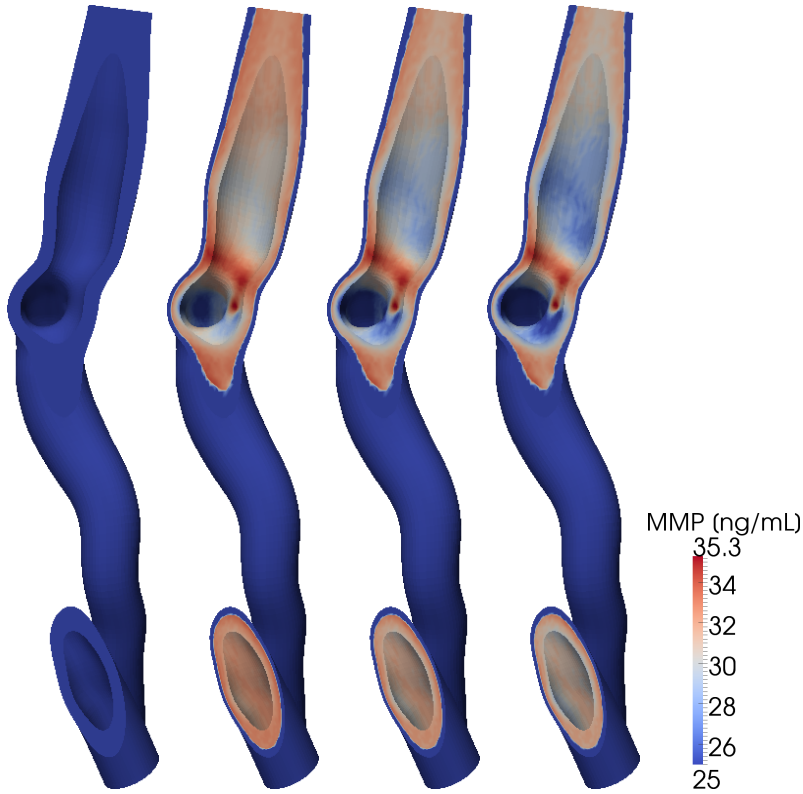

(a) t=0 (b) t=2 (c) t=5 (d) t=19 (e) t=0

Figure 5.9: Evolution of the mass production of MMP due to SMC activity in different transversal cuts.

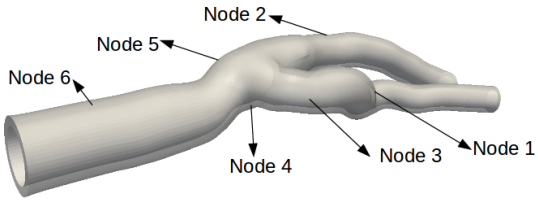

(a) Featured points in the media layer.

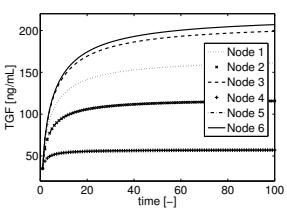

(b) Evolution of TGF-β.

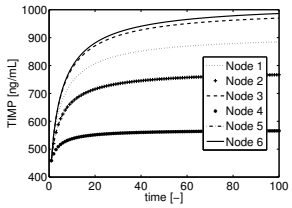

(c) Evolution of MMP

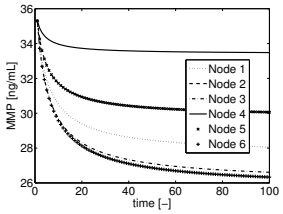

(d) Evolution TIMP

Figure 5.10: Evolution of the mass production of (a) TGF, (b) MMP and (c) TIMP at six featured points due to SMC activity.

phenomena (see, e.g. Philibert (2006) for a review), about Brownian movement by Einstein (1905) as well as the works of related atomistic and macroscopic transport by Maxwell (1871) and Huang (1987) have boosted a great amount of works and efforts in the study of mass transport.

In the field of biology and biomechanics mass transport toward and within the arterial wall is a fundamental process to understand not only different vascular diseases but also the normal evolution of arteries. Mass transport in arterial tissue of different kind of molecules occurs due to concentrations and pressure gradients across the thickness by the well known diffusion and convective phenomena (Tarbell, 2003a). Low-density proteins (LDL) are probably the most studied molecular transport since they are the main initiator of atheroesclerotic plaque (Lusis, 2000) and many works have showed up during the last years, see e.g. Curmi et al. (1990); Glagov et al. (1988); Cancel et al. (2007) and Kim and Tarbell (1994); Huang and Tarbell (1997); Tada and Tarbell (2002) for experimental and numerical works respectively. There are however other important molecules involved in hypertension that gain less attention but also play an im-

portant role in the collagen turnover. As we discussed in the introduction, we are looking at three substances: TGF-β, TIMP and MMP. In the next section we study how these three molecules move through the arterial wall based on their specific features.

5.2.2 Preliminary study of transport phenomena

Diffusion and convection of molecules is an important issue to be considered in mass transport within the arterial wall. In order to discern if these two phenomena are important in mass transport within the arterial wall is usual to calculate the Peclet number (Pe) (Eq. 5.11). For Pe $>>$ 1 convection have to be studied while for Pe $<<$ 1 diffusion dominates the problem.

$$\mathrm{Pe} = \frac{\mathrm{vl}}{\mathrm{D}}, \tag{5.11}$$

where v [m/s] is the fluid velocity through the thickness, l [m] is the thickness and D [m^2/s] the diffusion coefficient.

Diffusion coefficients are related to the molecular size and the size of the porous media where the molecule goes through. For a free media the diffusion coefficient, for the three substances considered in this work, is given by the Stokes-Einstein Equation (Einstein, 1905) as

$$D_\infty[m^2/s] = \frac{k_B T}{6\pi\mu a} = \begin{cases} 1.9227 \cdot 10^{-12} & \text{TGF-}\beta, a = 3.8 \cdot 10^{-9}\text{m} \\ 3.8455 \cdot 10^{-12} & \text{TIMP}, a = 7 \cdot 10^{-9}\text{m} \\ 2.1974 \cdot 10^{-12} & \text{MMP}, a = 4 \cdot 10^{-9}\text{m}, \end{cases} \tag{5.12}$$

where $k_B = 1.38 \cdot 10^{-23}[J/K]$ is the Boltzmann constant, T = 293[K] the absolute temperature which remain constant, $\mu = 4 \cdot 10^{-3}[N.s/m2]$ is the viscosity of the fluid and a is the particle radius obtained by superposing an sphere that contains the particle (see Fig. 5.1).

Diffusivity in a fiber-matrix media was derived by Ogston et al. (1973) and used later on by Kim and Tarbell (1994), among others. The effective diffusion

coefficient can be expressed as

$$D_m[m^2/s] = D_\infty exp\left[-[(1-\epsilon)^{0.5}(1+a/r_f)]\right] = \begin{cases} 8.081 \cdot 10^{-13} & \text{for TGF-}\beta \\ 1.613 \cdot 10^{-12} & \text{for TIMP} \\ 9.229 \cdot 10^{-13} & \text{for MMP,} \end{cases} \tag{5.13}$$

where r_f is the fiber radius which has an average value of $1\mu m$ and $\epsilon = 1 - V_f$ the void fraction and V_f the fiber volume fraction, which, based on data given by Huang and Tarbell (1997) and O'Connell et al. (2008), is approximately equal to 25%. Moreover, the contribution of the presence of SMC can be recovered (Huang and Tarbell, 1997) by

$$D_{eff}[m^2/s] = \frac{1}{1-\epsilon_{SMC}} \frac{1}{f(\epsilon_{SMC})} D = \begin{cases} 4.444 \cdot 10^{-13} & \text{for TGF-}\beta \\ 8.887 \cdot 10^{-13} & \text{for TIMP} \\ 5.075 \cdot 10^{-13} & \text{for MMP,} \end{cases} \tag{5.14}$$

where $f_{\epsilon_{SMC}} = 2.3899$ given a SMC volume fraction of $\epsilon_{SMC} = 0.45\%$ (Huang and Tarbell, 1997).

Going back to Eq. 5.11 we can obtain the Pecklet number for this problem as

$$\mathrm{Pe} = \frac{\mathrm{vl}}{\mathrm{D}_{eff}} \approx 10^2, \tag{5.15}$$

where v take a mean value of 0.05 $[\mu m/s]$ (Levick, 1987; Wang and Tarbell, 1995), l 1-0.6 [mm] thickness and the effective diffusive parameters given in Eq. 5.14, gives a Peclet number in the order of hundreds, which points out the necessity of taking into account the convective phenomena.

The coefficient related to the convective term, the lag coefficient of solute in the interstitial phase with fiber matrix, was showed by Curry (1984) to be

expressed as

$$K_{cf}[-] = 2 - \Phi = \begin{cases} 1.006 & \text{for TGF-}\beta \\ 1.011 & \text{for TIMP} \\ 1.006 & \text{for MMP,} \end{cases} \tag{5.16}$$

where Φ is the partition coefficient defined by Ogston et al. (1973) as

$$\Phi[-] = exp\left[-[(1-\epsilon)(2a/r_f + a^2/r_f^2)]\right] = \begin{cases} 0.994 & \text{for TGF-}\beta \\ 0.989 & \text{for TIMP} \\ 0.994 & \text{for MMP.} \end{cases} \tag{5.17}$$

As we did in previous coefficient, we need to weight the lag coefficient to include the SMC cell contribution as

$$K_{cf_{eff}}[-] = \frac{1}{1-\epsilon_{SMC}} K_{cf} = \begin{cases} 1.348 & \text{for TGF-}\beta \\ 1.341 & \text{for TIMP} \\ 1.348 & \text{for MMP.} \end{cases} \tag{5.18}$$

5.2.3 Convection-Diffusion problem in the arterial wall

Considering changes in mass as its basic characteristic, see e.g. the monographs by Welty et al. (2008) and Deen (2011), the balance of mass (Eq. 5.19) has to fulfill that the flux of mass and the mass source be in equilibrium with the change of material density

$$\mathrm{D}_t \rho_0 = \mathrm{Div}\mathbf{J} + \mathcal{R}_0 \quad \text{in } \Omega, \quad t \in (0, T), \tag{5.19}$$

where ρ_0 is the material density, $\mathbf{J}$ the mass flux and $\mathcal{R}_0$ the source of mass. The domain of interest, as previously introduced, will be denoted by Ω.

As it was demonstrated in the previous Section, the mass transport in arterial tissue is a diffusion-convection problem. To recover these issues the flux term is given by

$$\mathbf{J} = -\mathrm{D}\nabla\rho_0 - \rho_0 \mathrm{D}_t \mathbf{u}, \tag{5.20}$$

where the first term represents the diffusive contribution and is driven by density gradients. The second term represents the convective contribution and it is assumed to be controlled by pressure gradients with **u** the displacement vector. We can obtain the velocity through the solid by means of Darcy's law (Eq. 5.21). Note therefore, that Navier-Stokes equations are not used and velocity is not obtained independently but based on pressure gradients. Some authors (Tada and Tarbell, 2002) have also used Brinkman equation (Brinkman, 1947) for model the transmural flow.

$$\nabla \mathrm{p} = -\mu / K_p \mathrm{D}_t \mathbf{u}, \tag{5.21}$$

where p is the pressure and μ the viscosity of the fluid.

The parameter need to study the convection related term in blood vessels, according to the fiber-matrix theory, is the hydraulic permeability K_p which can be calculated with the Kozeny-Carman equation as discussed by Curry (1984).

$$K_p[m] = \frac{r_f^2 \epsilon^2}{4c_k(1-\epsilon)^2} = 1.389e-13, \tag{5.22}$$

where c_k is the Kozeny constant with a value equal to 5 (Huang and Tarbell, 1997). And again the permeability have to be recalculated to take into account SCM distribution. In a similar way

$$K_{p_{eff}}[m] = K_p \frac{1-\epsilon_{SMC}-0.3058\epsilon_{SMC}}{1-\epsilon_{SMC}+0.3058\epsilon_{SMC}} = 7.9721e-14. \tag{5.23}$$

5.2.4 Computational aspects

The partial differential equation presented in Eq. 5.19 is managed numerically to be solved within a Finite Element scheme. The basic procedure is here described for sake of clarity. The problem is solved in ABAQUS with standard elements and formulation therefore it does not give any new insight on the issue. By evaluating Eq. 5.19 in the domain Ω_0 and applying Divergence Theorem we get

$$\int_{\Omega_0} \mathrm{D}_t \rho_0 \mathrm{dV} = \int_{\delta\Omega_0} \mathbf{J} \cdot \mathbf{n} \mathrm{dV} + \int_{\Omega_0} \mathcal{R}_0 \mathrm{dV}. \tag{5.24}$$

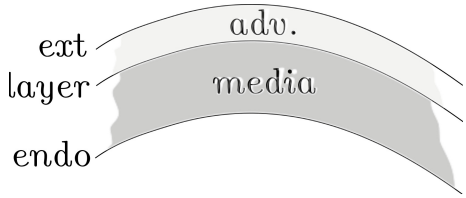

Figure 5.11: Sketch of the layers and boundary conditions in the mass transport problem.

The boundary of the problem (Eq. 5.25) $\delta\Omega_0$ is conditioned by Dirichlet boundary conditions over $\delta\Omega_0^d$ and Neumann boundary conditions over $\delta\Omega_0^n$.

$$\begin{aligned} \rho_0 &= \rho_0^* \text{ on } \delta\Omega_0^d, \\ \mathbf{J}\cdot\mathbf{n} &= R \text{ on } \delta\Omega_0^n. \end{aligned} \tag{5.25}$$

In particular we consider the following set of boundary conditions in the boundary problem in Fig. 5.11

$$\mathbf{J}\cdot\mathbf{n} = 0 \text{ on } \delta\Omega_{endo}^n \tag{5.26}$$

$$\mathbf{J}^{layer+}\cdot\mathbf{n}^{layer+} = \mathbf{J}^{layer-}\cdot\mathbf{n}^{layer-} \text{ on } \delta\Omega_{layer}^n \tag{5.27}$$

$$\mathbf{J}^{ext}\cdot\mathbf{n}^{ext} = 0 \text{ on } \delta\Omega_{ext}^d. \tag{5.28}$$

5.2.5 Finite element results

In this section we present the results of the mass transport from the media layer through the arterial wall. The results are presented in two longitudinal cuts and only for the adventitia layer, for sake of clarity. Note that fibroblast are located mainly in the adventitia layer and they are responsible for the synthesis of collagen molecules. Therefore, we focus on the substances turnover only in the adventitia layer. In Figs. 5.12 and 5.13 we show the evolution of the TGF-β content in the adventitia layer for different times and both cuts. Figs. 5.14, 5.15, 5.16 and 5.17 do for the evolution of TIMP-1 and MMP-1 respectively. The

results are simulated with the material parameters shown in Section 5.2.2. The concentration field of the three substances shows similar qualitative results since its trigger stimulus is the same, the stretch difference between the homeostatic and the hypertensive states. Qualitative results show that substances in the adventitia layer maintain a similar, although slightly below the concentration in the media layer, where these substances are synthesized. A higher mass transfer rate appears for the TIMP given the higher diffusion coefficient. We also show in Fig. 5.18 the mass evolution of the three substances at the six feature points highlighted in that figure.

5.3 Collagen remodeling

5.3.1 Introduction

As we introduced in a previous sections collagen is a fundamental component of many biological tissue and arteries in particular. There is a bunch of *in-vitro* and *in-vivo* experiments that show the influence of the mechanical load (Sumpio et al., 1988; Gupta and Grande-Allen, 2006) with vascular cells and the TGF-β turnover (Bishop et al., 1998; Butt and Bishop, 1997; O'Callaghan and Williams, 2000; Strauss and Rabinovitch, 2000) and with hypertensive patients (Diez and Laviades, 1997; Laviades et al., 1998). In this section we present a model for the production of collagen by fibroblast, which we directly relate with the amount of TGF-β. The collagen degradation is based on the amount of MMP in the tissue. Both deposition and degradation can occur at the intracellular (collagen molecules) or extracellular (tropocollagen) levels. There have been several *in-vitro* and *in-vivo* experiments studying these processes in detail.

5.3.2 Mass Source Model

With the relevant collagen turnover sources terms defined, we can establish the evolution of the collagen fibers density,

$$\mathcal{R}_{\text{col}} = \dot{\rho}_{\text{col}} = \gamma_{\text{dep}}\mathcal{R}_{\text{TGF}-\beta} + \gamma_{\text{abs}}\mathcal{R}_{\text{MMP}}, \tag{5.29}$$

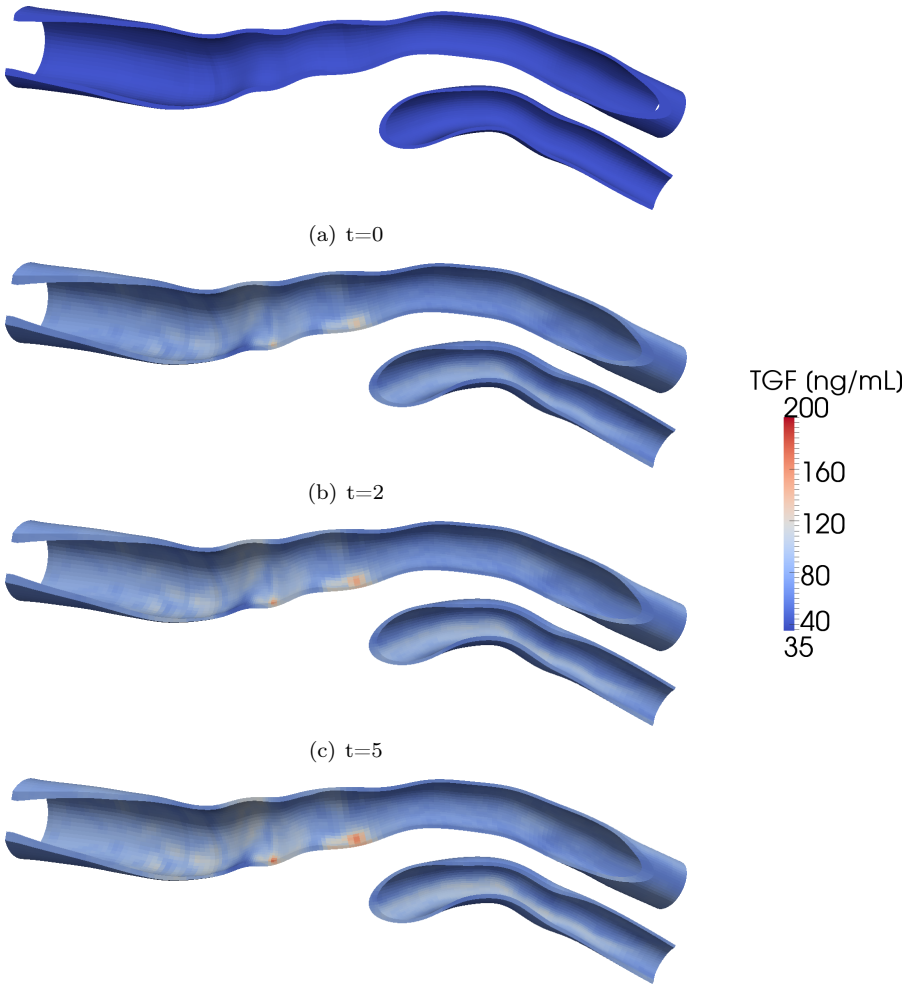

(a) t=0

(b) t=2

(c) t=5

(d) t=19

Figure 5.12: Evolution of the TGF-β content in the adventitia layer due to mass transport in the carotid wall in different depth cuts.

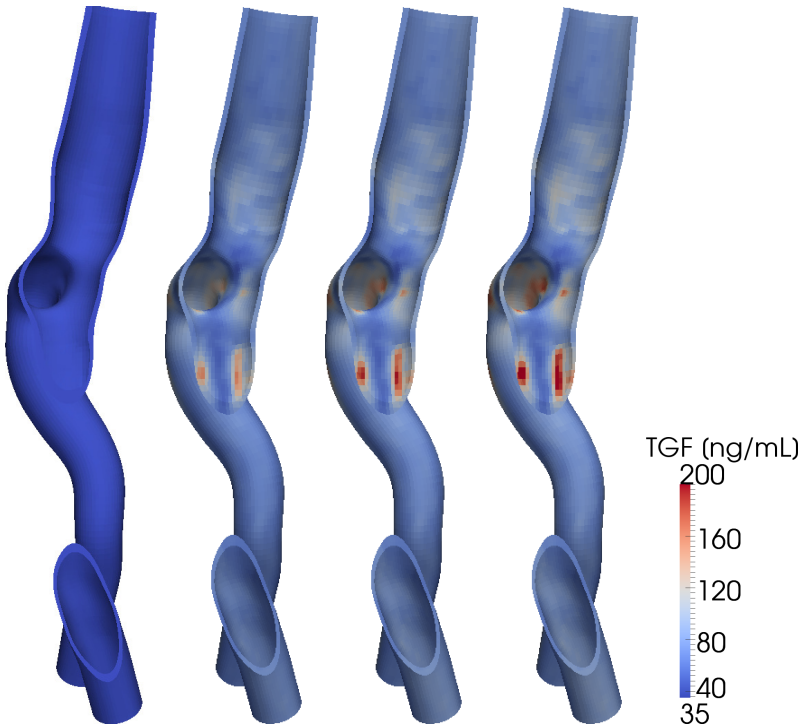

(a) t=0 (b) t=2 (c) t=5 (d) t=19

Figure 5.13: Evolution of the TGF-β content in the adventitia layer due to mass transport in the carotid wall in different transversal cuts.

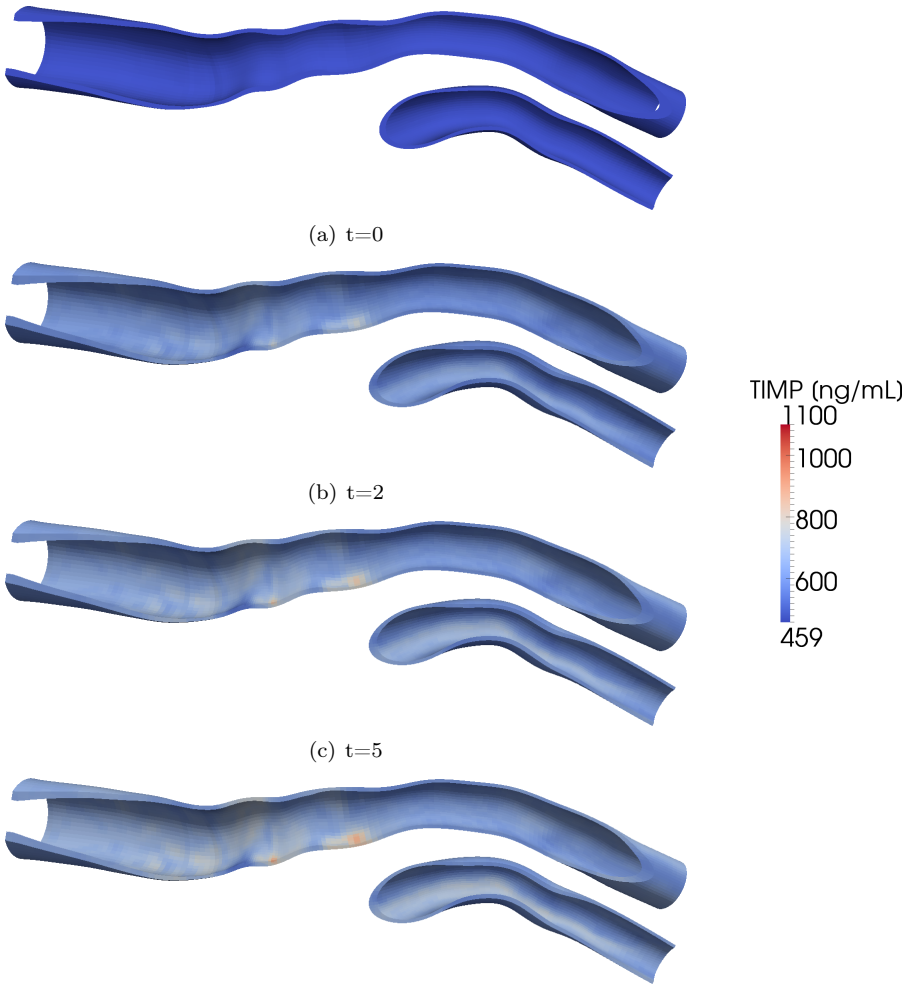

(a) t=0

(b) t=2

(c) t=5

(d) t=19

Figure 5.14: Evolution of the TIMP content in the adventitia layer due to mass transport in the carotid wall in different depth cuts.

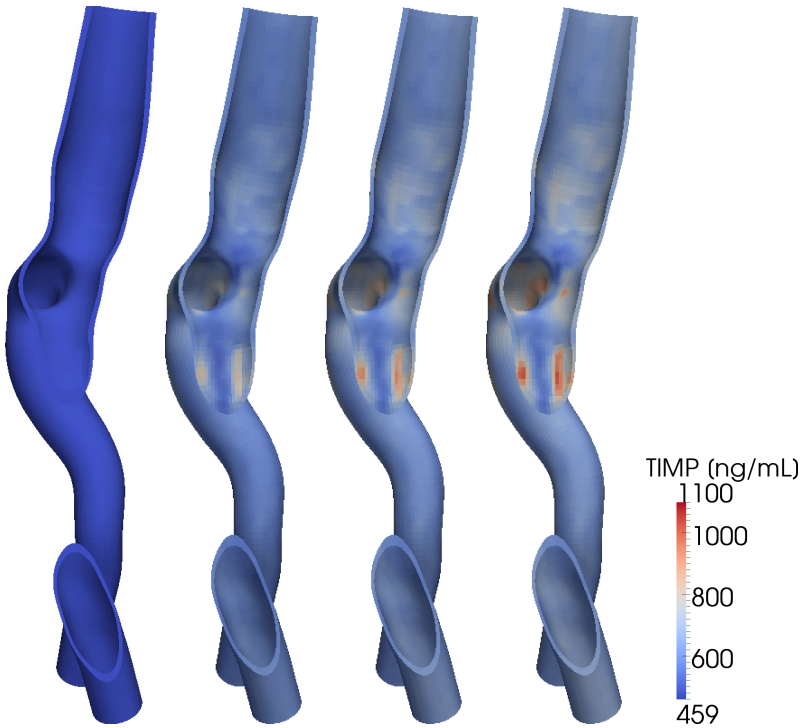

(a) t=0 (b) t=2 (c) t=5 (d) t=19

Figure 5.15: Evolution of the TIMP content in the adventitia layer due to mass transport in the carotid wall in different transversal cuts.

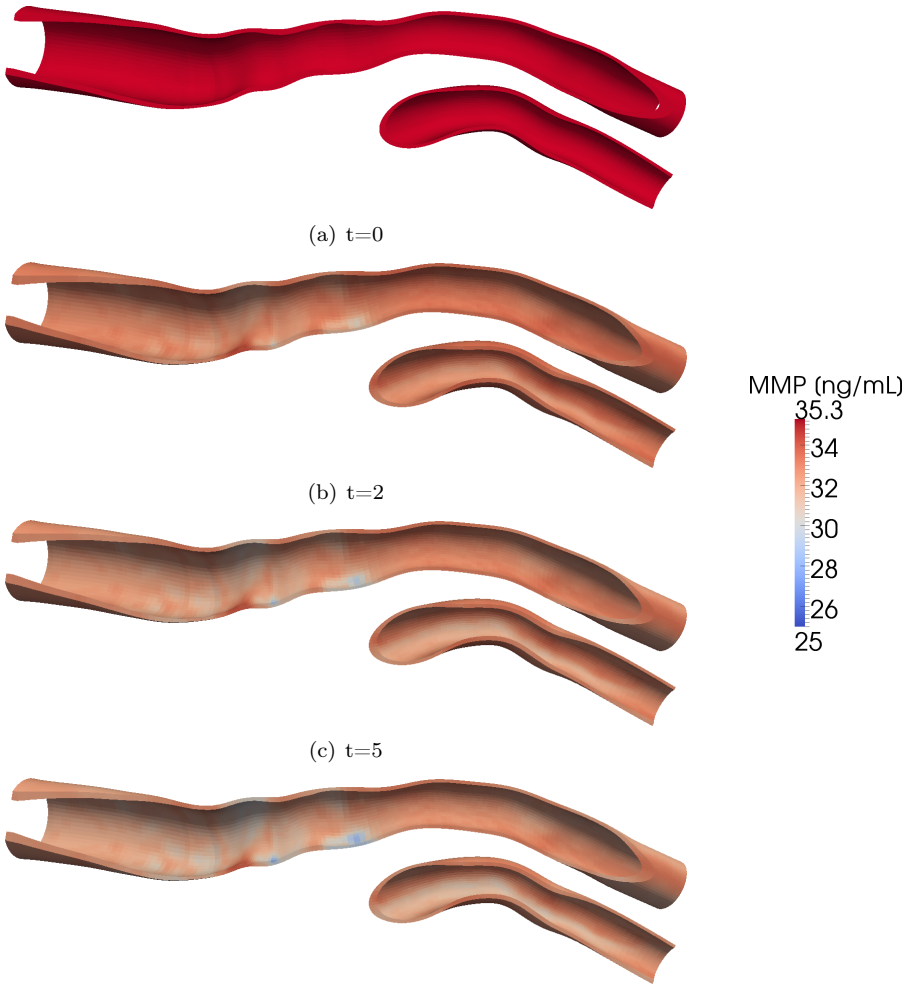

(a) t=0

(b) t=2

(c) t=5

(d) t=19

Figure 5.16: Evolution of the MMP content in the adventitia layer due to mass transport in the carotid wall in different depth cuts.

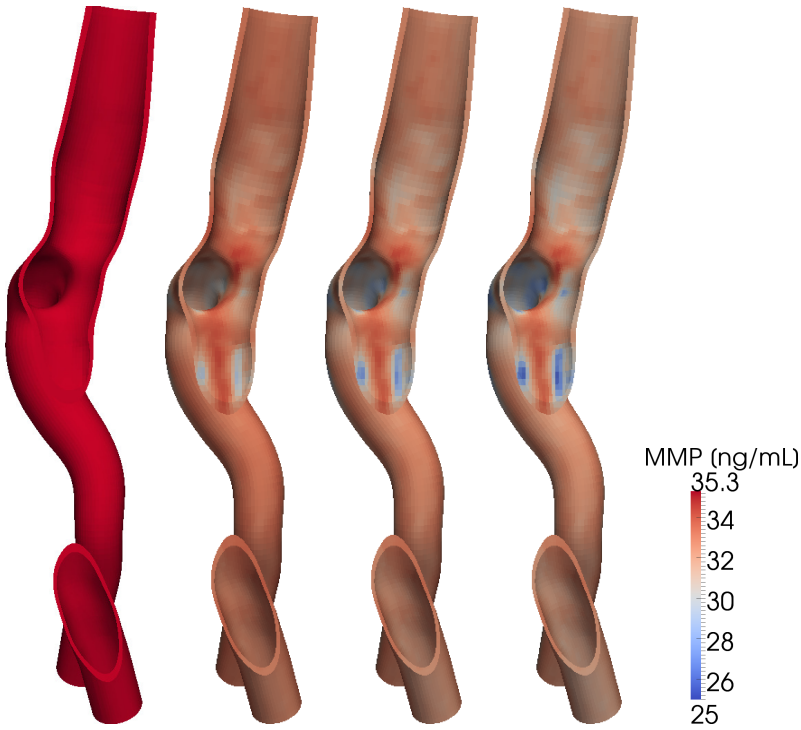

(a) t=0 (b) t=2 (c) t=5 (d) t=19

Figure 5.17: Evolution of the MMP content in the adventitia layer due to mass transport in the carotid wall in different transversal cuts.

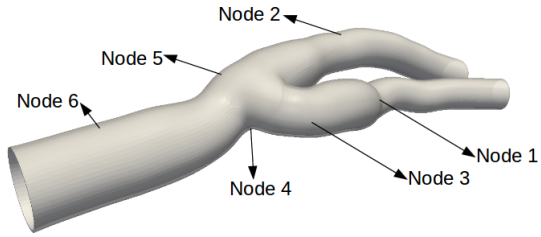

(a) t=0

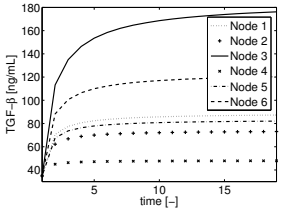

(b) t=0

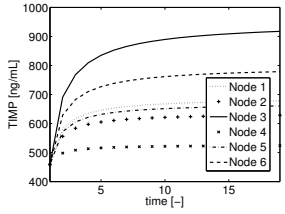

(c) t=2

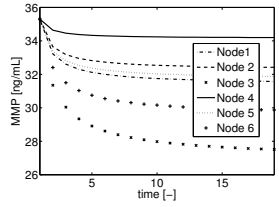

(d) t=5

Figure 5.18: Evolution of the mass transport in the adventitia of TGF (a), MMP (b) and TIMP (c) at six featured points due to SMC activity.

where $\gamma_{\text{dep}}, \gamma_{\text{abs}} \in \mathbb{R}^+$ denote the sensitivities of collagen deposition and absorption in response to changes in TGF-β and MMP, respectively. In summary, our model can capture three different scenarios, an overall increase, $\mathcal{R}_{\text{col}} > 0$, decrease, $\mathcal{R}_{\text{col}} < 0$, or maintenance of the collagen content, $\mathcal{R}_{\text{col}} = 0$. These scenarios have to be constrained by the next inequalities in order to ensure right collagen turnover.

$$\mathcal{R}_{col} \begin{cases} > 0 & \text{if} \quad \lambda_{\text{smc}} > \lambda^* \mapsto \gamma_{\text{dep}}/\gamma_{\text{abs}} > \mathcal{R}_{\text{MMP}}/\mathcal{R}_{\text{TGF}-\beta} \\ < 0 & \text{if} \quad \lambda_{\text{smc}} < \lambda^* \mapsto \gamma_{\text{dep}}/\gamma_{\text{abs}} < \mathcal{R}_{\text{MMP}}/\mathcal{R}_{\text{TGF}-\beta} \\ = 0 & \text{if} \quad \lambda_{\text{smc}} = \lambda^* \mapsto \gamma_{\text{dep}}/\gamma_{\text{abs}} = \mathcal{R}_{\text{MMP}}/\mathcal{R}_{\text{TGF}-\beta} \end{cases} \tag{5.30}$$

In addition, we take into account the results by Diez et al. (1995), where the serum concentration of procollagen peptides was examined. The authors studied the concentration of procollagen type I carboxy terminal peptide (PIP), which has been proposed as a marker of synthesis of collagen type I, displaying an in-

crease of 28%. The same authors found that the carboxy-terminal telopeptide of collagen type I (CITP), marker of extracellular collagen degradation, was increased by approximately a 9% (Laviades et al., 1998).

Accordingly, we simulate the case of hypertension, to explore to which extent our model is capable of reproducing these experimental findings. To quantify the collagen turnover in response to an increase in TGF-β and a decrease in MMP, as we calculated in Section 5.1.5, we compute the deposition and absorption, as $\dot{\rho}^{+}_{\text{col}} = \gamma_{\text{abs}}\,\dot{\rho}_{\text{TGF}-\beta}$ and $\dot{\rho}^{-}_{\text{col}} = \gamma_{\text{dep}}\,\dot{\rho}_{\text{MMP}}$ respectively. The material parameters are summarized in Table 5.3.

Table 5.3: Collagen turnover model. Material parameters for hypertensive case study.

material parameter	value	units
ρ^{*}_{col}	1	[g/mL]
γ_{dep}	90000	[−]
γ_{abs}	400000	[−]

In Fig. 5.19 we illustrate the impact of these changes on the evolution of the overall collagen content. With the help of the studies reported in the literature, we can correlate the collagen synthesis due to the TGF-β concentration changes as shown in Fig. 5.19(a). Fig. 5.19(b) illustrates collagen degradation due to the decrease in MMP. Fig. 5.19(c) displays the overall turnover of collagen, confirming the characteristic increase in collagen content for hypertensive patients.

As a resume, in Table 5.4, we provide the different material parameters presented in this section for the evolution of the collagen density model.

5.3.3 Mechanical Model and implementation

In the previous sections we have exploited an analytical model, and its computational implementation, of mass production, the diffusion of the main substances through the arterial wall, and how those phenomena cause a collagen turnover in the wall. In this subsection we are looking at how the arterial wall change its

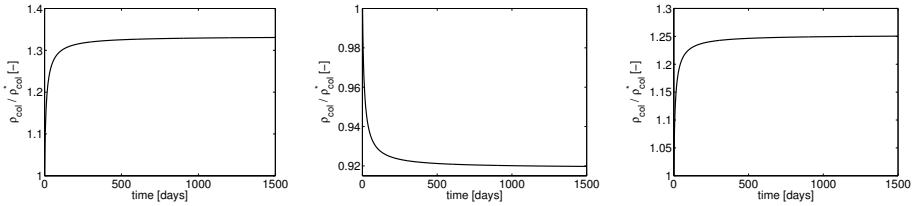

(a) Evolution of collagen density in response to increase in TGF-β

(b) Evolution of collagen density in response to decrease of TIMP

(c) Evolution of the collagen density in response to both increase in TGF-β and decrease in MMP

Figure 5.19: Evolution of the collagen content in hypertensive patients driven by an increase in TGF-β and a decrease in MMP.

mechanical properties due to collagen density changes. We begin recalling the baseline SEDF described in Eq. 3.10. This latter equation was described in terms of a constant density of the material constituents. We will modify the collagen SEDF to reflect its turnover as $\dfrac{\rho_{col}}{\rho^*_{col}}\Psi_{col}$.

The numerical implementation of the collagen mass source evolution yields a Euler-backwards scheme as performed in previous sections. We transform the the evolution equations Eq. 5.29 for collagen to its residual formats.

$$\mathsf{R}_{\text{col}} \quad = \quad \rho^{j+1}_{\text{col}} \quad - \quad \rho^{j}_{\text{col}} \quad - \quad \mathcal{R}_{\text{col}} \quad \Delta t = 0 \tag{5.31}$$

Note that this time there are not non-linear equations involved and the updated of the equation can be achieved based on Eq. 5.31. Subtitutying now Eq. 5.2 and Eq. 5.3 into Eq. 5.29, and based on affinity of SMC and collagen stretches ($\lambda_{SMC} \equiv \lambda_{col}$) we get

$$\mathcal{R}_{\text{col}} = \gamma_{\text{dep}} \left[\gamma_{\text{TGF}-\beta} \left[\frac{\rho_{\text{TGF}-\beta}}{\rho^*_{\text{TGF}-\beta}} \right]^{-m_{\text{TGF}-\beta}} \lambda_{\text{col}} - \lambda^*_{\text{TGF}-\beta} \right] + \gamma_{\text{abs}} \left[\gamma_{\text{TIMP}} \left[\frac{\rho_{\text{TIMP}}}{\rho^*_{\text{TIMP}}} \right]^{-m_{\text{TIMP}}} \lambda_{\text{col}} - \lambda^*_{\text{TIMP}} \right] \tag{5.32}$$

from where we can obtain the last term of Eq. 5.31 giving

Table 5.4: Collagen turnover model. Relevant material parameters, their physical interpretations and units.

material parameter	physiological interpretation	units
$\rho^*_{\mathrm{TGF}-\beta}$	initial density of TGF-β	[μg/mL]
ρ^*_{TIMP}	initial density of TIMP	[μg/mL]
ρ^*_{MMP}	initial density of MMP	[μg/mL]
ρ^*_{col}	initial density of collagen	[μg/mL]
$m_{\mathrm{TGF}-\beta}$	exponent of TGF-β evolution	[$-$]
m_{TIMP}	exponent of TIMP evolution	[$-$]
$\gamma_{\mathrm{TGF}-\beta}$	sensitivity of TGF-β to SMC stretch changes	[$-$]
γ_{TIMP}	sensitivity of TIMP to changes in SMC stretch	[$-$]
γ_{MMP}	sensitivity of MMP to changes in TIMP	[$-$]
γ_{dep}	sensitivity of collagen deposition to changes in TGF-β	[$-$]
γ_{abs}	sensitivity of collagen absorption to changes in MMP	[$-$]

$$\frac{\partial \dot{\rho}_{col}}{\partial \mathbf{C}} = \frac{1}{2\lambda_{col}} \left[\gamma_{\mathrm{dep}} \gamma_{\mathrm{TGF}-\beta} \left[\frac{\rho_{\mathrm{TGF}-\beta}}{\rho^*_{\mathrm{TGF}-\beta}} \right]^{-m_{\mathrm{TGF}-\beta}} + \gamma_{\mathrm{abs}} \gamma_{\mathrm{TIMP}} \left[\frac{\rho_{\mathrm{TIMP}}}{\rho^*_{\mathrm{TIMP}}} \right]^{-m_{\mathrm{TIMP}}} \right] \mathbf{n} \otimes \mathbf{n} \tag{5.33}$$

We can now get stress tensors and its linearization with respect to deformation for a next FE implementation. Piola-Kirchoff stress tensor reads

$$\mathbf{S}_{col} = \frac{\rho_{col}}{\rho^*_{col}} \frac{\partial \Psi_{col}}{\partial \mathbf{C}}, \tag{5.34}$$

and the tangent operator

$$\mathbf{C}_{col} = \frac{d\mathbf{S}_{col}}{d\mathbf{C}} = \left. \frac{\partial \mathbf{S}_{col}}{\partial \mathbf{C}} \right|_{\mathbf{C}} + \left. \frac{\partial \mathbf{S}_{col}}{\partial \mathbf{C}} \right|_{\rho}. \tag{5.35}$$

The first term yields the classical elastic modulus like

$$\left. \frac{\partial \mathbf{S}_{col}}{\partial \mathbf{C}} \right|_{\mathbf{C}} = \frac{\rho_{col}}{\rho^*_{col}} \mathbf{C}_{col}. \tag{5.36}$$

The second term is associated to the linearization of the stress tensor with respect to changes on the collagen turnover. This term can be split up as

$$\left.\frac{\partial \mathbf{S}_{col}}{\partial \mathbf{C}}\right|_{\rho} = \frac{\partial \mathbf{S}_{col}}{\partial \rho} \otimes \frac{\partial \rho}{\partial \mathbf{C}}, \tag{5.37}$$

with

$$\frac{\partial \mathbf{S}_{col}}{\partial \rho} = \frac{\mathbf{S}_{col}}{\rho^{*}_{col}} \qquad \text{and} \qquad \frac{\partial \rho}{\partial \mathbf{C}} = \Delta \mathrm{t}\, \left.\frac{\partial \mathsf{R}_{\mathrm{col}}}{\partial \rho_{\mathrm{col}}}\right|^{-1}_{\rho^{k}_{\mathrm{col}}} \frac{\partial \dot{\rho}_{col}}{\partial \mathbf{C}}, \tag{5.38}$$

where Eq. 5.38(1) is obtained by derivation of Eq. 5.31 with respect to the Cauchy-Green strain tensor and solving for $\partial_{\mathbf{C}}\rho$.

This is the procedure used to compute a consistent linearization of the problem. In our particular case, we have considered that substances are transported by diffusion and convection phenomena. Although a fully implicit formulation is also feasible, it turns into a much more complicated computational model, we refer to Kuhl (2003) where a complete definition of open systems and its numerical implementation is addressed. For sake of simplicity, we are considering a explicit formulation so we will rewrite the update of the collagen mass as

$$\rho^{j+1}_{\mathrm{col}} \quad = \quad \rho^{j}_{\mathrm{col}} \quad + \quad \hat{\mathcal{R}}_{\mathrm{col}} \quad \Delta t = 0 \tag{5.39}$$

where the residual is not needed anymore. The mass source is modified as

$$\hat{\mathcal{R}}_{\mathrm{col}} = \gamma_{\mathrm{dep}} \hat{\mathcal{R}}_{\mathrm{TGF}-\beta} + \gamma_{\mathrm{abs}} \hat{\mathcal{R}}_{\mathrm{MMP}} \tag{5.40}$$

$\hat{\mathcal{R}}_{\mathrm{TGF}-\beta}$ and $\hat{\mathcal{R}}_{\mathrm{MMP}}$ are actual amount of TGF-β and MMP at every integration point after the mass transport phenomena and we neglect the dependecy of these variables with respect to the stretch of the SMC. Therefore, the tangent modulus is reduced to

$$\mathbf{C}_{col} = \left.\frac{\partial \mathbf{S}_{col}}{\partial \mathbf{C}}\right|_{\mathbf{C}} \tag{5.41}$$

5.3.4 Results

In this last section we present the results of the increment of collagen content. The results are presented at 4 different longitudinal cuts in Fig. 5.20 and in Fig. 5.21 for the media and adventitia layer respectively. The results show the evolution

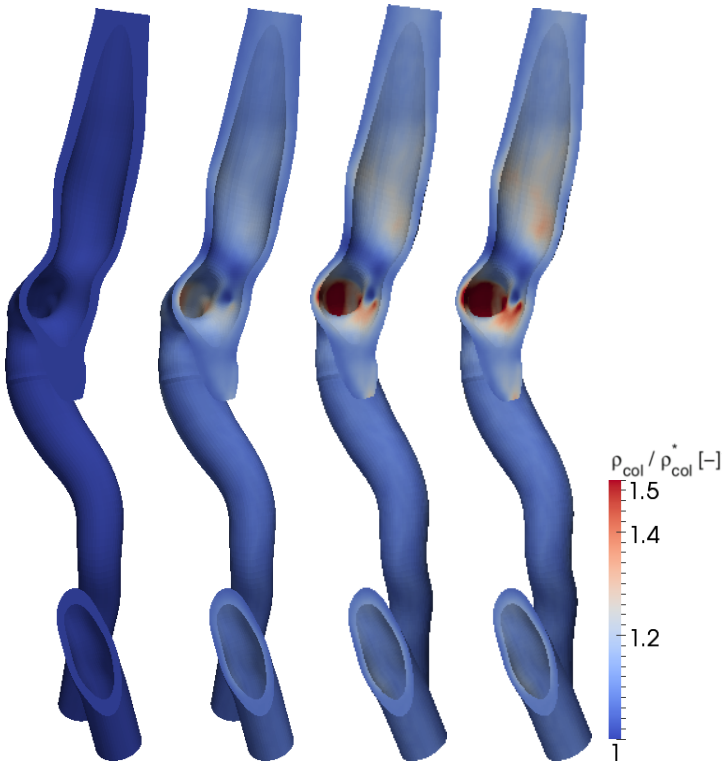

Figure 5.20: Evolution of the collagen content in ρ_{col}/ρ^*_{col} due to fibroblast realease and MMP degradation in the media layer.

of the collagen turnover due to the unbalance of TGF-β and MMP-1. Increase in collagen content is higher in the media than in the adventitia layer. Note that concentration of TGF-β and MMP-1 are lower in the adventitia after the transport of these substances from the media layer, where they are synthetized. Evolution in the media layer goes from an averaged value of 8-10% to maximums of 45-50% with some peaks of 80%.

Following the TGF-β, MMP and TIMP evolution in Fig. 5.18, collagen turnover in the six nodes of interest shows an maximum increase of collagen in the media layer of $\approx 35\%$, mean increases of $\approx 15\%$ and minimums at 3%. Re-

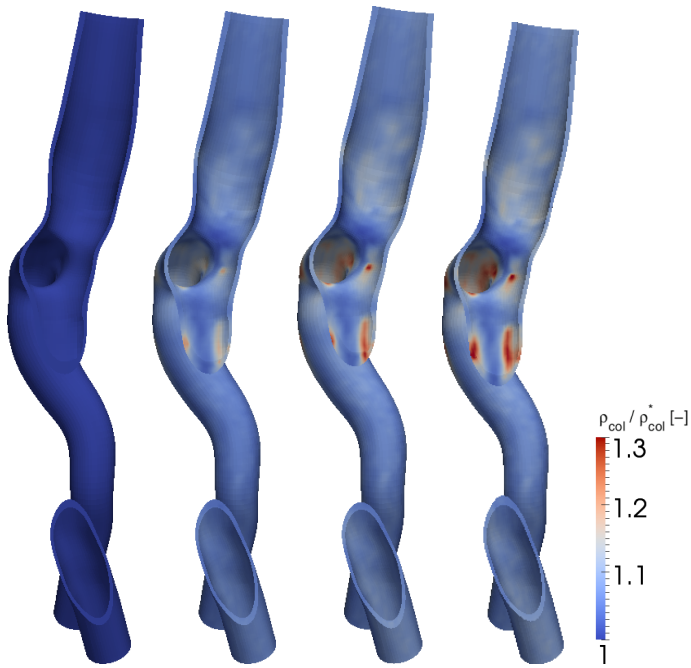

(a) t=0 (b) t=2 (c) t=5 (d) t=19

Figure 5.21: Evolution of the collagen content in ρ_{col}/ρ^*_{col} due to fibroblast realease and MMP degradation in the adventitia layer.

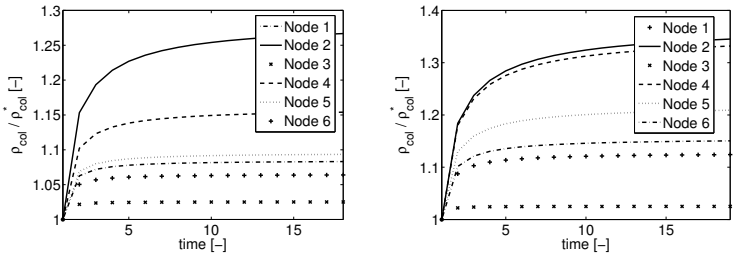

(a) Collagen evolution in adventitia layer. (b) Collagen evolution in media layer.

Figure 5.22: Evolution of the collagen content in the media and adventitia stress at the six nodes depicted in Fig. 5.18.

sults in the featured points in the adventitia layer shows mean values of $\approx 10\%$, with maximums at 30% and minimums around $3 - 5\%$.

Given the Neumann boundary conditions, increases of collagen content lead to the contraction in the lumen radio while maintain similar stress levels over the arterial wall. This means that the consequence of the collagen turnover is the diminishing of the lumen radio and not an increase of the stresses in the arterial wall. The contraction values of the carotid lumen due to the increase of collagen content are shown in Table 5.5 as well as the slices of interest. Several slices of the carotid are investigated where the contraction level (diameters ratio after and before collagen turnover) varies from $\approx 10 - 20\%$.

5.4 Conclusions

Arterial tissue undergoes important changes in its mechanical properties during the lifetime (Jani and Rajkumar, 2006) but also because of different pathologies. In this chapter we focused on the collagen turnover that occurs in hypertensive patients (Bishop et al., 1994; Laviades et al., 1998; McNulty et al., 2006). The main consequence of the increase in collagen content is the stiffening of the arterial wall.

To this end we developed a computational model to study the collagen turnover

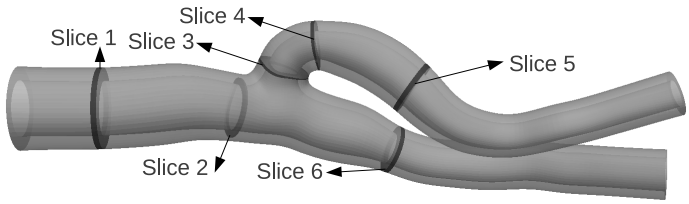

	Slice 1	Slice 2	Slice 3	Slice 4	Slice 5	Slice 6
Initial radio [mm]	4.8177	3.8292	2.9090	2.6611	3.5053	3.1023
Initial radio [mm]	4.0444	3.2109	2.6538	2.1879	2.8946	2.6078
Contraction [%]	19.21	19.25	9.61	21.62	11.98	18.89

Table 5.5: Variation on the lumen diameters at different positions due to the increase in collagen content .

in hypertensive disease. We first computed a two-step simulation of a carotid artery. The first one at physiological pressure in normotensive conditions and the second one at hypertension. The overall microstructure, and therefore the SMC, undergo an over-streching due to the over-pressure of hypertension conditions. We consider this increase of the SMC stretch as the trigger that boosts the synthesis of different substances. At this point, we computed the amount of TGF-β and TIMP-1 segregated by the SMC and the subsequent unbalance of MMP. In the next step we simulated the mass transport of these substances from the media layer through the adventitia layer. The interaction of MMP-1 with collagen as well as the stimulation of fibroblast by TGF-β make the collagen content to change, increasing in the case of hypertension.

During quite a long time, the turnover of the different constituents in the arterial wall have been studied experimentally and by mathematical and numerical models. Most of these models have been based in purely mechanical stimuli leaving out a huge amount of biochemical processes. Other models, which do include the synthesis and degradation of biological substances do not studied how the mechanical properties of the tissue change. There exist some models that do all these approaches together, but mostly analytically and in very simple geometries. In this chapter we have performed a mechano-chemical model of the evolution process of collagen turnover in the vessel wall during hypertension.

Our results of TGF-β, TIMP and MMP turnover correlate with experimental reports in Laviades et al. (1998), Schaan et al. (2007) and Porreca et al. (1997), among many others. In terms of the collagen content, our model shows increases of $\approx 15\%$ in the media layer and of $\approx 10\%$ in the adventitia. Maximums were around 35% and 25% in the media and adventitia layers respectively. These results are comparable with the experimental findings in, e.g., Bagshaw et al. (1987) reporting a 37% increase of collagen content or Hu et al. (2007b) showing a 30%. Hu et al. (2008) also report increases of 15% in hypertension following a decrease to normal values. They hypothesized that it was due to the enhance collagen degradation by MMPs. Eberth et al. (2010) also observed the collagen content to rise up to $\approx 20\%$ in an extensive model of carotid remodeling in altered pulsatility. Collagen turnover has a straight consequence in the arterial

compliance and distensibility due to the stiffening that the collagen provides. Our results reflect this behavior in terms of a lost of distensibility and decrease of the lumen diameter. These stiffening has been reported by, e.g., Hayashi et al. (1980); Hajdu and Baumbach (1994); Hu et al. (2007b,a) and Eberth et al. (2011). All these works show the stiffening that our model predicts.

There are, however, not few limitations. First, we have left out of this study a very important behavior of SMC, the myogentic tone. The myogenic tone makes arteries to adapt its lumen to maintain the same mechanical state in the wall. There are several models that study this fact and its associated active force, which is usually triggered by a mechanical or chemical stimuli. Although the model should differ in somehow if that feature would be included, the basic idea should kept the same.

In terms of computational issue, the model could be also be performed in a more elegant way. We did our simulations in a sequential way, so every results have to be written out and read in the next simulation. A fully couple formulation and simulation would be a more formal option. However, given the differences in the scale of times of each process, mass transfer, transport and collagen turnover, the splitting of each process is a reasonable approach. Another issue in the computational treatment of the problem is the meaningless of the time-related parameters.

There is also scope for improvement in the biochemical considerations of the model. First, in terms of better experimental data for the mass production by SMC for different load levels. Results on mass transport of these substances through the arterial wall, accurate results on the response of SMCs and fibroblasts to direct mechanical stimuli and the turnover of the biochemical substances would also be very useful. As we saw in our results collagen turnover occurs at different degrees depending what spot of the carotid we are looking at, depending directly of places with higher stretches. However, experimental results on stiffening and increase of the collagen content are usually reported in a general way, not describing variation of these quantities at different locations.

Besides overcoming the limitations mentioned in the last paragraph, the model can be easily extrapolated to simulate collagen turnover in other cardiovascular

tissue as the heart (Diez and Laviades, 1997), aorta (Wolinsky, 1971), and other biological tissues, etc.

6 Morphological changes of endothelial cells.

6.1 Introduction

It is well known that biological tissue remodels itself when driven by a given stimulus, e.g. mechanical loads such as an increase in blood pressure, and changes in the chemical environment that controls the signaling processes and the overall evolution of the tissue. Biological remodeling can occur in any kind of biological tissue. In particular, the study of collagen as the most important substance to be remodeled, in all its types (preferentially Type I and III), has been given considerable attention in the last few years (Driessen et al., 2003; Kuhl et al., 2005; Driessen et al., 2008). The reorientation of this kind of structures can be assumed to be the consequence of the reorientation of the fibrils or filaments that make them up. This phenomenon leads to changes in the micro-structural orientation and fiber shape (due to the reorientation of the fibrils (see e.g. Stopak and Harris (1982); Rubbens et al. (2009); Sander et al. (2009)). Several remodeling models have been proposed in recent years. Some of them analyze the reorientation of unidimensional fibers driven by different stimuli such as Menzel (2007), Himpel et al. (2008) or Karsaj et al. (2009). In Himpel et al. (2008), a complete consistent linearization of the equations in an implicit finite element framework was performed. Garikipati et al. (2006) presented an elegant energetic and stationary

study of the remodeling problem from a thermodynamic point of view.

Another important biological structure able to remodel itself is cell cytoskeleton. Cytoskekleton is composed of microtubules, microfilaments and a network of actin filaments among many other elements (see e.g the review of Mofrad and Kamm (2006) and references therein for details). Cells move and reorient their inner structure depending on the stiffness and strain of the substrate (Discher et al., 2005; De et al., 2007). Cytoskeleton shape can change due to the adaptation of the microtubules and filaments to a specific external mechano-chemical stimulus (Saez et al., 2005; De et al., 2008). There are several experimental tests in the literature showing morphological changes of the cell due to mechanical stimulation of the matrix where cells are located. There exists two main procedures to induce cell morphological changes, static and cyclic loading (De et al., 2007; De and Safran, 2008; Goli-Malekabadi et al., 2011). While static and low-frequency loading leads to a reorientation and remodeling of the cellular structure parallel to the stretching direction (Collinsworth et al., 2000; Bischofs and Schwarz, 2003), high-frequency cyclic loading does in nearly perpendicular (Hayakawa et al., 2001; Hsu et al., 2009; Faust et al., 2011). In high-frequency stimulus, the feeling agents of external enviroment, focal adhesions, are not able to follow such changes so no stress fibers and miosin motors are activated. However in static and low-frequency load states, focal adhesions react to such changes by means of an active internal tension of the stress fibers leading to changes in its morphology. These works usually present the evolution from a random distribution of the micro-structure of the cells to align with a particular direction. These experimental results are characterized by a gradually reorientation of the principal direction of the cell followed by a progressive remodeling of the microstructural element leading to a more pointed shape, see e.g. the experimental work of Dai et al. (2004) and references therein. In Fig. 6.1 we show some results presented by Hayakawa et al. (2001) where this behavior is seen. In many cases this change of shape, unlike changes in orientation, are measured by a shape-index in the biomedical community. The underlying biological processes are more in number and complexity. Some of them, like dynamic of focal adhesions, the tension exerted by molecular motors over actin stress fibers are among the most

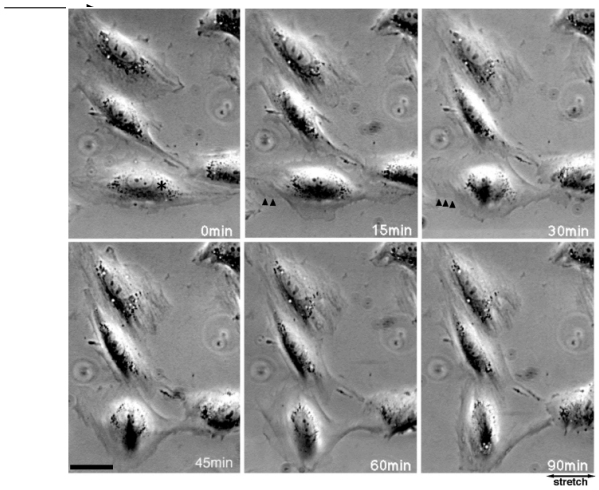

Figure 6.1: Results presented by Hoyakawa and co-works in a cyclically stretched cells test over 90 minutes. Looking at the cells we observe two different processes, a reorientation of the mean direction of the cell and a morphological change of the cells due to adaptation of the internal cell elements, such as microtubules and stress fibers. A more pointed distribution of the cell is obtained at the end of the experiment while the reorientation of the mean direction is gathered at the beginning of the test.

important aspects to be considered (see e.g. Mofrad and Kamm (2006) for an overall understanding of cell behavior). In reference to models capturing these features not much have been done while in terms of the orientation of the preferential direction of the cell, some of the most accepted models are those presented in De et al. (2007); De and Safran (2008) where the reorientation is assumed to be controlled by the matrix behavior and the forces that arise from the active regulation of the cell in a dipole-like manner. In terms of modeling changes on the morphology of cell shape due to external stimuli no many models exists in the literature, see e.g. Levesque et al. (1986); Ingber (2003); Ohashi and Sato (2005).

Introducing multi-scale approaches is a straightforward technique to take into account underlying evolving processes. The works of Ingber (Ingber, 2008) about tensegrity models of cell structures is a good example in the field of cell mechan-

ics. Miehe et al. (2004) performed a microsphere-based approach to study the microstructural behavior of polymers. Later, Caner and Carol (2006) applied this approach, also known as microplane, for vascular tissue. Microplane models were first used by Bazant and Oh (1985); Kuhl et al. (2000); Carol et al. (2004), among others, for studying the failure and plasticity of brittle materials, and they were later extended to other fields. Alastrué et al. (2009) used this approximation to model vascular tissue including the anisotropy of the tissue. To gain a deeper insight into the underlying changes in the microstructure, some authors have included information about the dispersion around the main orientation direction by using several statistical distributions. The von Mises distribution was introduced by Gasser et al. (2006) in the vascular framework to account for the dispersion. Later Alastrue et al. (2010b) used a Bingham distribution function (Bingham, 1974) to include the dispersion of the bundles and presenting a comparison of these two statistical functions. In this context, some works (Menzel, 2007; Kroon, 2010; Grytz and Meschke, 2010) have included these kinds of statistical functions to account for remodeling. In multiscale homogenization schemes, the macroscopic behavior is recovered by averaging the microstructural behavior represented, in the case of biological fibered tissue, by the mechanics of the fibrils or filaments. Previous authors (Alastrue et al., 2010b) have used exponential-type models, such as that proposed by Holzapfel et al. (2000). Recently Menzel and Waffenschmidt (2009) presented a microsphere-based approach for remodeling, where the fibrils behavior was modeled by the Worm-like Chain model (WLC). WLC models have been extensively used for analyzing behavior of the DNA double helix (see e.g. Bustamante et al. (2003)) and by Arruda and Boyce (1993) and Kuhl et al. (2005) to simulate elastomer and soft tissue respectively. Arruda and Boyce (1993) introduced this model in a non-affine isotropic eight chain model that has also been used by Bischoff et al. (2002). Garikipati et al. (2004) and Kuhl et al. (2005) extended it to anisotropic behavior. Alastrué et al. (2009) and Alastrue et al. (2010b) presented a comparison of both fibril models (exponential and WLC) in a microsphere-based approach. Note that along with the classical point of view of space orientations for microsphere-based models we also associate them to a physical orientation space of micro-structural elements,

e.g., collagen fibrils in collagen bundles or microtubules and actin filaments in cells.

In short, we present a new remodeling model in 3D, taking into account the reorientation of the mean direction of a given fibered structure and the reorientation of the individual fibrils or filaments leading to changes in the parameters of the associated statistical orientation density function. We begin discussing the material model used and in particular the WLC model adopted for each fibril. Later, we present the Bingham statistical distribution, its main properties and general shape. We make use of the microsphere-based approach as homogenization technique to move from the micro to the macroscale. In the following section, the evolution equation for remodeling are presented. We continue with the thermodynamic formulation of the problem obtaining the expression for the dissipation and a finite element case is carried out. In the subsequent section we discuss some examples to show the capabilities of our approach and we finish with a discussion of the advantages and limitations of the present contribution.

6.2 Macroscopic cell model

Our model is developed within a hyperelastic framework under large strain hypothesis. The aim of this section is to introduce the strain energy density function (SEDF) for fibered structures, for example, materials with bundles of collagen fibrils or cell cytoskeleton that will be used in this contribution. The main idea is to include microstructural information capable of reproducing the mechanical behavior and the shape of the spatial distribution of fibered constituents. A statistical distribution is considered to take into account the dispersion of the fibrils around a preferential orientation. Each fibril will be modeled by an individual strain energy function at the micro-level represented by the WLC model. We will finish this section with an academic example showing the mechanical behavior of the model and some simple examples of the passive mechanical behavior.

6.2.1 Micro-sphere-based anisotropic approach

The microsphere-based approach, also known as micro-plane models, constitutes an homogenization technique that has been used previously for brittle materials (Bazant and Prat, 1988), damage and fracture (Bazant and Oh, 1985; Carol et al., 2001; Kuhl et al., 2001), polymers (Miehe et al., 2004) and biological tissue (Alastrué et al., 2009), among many other applications. The homogenization or continuous averaging $\langle(\bullet)\rangle$ of a given variable $(\bullet)$ is carried out by integrating over the unit sphere surface. In order to perform a numerical implementation, the integral is computed by addition on m discrete orientation vectors with the corresponding weight factors w^i as

$$\langle(\bullet)\rangle = \frac{1}{4\pi}\int_{\mathbb{U}^2}(\bullet)\mathrm{dA} \approx \sum_{i=1}^{m} w^i(\bullet)_i, \tag{6.1}$$

where dA is the differential area element of the unit sphere that may be written in terms of the spherical angles $\alpha \in [0,\pi)$ and $\phi \in [0,2\pi)$ as $\mathrm{dA} = \sin(\alpha)\mathrm{d}\phi\mathrm{d}\alpha$. The normalizing term 4π is the unit sphere total area $A_{\mathbb{U}^2} = 4\pi$. Although the microsphere approach was initially conceived and used as a multi-scale homogenization technique, each unidirectional integration direction can be interpreted as the contribution of the fibrils around this direction weighted by its associated dA. The fibers contribution to the SEDF and to the Kirchhoff stress may then be homogenized over the whole set of dimensions as (we refer to Miehe et al. (2004) for a review of these equations):

$$\Psi_{\mathrm{ani}} = \frac{1}{4\pi}\int_{\mathbb{U}^2}\rho\psi(\bar{\lambda})dA \approx \sum_{i=1}^{m}\rho_i w^i \psi(\overline{\lambda}_i), \tag{6.2}$$

$$\bar{\boldsymbol{\tau}}_{\mathrm{ani}} = \frac{1}{4\pi}\int_{\mathbb{U}^2}\rho\bar{\mathbf{F}}\partial_{\bar{\mathbf{C}}}\psi(\bar{\lambda}_i)\bar{\mathbf{F}}^t dA \approx \sum_{i=1}^{m}\rho_i\bar{\boldsymbol{\tau}}_i w^i \approx \sum_{i=1}^{m}[\rho_i\psi'(\bar{\lambda}_i)\bar{\lambda}_i^{-1}\bar{\mathbf{t}}^i\otimes\bar{\mathbf{t}}^i]w^i, \tag{6.3}$$

where, Ψ_{ani} and ψ are the energy density functions in the macro and micro levels respectively, ρ is the statistical distribution with ρ_i the discrete value associated to each integration direction and which provide the anisotropy behavior. $\bar{\lambda}_i$ is the stretch ratio for each integration direction $\mathbf{r}^i$, and $\bar{\mathbf{t}}^i$ the isochoric spatial representation of the vector $\mathbf{r}^i$. The deviatoric part of the Kirchhoff stress tensor

related to the fiber contribution, $\boldsymbol{\tau}_{\text{ani}}$, is defined as $\boldsymbol{\tau}_{\text{ani}} = J^{-2/3}\text{dev}(\bar{\boldsymbol{\tau}}_{\text{ani}})$ with $\bar{\boldsymbol{\tau}}_{\text{ani}}$ the fictitious Kirchhoff stress tensor.

6.2.2 Behavior of the fibrils

At the micro scale, we chose the well-established WLC model (Kratky and Porod, 1949) to define the SEDF for every fibril or filament. The WLC was used in DNA modeling by Bustamante et al. (2003). Recently it was used by Garikipati et al. (2005), Kuhl et al. (2005) and Alastrué et al. (2009), among others, to model the behavior of biological tissue, as an extension of the WLC molecular model to approach continuum tissue. Therefore, the individual contribution of each fibril or filament $\psi(\bar{\lambda}_i)$ to the overall SEDF can be written as:

$$\psi(\bar{\lambda}_i) = \begin{cases} 0 & \text{if} \quad \bar{\lambda}_i < 1 \\ \underbrace{\frac{n\,k\Theta}{4\,A}\left[2\,\frac{\bar{r}_i^2}{L} + \frac{L}{1-\bar{r}_i/L} - \bar{r}_i\right.}_{\psi_{chn}} & \\ \underbrace{\left. - \ln(\bar{\lambda}_i^{4\,r_0^2})\left[\frac{1}{L} + \frac{1}{4\,r_0[1-r_0/L]^2} - \frac{1}{4\,r_0}\right]\right]}_{\psi_{rep}} & \text{if} \quad \bar{\lambda}_i \geq 1 \end{cases}, \tag{6.4}$$

with n the chain number density, $k = 1.381\text{x}10^{-23}(J/K)$ the Boltzmann constant and Θ the absolute temperature, e.g. $\Theta = 310K$ for biological tissue. The parameter A represents the persistence length (ratio between bending stiffness and thermal energy) and L the contour length. $\bar{\lambda}_i = [\mathbf{r}_i \cdot \bar{\mathbf{C}} \cdot \mathbf{r}_i]^{1/2}$ is the stretch of each fibril, $\bar{r}_i = \bar{\lambda}_i\, r_0$ and r_0 the initial end-to-end length. Note that, as discussed above, the behavior of the fibered structure is related to the anisotropic part of the SEDF. The contribution ψ_{chn} is due to individual chains, while the repulsive term ψ_{rep} is introduced to preserve zero initial stresses in the reference configuration (unit stretches) driven by the non-vanishing initial length r_0. Note that by modifying this term we would be able to obtain a residual stress in the reference configuration, although we have not included this modification in the present work. In both cases, fibers are assumed not to bear any load under compression. We can obtain the stress tensors from Eq. 6.4 and write the deviatoric

part of the Piola-Kirchhoff, $\bar{\mathbf{S}}_i = 2\partial_{\bar{\mathbf{C}}}\psi(\bar{\lambda}_i)$

$$\bar{\mathbf{S}}_i = \begin{cases} 0 & \text{if} \quad \bar{\lambda}_i < 1 \\ \dfrac{n\,K\Theta}{4\,A}\left[4\,\dfrac{\bar{\lambda}_i r_0^2}{L} + \dfrac{r_0}{[1-\bar{\lambda}_i r_0/L]^2} - r_0 \right. & \\ \left. -4\,\dfrac{r_0^2}{\bar{\lambda}_i L} - \dfrac{r_0}{\bar{\lambda}_i[1-r_0/L]^2} + \dfrac{r_0}{\bar{\lambda}_i}\right]\bar{\lambda}_i^{-1}\mathbf{r}^i\otimes\mathbf{r}^i & \text{if} \quad \bar{\lambda}_i \geq 1 \end{cases}, \tag{6.5}$$

and of the Kirchhoff stresses, $\bar{\boldsymbol{\tau}}_i = \bar{\mathbf{F}}\cdot\bar{\mathbf{S}}_i\cdot\bar{\mathbf{F}}^t$ (Marsden and Hughes, 1994; Holzapfel, 2000). Note that $\mathbf{r}^i\otimes\mathbf{r}^i$ transforms with the push-forward operation into $\bar{\mathbf{t}}^i\otimes\bar{\mathbf{t}}^i$ where $\mathbf{r}^i\in\Omega_0$ represents the orientation vector of the fibril or filament i in the reference configuration and $\bar{\mathbf{t}}^i\in\Omega$ the same vector $\mathbf{r}^i$ mapped into the current configuration in an affine manner by means of the isochoric push forward operator as $\bar{\mathbf{t}}^i = \bar{\mathbf{F}}\cdot\mathbf{r}^i$

6.2.3 The Bingham probability distribution

A more realistic behavior of the fibered structure can be obtained by considering a statistical distribution of the comprising fibrils to reflect the anisotropic response. We chose the Bingham orientation density distribution (Bingham, 1974) that provides more flexibility in modeling the dispersion of the fibrils than other distributions commonly used (Gasser et al., 2006; Alastrué et al., 2009; Menzel et al., 2008) in the framework of vascular tissue. The Bingham distribution was previously used by Alastrue et al. (2010b) to simulate the behavior of arterial tissue and may be expressed as

$$\rho(\mathbf{r};\,\mathbf{Z},\,\mathbf{Q}) = \left[F_{000}(\mathbf{Z},\mathbf{r})\right]^{-1}\,\mathrm{etr}\left(\mathbf{Z}\cdot\mathbf{Q}^{\mathrm{T}}\cdot\mathbf{r}\cdot\mathbf{r}^{\mathrm{T}}\cdot\mathbf{Q}\right), \tag{6.6}$$

where $\mathbb{U}^2$ represents the unit sphere, $\mathbf{r}\in\mathbb{U}^2$ are director vectors, $\mathrm{etr}\,(\bullet)\equiv\exp\left(\mathrm{tr}\,(\bullet)\right)$ and $\mathbf{Z}$ is a diagonal matrix with eigenvalues $\kappa_{1,2,3}$ that controls the concentration probability. $\mathbf{Q}\in\mathrm{SO}(3)$ represents the orthogonal local base that defines the directions of the statistical function. In fact, it is the difference between the pairs $[\kappa_1-\kappa_2]$, $[\kappa_1-\kappa_3]$ and $[\kappa_2-\kappa_3]$ that controls the shape of the

function over the unit sphere. $F_{000}(\mathbf{Z}, \mathbf{r})$ may be written as

$$F_{000}(\mathbf{Z}, \mathbf{r}) \;=\; [4\,\pi]^{-1} \int_{\mathbb{U}^2} \operatorname{etr}\left(\mathbf{Z} \cdot \mathbf{r} \cdot \mathbf{r}^{\mathrm{T}}\right) \mathrm{d}A. \tag{6.7}$$

In our approach, $\mathbf{Q}$ evolves to control the reorientation process of the maximal probability direction while $\mathbf{r}$ also evolves changing, explicitly, the concentration of the Bingham orientation distribution without loss of generality. For the sake of simplicity we will consider the maximal probability direction of the orientation distribution function (ODF) to be initially oriented along $\mathbf{Q}_{i,3}$ for $i = 1, 2, 3$ with $\kappa_3 \geq \kappa_2$ and $\kappa_1 = 0.0$. Figure 6.2 shows different shapes of the Bingham distribution for different values of $\kappa_{1,2,3}$.

The similarities between the structures in collagen bundles and cytoskeleton cells, and the discretization of the ODF over the unit sphere (Fig. 6.3) justify this approach. This assumption leads to a more real representation of the fiber distribution, as shown in Fig. 6.3, which corresponds to the functions depicted in Fig. 6.2. The fibrils distribution is represented weighted by the associated ρ in a gray scale, which will be discussed in detail below. At this point we would like to point out again that the classical assumption of an orientation space, that microsphere-based models deal with, is extended to assume a coupled orientation and physical space.

6.2.4 Anisotropic response

To illustrate the anisotropic response of the tissue with the model at hand, we discuss here some examples. Given a set of material parameters, we will perform an uniaxial tension test in each of the principal axes $\mathbf{e}_x, \mathbf{e}_y, \mathbf{e}_z$, applying a deformation gradient given by $\mathbf{F} = \lambda \mathbf{e}_x \otimes \mathbf{e}_x + 1/\sqrt{\lambda}\mathbf{e}_y \otimes \mathbf{e}_y + 1/\sqrt{\lambda}\mathbf{e}_z \otimes \mathbf{e}_z$, $\mathbf{F} = 1/\sqrt{\lambda}\mathbf{e}_x \otimes \mathbf{e}_x + \lambda \mathbf{e}_y \otimes \mathbf{e}_y + 1/\sqrt{\lambda}\mathbf{e}_z \otimes \mathbf{e}_z$ and $\mathbf{F} = 1/\sqrt{\lambda}\mathbf{e}_x \otimes \mathbf{e}_x + 1/\sqrt{\lambda}\mathbf{e}_y \otimes \mathbf{e}_y + \lambda \mathbf{e}_z \otimes \mathbf{e}_z$, respectively. We take arbitrary material parameters to show the different behavior gathered in each of the cases analyzed. The WLC parameters are taken as $r_0 = 1.0$, $L = 1.6$ and $A = 1.1$. In Fig. 6.4 we present the stress along three different stretching directions $(\mathbf{e}_x, \mathbf{e}_y, \mathbf{e}_z)$ for the concentration parameters given in Fig. 6.2b, c and d. For a revision of the behavior of the

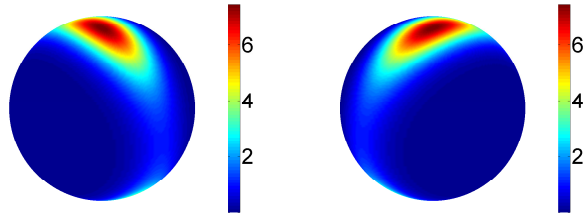

(a) $\kappa_{1,2,3} = 0.0, 8.0, 10.0$ (b) $\kappa_{1,2,3} = 8.0, 0.0, 10.0$

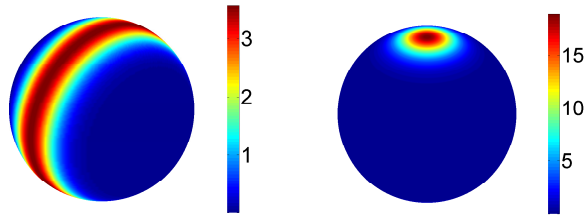

(c) $\kappa_{1,2,3} = 10.0, 0.0, 10.0$ (d) $\kappa_{1,2,3} = 0.0, 0.0, 10.0$

Figure 6.2: Shapes of the Bingham ODF and probability density values for different values of $\kappa_{1,2,3}$ and $\mathbf{Q} = \mathbf{e}_x \otimes \mathbf{e}_x + \mathbf{e}_y \otimes \mathbf{e}_y + \mathbf{e}_z \otimes \mathbf{e}_z$. (a) and (b) represent the same distribution shape but rotated 90^o, depending on where the non zero values are placed. (c) provides a planar-type distribution and (d) presents a von Mises distribution, that can be considered as a particularization of the Bingham ODF.

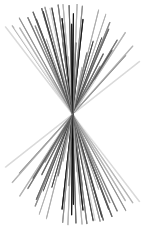

(a) Fibril representation for $\kappa_{1,2,3} = 0.0, 8.0, 10.0$ (Fig. 6.2(a))

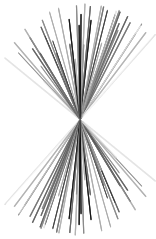

(b) Fibril representation for $\kappa_{1,2,3} = 8.0, 0.0, 10.0$ (Fig. 6.2(b))

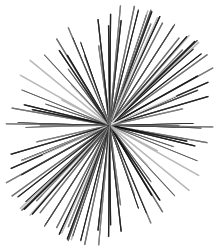

(c) Fibril representation for $\kappa_{1,2,3} = 10.0, 0.0, 10.0$ (Fig. 6.2(c))

(d) Fibril representation for $\kappa_{1,2,3} = 0.0, 0.0, 10.0$ (Fig. 6.2(d))

Figure 6.3: Representation of the fibrils within the fibered structure for the Bingham ODF represented in Fig 6.2.

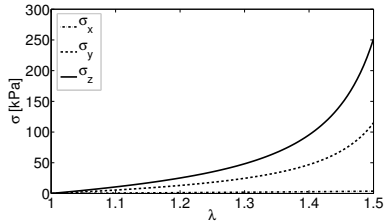

(a) Cauchy stresses along stretching directions for $\kappa_{1,2,3} = 10.0, 0.0, 8.0$

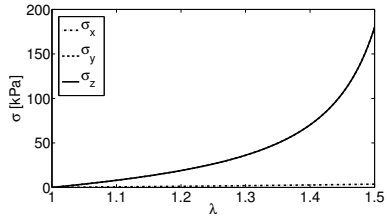

(b) Cauchy stresses along stretching directions for $\kappa_{1,2,3} = 10.0, 0.0, 10.0$

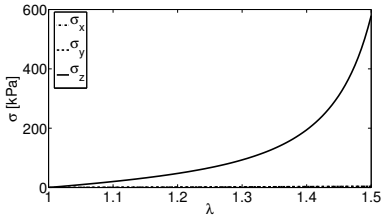

(c) Cauchy stresses along stretching directions for $\kappa_{1,2,3} = 10.0, 0.0, 0.0$

Figure 6.4: Cauchy stresses along stretching directions $\mathbf{e}_x, \mathbf{e}_y$ and $\mathbf{e}_z$ for the concentration parameters given in Fig. 6.2b, c and d.

chain for different sets of parameters, we refer to Arruda and Boyce (1993) and Kuhl et al. (2005) among others. The stress σ_z is the highest, since this is the preferential direction of the orientation distribution and therefore the one with the highest probability distribution and associated stiffness. In the direction of $\kappa_i = 0$, since there are hardly any fibrils, the stress is only due to the much softer ground matrix. The results obtained in Fig. 6.4a show a different response in σ_x, σ_y and σ_z due to the different probability distribution in those directions. In Fig. 6.4b we present a distribution in the plane $\mathbf{e}_z, \mathbf{e}_x$, so the stresses σ_z and σ_x coincide. In Fig. 6.4c the distribution is symmetrically placed around $\mathbf{e}_z$, which leads to a von Mises statistical orientation function.

6.3 Evolution equations

As explained above, the remodeling is controlled through two decoupled phenomena: first, the evolution of the orthogonal tensor $\mathbf{Q}$, which determines the rotation of the preferential directions and second the reorientation of the fibrils or filaments that changes the shape and parameters of the Bingham distribution. These processes can be identified in nature, e.g., with those processes discussed in the introduction section, such as rotations of cells like a dipole and a morphological change of its shape. We base our evolution equations on the reorientation process described by Menzel (2004). The realignment will be driven, at the moment, by a given general stimulus characterized by a second order tensor.

6.3.1 Preferential direction reorientation (PDR)

In this section we describe the reorientation of the whole fibered structure, given as the reorientation of the principal direction. The tensor $\mathbf{Q} \in \mathrm{SO}(3)$, from where the orientation of the Bingham is defined, will evolve toward a new base defined by the eigenvectors of the driving stimulus $\boldsymbol{\Xi}$, denoted by $\boldsymbol{\Xi}_I$. We define a rotation tensor, $\mathbf{R} \in \mathrm{SO}(3)$, as $\mathbf{R} = \boldsymbol{\Xi} \cdot \mathbf{Q}^{-1}$. For the evolution of $\mathbf{Q}$, a geometrically exact update will be used. The Euler theorem states that " Every element $\mathbf{R} \in \mathrm{SO}(3)$, with $\mathbf{R} \neq \mathbf{I}$, is a rotation through an angle $\theta = \|\boldsymbol{\omega}\| t$ about an axis $\boldsymbol{\omega}$", with $\boldsymbol{\omega} \in \mathbb{R}^3$ an eigenvector of $\mathbf{R}$ with eigenvalue 1, that fulfills $\mathbf{R}\boldsymbol{\omega} = \boldsymbol{\omega}$. $\mathbf{R}$ can be written in terms of the exponential mapping as $\mathbf{R} = \exp(-\boldsymbol{\varepsilon} \cdot \boldsymbol{\omega} t)$ with $\boldsymbol{\varepsilon}$ denotes the third-order permutation symbol. In short, it is possible to define a rotation vector $\boldsymbol{\omega}$, through which the initial base rotate to the final position (see Marsden and Ratiu (1999) for details). This approach follows that initially proposed by Menzel (2004) and Himpel et al. (2008) for one single fiber, Kuhl et al. (2005) in the eight-chain model and Karsaj et al. (2009) for 2D problems. From this, the rate of $\mathbf{Q}$ is given by

$$\dot{\mathbf{Q}} = \hat{\mathbf{n}}^{\boldsymbol{\omega}} \cdot \mathbf{Q}. \tag{6.8}$$

For the temporal discretization, we consider a time interval $\mathcal{T}$ and a number of subintervals, n, $\mathcal{T} = \bigcup_0^{n-1} [t^n, t^{n+1}]$ where the time increment is given by $\Delta t = t^{n+1} - t^n$. The evolution of the base at time n will evolve in the exponential

mapping context as

$$\mathbf{Q}^{n+1} = \exp(-\boldsymbol{\varepsilon} \cdot \boldsymbol{\omega} \Delta t) \cdot \mathbf{Q}^{n} \tag{6.9}$$

which describes a rotation of the orientation at time n, $\mathbf{Q}^n$, by the current rotation vector $\boldsymbol{\omega}$. Note that this approach follows an explicit updating scheme with dependencies on the current position, different from the implicit scheme in Menzel (2004) where the updated quantities were obtained by means of a Newton iteration scheme. However, as Kuhl et al. (2005) pointed out, it is a reasonable approach for the gradual realignment followed herein. Note that for $t \to \infty$, $\mathbf{Q}^{n+1} \mapsto \boldsymbol{\Xi}$. In order to compute the exponential map, this will be rewritten (see e.g. Marsden and Ratiu (1999)) by the Rodriguez formula, given $\mathbf{R}(\boldsymbol{\omega}) = \mathbf{R}(\mathbf{n}^{\boldsymbol{\omega}}, \omega)$ as

$$\exp(\hat{\mathbf{n}}^{\boldsymbol{\omega}} t) = [\sin(\|\boldsymbol{\omega}\| t)]\, \hat{\mathbf{n}}^{\boldsymbol{\omega}} + [1 - \cos(\|\boldsymbol{\omega}\| t)]\, \mathbf{n}^{\boldsymbol{\omega}} \otimes \mathbf{n}^{\boldsymbol{\omega}} + \cos(\|\boldsymbol{\omega}\| t)\mathbf{I}, \tag{6.10}$$

where $\mathbf{n}^{\boldsymbol{\omega}} = \boldsymbol{\omega}/\omega$, $\omega = \|\boldsymbol{\omega}\|$ and $\hat{\mathbf{n}}^{\boldsymbol{\omega}} = -\boldsymbol{\varepsilon} \cdot \mathbf{n}^{\boldsymbol{\omega}}$ are the norm of the angular velocity, its unit direction and the so called hat map of $\boldsymbol{\omega}$, respectively.

6.3.2 Changes in the fibered structure shape. Reorientation of the fibrils (RF)

In this section we describe the reorientation model for the fibrils or filaments. Some authors have modeled this phenomenon by means of the evolution of the statistical distributions (Driessen et al., 2003, 2008; Baaijens et al., 2010). Menzel et al. (2008) studied this issue by using a von Mises distribution and the evolution of the associated structural tensor. Recently Menzel and Waffenschmidt (2009) presented a work for remodeling within a microsphere approach, where from an initial isotropic state, the reorientation of each of the integration directions leads to an anisotropic behavior. This latter approach follows an approach similar to that described in Himpel et al. (2008) for one simple fiber, and is similar to the one used here for the evolution of the fibrils.

In this work we make use of the Bingham distribution (see Section 6.2.3), and three different options for defining its rate are discussed: (i) Defining a rate of

the diagonal tensor $\mathbf{Z}$. This approach has some disadvantages since the actual quantities that establish the function shape are the differences between the values of $\mathbf{Z}$, but not the values themselves. Therefore, it is not trivial to obtain an evolution equation that can be introduced consistently in the thermodynamic framework, that evolves correctly with any driven quantity and having a consistent physical interpretation. Moreover, this approach would introduce more phenomenological parameters. (*ii*) Defining second and fourth-order tensors following the developments by Menzel et al. (2008). This approach also has some difficulties regarding the definition of a closed parameterized form. The obtainment of these parameters turns out to be a complex task (see Menzel et al. (2008) for additional details of this procedure), and it is not the goal of this thesis. (*iii*) Definition of the rate equation for each integration direction to be reoriented. This procedure was initially proposed by Menzel and Waffenschmidt (2009) and is the approach adopted herein. Moreover, with such an approach, we are able to evolve the shape of the microstructure by means of the evolution of each integration direction. From our point of view, this approach allows a more free reorientation of the fibrils since they do not have to be subject to fit with any statistical distribution. Future works will investigate the potential of options (*i*) and (*ii*).

It is necessary to define the vector $\boldsymbol{\omega}_i$, which leads the evolution of the reorientation process. As mentioned above, we prefer to generalize the driving quantity leading the process, named $\boldsymbol{\Xi}$. We assume that the realignment depends on the maximum principal direction of $\boldsymbol{\Xi}$, such that $\mathbf{r}_i \longmapsto \boldsymbol{\Xi}_3$. We will denote by $I = 1, 2, 3$ the eigenvectors associated to the minimum, medium and maximum eigenvalues of $\boldsymbol{\Xi}$ respectively. This leads to

$$\boldsymbol{\omega}_i := \mathbf{r}_i \times \boldsymbol{\Xi}_3, \tag{6.11}$$

where $\boldsymbol{\omega}_i$ and $\mathbf{r}_i$ are the angular velocity and the unit vector of each integration direction as depicted in Fig. 6.5. Incorporating Eq. 6.11 into $\dot{\mathbf{r}}_i = \boldsymbol{\omega}_i \times \mathbf{r}_i$ we obtain

$$\dot{\mathbf{r}}_i = [\mathbf{I} - \mathbf{r}_i \otimes \mathbf{r}_i] \cdot \boldsymbol{\Xi}_3. \tag{6.12}$$

However, we will again make use of the updating scheme presented in the section

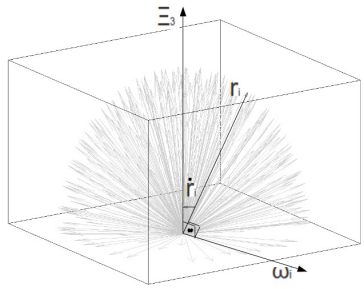

Figure 6.5: Evolution of each integration direction.

above, based on the exponential map, and again adopt an explicit updating. Therefore, we approximate the updated vector as

$$\mathbf{r}_i^{n+1} = exp(\hat{\mathbf{n}}_i^{\boldsymbol{\omega}} \Delta t) \cdot \mathbf{r}_i^n. \tag{6.13}$$

Remark 14 ***Reconstruction of the Bingham distribution from the re-oriented integration directions.*** *Once the integration directions evolve, it is obvious that the distribution of the fibrils changes independently of the initial Bingham ODF, but it is not so clear how the values of* $\mathbf{Z}$ *change. In order to recover an approximated Bingham distribution, mainly for visualization purposes we adopt the following methodology. Given an updated state, after reorientation of the integration directions (ID) at the current time n:*

- *We define a structural tensor* $\boldsymbol{\rho}$ *at time n as*

$$\boldsymbol{\rho}^n = \frac{1}{4\pi} \int_{\mathbb{U}^2} \rho(\mathbf{r}^n;\, \mathbf{Z},\, \mathbf{Q}^n) \mathbf{r}^n \otimes \mathbf{r}^n \, dA \tag{6.14}$$

- *At this point we can follow two options:*
  i) We solve the non-linear equation system (Eq. 6.15) obtaining the new values of $\mathbf{Z}$*, named* $\hat{\mathbf{Z}}$*, from the right side of the equality.*

$$\frac{1}{4\pi} \int_{\mathbb{U}^2} \rho(\mathbf{r}^n;\, \mathbf{Z},\, \mathbf{Q}^n) \mathbf{r}^n \otimes \mathbf{r}^n \, dA = \frac{1}{4\pi} \int_{\mathbb{U}^2} \rho(\mathbf{r};\, \hat{\mathbf{Z}},\, \mathbf{Q}) \mathbf{r} \otimes \mathbf{r} \, dA. \tag{6.15}$$

ii) We can construct a data base with pairs of data relating the values of each $\boldsymbol{\rho}^n$ *with its respective* $\mathbf{Z}$ *tensor. We followed this latter method for* $\kappa_{1,2,3} = 1...100$*, leading to a database of* $10^6 \times 3$ *elements for* κ *and* $10^6 \times 3$ *elements for the diagonal components of* $\boldsymbol{\rho}$*.*

6.4 Dissipation

The starting point of this section arises from the first and second laws of thermodynamics given in the material description, that may be written as:

$$\dot{e} = \mathbf{P} : \dot{\mathbf{F}} - \mathrm{DIV}\hat{\mathbf{Q}} \qquad \text{and} \qquad \gamma = \dot{\eta} - \mathrm{DIV}\frac{\hat{\mathbf{Q}}}{\theta}, \tag{6.16}$$

where $\dot{e}$ is the internal energy rate of the system, $\mathbf{P}$ the first Piola-Kirchhoff stress, $\hat{\mathbf{Q}}$ the heat flux, η the entropy density, θ the absolute temperature and γ an entropy production term coming from irreversible processes (see e.g. Truesdell and Noll (2004)). Combining the Legendre transformation $\Psi = e - \eta\theta$ in Eq. 6.16, with the Helmholtz free energy density Ψ, we can write the Clausius-Plank inequality as

$$\mathcal{D} = -\dot{\Psi} + \mathbf{P} : \dot{\mathbf{F}} + \frac{\hat{\mathbf{Q}} \cdot \mathrm{DIV}\theta}{\theta} \geq 0 \tag{6.17}$$

where $\mathcal{D} \geq 0$ is the internal dissipation or the local entropy production, also named $\theta\dot{\gamma}$. This inequality has important implications in remodeling processes, since it is well known that this is an irreversible process and Eq. 6.17 is a inequality. Usually in mechanics, the last term is neglected since no thermal effects are considered. We do not omit it in this first description in order to hold a more general formulation. We now split the Helmholtz free-energy function as $\Psi = \Psi_{\mathrm{mech}} + \Psi_{\mathrm{chem}}$. The mechanical part Ψ_{mech} refers to the classical energy used in non-linear mechanics and Ψ_{chem} to the chemical metabolic component. Although the exchange of energy through chemical processes is essential, obtaining Ψ_{chem} is complex and to the authors knowledge has not been sufficiently developed. As previously mentioned, we will ignore heat sources and will only consider isothermal processes. Most biological tissues works and develops at approximately constant temperature so only the mechanical part will be considered. As observed above, the dependencies of the mechanical term lies in $\Psi^{\mathbf{F}}_{\mathrm{mech}} = \Psi_{\mathrm{mech}}(\mathbf{F}, \mathbf{r}, \mathbf{Q})$ or, in terms of the right Cauchy-green tensor $\mathbf{C}$, in

$\Psi^{\mathbf{C}}_{\text{mech}} = \Psi_{\text{mech}}(\mathbf{C}, \mathbf{r}, \mathbf{Q})$. Focusing on the anisotropic part of the SEDF, which is the contribution we assume reorients itself, we can define

$$\Psi_{\text{ani}} = \frac{1}{4\pi} \int_{\mathbb{U}^2} \rho(\mathbf{Q}, \mathbf{r}) \psi(\bar{\lambda}) dA, \tag{6.18}$$

with the material derivative

$$\dot{\Psi}_{\text{ani}} = \partial_{\mathbf{C}} \Psi_{\text{ani}} : \dot{\mathbf{C}} + \partial_{\mathbf{r}} \Psi_{\text{ani}} \cdot \dot{\mathbf{r}} + \partial_{\mathbf{Q}} \Psi_{\text{ani}} : \dot{\mathbf{Q}}. \tag{6.19}$$

From the first term we obtain the constitutive equation for deviatoric part of the anisotropic stress as $\mathbf{S}_{\text{ani}} = J^{-2/3}\text{DEV}(\bar{\mathbf{S}}_{\text{ani}})$, where $(\bar{\mathbf{S}}_{\text{ani}})$ is the fictitious second Piola-Kirchhoff stress tensor defined as

$$\bar{\mathbf{S}}_{\text{ani}} = \frac{1}{4\pi} \int_{\mathbb{U}^2} n\rho \partial_{\bar{\mathbf{C}}} \psi(\bar{\lambda}) dA = \frac{1}{4\pi} \int_{\mathbb{U}^2} n\rho \bar{\lambda}^{-1} \psi'(\bar{\lambda}) \mathbf{r} \otimes \mathbf{r} dA \tag{6.20}$$

(see Eq. 6.5 for a complete description of the stress tensors), reducing the inequality to

$$\mathcal{D}_{int} = -\partial_{\mathbf{r}} \Psi_{\text{mech}} \cdot \dot{\mathbf{r}} - \partial_{\mathbf{Q}} \Psi_{\text{mech}} : \dot{\mathbf{Q}} = \underbrace{-\frac{1}{4\pi} \int_{\mathbb{U}^2} \psi \partial_{\mathbf{Q}} \rho : \dot{\mathbf{Q}} dA}_{\mathcal{D}_{\text{PDR}}} \underbrace{- \frac{1}{4\pi} \int_{\mathbb{U}^2} [\rho \partial_{\mathbf{r}} \psi + \psi \partial_{\mathbf{r}} \rho] \cdot \dot{\mathbf{r}} dA}_{\mathcal{D}_{\text{RF}}} \tag{6.21}$$

The first term is related to dissipation due to reorientation ($\mathcal{D}_{\text{PDR}}$) of the principal direction of the bundle while the second term ($\mathcal{D}_{\text{RF}}$) is caused by reorientation of the individual fibrils or filaments, which leads to a change in the bundle shape.

$$\mathcal{D}_{\text{PDR}} = -\frac{1}{4\pi} \int_{\mathbb{U}^2} \left[\psi \partial_{\mathbf{Q}} \rho : \dot{\mathbf{Q}} \right] dA = -\frac{1}{4\pi} \int_{\mathbb{U}^2} \left[2\mathbf{r} \cdot \left[\mathbf{r}^T \cdot \mathbf{Q} \cdot \mathbf{Z} \right] \rho \psi : \dot{\mathbf{Q}} \right] dA \tag{6.22}$$

and

$$\mathcal{D}_{\text{RF}} = -\frac{1}{4\pi} \int_{\mathbb{U}^2} [\rho \partial_{\mathbf{r}} \psi + \psi \partial_{\mathbf{r}} \rho] \cdot \dot{\mathbf{r}} dA = -\frac{1}{4\pi} \int_{\mathbb{U}^2} \left[S_i \bar{\mathbf{C}} \cdot \mathbf{r} \rho + \rho 2 \mathbf{Q} \cdot \mathbf{Z} \cdot \mathbf{Q}^T \cdot \mathbf{r} \psi + \rho_m \psi \right] \cdot \dot{\mathbf{r}} dA, \tag{6.23}$$

with $\partial_{\bar{\lambda}^2} \psi = S_i/2$, $\partial_{\mathbf{r}} \bar{\lambda}^2 = 2\bar{\mathbf{C}} \cdot \mathbf{r}$ and

$$\rho_m = \left[\int_{\mathbb{U}^2} [4\,\pi]^{-1} \, 2\mathbf{Z} \cdot \mathbf{r} \, \text{etr} \left(\mathbf{Z} \cdot \mathbf{r} \cdot \mathbf{r}^{\mathrm{T}} \right) \mathrm{d}A \right]^{-1} \text{etr} \left(\mathbf{Z} \cdot \mathbf{Q}^{\mathrm{T}} \cdot \mathbf{r} \cdot \mathbf{r}^{\mathrm{T}} \cdot \mathbf{Q} \right). \tag{6.24}$$

In subsequent sections we provide the dissipation values for several examples.

6.5 Particularization for biological tissue

The previous sections have omitted any reference to specific quantities that drive the remodeling process. In the following section we discuss some of the driving quantities most commonly discussed in the bibliography. Moreover, we also present a comparison of the behavior of the model with various previously proposed driving quantities. As pointed out in the Introduction section, it is still unclear if this quantity is associated to strains, stresses or mix-variant types such as the Mandel tensor (see e.g. reviews in Humphrey (2001); Cowin (2004); De et al. (2007) and references therein). Kuhl et al. (2005) and Himpel et al. (2008) followed a strain based approach while Driessen et al. (2004) suggested the orientation along a direction between the two principal directions of maximum strain. Other authors (Hariton et al., 2007; Driessen et al., 2003; Kuhl and Holzapfel, 2007; Grytz and Meschke, 2010) suggested stress-based models to drive the process, some of them aligned with the maximum principal direction or with respect to a direction between the two maximum principal directions. This option is frequently applied to cardiovascular tissue where the fibers remodel to compensate variations in both internal pressure and wall shear stress (Taber, 1998; Alford et al., 2008). Finally, other authors (Imatani and Maugin, 2002; Menzel et al., 2008) proposed a mix-variant Mandel-type tensor. It is also worth commenting on the particular state reached when the strain and stress tensors are coaxial and a critical state of the free energy is achieved (Cowin, 1994; Vianello, 1996) in which case $\mathbf{M} = \mathbf{C} \cdot \mathbf{S}$ turns out to be symmetric. Anisotropic materials are not coaxial in general and this state is only maintained while the Piola-Kirchhoff stresses and the Cauchy-Green tensor keep non-coaxiality.

The aim of this analysis is not to provide any new hypothesis or clarification about which quantity is the correct one but to compare the evolution of the dissipation achieved with the three types of driving quantities described below. The whole process will be split into two steps.

6.5.1 Preferential direction reorientation

The first type corresponds to the reorientation of the preferential directions, defined by means of a rotation tensor $\mathbf{Q}$ that will be driven by the principal Cauchy-Green strain directions ($\mathbf{\Xi}_I^{\mathbf{C}}$), principal Cauchy stresses ($\mathbf{\Xi}_I^{\mathbf{S}}$) or principal directions of the Mandel tensor ($\mathbf{\Xi}_I^{\mathbf{M}}$). This does not uniquely define the evolution of $\mathbf{Q}$, so we have to enforce the preferential direction, that is the direction with the maximum fibril concentration, to reorient itself towards the maximum principal direction of the driving quantity $\mathbf{\Xi}$. This description is not influenced by the magnitude of the driving stimulus but only by the angle between the initial and the goal directions. In order to improve this limitation we introduce a magnitude-dependent parameter $\zeta^{\mathbf{\Xi}}$ as

$$\zeta^{\mathbf{\Xi}} = \begin{cases} 0 & \text{if} \quad \Lambda_3^{\mathbf{\Xi}}/\Lambda_1^{\mathbf{\Xi}} \leq \zeta_0^{\mathbf{\Xi}} \\ \\ \Lambda_3^{\mathbf{\Xi}}/\Lambda_1^{\mathbf{\Xi}} - \zeta_0^{\mathbf{\Xi}} & \text{if} \quad \Lambda_3^{\mathbf{\Xi}}/\Lambda_1^{\mathbf{\Xi}} > \zeta_0^{\mathbf{\Xi}} \end{cases} , \tag{6.25}$$

where $\mathbf{\Xi}$ denotes the driving quantity ($\mathbf{C}$, $\mathbf{S}$ or $\mathbf{M}$), $\Lambda_3^{\mathbf{\Xi}}/\Lambda_1^{\mathbf{\Xi}} \in [1, \text{inf})$ the ratio between the maximum and minimum eigenvalues of the chosen driving quantity $\mathbf{\Xi}$ and $\zeta_0^{\mathbf{\Xi}}$ a threshold value that sets the coefficient value at which the reorientation process starts. Besides the magnitude of the driving quantity, it seems reasonable to suppose that natural tissue adapts to a given load in different ways, e.g. collagen fibrils remodel in a different way than microtubules of a cell. We therefore introduce the last material parameter, $\zeta_*^{\mathbf{\Xi}}$, that provides a measure of how the tissue opposes its reorientation, decreasing for higher reorientation rates. We propose to fulfill $\Delta t \zeta^{\mathbf{\Xi}}/\zeta_*^{\mathbf{\Xi}} \leq 1$, leading to the following updating scheme of Eq. 6.9

$$\mathbf{Q}^{n+1} = exp(\zeta^{\mathbf{\Xi}} \hat{\mathbf{n}}^{\boldsymbol{\omega}} \Delta t/\zeta_*^{\mathbf{\Xi}}) \cdot \mathbf{Q}^n \tag{6.26}$$

6.5.2 Reorientation of the fibrils

The second step deals with the remodeling of the fibered structure which is basically, as discussed above, a reorientation of the fibrils or filaments that make up such a structure. The driving quantity will be the same and, again, we introduce a magnitude-dependent parameter $\bar{\zeta}^{\mathbf{\Xi}}$ and the corresponding material dependent

parameter $\bar{\zeta}_*^{\Xi}$. We have adopted the same definition as in the reorientation process, being

$$\bar{\zeta}^{\Xi} = \begin{cases} 0 & \text{if} \quad \Lambda_3^{\Xi}/\Lambda_1^{\Xi} \leq \bar{\zeta}_0^{\Xi} \\ \\ \Lambda_3^{\Xi}/\Lambda_1^{\Xi} - \bar{\zeta}_0^{\Xi} & \text{if} \quad \Lambda_3^{\Xi}/\Lambda_1^{\Xi} > \bar{\zeta}_0^{\Xi} \end{cases}, \tag{6.27}$$

with $\bar{\zeta}_0^{\Xi}$ the value at which the remodeling starts. And again, the updating scheme of Eq. 6.13 changes to

$$\mathbf{r}^{n+1} = exp(\bar{\zeta}^{\Xi}\hat{\boldsymbol{\Xi}}^{\boldsymbol{\omega}}\Delta t/\bar{\zeta}_*^{\Xi}) \cdot \mathbf{r}^n. \tag{6.28}$$

Remark 15 ***Coupling of reorientation models.*** *The reorientation processes discussed above occur simultaneously in biological tissue, but in different ways. For example, after the reorientation of the whole structure gets under way, a certain time later, the reorientation of the fibrils or filaments of the structure starts. Both can occur at the same time, perhaps at different rates. However, there are no available experimental tests that clearly distinguish between both processes. Therefore, in order to show the capabilities of this model, and without loss of generality, we will assume for section 6.6 that the reorientation process occur first and only when the preferential direction is aligned with the eigenvector associated to the maximum eigenvalue of the driving quantity the remodeling process will start. Upon the assumption of decoupled reorientations, we can set* $\bar{\zeta}_0^{\Xi}$ *to* $\bar{\zeta}_0^{\Xi} \geq max\{\Lambda_3^{\Xi}/\Lambda_1^{\Xi}\}$ *achieved along the PDR process to allow for a smooth transition from one process to the other. In this way, we will consider them as decoupled in Section 6.6. However, for Section 6.7 a coupled evolution will be considered by a material parameter,* $\varsigma = 1/[1 + exp(\varsigma_c * [\|\boldsymbol{\omega}\|t - \varsigma_s])]$*. This equation follows a sigmodal function and the parameters* ς_c *and* ς_s *control the rotation value of the PDR at which RF begins and its rate, respectively.* ς *multiplies the arguments of the exponential in Eq. 6.32.*

6.6 Results

6.6.1 Principal direction reorientation

The main features of the preferential direction reorientation model under discussion and some of the results obtained are presented in this section. We have chosen a homogeneous deformation problem controlled by displacement. We use the deformation gradient given by $\mathbf{F} = 1/\sqrt{\lambda}\mathbf{e}_x \otimes \mathbf{e}_x + 1/\sqrt{\lambda}\mathbf{e}_y \otimes \mathbf{e}_y + \lambda\mathbf{e}_z \otimes \mathbf{e}_z$, the set of concentration parameters $\kappa_{1,2,3} = [10, 8, 0]$ and an initial $\mathbf{Q} = \mathbf{e}_x \otimes \mathbf{e}_x + \mathbf{e}_z \otimes \mathbf{e}_y + \mathbf{e}_y \otimes \mathbf{e}_z$, which places the preferential direction of the fibered structure perpendicular to the stretching direction. All these parameters have been chosen to show the behavior of the model and they do not have been fitted from experimental data. The parameters from the WLC model are set to $r_0 = 1$, $L = 2$, $A = 1.3$, $n = 7.0$ x 10^{21}, $k = 1.381$ x $10^{-23} J/K$ and $\theta = 300K$ (Kuhl et al., 2005). We present results for the three types of driving quantities analyzed ($\mathbf{C}$, $\mathbf{S}$ and $\mathbf{M}$). The normalized time interval has been discretized in 100 time steps with $\Delta t = 0.1$.

We first analyzed the results without taking into account the sensing model described in Section 6.5. In Fig. 6.6 we present the evolution of the tensor $\mathbf{Q}$ every ten steps in a stereographic projection, used previously by Menzel and Steinmann (2003), among others, for plasticity and by Alastrué et al. (2009) to represent the stress in blood vessel fibers. The results show almost no difference between the updated positions of $\mathbf{Q}$ for the three driving quantities. Nevertheless, in the zoom shown in Fig 6.6(b) we see that the position driven by the Mandel tensor is placed between those driven by strain (closer to the goal position, so faster) and stress (the slower).

An alternative for visualizing the material evolution is to compute an anisotropic measurement as proposed by Menzel and Steinmann (2003). In this way, we can measure how fast the reorientation is by means of the scalar

$$\delta(\mathbf{C}, \mathbf{S}) = \frac{\|\mathbf{C} \cdot \mathbf{S} - \mathbf{S} \cdot \mathbf{C}\|}{\|\mathbf{S}\|\|\mathbf{C}\|}. \tag{6.29}$$

We represent the Cauchy stress evolution, anisotropy (given by Eq. 6.29) and

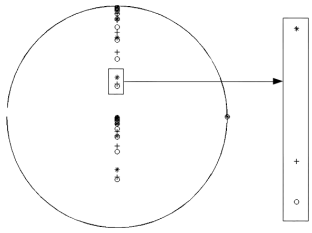

Figure 6.6: Evolution of $\mathbf{Q}$ driven by $\mathbf{C}(o)$, $\mathbf{S}(*)$ and $\mathbf{M}(+)$ and detail fora specific time.

dissipation in the present example. Fig. 6.7(a) shows that that the stress rises from about 12 kPa (stiffness of the extracellular matrix) up to 33 kPa due to the contribution of the bundle that progressively aligns with respect to the stretching direction. Fig. 6.7(b) shows the anisotropic measure evolution and Fig. 6.7(c) the dissipation evolution. We can observe that the difference is quite small. We impose a stop criteria for rotation angles less than 0.01 degrees. For such an assumption we get up to step 49, 73 and 54 for the strain, stress and Mandel driven problem respectively. If we compute the dissipation numerically, we obtain from Eq. 6.22, $\mathcal{D}_{\mathbf{C}} = 3.446\text{x}10^2$ [kPa/time], $\mathcal{D}_{\mathbf{S}} = 2.860\text{x}10^2$ [kPa/time] and $\mathcal{D}_{\mathbf{M}} = 3.303\text{x}10^2$ [kPa/time] which established stress as the least dissipative quantity. We can observe the behavior highlighted in Fig 6.8 for the complete model by checking out the last step in which the angle between the principal direction and the goal direction is less than 0.01, which we consider to be the equilibrium situation. In Table 6.1 we show the equilibrium step for each driving quantity and for two fiber parameters for the WLC model, a softer one L= 2.0, and a stiffer one L= 1.8, and the rest of the parameters as set above. Note that values of the contour length L close to end-to-end value r_0 represent stiffer values than those much higher than r_0. For higher stiffness, the contribution of the fibers to the stress increases leading to a slower rate of reorientation, in the case of stress and Mandel driving quantity. However, when the process is driven by strains, the equilibrium is achieved in the same time step for the two degrees of stiffness.

Remark 16 ***Stiffness material dependence.*** *The behavior of the reorien-*

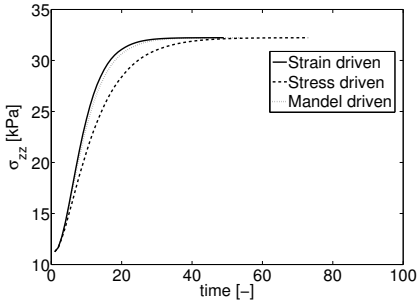

(a) Stress evolution in direction $\mathbf{e}_z$

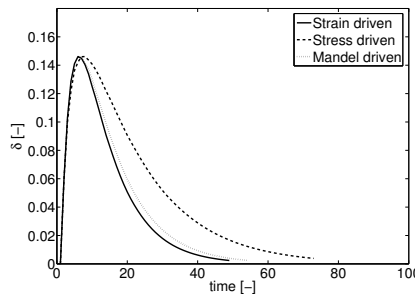

(b) Anisotropy evolution

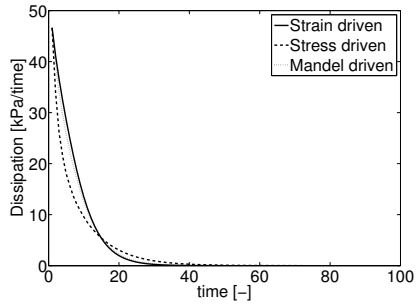

(c) Dissipation evolution

Figure 6.7: Evolution of stress, anisotropy and dissipation.

Stiffer			Softer		
strain	stress	Mandel	strain	stress	Mandel
49	73	54	49	100	23

Table 6.1: Time step in which equilibrium is achieved for different degrees of stiffness and different driving quantities.

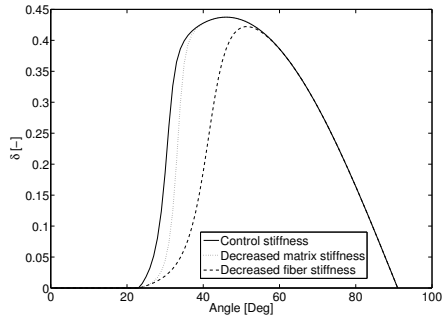

Figure 6.8: Evolution of anisotropy for a 1D fiber.

tation process must also be related to the ratio between the anisotropic and the isotropic part of the stiffness. To analyze this aspect we perform a simple case of a 1D fiber, placed initially perpendicular to the stretching direction and gradually moving towards the direction of this load. As we can see in Fig 6.8, the higher the matrix-stiffness/fiber-stiffness ratio the faster the reorientation. This shows that for higher ratios, the principal stress value and the associated direction of the ground substance have greater relevance in the overall stress response. Besides, up to 23 degrees there is no anisotropy since the fibrils are under compression and, therefore, they do not contribute to stress. On this point, some fibrils begin to bear load contributing to the anisotropic behavior of the material.

The particularization to biological tissue discussed in Section 6.5 is now included. We take into account the dependence on the magnitude of the load. With this aim we introduce in the remodeling approach the material parameters $\zeta^{\mathbf{\Xi}}$, $\zeta_*^{\mathbf{\Xi}}$ and $\zeta_0^{\mathbf{\Xi}}$ (fixed to 1 for strain driven and 0 for the stress driven). We will study the model for $\zeta_*^{\mathbf{\Xi}} = 2, 10$. Fig. 6.9 shows the situation of $\mathbf{Q}$ every step. Higher values of $\zeta_*^{\mathbf{\Xi}}$ lead to lower rates of evolution. The process driven by $\mathbf{M}$ presents higher rates than those driven by stress, while the latter are higher than those driven by strain.

We also present the anisotropy evolution for each of the situation discussed above. As the previous results show, it can be seen that the preferential direction aligns more slowly with the principal direction with higher values of $\zeta_*^{\mathbf{\Xi}}$. Table

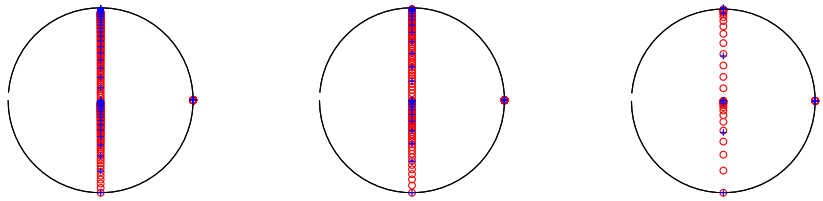

(a) Change with **C** (b) Change with **S** (c) Change with **M**

Figure 6.9: Evolution of **Q** driven by different quantities. Blue crosses indicate the results for $\zeta_*^{\boldsymbol{\Xi}} = 2$ and red circles those for $\zeta_*^{\boldsymbol{\Xi}} = 10$.

$\zeta_*^{\boldsymbol{\Xi}} = 2$			$\zeta_*^{\boldsymbol{\Xi}} = 10$		
strain	stress	Mandel	strain	stress	Mandel
29	14	4	>100	72	16

Table 6.2: Time step in which equilibrium is achieved for different driving quantities and material parameters $\zeta_*^{\boldsymbol{\Xi}} = 2$ and $\zeta_*^{\boldsymbol{\Xi}} = 10$.

6.2 shows the step at which we obtain a rotation lesser than 0.01 degrees, which can be considered as the equilibrium situation.

We present in Fig. 6.11 the dissipation evolution of the examples proposed in this section. Note that the scale in the vertical axes is modified in the different subfigures. Consistent with the previous results, the process driven by strain and higher values of $\zeta_*^{\boldsymbol{\Xi}}$ is the least dissipative and, therefore, the optimum from an energetic point of view. It should be noted that these results are obtained from the assumed biological sensing parameters that should be experimentally validated and fitted to obtain realistic conclusions. We refer to the results shown in Fig. 6.7 where no material parameter has been included and, therefore a clearer interpretation of the role of the different driving quantities can be achieved. As can be seen in Fig. 6.11, and more clearly in Table 6.3, the quantity that produces the least dissipation is strain, as as mentioned above, followed by stress and Mandel respectively. Dissipation is also lower for higher values of $\zeta_*^{\boldsymbol{\Xi}}$.

Finally we present the evolution of the ODF over time in Fig. 6.12, which shows the Bingham representation at different steps for the case of driving stress

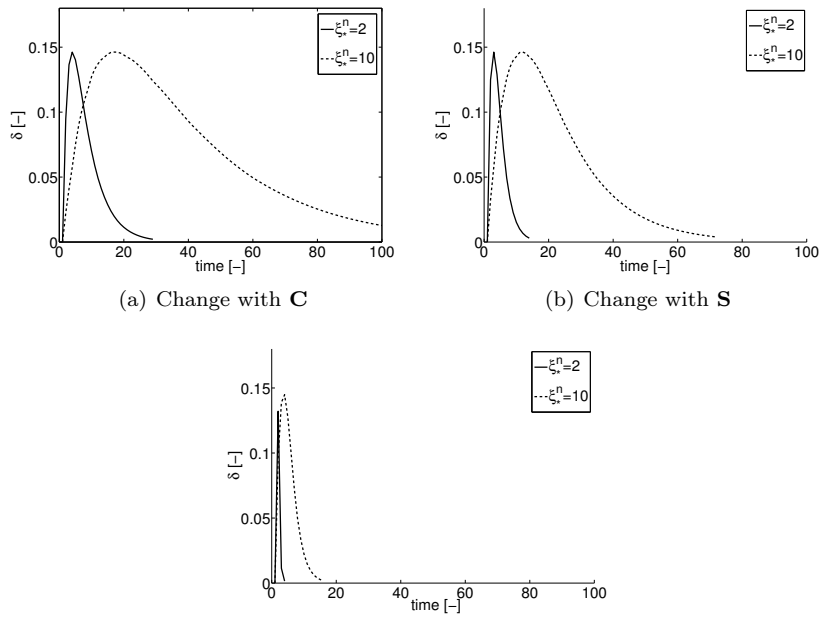

(a) Change with **C**

(b) Change with **S**

(c) Change with **M**

Figure 6.10: Anisotropy measure δ for the different driving quantities and $\zeta_*^{\boldsymbol{\Xi}} = 2$ and $\zeta_*^{\boldsymbol{\Xi}} = 10$.

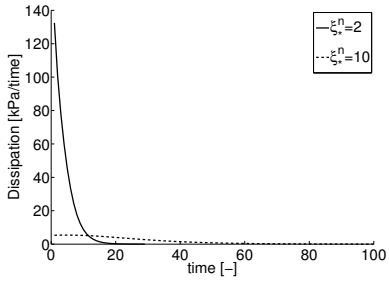

(a) Dissipation driven by $\mathbf{C}$

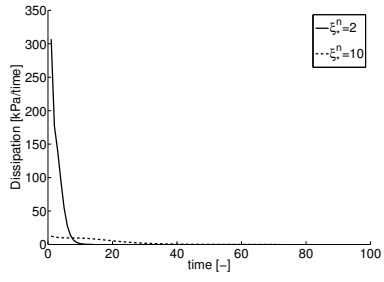

(b) Dissipation driven by $\mathbf{S}$

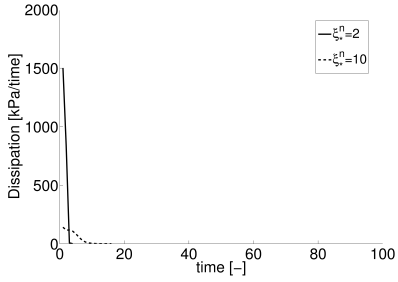

(c) Dissipation driven by $\mathbf{M}$

Figure 6.11: Dissipative evolution for the different driving quantities and $\zeta_*^{\boldsymbol{\Xi}} = 2$ and $\zeta_*^{\boldsymbol{\Xi}} = 10$.

and $\zeta_*^{\boldsymbol{\Xi}} = 10$.

6.6.2 Reorientation of the fibrils

In this Section we give some examples to illustrate the model described in Section 6.3.2, where the fibrils or filaments that make up a fibered structure reorient themselves with the maximum eigenvector of a given driving quantity. The material parameters of the WLC model are fixed for all the examples to the same values given in the above section, $r_0 = 1$, $L = 2$, $A = 1.3$, $n = 7.0\text{x}10^{21}$, $k = 1.381\text{x}10^{-23} J/K$ and $\theta = 300K$. All the specimens are stretched with $\mathbf{F} = 1/\sqrt{\lambda}\mathbf{e}_x \otimes \mathbf{e}_x + 1/\sqrt{\lambda}\mathbf{e}_y \otimes \mathbf{e}_y + \lambda \mathbf{e}_z \otimes \mathbf{e}_z$ with $\lambda = 2$ instantaneously applied

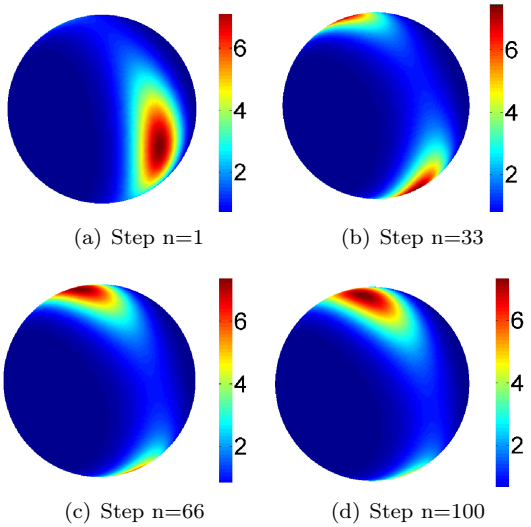

(a) Step n=1 (b) Step n=33

(c) Step n=66 (d) Step n=100

Figure 6.12: Evolution of principal direction of the ODF for different steps. (a) the distribution at step 1, (b) for step 33 ,(c) for step 66 and finally (d) at the end of the analysis.

$\zeta_*^{\Xi} = 2$			$\zeta_*^{\Xi} = 10$		
strain	stress	Mandel	strain	stress	Mandel
$5.328\text{x}10^2$	$8.269\text{x}10^2$	$5.912\text{x}10^4$	$1.730\text{x}10^2$	$2.239\text{x}10^2$	$6.742\text{x}10^3$

Table 6.3: Energy dissipated for each type of driving quantity.

and maintained to the end of the reorientation. We set $\Delta t = 0.01$. The Bingham parameters are $\kappa_{1,2,3} = [0, 8, 10]$ and $\mathbf{Q} = \mathbf{I}$ (being $\mathbf{I}$ the second order identity tensor), and we therefore ensure that the principal direction of the structure is previously aligned with the maximum principal direction of the driving quantity. We consider the biological sensing by the use of the material parameter $\bar{\zeta}^{\boldsymbol{\Xi}}$ defined in Eq. 6.33. Moreover, as in the above section, we have included the material parameter $\bar{\zeta}^{\boldsymbol{\Xi}}_*$, which is fixed to $\bar{\zeta}^{\boldsymbol{\Xi}}_* = 4, 20$ for comparison. This corresponds to double the value of $\zeta^{\boldsymbol{\Xi}}_*$. As in the case of the macro remodeling, we carry out the process using the different driving quantities. In Fig. 6.13, we present the evolution of the diagonal components of $\boldsymbol{\rho}$ (Eq. 6.35), which measure the evolution of the concentration of the fibrils. Again, the remodeling driven by strain is shown to be the slowest, followed by Mandel and stress. The processes with $\bar{\zeta}^{\boldsymbol{\Xi}}_* = 20$ are slower than those with $\bar{\zeta}^{\boldsymbol{\Xi}}_* = 4$, as expected.

We can also show (Fig. 6.14) the evolution of the fibrils as the evolution of the integration directions.

In order to view this evolution we make use of the procedure discussed in Remark 14. Fig. 6.15 shows the Bingham representation at different steps for the case of driving stress and $\bar{\zeta}^{\boldsymbol{\Xi}}_* = 20$. As we can see, its shape ends toward a very concentrated von Mises distribution, i.e., toward a 1D single fiber orientation.

To conclude this Section, we present the dissipative nature of the model graphically in Fig. 6.16 and quantitatively in Table 6.4. The results suggest that the dissipative process is highly sensitive to $\bar{\zeta}^{\boldsymbol{\Xi}}_*$. For $\bar{\zeta}^{\boldsymbol{\Xi}}_* = 4$, strain driven problem is the most dissipative, followed by stress and Mandel. However, for $\bar{\zeta}^{\boldsymbol{\Xi}}_* = 20$, the strain quantity becomes the least dissipative and the Mandel tensor the most dissipative. Nevertheless, as suggested above, we would need experimental data to obtain further conclusions on this issue. In order to compare the dissipative nature of the model presented here with that described in the previous section, we need to compute the dissipation with values of $\bar{\zeta}^{\boldsymbol{\Xi}}_* = 1$ and $\zeta^{\boldsymbol{\Xi}}_* = 1$. In this case the dissipation takes the following values: $\mathcal{D}_{\mathbf{C}} = 2.636$ x 10^2 [kPa/time], $\mathcal{D}_{\mathbf{S}} = 2.636$ x 10^2 [kPa/time] and $\mathcal{D}_{\mathbf{M}} = 2.638$ x 10^2 [kPa/time]. They are almost equal and very similar to those in the dissipative PDR process. Again, some experimental tests would be helpful in order to reach further conclusions.

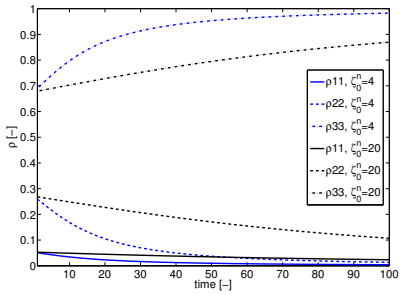

(a) Evolution of the microstructure distribution driven by **C**

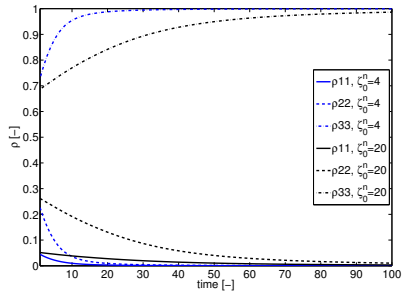

(b) Evolution of the microstructure distribution driven by **S**

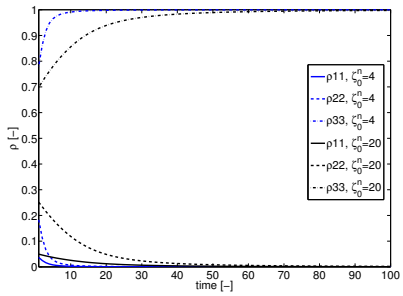

(c) Evolution of the microstructure distribution driven by **M**

Figure 6.13: Evolution of the microstructure by means of the diagonal components of $\boldsymbol{\rho}$.

	$\zeta_*^n = 4$			$\zeta_*^n = 20$		
	strain	stress	Mandel	strain	stress	Mandel
$\mathcal{D}$[kPa/time]	2.173x10^2	2.033x10^2	1.690x10^2	1.670x10^2	2.207x10^2	2.199x10^2

Table 6.4: Energy dissipated per each type of driving quantity and for $\bar{\zeta}_*^{\boldsymbol{\Xi}} = 4, 20$.

(a) $\kappa_{1,2,3} = 0, 8, 10$

(b) $\kappa_{1,2,3} = 0, 28, 38$

(c) $\kappa_{1,2,3} = 0, 43, 75$

(d) $\kappa_{1,2,3} = 0, 48, 112$

Figure 6.14: Evolution of the fibrils for different steps. (a) the initial distribution with $\kappa_{1,2,3} = 0, 8, 10$, (b) for step 33 leading to $\kappa_{1,2,3} = 0, 28, 38$, $\kappa_{1,2,3} = 0, 43, 75$ for step 66 in (c) the end of the analysis with $\kappa_{1,2,3} = 0, 48, 112$ in (d).

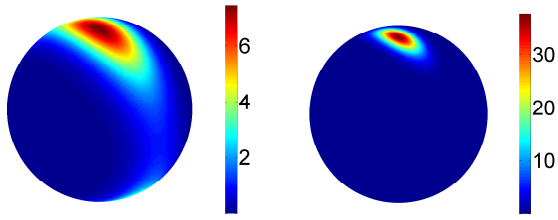

(a) $\kappa_{1,2,3} = 0, 8, 10$ (b) $\kappa_{1,2,3} = 0, 28, 38$

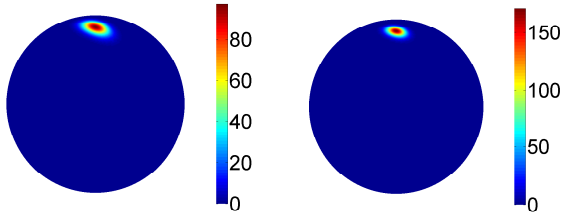

(c) $\kappa_{1,2,3} = 0, 43, 75$ (d) $\kappa_{1,2,3} = 0, 48, 112$

Figure 6.15: Evolution of the distribution for different steps. (a) the distribution at step 1 with $\kappa_{1,2,3} = 0, 8, 10$, (b) for step 33 leading to $\kappa_{1,2,3} = 0, 28, 38$, $\kappa_{1,2,3} = 0, 43, 75$ for step 66 in Fig. (c), the end of the analysis with $\kappa_{1,2,3} = 0, 48, 112$ in (d). For t$\mapsto \infty$ the Bingham distribution leads to very concentrated von Mises distributions.

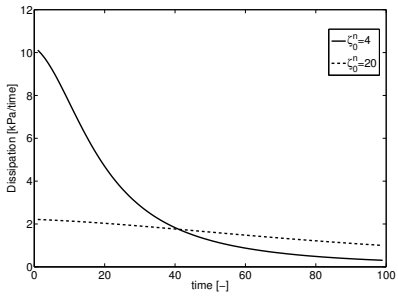

(a) Dissipation driven by $\mathbf{C}$

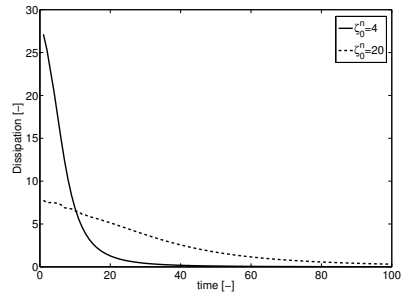

(b) Dissipation driven by $\mathbf{S}$

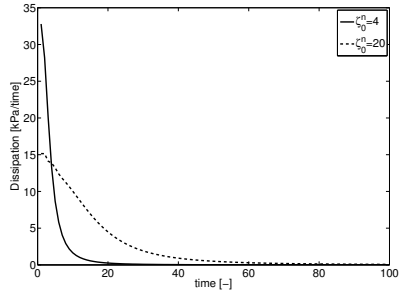

(c) Dissipation driven by $\mathbf{M}$

Figure 6.16: Dissipation of the model for the different driven quantities and material parameters $\bar{\zeta}_*^{\Xi} = 4, 20$.

Remark 17 ***Equibiaxial and volumetric states.*** *Equibiaxial and volumetric loads are special situations that should be carefully treated. From our model, any initial position of the principal directions (and therefore* $\mathbf{Q}$*) will not evolve under volumetric load, since in that situation any three orthogonal directions are principal directions, including those of* $\mathbf{Q}$*. In the equibiaxial case, the principal directions will evolve to the plane containing the two maximum stress directions along the direction of minimum length and then they will be balanced there, since any perpendicular direction to that plane is an eigenvector.*

Remark 18 ***No load state.*** *Another important issue to take into account is the stationarity of the model under no load. As it was pointed out by Garikipati et al. (2005), a proposed model must not evolve under an undeformed state. Our model solves this issue by means of the* ζ_0^n *parameter that does not allow any movement in the unloaded state.*

6.7 A finite element case: morphological changes of cells.

In this Section we compute a finite element model presenting a biological example of the model discussed above and non-homogeneous states of deformation. We have outlined the main steps of the algorithmic scheme in Table 6.5. As we discussed in the Introduction section, cell changes its mean orientation and its morphological shape. Experiments are focused on static loading, where cells align with the direction of stretching, and cyclic mechanical test, where cells align perpendicular to the direction of stretching. In the following example we will restrict ourselves to the static loading case. To do so, we model a thin sheet of material, 40mm x 20mm x 0.5 mm, as shown in Fig. 6.17(a) and discretized in 800 hexahedral elements. Left side of the specimen is fixed while in the right one, displacement or force can be imposed. In fact, we investigate the influence of both cases of boundary condition. We first compute the imposed displacement case, stretch value of 50% of the initial length in $\mathbf{e}_1$. We retrieve the reaction forces on the right side of the model to be, after that, imposed in a force driven simulation.

Table 6.5: Algorithm to compute remodeling of cell-like structures.

Input: $\mathbf{F}^{j+1}$, internal variables at time j

I Evaluate kinematics $\mathbf{C}^{j+1}$ and constitutive equations Ψ^{j+1}, $\mathbf{S}^{j+1}$ and $\mathbf{M}^{j+1}$

II Compute goal tensor $\boldsymbol{\Xi}$ by $\mathbf{C}^{j+1}$, $\mathbf{S}^{j+1}$ or $\mathbf{M}^{j+1}$

III Update orientation variables.
Evaluate exponential mapping for the evolution of $\mathbf{Q}^{j+1}$ and $\mathbf{r}_i^{j+1}$

$$\mathbf{Q}^{j+1} = exp(\zeta^{\boldsymbol{\Xi}}\hat{\mathbf{n}}^{\boldsymbol{\omega}}\Delta t/\zeta_*^{\boldsymbol{\Xi}}) \cdot \mathbf{Q}^j \tag{6.30}$$

$$\mathbf{r}^{j+1} = exp(\bar{\zeta}^{\boldsymbol{\Xi}}\hat{\mathbf{n}}^{\boldsymbol{\omega}}\Delta t/\bar{\zeta}_*^{\mathbf{j}}) \cdot \mathbf{r}^j \tag{6.31}$$

IV Compute dissipation, $\mathcal{D}_{\mathrm{PDR}}$ and $\mathcal{D}_{\mathrm{RF}}$ as described in Eq. 6.22 and Eq. 6.23 and anisotropy δ as in Eq. 6.29.

V Calculate stresses $\boldsymbol{\tau}^{j+1}$ and tangent operator related to the Jaumann rate as
$\boldsymbol{\tau}^{j+1} \approx 2\mathbf{b}^{j+1} \cdot (C_1 - C_2 I_1^{j+1}) + \sum_{i=1}^m \rho_i \bar{\boldsymbol{\tau}}_i^{j+1} w^i \approx \sum_{i=1}^m [\rho_i \psi'(\bar{\lambda}_i)\bar{\lambda}_i^{-1}\bar{\mathbf{t}}_i^{j+1} \otimes \bar{\mathbf{t}}_i^{j+1}]w^i$
$\overset{\nabla^{j+1}}{\mathbf{c}} = [\mathbf{c}^{j+1} + 1/2[\delta\tau^{j+1} + \tau^{j+1}\delta + \delta\tau^{j+1} + \tau^{j+1}\delta]]/J$ with
$\mathbf{c}^{j+1} \approx \sum_{i=1}^m n\rho_i w_i [\psi_i^{''j+1} - \psi_i^{'j+1}\overline{\lambda}^{-1}]\overline{\lambda}^{-2}\bar{\mathbf{t}}_i^{j+1} \otimes \bar{\mathbf{t}}_i^{j+1} \otimes \bar{\mathbf{t}}_i^{j+1} \otimes \bar{\mathbf{t}}_i^{j+1}$

Output: $\boldsymbol{\tau}^{j+1}, \overset{\nabla^{j+1}}{\mathbf{c}}, \mathbf{Q}^{j+1}, \mathbf{r}^{j+1}, \mathcal{D}_{\mathrm{PDR}}, \mathcal{D}_{\mathrm{RF}}, \delta$

Obviously, the stress and strain field over the specimen is the same in both of them before remodeling but their evolution is different for the Neumann and Dirichlet boundary value problem. Moreover, to allow a more general simulation of distribution of the cells, as it is usually the case in experimental procedures, we set a random orientation of the cell in each integration point as well as the concentration values of the statistical distribution $\kappa_{1,2,3}$. Let us also describe the evolution of the micro-structural information. In order to do so in the following results we look at three different points of the material which are, in somehow, meaningful. They are shown in Fig. 6.17(a) as point 1, 2 and 3, and will be referred so in the following. These values are described in Fig. 6.17(b-d).

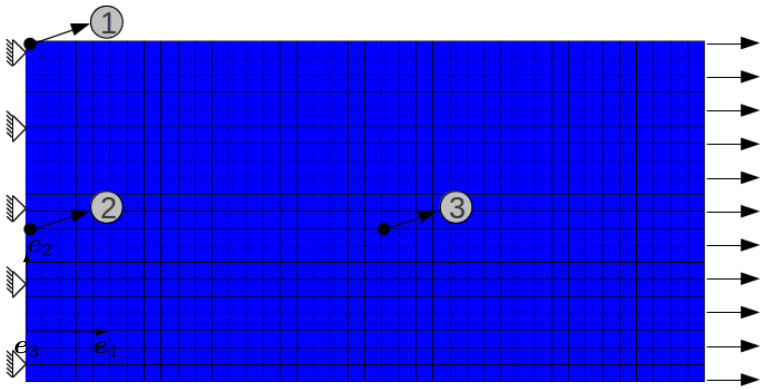

(a) Geometry and boundary condition of the finite element model. Point 1, 2 and 3 have been marked for micro-structural plotting purposes.

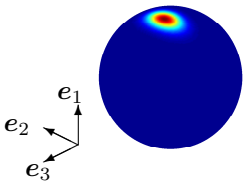

(b) ODF in point 1. $\mathbf{Q}_{i,1}$= 0.08 -0.81 -0.56 and $\mathbf{Q}_{i,2}$=-0.73 0.33 -0.58 and κ = 31.6, 16.9, 0.0

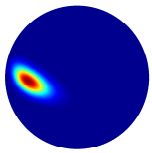

(c) ODF in point 2. $\mathbf{Q}_{i,1}$= 0.67 0.05 -0.73 and $\mathbf{Q}_{i,2}$=-0.68 0.41 -0.60 and $\kappa = 49.8, 40.1, 0.0$

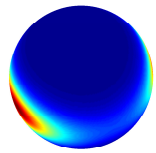

(d) ODF in point 3. $\mathbf{Q}_{i,1}$= 0.95 -0.15 0.25 and $\mathbf{Q}_{i,2}$=-0.27 -0.15 0.94 and $\kappa = 8.1, 6.4, 0.0$

Figure 6.17: Description of the initial values of the ODF distribution for the three marked points and boundary condition of the finite element model with micro-structural information.

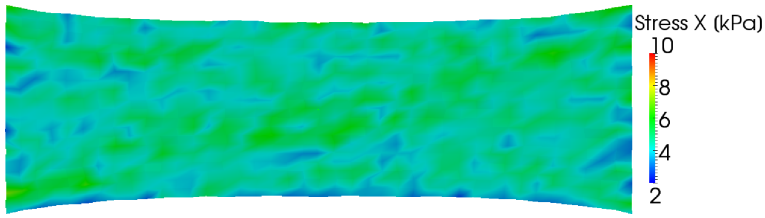

Figure 6.18: Stress field in X direction for the static simulation. The stress field shows a highly non-uniform distribution of the stresses due to the random distribution of the micro-structure.

The stress field in the deformed configuration is shown in Fig. 6.18. For sake of simplicity we will compute strain and stress-driven problems, since they are the most used variables to be compare with in the literature. Moreover, and again to keep the problem as simply as possible, we set ζ_*^{Ξ} and $\overline{\zeta}_*^{\Xi}$ equal to one, and since we demonstrated in Section 6.6, Mandel-driven cases remain, in trends and values, between those achieved by strain and stress cases. In Fig. 6.19 we plot the reaction force and the displacement on the right side of the phantom for the displacement and force driven problem respectively. We can easily see how the material stiffens due to the reorientation of the micro-structure for the problem driven by displacement and the shortening of the sample when the problem is driven by force. We also present stress and anisotropy fields for every boundary problem discussed above for different time steps. They are presented in Figs. 6.20,6.21,6.22,6.23

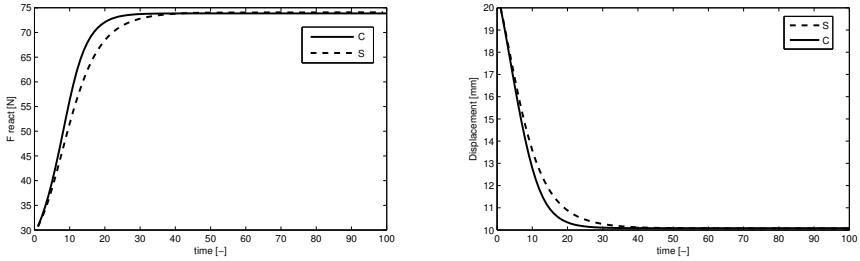

(a) Evolution of the reaction forces for the displacement driven problem.

(b) Evolution of the displacements for the force driven problem.

Figure 6.19: Evolution of the displacement and reaction forces for different boundary conditions problems.

(a) Stress field in X direction at step time 10 for the displacement driven problem.

(b) Stress field in X direction at step time 100 for the displacement driven problem.

(c) Stress field in X direction at step time 10 for the force driven problem.

(d) Stress field in X direction at step time 100 for the force driven problem.

Figure 6.20: Evolution of stress for different boundary value problems, Dirichlet (a-b) and Neumann (c-d) for remodeling driven by strain.

(a) Stress field in X direction at step time 10 for the displacement driven problem.

(b) Stress field in X direction at step time 100 for the displacement driven problem.

(c) Stress field in X direction at step time 10 for the force driven problem.

(d) Stress field in X direction at step time 100 for the force driven problem.

Figure 6.21: Evolution of stress for different boundary value problems, Dirichlet (a-b) and Neumann (c-d) for remodeling driven by stress.

(a) Anisotropy field at step time 10 for the displacement driven problem.

(b) Anisotropy field at step time 100 for the displacement driven problem.

(c) Anisotropy field at step time 10 for the displacement driven problem.

(d) Anisotropy field at step time 100 for the displacement driven problem.

Figure 6.22: Evolution of anisotropy for different boundary value problems, Dirichlet (a-b) and Neumann (c-d) for remodeling driven by strain.

(a) Anisotropy field at step time 10 for the displacement driven problem.

(b) Anisotropy field at step time 100 for the displacement driven problem.

(c) Anisotropy field at step time 10 for the displacement driven problem.

(d) Anisotropy field at step time 100 for the displacement driven problem.

Figure 6.23: Evolution of anisotropy for different boundary value problems, Dirichlet (a-b) and Neumann (c-d) for remodeling driven by stress.

We are going to look at the evolution of the micro-structure, which fits in with the cell structure. First, we present the anisotropy evolution in Fig. 6.24. Figures show less uniform evolution than the cases presented in Section 6.6 due to the non-uniform deformation state. All of the three points end up with an anisotropy measure close to zero, which represent a bundle aligned with the direction of the maximum strain. Due to the random orientation and concentration of the cells of interest, the initial anisotropy value is also different for the three of them.

6.8 Application to the endothelial cell morphology

It is well know that endothelial cells line over the lumen adapt its morphology based on the WSS of the arterial wall. Several references and examples were commented in the introduction of this Chapter. In this section we adapt the methodology developed previously to predict the morphological features of the EC in different zones of the carotid artery where EC align in the direction of the flow for laminar and high wall shear stress value. Blackman et al. (2002) showed that steady laminar flow and pulsatil flow make EC to reorient in the direction of the flow and that the aspect ratio of the cells increase in a very similar fashion. Galbraith et al. (1998) studied the structural organization of several elements of the cell (microfilaments, microtubules and intermediate filaments) also seeing the main orientation of cell align in the direction of the flow. In similar studies Levesque et al. (1986) and Kim et al. (1989) showed that in arterial coarctated model EC in the laminar zone before coarctation presented very tip-shapes while in the turbulent zone, after coarctation, EC showed a more random structure. Levesque et al. (1986) reported shape indexes (SI) of 0.2 for the laminar zones while turbulent flow induces SI fro 0-4 to 1. Farcas et al. (2009) reported changes in the SI from 0.6 to 0.3-04. Malek and Izumo (1996); Ohashi and Sato (2005) among others have shown this same behavior in their works. In a review article Chien (2007) resume some of the characteristic morphological changes due to different mechanical stimuli.

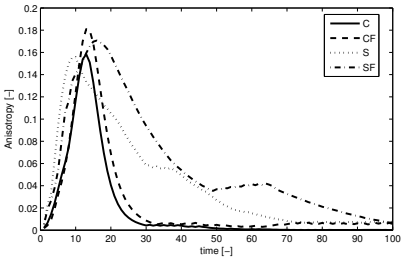

(a) Evolution for Point 1.

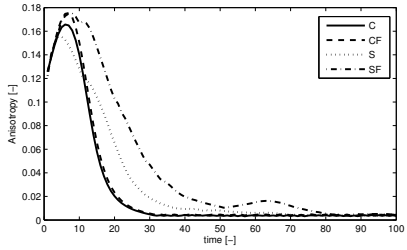

(b) Evolution for Point 2.

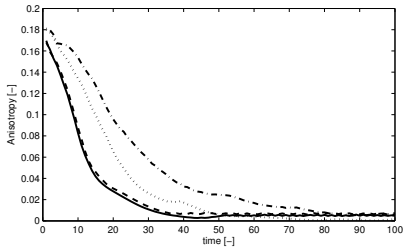

(c) Evolution for Point 3.

Figure 6.24: Anisotropy evolution for the three points of interest for strain (C and CF) and stress (S and SF) driven problems and different boundary conditions, Dirichlet (C and S) and Neumann (CF and SF).

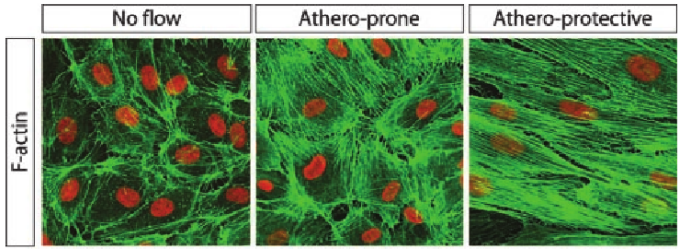

Figure 6.25: Cell morphology in a no-flow situation and athero-prone and protective flow condition reported by Dai et al. (2004).

Davies et al. (1986) presented a study pointing out that, although high shear stress in laminar flow promote cell alignment in the direction of the flow, low turbulent shear stress promote synthesis of endothelial DNA even in the absence of a organized structure of the cells suggesting that this type of flow is prone to develop atherome plaque. Another feature of all these studies is the formation of stress fibers in the direction of the fluid for the laminar flow and in a random distribution in case of turbulent patterns. Stress fibers (see ,e.g., Mofrad and Kamm (2006)) are important structural elements and their formation lead to changes in the mechanical behavior of the cell. We will ignore these phenomena in this study.

The goal of this section is the simulation of the EC remodeling feature by means of the models presented in this work. In particular we look at the work of Dai et al. (2004) that studies this very same issue in a carotid artery based on two different waveforms, an athero-protective (related to high laminar shear stress) and a athero-prone waveform (related to recirculation in low wall shear stress). We can see the structure the cell organization in both types of saturation in Fig. 6.25. The streamlines velocities and the values of WSS of the fluid simulation of the carotid artery (Malve et al., 1996) are shown in Fig. 6.26.

The starting point of this approach consist of micro-sphere cell-like structures placed over the arterial lumen. The initial shape of the EC correspond with a orthotropic distribution, this is a cell with a round shape (see Fig. 6.27(a-b) and structure with the orthotropic plane tangent to the surface of the lumen. The

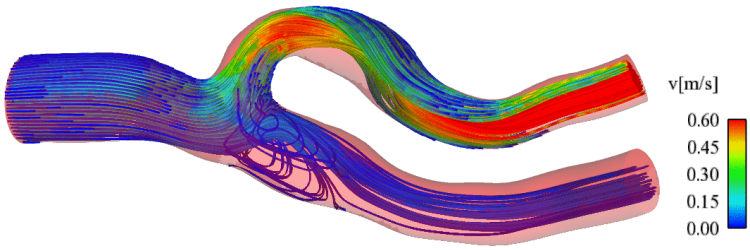

(a) Velocity streamlines (Malve et al., 1996).

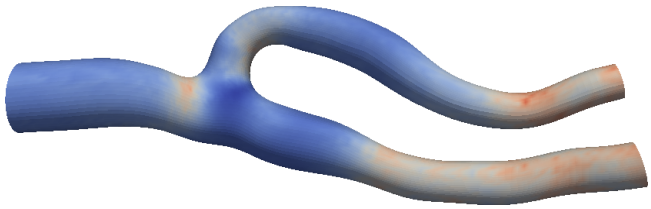

(b) WSS values.

Figure 6.26: Fluid simulation variables in the model of the human carotid.

structure of the model is pictured in Fig. 6.27(c-d) which is represented by the mechanical and geometrical approach discussed in Section 6.2.

The morphological changes that we described above are simulated by means of the remodeling approach developed during the previous sections. We use the model described in 6.5.2 so the orientation of the preferential direction will be neglected for this simulations and only the reorientation of the micro-structure will be considered instead of also considering the reorientation of the whole cell. As we discussed, this approach describe a reorientation of the fibrils or filaments that make up such a structure. In this case the driving stimuli is the wall shear stress in the arterial lumen based on results of a fluid-dynamic simulation. The morphological changes will be based on the updating procedure described in Eq. 6.13 as

$$\mathbf{r}^{n+1} = exp(\bar{\zeta}^{\boldsymbol{\Xi}}\hat{\boldsymbol{\Xi}}^{\boldsymbol{\omega}}\Delta t/\bar{\zeta}_{*}^{\boldsymbol{\Xi}}) \cdot \mathbf{r}^{n}. \tag{6.32}$$

For the magnitude-dependent parameter $\bar{\zeta}^{\boldsymbol{\Xi}}$. We have adopted the same defini-

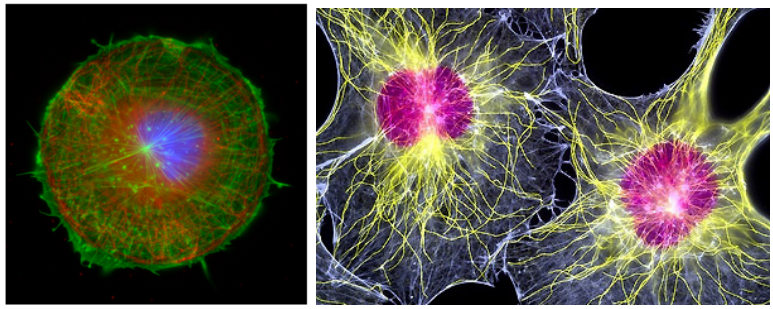

(a) Cell structure reported by Schauer (2013).

(b) Cell structure reported by Education (2013).

(c) Structure of the cell model.

(d) Structure of the cell model.

Figure 6.27: Structure of the cell from real images (a-b) and the proposed model (c-d).

tion as in the reorientation process, where $\boldsymbol{\tau}_w$ is the wall shear stress, being

$$\bar{\zeta}^{\boldsymbol{\Xi}} = \int_0^t \|\boldsymbol{\tau}_w\| dt, \tag{6.33}$$

which represent the mean wall shear stress. The corresponding material dependent parameter $\bar{\zeta}_*^{\boldsymbol{\Xi}}$ is considered now a function of the Oscillatory Shear Index (OSI), defined as

$$\text{OSI} = \frac{\int_0^t \|\boldsymbol{\tau}_w\| dt}{\| \int_0^t \boldsymbol{\tau}_w dt \|}, \tag{6.34}$$

$\bar{\zeta}_*^{\boldsymbol{\Xi}} = 1/\text{OSI}$. The OSI, variable that indicate the degree of variation in the direction of the flow, vary from 1 for a constant direction of the flow to 0 for a variation of 180 degrees in the direction of the flow. This is the reason for considering OSI as one of the parameters related to the remodeling on EC in blood flow conditions.

To measure the shape variation we compute the followingstructural tensor, $\boldsymbol{\rho}$,

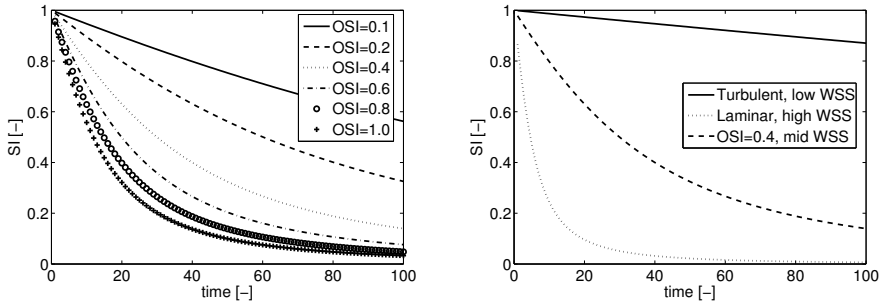

(a) Micro-structure at the step t=10.

(b) Micro-structure at the initial step time.

Figure 6.28: Evolution of the strain driven problem with Dirichlet condition at different time steps.

as

$$4\pi\boldsymbol{\rho}^n = \int_{\mathbb{U}^2} \rho(\mathbf{r}^n;\, \mathbf{Z},\, \mathbf{Q}^n)\mathbf{r}^n \otimes \mathbf{r}^n \mathrm{dA}. \tag{6.35}$$

As we discussed before, this tensor provide a symmetric second order tensor, where initially two of the diagonal components are equal and during the evolution process one of them turn to the unity and the other to zero. The ratio between these two values can be taken as the shape index factor, SI $= \rho_{33}/\rho_{22}$. Moreover we consider the range of OSI values [0-1] and the range of mean WSS [0-10] Pa to demonstrate the evolution capabilities of the model. We show in Fig. 6.28 the evolution of the SI for different values of OSI and a mean WSS of 3 Pa. In Fig. 6.28(b) we present the evolution of the SI for a OSI=0.1 and low mean WSS (WSS=1Pa), OSI=1 and high mean WSS (WSS=10) and a intermediate situation (OSI=0.4, WSS=5Pa). Results math nicely with the experimental finding described above. Flow with OSI=0.1 with low mean WSS keep very rounded shapes while flow with OSI=1 and high mean WSS lead to very pointed structures. In Fig. 6.29 we capture the evolution of the cell structure during the remodeling process.The figures, representing the microtubules coming from the centrosome, can be identified with pictures with pictures from cell organization.

We also show the evolution of the SI agains values of mean wall shear stress

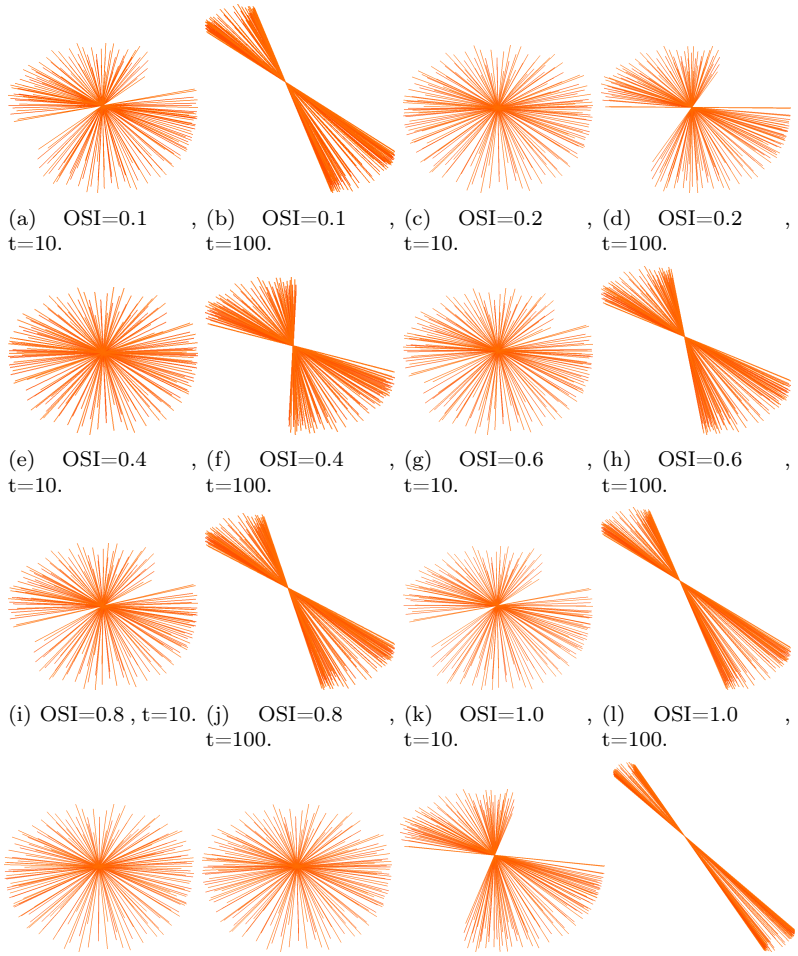

(a) OSI=0.1 , t=10. (b) OSI=0.1 , t=100. (c) OSI=0.2 , t=10. (d) OSI=0.2 , t=100.

(e) OSI=0.4 , t=10. (f) OSI=0.4 , t=100. (g) OSI=0.6 , t=10. (h) OSI=0.6 , t=100.

(i) OSI=0.8 , t=10. (j) OSI=0.8 , t=100. (k) OSI=1.0 , t=10. (l) OSI=1.0 , t=100.

(m) OSI=0.1, WSS=1.0 , t=10. (n) OSI=0.1, WSS=1.0 , t=100. (o) OSI=1.0, WSS=10.0 , t=10. (p) OSI=1.0, WSS=10.0 , t=100.

Figure 6.29: Evolution of the cell structure for different combination of WSS and OSI values at different time steps.

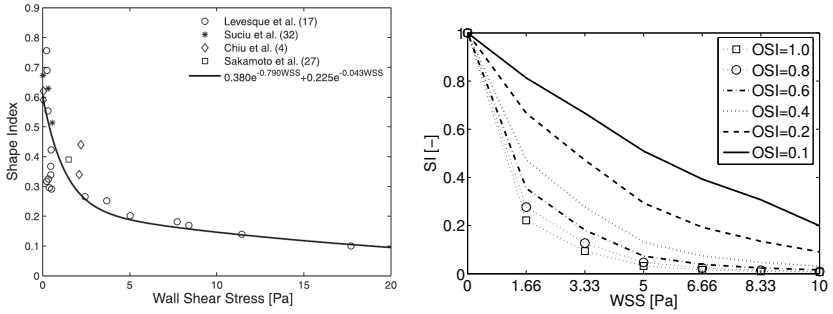

(a) Experimental data collected in Olgac et al. (2008)

(b) Evolution of the SI for different WSS values.

Figure 6.30: Evolution of the SI for different values WSS values for experimental data (a) and the model presented here (b).

at a laminar flow. These data was collected by Olgac et al. (2008) on different studies as we show in Fig. 6.30(a). Our simulations show very similar behavior as we can see in Fig 6.30(b).

6.9 Discussion

The adaptation of biological tissues has been a very active research field in recent years. The three principal processes of adaptation of biological tissue to mechano-chemical stimuli from a continuum point of view are remodeling, growth and morphogenesis (see e.g Humphrey (2009); Taber (2009); Ambrosi et al. (2011)). In this contribution we have focused on the reorientation process of fibered biological structures, proposing a complete 3D model that accounts for the reorientation of both the main direction of the structure and the fibrils or filaments that compose such a fibered structure. Most previous works have described the reorientation of a simple 1D fiber while, more recently, some others have taken into account the remodeling of the underlying structure by means of changes in its statistical distribution (Baaijens et al., 2010; Menzel et al., 2008). We have adopted a Bingham orientation distribution which allows a much more flexible description of the fibered structure. Our goal was to develop a model to be capable of de-

scribing both the remodeling of the principal direction and the distribution of the microstructure. We considered a microsphere-based model that allowed us to include the two aspects of the problem. A multi-scale scheme that couples the microstructural behavior and the macroscopic scale is used, also allowing the fibered microstructure to be defined in terms of the fibrils or filaments that make it up. We also extend the usual orientation space description of the micro-sphere model to be coupled with a physical space. In this way we compute the reorientation of the mean direction in the macroscale and the reorientation of the microstructure, upscaling the variables from the lower scale to the macroscopic behavior by means of a homogenization scheme.

Numerous works have analyzed different types of driving quantities in these processes (see e.g. Kuhl et al. (2005); De et al. (2008); Baaijens et al. (2010) and references therein), stress and strain being the most common. We have considered three driving quantities, strain, stress and a mix-variant Mandel-type tensor for driving the reorientation process. We assume the principal directions of these quantities as the goal to drive the reorientation process. To complete the model, we included two further material parameters. The first takes into account the magnitude of the driving quantities, since it seems natural to assume that the magnitude influences the evolution rate. The second was included to reflect the fact that different living structures can react to the same load in different ways.

After presenting some analytic cases of our model to study its behavior for different material parameters and different boundary conditions, we have extended the model to be included in a finite element scheme. It allowed us to compute a more realistic biological problem. We studied the remodeling of a plaque made up of a matrix seeded by a cell colony. The initial values of their orientation and shape was assumed to be random and our simulation showed a good qualitatively agreement with experimental findings. They showed a first orientation of the mean orientation followed by a change of their initial shape due to the reorganization of the interior structure.

As an extension to the proposed model we exploit the option of modeling the adaptation of EC to the stimuli of the wall shear stress. The model was based on the remodeling of the micro-structure developed during the previous

sections neglecting in this case any reorientation of the cell as a whole structure. Different flow features of the flow, as the WSS or the OSI, were considered to investigate the remodeling process of the EC. The OSI, a measure of the variation of the direction of the flow, and the WSS are usual indicators of different the cell morphology. Our simulation show that the SI of the cells under certain flow condition described the actual morphology of EC in experimental data. The model represent a relatively simple view of the macroscopic remodeling of the cell structure. It have shown to be suitable for the study of the the remodeling process and it could be used to study , e.g., the synthesized of different substances related to the EC adaptation.

The presented model has enormous capabilities for characterizing the evolution of complex biological fibered structures such as, for example, collagen bundles or cells. However there are certain limitations which need to be overcome in order to significantly improve it. The first, which does not apply only to our model, is the determination of those parameters related with the reorientation rate. If these were measured, our model could shed some light on which quantity actually drives these processes. We are thinking, for example, in a cell stretched by its substrate. In such a situation, tracking all the microtubules could help us to fit not only the material parameters but also the proposed driving quantities which best fit such experiments. In this contribution we have made use of a Bingham distribution to reflect the fibers or cells distribution. This assumption, although relatively simple and useful for a first attempt would be not the best option if an accurate and real structure want to be study. The microtubule or stress fiber tracking mentioned above could be used to construct a specific physical and orientation space to compute both reorientation and homogenization procedure. Currently, we have a fixed position for them over the unit sphere, and their actual number contributing to the mechanical behavior is limited by the shape of the statistical function. From our point of view, the most of future work would be focus on extending the model to the numerical simulation of cell mechanics. The amount of information that could be gathered from specialized literature is huge. For example, the active behavior force exerted by the stress fibers, the amount of actin generated due to a mechanical stimulus, the dynamic polymerization of

actin and tubulin, the use of the model to study the evolution of endothelial cells due to changes in the wall shear stress in blood vessels, and the list go on far away. Although the experiments needed to accurately fit such models is a tough task and very sophisticated and expensive instruments are needed, the theoretical and computational models would bring out an interesting mathematical description of these astonishing biological processes.

In short, we have proposed a novel general 3D reorientation model for both, the principal direction of the structure and the underlying fibered structure. We have used an exact updating scheme for these reorientations. This approach allows to model different remodeling processes in biological tissues, and with the appropriate experiments could lead to a better knowledge of how biological tissue adapts to its specific environment. Combined with the development of a growth model (see Humphrey (2009); Ambrosi et al. (2011)) our approach could help to modeling and predicting the overall behavior of tissue reacting to external stimuli, via the reorientation and growth (positive or negative), of its microstructure. We believe it have been and will represent a challenging area of research.

7 Conclusions

In this work a complete framework for simulating the consequences of hypertension in the arterial tissue is developed. We focused on three important effects of hypertension in the arterial wall. Before dealing with the evolution models, we modeled geometrically and mechanically a human carotid artery which was used to create finite element model. Mechanical properties were obtained from data in literature. We formulated a constitutive model that was used for fitting these data. The finite element model was used to gather strain and stress values in normotensive and hypertensive conditions. We used the increase of stretches in the smooth muscle cells to trigger two evolution models. Our first model dealt with the thickening of the arterial wall due to the hypertrophy of the smooth muscle cells. We used a kinematic description of the problem which was consistently included in our finite element model. Based on the same stimuli, we computed the collagen turnover that lead to the well know stiffen of the arterial wall in hypertension. Finally we studied the remodeling of endothelial cells due to the characteristic of the blood flow in the carotid artery.

In each chapter of this work a specific **conclusions** of each issue have been discussed.

- We showed that previous mechanical constitutive models fail in the characterization of some experimental test. Although they describe them good

enough when every material parameters is free to be fitted. However when the anisotropic direction of the tissue is provided, and therefore is not a fitting parameter, these models could not describe the tissue features in some cases. In this thesis, we provided an extension of previous hyperelastic models that takes into account the cross-links that collagen fiber bundles have. This features allow us to fit such experimental data. We also showed that the stress values in a human carotid artery are similar to those presented in previous models.

- Based on this mechanical model, we followed describing the arterial thickening of the carotid artery. We used a well established model of volumetric growth to describe such a thickening based on a stretch-based stimuli. We showed that the underlying hypertrophy of the smooth muscle cells can describe the thickening of the arterial wall. The model fitted well with experimental data described in literature both in qualitatively and quantitatively over time. The model reveal a very homogeneous growth factor across the media layer which can be related with the homogeneous stretch ratio between the hypertensive and normotensive state. The simulations also shown that while the stresses in the media layer decrease due to the growing process stresses, in the adventitia layer increase due to the expansion that the smooth muscle cells impose. This is in agreement with the idea that adventitia layer acts as a protective layer.

- We study the density increase of the collagen fibers using the same stretch stimuli on the smooth muscle cells. Based on the turnover of TGF-β, MMP and TIMP we showed that collagen density increase indeed. This fact match with the experimental observation that the arterial wall in hypertensive patients stiff due to the increase of the collagen content. The stiffening of the tissue undergoes a contraction of the artery lumen wich is also in agreement with the fact that adaptation in arterial tissue try to compensate the consequences of the over-stimuli, in this case, the over pressure.

- Finally, we model the adaptation of fibered structures to mechanical stimuli. We study how these phenomena evolve due to strain, stress Mandel-based

quantities and how they differ when the actual mechanical load is due to forces or displacements. This methodology is applied to model the adaptation of endothelial cells to the wall shear stress, which has been reported to have a key role in several adaptation processes in the arterial wall, such as the growth of atherome plaque. We used a micro-sphere based approach to deal with it and the results showed that the model describe the experimental data found in literature for different types of flow.

This work do not close at all the goal of this research field but instead open new option for **future work**, from a theoretical and computational point of view the study of adaptation in arterial tissue. Among some of the future lines of research, may be the most important are the following. In the mechanical part of the problem, that described in Chapter 3, the inclusion of residual stresses should be, probably, the most important work to be done. Residual stresses have shown to change the stress field across the arterial wall and that they change over time due to the different adaptation processes described in this thesis. The modeling of the myogenic tone of the smooth muscle cells is also an important issue that would improve the present model. It could change the stimuli considered during this thesis as well as the final state of the adaptation process since the geometry in the hypertensive state could differ.

In terms of the volumetric growth model the most important limitations are the pre-imposition of the final growth state and the lack of physical meaning of the time parameters. The study of more open and physical evolution equations for the growth would be also an interesting research topic.

Regarding the collagen turnover a more consistent formulation of the thermodynamic problem to be implicitly solved would gain, at least, a more well-turned computational and theoretical approach. There are also place for improvement in the biological point of view, since our model takes a relatively simple description of the mechano-biological process.

For the study of cell-type structures defined at the end of this thesis, we just provided the theoretical and computational framework to describe the actual adaptation, of e.g. endothelial cells, to the action of the blood flow. The study

of how this structure remodeled due to the flow changes in hypertensive patients or, e.g., how actin fibers growth due to, and orient toward, a mechanical stimuli is also a point for future research.

A

Resumen en Español

A.1 Resumen

El trabajo desarrollado en esta tesis se centra en el desarrollo de un modelo teórico y computacional de los procesos mecano biológicos que ocurren en el tejido arterial en hipertensión. El tejido arterial se adapta de forma activa a diferentes estímulos mecanicos y químicos donde las propiedades mecánicas del propio tejido juegan un papel fundamental. En hipertesión, el estímulo mecánico que desencadena estos procesos es el incremento de presión sanguínea así como cambios en el flujo sanguíneo.

Este trabajo se centra en cuatro aspectos caraterísticos de los procesos hipertensivos. Primero se estudia el comportamiento mecánico del tejido arterial, en particular se centra en el comportamiento de arteria humana de la cual obtenemos un modelo de elementos finitos sobre el que aplicar los diferentes modelos que se desarrollan a lo largo de este trabajo.

Los dos primeros aspectos relacionados con la adaptación del tejido en condiciones hipertensas es el crecimiento y remodelación del las células musculares y del colágeno contenido en la pared arterial. Su descripción mecánica se desarrolla, por tanto, dentro del campo de sistemas abiertos, entendiéndose por tales aquellos en los que se permite un aumento o pérdida de masa debido a cambios

de volumen o densidad. El engrosamiento característico de la pared arterial se describe a través de un modelo de crecimiento volumétrico, mientras que el incremento en el contenido de colágeno se modela a través de un cambio de densidad. Ambos modelos son descritos, primero teóricamente, para ser posteriormente implementados computacionalmente en un esquema de ele-mentos finitos. En la última parte de este trabajo se ha desarrollado un modelo de remodelación de estructuras fibradas aplicado a los cambios morfológicos que se producen en las células endoteliales ante diferentes patrones de flujo sanguíneo.

A.2 Estado de la cuestión

A.2.1 Enfermedades cariovasculares: La hipertensión

Las enfermedades cardiovasculares son una de las causas de muerte más importantes en países desarrollados (Chockalingam, 2007). Entre todos los tipos de alteraciones del sistema cardiovascular, la hipertensión es, probablemente, una de las más habituales y, por tanto, de las más estudiadas. Los últimos datos disponibles prevén un total de mil millones de adultos sufriendo hipertensión, lo que equivale a alrededor del 25 % de la población mundial (Elliott, 2003). Además, solo entre un 50 ó 70 %, según datos de países subdesarrollados o en vias de desarrollo, son conscientes de su dolencia. La hipertensión, por sí misma, no representa un claro peligro, aunque se considera un factor de riesgo para otras cardiovasculopatías como la rotura de placa de ateroma. Existe, por tanto, una necesidad de estudios que ayuden, tanto a conocer mejor el origen y desarrollo de la enfermedad, como a desarrollar protocolos para una mejor prevención y tratamiento de la misma (Mancia et al., 2003).

Los procesos hipertensivos están marcados por un aumento de la presión en el tronco arterial, ya sea de su valor medio, del valor sistólico o diastólico. En cualquiera de estos casos, existen cambios importantes en el entorno mecánico de la red vascular. Este aumento de presión desencadena una cascada de procesos mecano-químicos, los cuales hacen variar las propiedades mecánicas y morfológicas de la pared arterial (Kaplan and Victor, 2009). El corazón experimenta un

engrosamiento de sus ventrículos debido al sobreesfuerzo que debe realizar para bombear sangre a mayor presión.

Durante estos procesos la pared arterial experimenta importantes cambios estructurales. Existe una respuesta a corto plazo a la sobrepresión mediante una contracción activa de las células musculares. Esta respuesta es conocida como tono miogénico y tiene como objetivo restablecer la tensión fisiológica sobre la pared arterial y la tensión de cortadura en el lumen a valores homeostáticos (Dangelo and Meininger, 1994). A largo plazo, la hipertensión se caracteriza por un engrosamiento y rigidización de la pared arterial. El engrosamiento está relacionado con la hipertrofia (crecimiento en volumen) o hiperplasia (crecimiento en número) de las células musculares lisas (Owens et al., 1981). Por último, la rigidización de la pared arterial está relacionada con un aumento del porcentaje de colágeno (Diez and Laviades, 1997; O'Callaghan and Williams, 2000).

A.2.2 La biomecánica computacional

Durante los últimos años, o incluso décadas, ha habido un incremento importante de esfuerzo investigador en el ámbito de la biomecánica computacional (Fung, 1990; Humphrey, 2002). Una gran parte del conocimiento adquirido durante muchos años de estudio en mecánica de medios continuos (Marsden and Hughes, 1994; Holzapfel, 2000) y en métodos numéricos (Hughes, 2000; Stein et al., 2004) están siendo utilizados para estudiar el comportamiento de diferentes tejidos biológicos, como el corazón (McCulloch et al., 1998), globo ocular (Pandolfi and Manganiello, 2006), hueso (Weinbaum et al., 1994), arterias (Holzapfel et al., 2000) o ligamentos (Peña et al., 2006). El estudio de estos materiales desde el punto de vista de la mecánica de medios continuos permite su descripción matemática, estableciendo un primer paso para la comprensión del problema. Se han desarrolla-dos multitud de modelos mecánicos para describir procesos como la hipertrofia cardiaca, la pérdida de masa ósea, daño vascular debido a material quirúrgico, caracterización de diferentes fenómenos inelásticos del material, etc.

El uso de técnicas computacionales, entre las que cabe destacar el método de los elementos finitos (Hughes, 2000) o elementos de contorno (Sukumar et al.,

1998), ha sido de gran importancia en el campo de la biomecánica. Ha permitido emplear los modelos antes descritos en geometrías complejas y avanzar respecto de los modelos analíticos. Los modelos de elementos finitos nos permiten, por ejemplo, analizar el estado tensional de una geometría de aorta o de fémur para un paciente específico.

El desarrollo de un modelo de hipertensión en arterias es un proceso que involucra diversos campos de investigación. Durante años el estudio mecánico y numérico del sistema cardiovascular ha estado limitado al comportamiento pasivo del tejido. En este aspecto existen numerosos modelos en la literatura que, de una manera fenomenológica, reproducen dicho comportamiento. Sin embargo cada vez son más los modelos que incluyen información micro-estructural con el objetivo de obtener una mejor caracterización del material. Este avance en la simulación de tejidos biológicos ha sido posible gracias a mejoras en las técnicas experimentales de medida, así como de modelos computacionales más robustos.

La estructura de la pared arterial es altamente compleja (O'Callaghan and Williams, 2000) (Fig. A.1). Entre sus principales componentes destaca el colágeno, el cual aporta integridad estructural al material, elastina, células musculares lisas, encargadas del tono vasal y de las secreción de diferentes substancias, así como fibroblastos encargados de, por ejemplo, la síntesis del material extra-celular (Fung, 1990). El agua es el mayor componente de los vasos sanguíneos, confiriéndoles un comportamiento quasi-incompresible. Además de su alta hete-rogeinedad, su comportamiento está determinado por una alta no linealidad en su respuesta tensional. Así mismo presentan un alto grado de anisotropía debido a una disposición muy direccional de los elementos antes descritos. Tanto las fibras de colágeno como las células musculares presentan habitualmente una distribución preferencial de dirección.

Las fibras de colágeno están formadas por agregados de moléculas de tropocolágeno, segregados a su vez por células en el espacio extracelular donde son ensambladas formando fibras de colágeno (Bhattacharjee and Bansal, 2005). Debido al sobreesfuerzo experimentado por la células musculares causado por un aumento de presión, éstas inician la síntesis de diferentes sustancias, como factores de crecimiento e inhibidores de metaloproteínas (encargadas de degradar el colágeno)

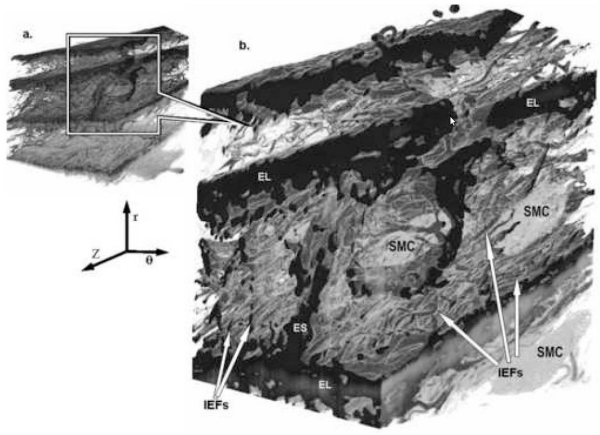

Figure A.1: Representación de la microestructura de una aorta de cerdo a través de Scanning Electron Microscopy (SEM) (O'Connell et al., 2008).

(Sumpio et al., 1988; Haga et al., 2007). El aumento o disminución de estas sustancias hacen cambiar la tasa de producción de colágeno, lo que en último término se traduce en una mayor rigidez de la pared arterial.

No ha sido hasta la última década cuando han aumentado, tanto en número como en calidad, los modelos teóricos y computacionales del comportamiento activo de estos materiales (Humphrey, 2009). Dentro del estudio del comportamiento activo se pueden citar cuatro grandes campos de investigación. El primero, es el comportamiento activo de las células musculares de todo el sistema cardiovascular, tales como procesos electro-fisiológicos del corazón (Rogers and McCulloch, 1994; Hunter et al., 1998) y la activación de células musculares lisas en el sistema periférico vascular (Murtada et al., 2010). El segundo campo es el estudio de procesos bioquímicos y biofísicos (Tarbell et al., 2005; Mofrad and Kamm, 2010). El tejido vascular está compuesto por diferentes células que tienen como objetivo transmitir el entorno mecánico y químico del ambiente que les rodeada y adaptarse a ellas a través de la secreción de sustancias químicas, remodelación de su estructura, muerte celular, diferenciación, etc (Li et al., 2005; Haga et al., 2007). Este campo de investigación es relativamente nuevo y los modelos numéricos que los describen están, a día de hoy, en una etapa inicial. Sin

embargo, se ha estudiado en más profundidad los procesos de difusión y cambios de densidad que se producen en diferentes tejidos. En este sentido existen trabajos previos en los que se estudia los cambios de densidad debido a alteraciones en el entorno mecánico y en el ambiente químico que se producen sobre el tejido (Kuhl and Steinmann, 2003; Tarbell, 2003b). Por último, también se han hecho grandes avances en la simulación de modelos de crecimiento volumétrico del material, debido a hipertrofia o hiperplasia, muerte o división de las células que lo componen (Kuhl et al., 2003b; Goektepe et al., 2010). Existen modelos que engloban todos estos procesos y que basan su análisis en la teoría de la regla de las mezclas (Humphrey and Rajagopal, 2002).

El trabajo de esta tesis analiza y modela diferentes procesos de adaptación en el tejido vascular, bajo el punto de vista de mecánica de medios continuos, desde el inicio de la presión arterial, pasando por la activación de las células responsables de sentir los cambios mecánicos que sobre ellas se producen. Estas células promueven la liberación y absorción de sustancias encargadas de remodelar la estructura y densidad de las fibras de colágeno y del tamaño de las células musculares.

A.3 Objetivos y metodología

El objetivo de esta tesis es el desarrollo teórico y computacional de un modelo capaz de reproducir los principales procesos que se observan experimentalmente en arterias de pacientes hipertensivos. Estos modelos, que se definen matemáticamente dentro del marco de la mecánica de medios continuos, los cuales son implementados a posteriori en un esquema de elementos finitos. El objetivo es obtener resultados númericos en geometrías de paciente específico reales. En particular, basaremos el trabajo en una geometría de carótida humana. Este objetivo es abordado estableciendo una metodología, obtenida de imágenes médicas, que incluye los diferentes procesos observados en hipertensión y que se exponen a continuación.

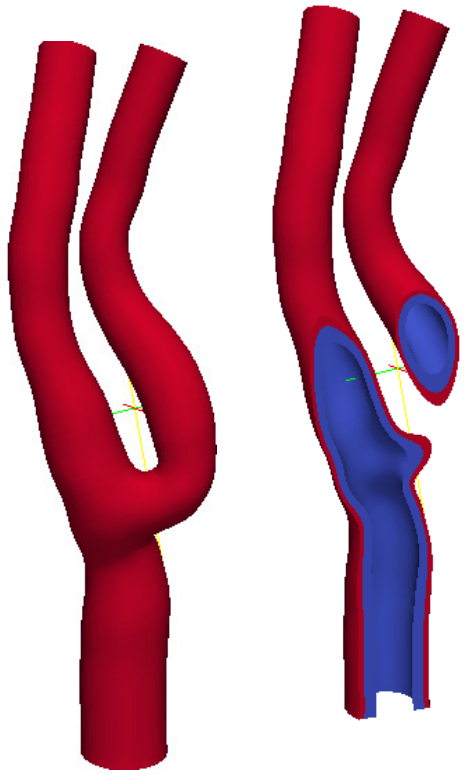

(a) Modelo de geometría carótida.

(b) Detalle de una corte del modelo de carotida.

Figure A.2: Geometría reconstruida de una carótida humana para su análisis por el método de los elementos finitos.

- Modelo pasivo de la pared arterial. En concreto se elige una geometría de carótida humana obtenida a través de imagen por Resonancia Magnética Nuclear (RMN) de un paciente específico. Se obtienen, de datos de literatura, valores de propiedades mecánicas de carótidas humanas variables a lo largo de eje arterial, así como la inclusión de la hipótesis de un espesor variable de la pared, para la capa media y adventicia. Dicha geometría se analiza con el fin de obtener valores de tensión en estados de homeostasis e hipertensión. El objetivo de esta primera fase es la obtención de variables

mecánicas sobre la pared arterial.

- Otras de las sustancias generadas, llamadas factores de crecimiento, promueven la hiperplasia e hipertrofia de las células musculares, lo que se traduce en un engrosamiento de la pared arterial. Con el fin de estudiar estos fenómenos se realiza un modelo computacional de crecimiento volumétrico, basado nuevamente en el alargamiento que se produce en las células musculares. Esto permite observar el engrosamiento de la pared arterial. El modelo se implementa nuevamente en un código de elementos finitos, lo que nos permite estudiar el engrosamiento de la pared de carótida real humana.

- Los cambios en las tensiones y estados de deformación en la pared arterial son los estímulos necesarios para la activación de las células musculares lisas. El objetivo en este apartado es definir un modelo que, en función del estimulo mecánico, genere diferentes sustancias biológicas, difundiéndose a través de la pared arterial. Se realiza, por tanto, un modelo de generación y difusión de masa a través de la pared arterial. Algunas de las sustancias consideradas y su interacción con diferentes células de la pared arterial, desequilibran el proceso de síntesis y absorción de las fibras de colágeno. Dichas fibras son las principales responsables de la integridad estructural de la arteria y, por tanto, su disminución o aumento se traduce en un comportamiento mecánico muy diferente. Se opta por definir un modelo mecánico de cambio de densidad de las fibras de colágeno, que integrado en un esquema de elementos finitos permite la simulación del proceso en su conjunto.

- En la última parte de este trabajo, se desarrolla un modelo de adaptación de estructuras fibradas ante estímulos mecánicos. Se estudia como estas estructuras se remodelan debido a variables de tipo deformación o tensión y cuales son las diferencias ante cargas en fuerza o desplazamiento. Este modelo mecánico se aplica a reproducir la adaptación de las células endoteliales ante las tensiones tangenciales en la pared de la carótida. Estos procesos de remodelación en las células endoteliales desencadenan otros muchos procesos de adaptación en la pared arterial como, por ejemplo, el crecimiento de

la placa de ateroma. Se plantea un modelo basado en la microesfera para modelar estas estructuras.

A.4 Conclusiones

Durante el trabajo de esta tesis se han desarrollado modelos teóricos y computacionales para el estudio de los procesos de adaptación del tejido cardiovascular a las alteraciones del flujo en condiciones de hipertensión.

Se empezó el trabajo revisando modelos constitutivos de la literatura encontrándose que los más utilizados no eran capaces de caracterizar ciertos aspectos de algunos ensayos experimentales. Aunque son capaces de reproducir estos ensayos, cuando todos los parámetros del material se dejan libres para ser ajustados, éstos fallan una vez que, por ejemplo, se aportaba la información de la direcciones de anisotropía obtenidas experimentalmente, y por tanto no era un parámetro de ajuste. Durante esta tesis se han extendido modelos hiperelásticos previos incorporando los enlaces que existen entre las fibras de colágeno. Teniendo en cuenta esta característica es posible ajustar aquellos ensayos que no se podían describir con modelos previos. También se han obtenido imágenes reales de carótidas de humano con las que se ha reconstruido un modelo de elementos finitos sobre el que se han aplicado el resto de modelos que se desarrollan a lo largo de esta tesis. La aplicación del modelo constitutivo propuesto a la geometría de carótida de humano proporcionó valores de tensiones comparables con valores encontrados en literatura.

Basados en este modelo mecánico, se continuó modelando el aumento de espesor de la pared arterial. Para ello se han usado modelos de crecimiento volumétrico que decriben el engrosamiento del tejido basados en un estímulo que considera el alargameinto de las células musculares. Se mostró que, a través de la hipertrofia de las células musculares, se puede describir el engrosamiento de la pared arterial. Los resultados de este modelo están en consonancia con los datos encontrados en literatura tanto cuantitativa con cualitativamente. Los resultados revelaron un factor de crecimiento muy homogéneo en la capa media de la arteria carótida, donde se localizan las células musculares. Este resultado está en

relación con la homogeneidad en el cociente entre los alargamientos de las células musculares en el estado hipertensivo y normotensivo. Las simulaciones también mostraron que, mientras las tensión en la capa media decrecen debido al efecto del crecimiento, en la capa adventicia éstas se incrementan debido al empuje que las células musculares ejercen sobre dicha capa. Este resultado está relacionado con la idea de que la capa adventicia actúa como una capa protectora de la pared arterial.

Posteriormente considerando el mismo estímulo, el alargamiento de las células musculares, estudiamos el incremento de densidad de las fibras de colágeno. Basado en el desequilibrio entre la creación y degeneración de TGF-β, TIMP y MMP se ha mostrado que la cantidad de colágeno en la pared arterial se incrementa tal y como muestran los resultados experimentales. Este resultado concuerda también con la observación experimental en la que la pared arterial se rigidiza debido al incremento de la cantidad de colágeno. Esta rigidización desencadena una contracción del diámetro de la pared arterial, lo que está igualmente en relación con la idea que la adaptación del tejido vascular intenta compensar las alteraciones en el ambiente mecánica que se producen debido a un estímulo, en este caso la hipertensión.

Finalmente se ha modelado la adaptación de estructuras fibradas ante estímulos mecánicos. Se estudió como estas estrcuturas evolucionan debido a variables basadas en deformación, tensión o de tipo Mandel y como esta evolución se modifica dependiendo de si la carga se ha aplicado en desplazameinto o en fuerza. Esta metodología se ha aplicado en modelar la adaptación de las células endoteliales sometidas a las tensiones tangenciales que se producen en el lumen debido al flujo sanguíneo, el cual sabe que ejerce un papel clave en la adaptación de la pared arterial, como en el crecimiento de la placa de ateroma. Se ha utilizado un modelo basado en la microesfera para modelar dichas estructuras. Las simulaciones realizadas muestran que los resultados obtenidos decriben de forma adecuada las datos experimentales publicados en literatura para diferentes tipos de flujo arterial.

A.5 Lineas futuras

El trabajo realizado en esta tesis no cierra, en absoluto, todos los aspectos alcanzables en este tipo de estudios, sino que abre nuevas líneas para el estudio teórico y computacional de la adaptación del tejido vascular. Dentro de las posibles líneas futuras de investigación destacaremos a continuacion algunas de ellas. En la parte mecánica del problema, descrita en el capitulo 3, la incorporación al modelo actual de las tensiones residuales podría ser el trabajo futuro más importante. Se sabe que las tensiones residuales en el tejido vascular pueden alterar de forma importante el estado tensional en la pared arterial y éste puede cambiar debido a los procesos de adaptación que se estudian en esta tesis. El modelado del tono miogénico de las células musculares lisas es también un aspecto importante que debe incorporarse al modelo. Podría cambiar el valor y gradiente del estímulo considerado durante este trabajo, además del estado final de los procesos de adaptación tanto de crecimiento volumétrico como de densidad, ya que la geometría en el estado hipertenso podría variar. En cuanto al modelo de crecimiento volumétrico, las limitaciones más importantes son la preimposición del estado final de crecimiento, así como la falta de significado físico claro de las parámetros temporales. Sería deseable la inclusión de ecuaciones de evolución más abiertas y con mayor sentido físico. En cuanto al modelo de cambio de densidad de las fibras de colágeno, una formulación más consistente del problema termodinámico que fuera implícitamente resuelto resultaría en una descripción teórica y computacional más elegante. Otro aspecto importante a mejorar es el aspecto biológico del problema, ya que nuestra descripción asume un modelo relativamente simple de los procesos mecano-biológicos presentes en estos fenómenos. En el estudio de la adapatación de las estructuras celulares definido al final de esta tesis, se propone únicamente un marco teórico y computacional que describe la adaptación de las células endoteliales a diferentes tipos de flujos. El estudio de cómo estas estructuras se adaptan a diferentes situaciones en condiciones de hipertensión, o cómo las fibras de actina crecen y se orientan en dirección de un cierto estímulo serían también campos interesantes para futuras de investigaciones.

A.6 Publicaciones

1. V. Alastrué, P. Sáez, M. A. Martinez, M. Doblaré. On the use of the Bingham statistical distribution in microsphere-based constitutive models for arterial tissue. *Mechanics Research Communications* 37(8):700-706, 2010.

2. P. Sáez, E. Peña, M. A. Martinez, M. Doblaré. A microsphere-based approach to damage in soft fibered tissue. *Biomechanics and Modeling in Mechanobiology.* 11(5):595–608, 2012.

3. P. Sáez, E. Peña, M. Doblaré., M. A. Martinez. An anisotropic microsphere-based approach for fiber orientation adaptation in soft tissue. *IEEE Transactions On Biomedical Engineering*, 58:3500–3503, 2011.

4. P. Sáez, E. Peña, M.A. Martínez, E. Kuhl. Mathematical modeling of collagen turnover in biological tissue. DOI:10.1007/s00285-012-0613-y.

5. P. Sáez, E. Peña, M. Doblaré, M.A. Martínez. 3D Generalized microstructural remodeling: Evolution and dissipation. In press. Int. J. Solids Struct. (2013).

6. P. Sáez, E. Peña, M.A. Martínez. On the micro-structural modeling of patient specific human carotid artery. Submitted for publication.

7. P. Sáez, E. Peña, M.A. Martínez, E. Kuhl. Computational modeling of hypertensive anisotropic growth.

8. P. Sáez, E. Peña, J. M. Tarbell, E. Kuhl, M.A. Martínez. A computational model of collagen turnover in the carotid artery under hypertensive conditions. Submitted for publication.

A.7 Congresos

1. P. Sáez, V. Alastrué, E. Peña, M. A. Martinez, M. Doblaré. Modelo de daño para materiales biológicos fibrados basado en su comportamiento mi-

croestrutural. (2009) *XXVII Congreso Anual de la sociedad Española de Ingeniería Biomédica-CASEIB*. Cadiz, Spain.

2. E. Peña, P. Sáez, V. Alastrué, M.A. Martínez and M. Doblaré. On modelling softening and damage effects in fibrous soft biological materials. (2009) *International Workshop on Continuum Biomechanics of Biological Tissue*. Castro Urdiales (Spain).

3. T. Waffenschmidt, P. Sáez, V. Alastrué, E. Peña, A. Menzel, M. Doblaré. A computational micro-sphere approach applied to the modelling of anisotropic soft biological tissues. (2010) *IV European Congress on Computational Mechanics (ECCM IV): Solids, Structures and Coupled Problems in Engineering*. Paris (France).

4. P. Sáez, V. Alastrué, E. Peña, M. A. Martinez, M. Doblaré. A micro-sphere approach to the modeling of anisotropic damage in blood vessels. (2010) *17th Congress of the European Society of Biomechanics (ESB)*. Edinburgh (UK).

5. P. Sáez, V. Alastrué, E. Peña, M. A. Martinez, M. Doblaré. A Damage Model based on Micro-structural Approach in Soft Fibered Tissue. (2010) *6th World Congress of Biomechanics*. Singapore.

6. P. Sáez, E. Peña, M. Doblaré, M. A. Martinez. Mechanical Adaptation in Fibered Biological Tissue vessels. (2011) *2nd Bio Mechanical Engineering Conference*. Stanford, US.

7. E. Peña, P. Sáez, M. Doblaré, M. A. Martinez. A Microstructural Approach to Modelling Inelastic Effects in Fibred Biological Tissues. (2011) *11th. International Conference on Computational Plasticity. Fundamentals and Applications. COMPLAS 2011*. Barcelona, Spain.

8. M. A. Martínez, P. Sáez, T. Waffenschmidt, E. Penã, M. Doblaré, A, Menzel. Different Damage Model Approaches in a Microsphere-Based Framework. Application to Soft Biological Tissues. (2011) *IUTAM Symposium on Computer Models in Biomechanics From Nano to Macro*. Stanford, US.

9. P. Sáez, E. Peña, M. Doblaré, MA. A. Martínez. 3D Remodeling Model for Fibered Biological Tissue. (2011) *IUTAM Symposium on Computer Models in Biomechanics From Nano to Macro.* Stanford, US.

10. E. Peña, A. García, P. Sáez, T. C. Gasser, M. A. Martínez. Structural Experimental Characterization and Micro-Macro Modeling of Collagen Fiber Distribution in Carotid Arteries (2011) *IUTAM Symposium on Computer Models in Biomechanics From Nano to Macro.* Stanford, US.

11. P. Sáez, M. Malve, E. Peña, M. A. Martínez, E. Kuhl. Computational mechanics of an adaptation model for blood vessels (2012) *23rd International Congress of Theoretical and Applied Mechanics (ICTAM 2012.*Beijing (China).

12. E. Peña, P. Sáez, M.A. Martínez. Microstructural constitutive model of inelastic effects in soft fibred tissues (2012). *6th European Congress On Computational Methods In Applied Sciences And Engineering (ECCOMAS 2012).* Viena (Austria).

13. P. Sáez, M. Malve, E. Peña, M. A. Martínez, E. Kuhl. Computational Growth Model of the Carotid Artery Bifurcation in Hypertensive Disease (2013). *11th International Symposium on Computer Methods in Biomechanics and Biomedical Engineering.* Salt Lake City, USA.

14. P. Sáez, M. Malve, E. Peña, M. A. Martínez. A computational model of endothelial cell reorientation due to arterial flow (2013). *19th Congress of the European Society of Biomechanics (ESB2013).* Patras, Greece.

Bibliography

Aaron, B. B., Gosline, J. M., 1981. Elastin as a random-network elastomer - a mechanical and optical analysis of single elastin fibers. Biopolymers 20 (6), 1247–1260.

Alastrué, V., Calvo, B., Pena, E., Doblare, M., Feb. 2006. Biomechanical modeling of refractive corneal surgery. J Biomech Eng 128 (1), 150–160.

Alastrue, V., Garcia, A., Pena, E., Rodriguez, J. F., Martinez, M. A., Doblare, M., Jan. 2010a. Numerical framework for patient-specific computational modelling of vascular tissue. Int J Numer Method Biomed Eng 26 (1), 35–51.

Alastrué, V., Martinez, M. A., Doblare, M., Menzel, A., Jan. 2009. Anisotropic micro-sphere-based finite elasticity applied to blood vessel modelling. J Mech Phys Solids 57 (1), 178–203.

Alastrué, V., Peña, E., Martinez, M. A., Doblare, M., Oct. 2007. Assessing the use of the "opening angle method" to enforce residual stresses in patient-specific arteries. Ann Biomed Eng 35 (10), 1821–1837.

Alastrue, V., Saez, P., Martinez, M. A., Doblare, M., Dec. 2010b. On the use of

the bingham statistical distribution in microsphere-based constitutive models for arterial tissue. Mech Res Commun 37 (8), 700–706.

Alford, P., Humphrey, J., Taber, L., 2008. Growth and remodeling in a thick-walled artery model: effects of spatial variations in wall constituents. Biomech Model Mechan 7, 245–262.

Ambrosi, D., Ateshian, G. A., Arruda, E. M., Cowin, S. C., Dumais, J., Goriely, A., Holzapfel, G. A., Humphrey, J. D., Kemkemer, R., Kuhl, E., Olberding, J. E., Taber, L. A., Garikipati, K., Apr. 2011. Perspectives on biological growth and remodeling. J Mech Phys Solids 59 (4), 863–883.

Anderson, E. A., SINKEY, C. A., LAWTON, W. J., MARK, A. L., Aug. 1989. Elevated sympathetic-nerve activity in borderline hypertensive humans - evidence from direct intraneural recordings. Hypertension 14 (2), 177–183.

Arruda, E. M., Boyce, M. C., Feb. 1993. A three-dimensional constitutive model for the large stretch behavior of rubber elastic materials. J Mech Phys Solids 41 (2), 389–412.

Association, A. H., 2012. Heart disease and stroke statistics.
URL `www.heart.org/statistics`

Ateshian, G. A., Nov. 2007. On the theory of reactive mixtures for modeling biological growth. Biomech Model Mechan 6 (6), 423–445.

Baaijens, F., Bouten, C., Driessen, N., Jan. 2010. Modeling collagen remodeling. J Biomech 43 (1), 166–175.

Bagshaw, R. J., Barrer, S. J., Cox, R. H., Nov. 1987. Connective-tissue analysis of the canine circle of willis in hypertension. Neurosurgery 21 (5), 655–659.

Baselt, D. R., Revel, J. P., Baldeschwieler, J. D., Dec. 1993. Subfibrillar structure of type-i collagen observed by atomic-force microscopy. Biophys J 65 (6), 2644–2655.

Bazant, Z. P., Oh, B. H., 1985. Microplane model for progressive fracture of concrete and rock. J Eng Mech-ASCE 111 (4), 559–582.

Bazant, Z. P., Prat, P. C., Oct. 1988. Microplane model for brittle-plastic material .i. theory. J Eng Mech-ASCE 114 (10), 1672–1687.

Bell, E., Ivarsoon, B., Merrill, C., 1979. Production of a tissue-like structure by contraction of collagen lattices by human-fibroblasts of different proliferative potential invitro. P Natl Acad Sci USA 76 (3), 1274–1278.

Bella, J., Eaton, M., Brodsky, B., Berman, H. M., Oct. 1994. Crystal-structure and molecular-structure of a collagen-like peptide at 1.9-angstrom resolution. Science 266 (5182), 75–81.

Bhattacharjee, A., Bansal, M., Mar. 2005. Collagen structure: The madras triple helix and the current scenario. IUBMB Life 57 (3), 161–172.

Bingham, C., 1974. An antipodally symmetric distribution on the sphere. Ann Stat 2 (6), 1201–1225.

Bischoff, J. E., Arruda, E. A., Grosh, K., Sep. 2002. A microstructurally based orthotropic hyperelastic constitutive law. J Appl Mech 69 (5), 570–579.

Bischofs, I. B., Schwarz, U. S., Aug. 2003. Cell organization in soft media due to active mechanosensing. Proc Nat Acad Sci USA 100 (16), 9274–9279.

Bishop, J. E., Butt, R., Dawes, K., Laurent, G., Jul. 1998. Mechanical load enhances the stimulatory effect of pdgf on pulmonary artery fibroblast procollagen synthesis. Chest 114 (1), 25S–25S.

Bishop, J. E., Lindahl, G., Apr. 1999. Regulation of cardiovascular collagen synthesis by mechanical load. Cardiovasc Res 42 (1), 27–44.

Bishop, J. E., Rhodes, S., Laurent, G. J., Low, R. B., Stirewalt, W. S., Oct. 1994. Increased collagen-synthesis and decreased collagen degradation in right-ventricular hypertrophy induced by pressure-overload. Cardiovas Res 28 (10), 1581–1585.

Blackman, B. R., Garcia-Cardena, G., Gimbrone, M. A., Aug. 2002. A new in vitro model to evaluate differential responses of endothelial cells to simulated arterial shear stress waveforms. J Biomech Eng-T ASME 124 (4), 397–407.

Bonet, J., Wood, R. D., 1997. Nonlinear Continuum Mechanics for Finite Element Analysis. Cambridge University Press.

Border, W. A., Noble, N. A., Nov. 1994. Transforming growth-factor-beta in tissue fibrosis. New Engl J Med 331 (19), 1286–1292.

Borges, L. F., Gutierrez, P. S., Cosiski Marana, H. R., Taboga, S. R., 2007. Picrosirius-polarization staining method as an efficient histopathological tool for collagenolysis detectin in vesical prolapse lesions. Micron 38 (6), 580–583.

Boutouyrie, P., Bussy, C., Lacolley, P., Girerd, X., Laloux, B., Laurent, S., Sep. 1999. Association between local pulse pressure, mean blood pressure, and large-artery remodeling. Circulation 100 (13), 1387–1393.

Bozec, L., Horton, M., Jun. 2005. Topography and mechanical properties of single molecules of type i collagen using atomic force microscopy. Biophys J 88 (6), 4223–4231.

Brayden, J. E., Nelson, M. T., Apr. 1992. Regulation of arterial tone by activation of calcium-dependent potassium channels. Science 256 (5056), 532–535.

Bridget, B. K .and Fuster, V., 2010. Promoting Cardiovascular Health in the Developing World: A Critical Challenge to Achieve Global Health. THE NATIONAL ACADEMIES PRESS,Washington, D.C.

Brinkman, H. C., 1947. A calculation of the viscous force exerted by a flowing fluid on a dense swarm of particles. Appl Scientific Res 1 (1), 27–34.

Brunner, H., Cockcroft, J. R., Deanfield, J., Donald, A., Ferrannini, E., Halcox, J., Kiowski, W., Luscher, T. F., Mancia, G., Natali, A., Oliver, J. J., Pessina, A. C., Rizzoni, D., Rossi, G. P., Salvetti, A., Spieker, L. E., Taddei, S., Webb, D. J., Feb. 2005. Endothelial function and dysfunction. part ii: Association with cardiovascular risk factors and diseases. a statement by the working group on endothelins and endothelial factors of the european society of hypertension. J Hypertens 23 (2), 233–246.

Burke, J. M., Ross, R., 1979. Synthesis of connective tissue macromolecules by smooth muscle. International review of connective tissue research 8, 119–57.

Burrowes, K. S., Hunter, P. J., Tawhai, M. H., Aug. 2005. Anatomically based finite element models of the human pulmonary arterial and venous trees including supernumerary vessels. J Appl Physiol 99 (2), 731–738.

Bustamante, C., Bryant, Z., Smith, S. B., Jan. 2003. Ten years of tension: single-molecule DNA mechanics. Nature 421 (6921), 423–427.

Butt, R. P., Bishop, J. E., Apr. 1997. Mechanical load enhances the stimulatory effect of serum growth factors on cardiac fibroblast procollagen synthesis. J Mol Cell Cardiol 29 (4), 1141–1151.

Butt, R. P., Laurent, G. J., Bishop, J. E., Nov. 1995. Collagen production and replication by cardiac fibroblasts is enhanced in response to diverse classes of growth-factors. Eur J Cell Biol 68 (3), 330–335.

Cancel, L. M., Fitting, A., Tarbell, J. M., Jul. 2007. In vitro study of ldl transport under pressurized (convective) conditions. Am J Physiol-Heart C 293 (1), H126–H132.

Caner, F. C., Carol, I., Jun. 2006. Microplane constitutive model and computational framework for blood vessel tissue. J Biomech Eng 128 (3), 419–427.

Carol, I., Jirasek, M., Bazant, Z., Apr. 2001. A thermodynamically consistent approach to microplane theory. part i. free energy and consistent microplane stresses. Int J Solids Struct 38 (17), 2921–2931.

Carol, I., Jirasek, M., Bazant, Z. P., Jan. 2004. A framework for microplane models at large strain, with application to hyperelasticity. Int J Solids Struct 41 (2), 511–557.

Carretero, O. A., Oparil, S., Jan. 2000. Essential hypertension part i: Definition and etiology. Circulation 101 (3), 329–335.

Chien, S., 2007. Mechanotransduction and endothelial cell homeostasis: the wisdom of the cell. Am J Physiol Heart Circ Physiol 292 (3), H1209–1224.

Chobanian, A. V., Bakris, G. L., Black, H. R., Cushman, W. C., Green, L. A., Izzo, J. L., Jones, D. W., Materson, B. J., Oparil, S., Wright, J. T., Roccella, E. J., May 2003. The seventh report of the joint national committee on prevention, detection, evaluation, and treatment of high blood pressure - the jnc 7 report. Jama-journal of the American Medical Association 289 (19), 2560–2572.

Chockalingam, A., May 2007. Impact of world hypertension day. Can J Cardiol 23 (7), 517–519.

Clark, J., Glagov, S., 1985. Transmural organization of the arterial media. the lamellar unit revisited. Arterioscler Thromb Vasc Biol 5 (1), 19–34.

Collinsworth, A. M., Torgan, C. E., Nagda, S. N., Rajalingam, R. J., Kraus, W. E., Truskey, G. A., Nov. 2000. Orientation and length of mammalian skeletal myocytes in response to a unidirectional stretch. Cell Tissue Red 302 (2), 243–251.

Conway, J., 1984. Hemodynamic aspects of essential-hypertension in humans. Physiol Rev 64 (2), 617–660.

Cowin, S. C., 1994. Optimization of the strain-energy density in linear anisotropic elasticity. J Elasticity 34 (1), 45–68.

Cowin, S. C., 2004. Tissue growth and remodeling. Annu Rev Biomed Eng 6, 77–107.

Curmi, P. A., Juan, L., Tedgui, A., Jun. 1990. Effect of transmural pressure on low-density-lipoprotein and albumin transport and distribution across the intact arterial-wall. Circ Res 66 (6), 1692–1702.

Curry, R. M., 1984. Mechanics and thermodynamics of transcapillary exchange. In: The Cardiovascular System. Microcirculation. American Physiological Society.

Dai, G. H., Kaazempur-Mofrad, M. R., Natarajan, S., Zhang, Y. Z., Vaughn, S., Blackman, B. R., Kamm, R. D., Garcia-Cardena, G., Gimbrone, M. A., Oct.

2004. Distinct endothelial phenotypes evoked by arterial waveforms derived from atherosclerosis-susceptible and -resistant regions of human vasculature. Proc Nat Acad Sci USA 101 (41), 14871–14876.

Dangelo, G., Meininger, G. A., Jun. 1994. Transduction mechanisms involved in the regulation of myogenic activity. Hypertension 23 (6), 1096–1105.

Davies, P. F., Remuzzi, A., Gordon, E. J., Dewey, C. F., Gimbrone, M. A., Apr. 1986. Turbulent fluid shear-stress induces vascular endothelial-cell turnover invitro. Proc Nat Acad Sci USA 83 (7), 2114–2117.

Davis, M. J., Hill, M. A., Apr. 1999. Signaling mechanisms underlying the vascular myogenic response. Physiol Rev 79 (2), 387–423.

De, R., Safran, S. A., Sep. 2008. Dynamical theory of active cellular response to external stress. Phys Rev E 78 (3), 031923.

De, R., Zemel, A., Safran, S. A., Sep. 2007. Dynamics of cell orientation. Nat Phys 3 (9), 655–659.

De, R., Zemel, A., Safran, S. A., Mar. 2008. Do cells sense stress or strain? measurement of cellular orientation can provide a clue. Biophys J 94 (5), L29–L31.

Deen, W. M., 2011. Analysis of Transport Phenomena. Oxford University Press.

Delfino, A., Stergiopulos, N., Moore, J. E., Meister, J. J., Aug. 1997. Residual strain effects on the stress field in a thick wall finite element model of the human carotid bifurcation. J Biomech 30 (8), 777–786.

Demiray, H., Weizsacker, H. W., Pascale, K., Erbay, H., 1988. A stress-strain relation for a rat abdominal aorta. J Biomech 21 (5), 369–374.

Diez, J., Laviades, C., Aug. 1997. Monitoring fibrillar collagen turnover in hypertensive heart disease. Cardiovas Res 35 (2), 202–205.

Diez, J., Laviades, C., Mayor, G., Gil, M. J., Monreal, I., Mar. 1995. Increased serum concentrations of procollagen peptides in essential-hypertension - relation to cardiac alterations. Circulation 91 (5), 1450–1456.

Discher, D. E., Janmey, P., Wang, Y. L., Nov. 2005. Tissue cells feel and respond to the stiffness of their substrate. Science 310 (5751), 1139–1143.

Driessen, N. J. B., Cox, M. A. J., Bouten, C. V. C., Baaijens, F. P. T., Apr. 2008. Remodelling of the angular collagen fiber distribution in cardiovascular tissues. Biomech Model Mechan 7 (2), 93–103.

Driessen, N. J. B., Peters, G. W. M., Huyghe, J. M., Bouten, C. V. C., Baaijens, F. P. T., Aug. 2003. Remodelling of continuously distributed collagen fibres in soft connective tissues. J Biomech 36 (8), 1151–1158.

Driessen, N. J. B., Wilson, W., Bouten, C. V. C., Baaijens, F. P. T., Jan. 2004. A computational model for collagen fibre remodelling in the arterial wall. J Theor Biol 226 (1), 53–64.

Eberth, J. F., Cardamone, L., Humphrey, J. D., Sep. 2011. Evolving biaxial mechanical properties of mouse carotid arteries in hypertension. J Biomech 44 (14), 2532–2537.

Eberth, J. F., Popovic, N., Gresham, V. C., Wilson, E., Humphrey, J. D., Dec. 2010. Time course of carotid artery growth and remodeling in response to altered pulsatility. Am J Physiol-Heart C 299 (6), H1875–H1883.

Education, D. S., 2013.
URL `http://www.dynamicscience.com.au`

Einstein, A., Jul. 1905. The motion of elements suspended in static liquids as claimed in the molecular kinetic theory of heat. Annalen Der Physik 17 (8), 549–560.

Elliott, W. J., 2003. The economic impact of hypertension. J Clin Hypertens (Greenwich, Conn.) 5 (3 Suppl 2), 3–13.

Farcas, M. A., Rouleau, L., Fraser, R., Leask, R. L., Oct. 2009. The development of 3-d, in vitro, endothelial culture models for the study of coronary artery disease. Biomed Eng Online 8, 30.

Faust, U., Hampe, N., Rubner, W., Kirchgessner, N., Safran, S., Hoffmann, B., Merkel, R., Dec. 2011. Cyclic stress at mhz frequencies aligns fibroblasts in direction of zero strain. Plos One 6 (12), e28963.

Feihl, F., Liaudet, L., Levy, B. I., Waeber, B., May 2008. Hypertension and microvascular remodelling. Cardiovas Res 78 (2), 274–285.

Fick, A., 1855. On liquid diffusion. Phil. Mag 10, 30–39.

Fisher, R., May 1953. Dispersion on a sphere. Proc R Soc Lon Ser-A 217, 295–305.

Folkow, B., 1982. Physiological-aspects of primary hypertension. Physiol Rev 62 (2), 347–504.

Folkow, B., Grimby, G., Thulesius, O., 1958. Adaptive structural changes of the vascular walls in hypertension and their relation to the control of the peripheral resistance. Acta Physiol Scand 44 (3-4), 255–272.

Fountain, H., 2012.
URL `http://www.nytimes.com/`

Fratzl, P., 2008. Collagen: Structure and Mechanics. Springer (New York).

Fridez, P., Makino, A., Kakoi, D., Miyazaki, H., Meister, J. J., Hayashi, K., Stergiopulos, N., Jul. 2002. Adaptation of conduit artery vascular smooth muscle tone to induced hypertension. Ann Biomed Eng 30 (7), 905–916.

Fung, Y., Liu, S., 1989. Change of residual strains in arteries due to hypertrophy caused by aortic constriction. Circ Res 65 (5), 1340–1349.

Fung, Y. C., 1990. Biomechanics: Mechanical Properties of Living Tissues. Springer.

Fung, Y. C., Fronek, K., Patitucci, P., 1979. Pseudoelasticity of arteries and the choice of its mathematical expression. Am J Physiol Heart Circ Physiol 237 (5), H620–631.

Galbraith, C. G., Skalak, R., Chien, S., 1998. Shear stress induces spatial reorganization of the endothelial cell cytoskeleton. Cell Motil Cytoskel 40 (4), 317–330.

Galis, Z. S., Khatri, J. J., Feb. 2002. Matrix metalloproteinases in vascular remodeling and atherogenesis - the good, the bad, and the ugly. Circ Res 90 (3), 251–262.

Galis, Z. S., Muszynski, M., Sukhova, G. K., Simonmorrisey, E., Unemori, E. N., Lark, M. W., Amento, E., Libby, P., Jul. 1994. Cytokine-stimulated human vascular smooth-muscle cells synthesize a complement of enzymes required for extracellular-matrix digestion. Circ Res 75 (1), 181–189.

Ganghoffer, J. F., Sep. 2010. Mechanical modeling of growth considering domain variation. part ii: Volumetric and surface growth involving eshelby tensors. J Mech Phys Solids 58 (9), 1434–1459.

Gao, H., Long, Q., 2008. Effects of varied lipid core volume and fibrous cap thickness on stress distribution in carotid arterial plaques. J Biomech 41, 3053–3059.

Gao, H., Long, Q., Graves, M., Gillard, J., Li, Z., 2009. Carotid arterial plaque stress analysis using fluid-structure interactive simulation based on in-vivo magnetic resonance images of four patients. J Biomech 42, 1416–1423.

Garcia, A., 2012. Experimental and numerical framework for modelling vascular diseases and medical devices. Ph.D. thesis, University of Zaragoza.

Garcia, A., Pena, E., Laborda, A., Lostale, F., De Gregorio, M. A., Doblare, M., Martinez, M. A., Jul. 2011. Experimental study and constitutive modelling of the passive mechanical properties of the porcine carotid artery and its relation to histological analysis: Implications in animal cardiovascular device trials. Med Eng Phys 33 (6), 665–676.

Garikipati, K., Arruda, E. M., Grosh, K., Narayanan, H., Calve, S., Jul. 2004. A continuum treatment of growth in biological tissue: the coupling of mass transport and mechanics. J Mech Phys Solids 52 (7), 1595–1625.

Garikipati, K., Narayanan, H., Arruda, E. M., Grosh, K., Calve, S., 2005. Material forces in the context of biotissue remodelling. In: Steinmann, P., Maugin, G. A. (Eds.), Mechanics of Material Forces. Springer, New York.

Garikipati, K., Olberding, J., Narayanan, H., Arruda, E., Grosh, K., Calve, S., Jul. 2006. Biological remodelling: Stationary energy, configurational change, internal variables and dissipation. J Mech Phys Solids 54 (7), 1493–1515.

Gasser, T. C., Gallinetti, S., Xing, X., Forsell, C., Swedenborg, J., Roy, J., 2012. Spatial orientation of collagen fibers in the abdominal aortic aneurysm's wall and its relation to wall mechanics. Acta Biomater Accepted for publication.

Gasser, T. C., Ogden, R. W., Holzapfel, G. A., 2006. Hyperelastic modelling of arterial layers with distributed collagen fibre orientations. J Roy Soc Interface 3, 15–35.

Glagov, S., Zarins, C., Giddens, D. P., Ku, D. N., Oct. 1988. Hemodynamics and atherosclerosis - insights and perspectives gained from studies of human arteries. Arch Pathol Lab Med 112 (10), 1018–1031.

Gleason, R., Humphrey, J., Jun. 2005. Effects of a sustained extension on arterial growth and remodeling: a theoretical study. J Biomech 38 (6), 1255–1261.

Gleason, R. L., Humphrey, J. D., 2004. A mixture model of arterial growth and remodeling in hypertension: Altered muscle tone and tissue turnover. J Vasc Res 41 (4), 352–363.

Goektepe, S., Abilez, O. J., Kuhl, E., Oct. 2010. A generic approach towards finite growth with examples of athlete's heart, cardiac dilation, and cardiac wall thickening. J Mech Phys Solids 58 (10), 1661–1680.

Goli-Malekabadi, Z., Tafazzoli-Shadpour, M., Rabbani, M., Janmaleki, M., Oct. 2011. Effect of uniaxial stretch on morphology and cytoskeleton of human mesenchymal stem cells: static vs. dynamic loading. Biomedizinische Technik 56 (5), 259–265.

Goriely, A., Amar, M., Sep. 2007. On the definition and modeling of incremental, cumulative, and continuous growth laws in morphoelasticity. Biomech Model Mechan 6 (5), 289–296.

Grytz, R., Meschke, G., Apr. 2010. A computational remodeling approach to predict the physiological architecture of the collagen fibril network in corneoscleral shells. Biomech Model Mechan 9 (2), 225–235.

Gupta, V., Grande-Allen, K. J., Dec. 2006. Effects of static and cyclic loading in regulating extracellular matrix synthesis by cardiovascular cells. Cardiovas Res 72 (3), 375–383.

Haga, J. H., Li, Y. S. J., Chien, S., 2007. Molecular basis of the effects of mechanical stretch on vascular smooth muscle cells. J Biomech 40 (5), 947–960.

Hajdu, M. A., Baumbach, G. L., Mar. 1994. Mechanics of large and small cerebral-arteries in chronic hypertension. Am J Physiol 266 (3), H1027–H1033.

Hamet, P., Hadrava, V., Kruppa, U., Tremblay, J., Jun. 1991. Transforming growth-factor beta-1 expression and effect in aortic smooth-muscle cells from spontaneously hypertensive rats. Hypertension 17 (6), 896–901.

Hariton, I., deBotton, G., Gasser, T. C., Holzapfel, G. A., Apr. 2007. Stress-driven collagen fiber remodeling in arterial walls. Biomech Model Mechan 6 (3), 163–175.

Harrigan, T. P., Hamilton, J. J., May 1992. An analytical and numerical study of the stability of bone remodeling theories - dependence on microstructural stimulus. J Biomech 25 (5), 477–488.

Hayakawa, K., Sato, N., Obinata, T., Aug. 2001. Dynamic reorientation of cultured cells and stress fibers under mechanical stress from periodic stretching. Exp Cell Res 268 (1), 104–114.

Hayashi, K., Handa, H., Nagasawa, S., Okumura, A., Moritake, K., 1980. Stiffness and elastic behavior of human intracranial and extracranial arteries. J Biomech 13 (2), 175–179.

Heidenreich, E. A., Ferrero, J. M., Doblare, M., Rodriguez, J. F., Jul. 2010. Adaptive macro finite elements for the numerical solution of monodomain equations in cardiac electrophysiology. Ann Biomed Eng 38 (7), 2331–2345.

Himpel, G., Kuhl, E., Menzel, A., Steinmann, P., 2005. Computational modelling of isotropic multiplicative growth. CMES 8 (2), 119–134.

Himpel, G., Menzel, A., Kuhl, E., Steinmann, P., Mar. 2008. Time-dependent fibre reorientation of transversely isotropic continua . finite element formulation and consistent linearization. Intl J Numer Meth Eng 73 (10), 1413–1433.

Holzapfel, G. A., 2000. Nonlinear Solid Mechanics: A Continuum Approach for Engineering. John Wiley & Sons.

Holzapfel, G. A., 2004. Encyclopedia of Computational Mechanics.

Holzapfel, G. A., Gasser, T. C., Ogden, R. W., Jul. 2000. A new constitutive framework for arterial wall mechanics and a comparative study of material models. J Elasticity 61 (1), 1–48.

Holzapfel, G. A., Sommer, G., Gasser, C. T., Regitnig, P., Nov. 2005. Determination of layer-specific mechanical properties of human coronary arteries with nonatherosclerotic intimal thickening and related constitutive modeling. Am J Physiol Heart Circ Physiol 289 (5), H2048–2058.

Hsu, H. J., Lee, C. F., Kaunas, R., Mar. 2009. A dynamic stochastic model of frequency-dependent stress fiber alignment induced by cyclic stretch. Plos One 4 (3), e4853.

Hu, J. J., Ambrus, A., Fossum, T. W., Miller, M. W., Humphrey, J. D., Wilson, E., Apr. 2008. Time courses of growth and remodeling of porcine aortic media during hypertension: A quantitative immunohistochemical examination. J Histochem Cytochem 56 (4), 359–370.

Hu, J. J., Baek, S., Humphrey, J. D., 2007a. Stress-strain behavior of the passive basilar artery in normotension and hypertension. J Biomech 40 (11), 2559–2563.

Hu, J.-J., Fossum, T. W., Miller, M. W., Xu, H., Liu, J.-C., Humphrey, J. D., Jan. 2007b. Biomechanics of the porcine basilar artery in hypertension. Ann Biomed Eng V35 (1), 19–29.

Huang, K., 1987. Statistical Mechanics. Wiley, 2 edition.

Huang, Z. J., Tarbell, J. M., Jul. 1997. Numerical simulation of mass transfer in porous media of blood vessel walls. Am J Physiol-Heart C 273 (1), H464–H477.

Hughes, T. J. R., 2000. The Finite Element Method. Linear Static and Dynamic Finite Element Analysis. Dover Publications.

Hulmes, D. J. S., WESS, T. J., PROCKOP, D. J., FRATZL, P., May 1995. Radial packing, order, and disorder in collagen fibrils. Biophys J 68 (5), 1661–1670.

Humphrey, J., Rajagopal, K., Nov. 2003. A constrained mixture model for arterial adaptations to a sustained step change in blood flow. Biomech Model Mechan V2 (2), 109–126.

Humphrey, J. D., Dec. 2001. Stress, strain, and mechanotransduction in cells. J Biomech Eng 123 (6), 638–641.

Humphrey, J. D., 2002. Cardiovascular Solid Mechanics: Cells, Tissues, and Organs. Springer-Verlag.

Humphrey, J. D., Jan. 2003. Continuum biomechanics of soft biological tissues. P Roy Soc A-Math Phy 459 (2029), 3–46.

Humphrey, J. D., 2009. Need for a continuum biochemomechanical theory of soft tissue and cellular growth and remodeling. In: Biomechanical Modelling at the Molecular, Cellular and Tissue Levels. Springer Vienna.

Humphrey, J. D., Rajagopal, K. R., Mar. 2002. A constrained mixture model for growth and remodeling of soft tissues. Math Models Methods Appl Sci 12 (3), 407–430.

Hunter, P. J., McCulloch, A. D., ter Keurs, H. E. D. J., 1998. Modelling the mechanical properties of cardiac muscle. Prog Biophys Mol Biol 69 (2-3), 289–331.

Imatani, S., Maugin, G. A., 2002. A constitutive model for material growth and its application to three-dimensional finite element analysis. Mech Res Commun 29 (6), 477–483.

Ingber, D. E., Apr. 2003. Tensegrity i. cell structure and hierarchical systems biology. J Cell Sci 116 (7), 1157–1173.

Ingber, D. E., Jun. 2008. Tensegrity-based mechanosensing from macro to micro. Progress In Biophysics & Molecular Biology 97 (2-3), 163–179.

Jani, B., Rajkumar, C., Jun. 2006. Ageing and vascular ageing. Postgrad Med J 82 (968), 357–362.

Jeffery, T. K., Wanstall, J. C., Oct. 2001. Pulmonary vascular remodeling: a target for therapeutic intervention in pulmonary hypertension. Pharmacol Therapeut 92 (1), 1–20.

Jousilahti, P., Vartiainen, E., Tuomilehto, J., Puska, P., Mar. 1999. Sex, age, cardiovascular risk factors, and coronary heart disease - a prospective follow-up study of 14 786 middle-aged men and women in finland. Circulation 99 (9), 1165–1172.

Junqueira, L. C. U., Bignolas, G., Brentani, R. R., 1979. Picrosirius staining plus polarization microscopy, a specific method for collagen detection in tissue-sections. Histochem J 11 (4), 447–455.

Kaplan, N. . M., Victor, R. G., 2009. Kaplan's Clinical Hypertension. Lippincott Williams & Wilkins.

Kardas, D., Nackenhorst, U., Balzani, D., 2012. Computational model for the cell-mechanical response of the osteocyte cytoskeleton based on self-stabilizing tensegrity structures. Biomech Model Mechan.

Karsaj, I., Sansour, C., Soric, J., Oct. 2009. The modelling of fibre reorientation in soft tissue. Biomech Model Mechan 8 (5), 359–370.

Kielty, C. M., 2006. Elastic fibres in health and disease. Expert reviews in molecular medicine 8 (19), 1–23.

Kielty, C. M., Sherratt, M. J., Shuttleworth, C. A., Jul. 2002. Elastic fibres. J Cell Sci 115 (14), 2817–2828.

Kim, D. W., Gotlieb, A. I., Langille, B. L., Jul. 1989. Invivo modulation of endothelial-f-actin microfilaments by experimental alterations in shear-stress. Arteriosclerosis 9 (4), 439–445.

Kim, W. S., Tarbell, J. M., May 1994. Macromolecular transport through the deformable porous-media of an artery wall. J Biomech Eng-T ASME 116 (2), 156–163.

Klisch, S. M., Sah, R. L., Hoger, A., Jun. 2005. A cartilage growth mixture model for infinitesimal strains: solutions of boundary-value problems related to in vitro growth experiments. Biomech Model Mechan 3 (4), 209–223.

Koenders, M. M. J. F., Yang, L., Wismans, R. G., van der Werf, K. O., Reinhardt, D. P., Daamen, W., Bennink, M. L., Dijkstra, P. J., van Kuppevelt, T. H., Feijen, J., May 2009. Microscale mechanical properties of single elastic fibers: The role of fibrillin-microfibrils. Biomaterials 30 (13), 2425–2432.

Kratky, O., Porod, G., 1949. Rontgenuntersuchung geloster fadenmolekule. Recl Trav Cnim Pay B 68 (12), 1106–1122.

Kroon, M., Jun. 2010. A continuum mechanics framework and a constitutive model for remodelling of collagen gels and collagenous tissues. J Mech Phys Solids 58 (6), 918–933.

Kuhl, E., 2003. Theory and numerics of open system continuum thermodynamics - spatial and material settings -. Ph.D. thesis, University of Kaiserslautern.

Kuhl, E., Garikipati, K., Arruda, E. M., Grosh, K., Jul. 2005. Remodeling of biological tissue: Mechanically induced reorientation of a transversely isotropic chain network. J Mech Phys Solids 53 (7), 1552–1573.

Kuhl, E., Holzapfel, G., Nov. 2007. A continuum model for remodeling in living structures. J Mater Sci 42 (21), 8811–8823.

Kuhl, E., Menzel, A., Steinmann, P., Sep. 2003a. Computational modeling of growth. Comput Mech V32 (1), 71–88.

Kuhl, E., Menzel, A., Steinmann, P., Sep. 2003b. Computational modeling of growth - a critical review, a classification of concepts and two new consistent approaches. Comput Mech 32 (1-2), 71–88.

Kuhl, E., Ramm, E., de Borst, R., 2000. An anisotropic gradient damage model for quasi-brittle materials. Comput Method Appl M 183 (1-2), 87–103.

Kuhl, E., Steinmann, P., 2003. Theory and numerics of geometrically non-linear open system mechanics. Int J Numer Meth Eng 58 (11), 1593–1615.

Kuhl, E., Steinmann, P., Carol, I., Apr. 2001. A thermodynamically consistent approach to microplane theory. part ii. dissipation and inelastic constitutive modeling. Int J Solids Struct 38 (17), 2933–2952.

Landuyt, M., 2006. Structural quantification of collagen fibers in abdominal aortic aneurysms. Master's thesis, Royal Institute of Technology in Stockholm, Department of Solid Mechanics and Ghent University, Department of Civil Engineering.

Laviades, C., Varo, N., Fernandez, J., Mayor, G., Gil, M. J., Monreal, I., Diez, J., Aug. 1998. Abnormalities of the extracellular degradation of collagen type i in essential hypertension. Circulation 98 (6), 535–540.

Lee, E. H., 1969. Elastic-plastic deformation at finite strains. J Appl Mech 36 (1), 1–&.

Leonard, S. L., 2008. Braunwald's Heart Disease Review and Assessment. Saunders.

Levesque, M. J., Liepsch, D., Moravec, S., Nerem, R. M., Mar. 1986. Correlation of endothelial-cell shape and wall shear-stress in a stenosed dog aorta. Arteriosclerosis 6 (2), 220–229.

Levick, J. R., Oct. 1987. Flow through interstitium and other fibrous matrices. Q J Exp Physiol CMS 72 (4), 409–438.

Li, Y. S. J., Haga, J. H., Chien, S., Oct. 2005. Molecular basis of the effects of shear stress on vascular endothelial cells. J Biomech 38 (10), 1949–1971.

Lifton, R. P., Gharavi, A. G., Geller, D. S., Feb. 2001. Molecular mechanisms of human hypertension. Cell 104 (4), 545–556.

Lillie, M. A., David, G. J., Gosline, J. M., 1998. Mechanical role of elastin-associated microfibrils in pig aortic elastic tissue. Connec Tissue Research 37 (1-2), 121–141.

Lusis, A. J., Sep. 2000. Atherosclerosis. Nature 407 (6801), 233–241.

Malek, A. M., Izumo, S., Apr. 1996. Mechanism of endothelial cell shape change and cytoskeletal remodeling in response to fluid shear stress. J Cell Sci 109, 713–726.

Malve, M., Chandra, S., García, A., Mena, A., Martínez, M. A., Finol, E. A., Doblaré, M., 1996. Impedance-based outflow boundary conditions for human carotid haemodynamics. Comput Meth Biomech Biomed Eng DOI:10.1080/10255842.2012.744396, pMID: 23387938.
URL `http://www.tandfonline.com/doi/abs/10.1080/10255842.2012.744396`

Mancia, G., Rosei, E. A., Cifkova, R., DeBacker, G., Erdine, S., Fagard, R., Farsang, C., Heagerty, A. M., Kawecka-Jaszcs, K., Kiowski, W., Kjeldsen, S., Luscher, T., McInnes, G., Mallion, J. M., Brien, E. O., Poulter, N. R., Priori, S. G., Rahn, K. H., Rodicio, J. L., Ruilope, L. M., Safar, M., Staessen, J. A., van Zwieten, P., Waeber, B., Williams, B., Zanchetti, A., Zannad, F., Jun. 2003. 2003 european society of hypertension - european society of cardiology guidelines for the management of arterial hypertension. J Hypertens 21 (6), 1011–1053.

Marsden, J. E., Hughes, T. J. R., 1994. Mathematical Foundations of Elasticity. Dover Publications.

Marsden, J. E., Ratiu, T. S., 1999. Introduction to Mechanics and Symmetry: A Basic Exposition of Classical Mechanical Systems. Springer Verlag.

Massague, J., Dec. 2000. How cells read tgf-beta signals. Nat Rev Mol Cell Bio 1 (3), 169–178.

Massague, J., Jul. 2008. Tgf beta in cancer. Cell 134 (2), 215–230.

Massague, J., Blain, S. W., Lo, R. S., Oct. 2000. Tgf beta signaling in growth control, cancer, and heritable disorders. Cell 103 (2), 295–309.

Maurin, B., Canadas, P., Baudriller, H., Montcourrier, P., Bettache, N., 2008. Mechanical model of cytoskeleton structuration during cell adhesion and spreading. J Biomech 41 (9), 2036–2041.

Maxwell, J. C., 1871. Theory of heat. Westport, Conn., Greenwood Press.

McCulloch, A., Bassingthwaighte, J., Hunter, P., Noble, D., 1998. Computational biology of the heart: from structure to function. Prog Biophys Mol Biol 69 (2-3), 153–155.

McNulty, M., Mahmud, A., Spiers, P., Feely, J., Nov. 2006. Collagen type-i degradation is related to arterial stiffness in hypertensive and normotensive subjects. J Hum Hypertens 20 (11), 867–873.

Menzel, A., Mar. 2004. Modelling of anisotropic growth in biological tissues. Biomech Model Mechan 3 (3), 147–171.

Menzel, A., 2007. A fibre reorientation model for orthotropic multiplicative growth. Biomech Model Mechan 6, 303–320.

Menzel, A., Harrysson, M., Ristinmaa, M., 2008. Towards an orientation-distribution-based multi-scale approach for remodelling biological tissues. Comput Meth Biomech Biomed Eng 11 (5), 505–524.

Menzel, A., Steinmann, P., Apr. 2003. Geometrically non-linear anisotropic inelasticity based on fictitious configurations: Application to the coupling of continuum damage and multiplicative elasto-plasticity. Int J Numer Meth Eng 56 (14), 2233–2266.

Menzel, A., Waffenschmidt, T., Sep. 2009. A microsphere-based remodelling formulation for anisotropic biological tissues. Phil Trans R Soc A 367 (1902), 3499–3523.

Miehe, C., Göktepe, S., Lulei, F., Nov. 2004. A micro-macro approach to rubber-like materials–part i: the non-affine micro-sphere model of rubber elasticity. J Mech Phys Solids 52 (11), 2617–2660.

Mofrad, M. K., Kamm, R. D., 2006. Cytoskeletal Mechanics - Models and Measurements. Cambridge University Press.

Mofrad, M. R. K., Kamm, R. D. (Eds.), 2010. Cellular Mechanotransduction. Cambridge University Press.

Mulvany, M. J., Aalkjaer, C., Oct. 1990. Structure and function of small arteries. Physiol Rev 70 (4), 921–961.

Murtada, S. I., Kroon, M., Holzapfel, G. A., Dec. 2010. A calcium-driven mechanochemical model for prediction of force generation in smooth muscle. Biomech Model Mechan 9 (6), 749–762.

Nagase, H., Woessner, J. F., Jul. 1999. Matrix metalloproteinases. J Biol Chem 274 (31), 21491–21494.

Narayan, K. M. V., Boyle, J. P., Thompson, T. J., Sorensen, S. W., Williamson, D. F., Oct. 2003. Lifetime risk for diabetes mellitus in the united states. Jama-journal of the American Medical Association 290 (14), 1884–1890.

Needleman, S. E., 2009.

O'Brien, E., Beevers, D. G., Lip, G. Y. H. (Eds.), 2007. ABC of Hypertension. BMJ Books.

O'Callaghan, C. J., Williams, B., Sep. 2000. Mechanical strain-induced extracellular matrix production by human vascular smooth muscle cells - role of tgf-beta 1. Hypertension 36 (3), 319–324.

O'Connell, M. K., Murthy, S., Phan, S., Xu, C., Buchanan, J., Spilker, R., Dalman, R. L., Zarins, C. K., Denk, W., Taylor, C. A., Apr. 2008. The three-dimensional micro- and nanostructure of the aortic medial lamellar unit measured using 3d confocal and electron microscopy imaging. Matrix Biol 27 (3), 171–181.

Ogden, R. W., 1996. Non-Linear Elastic Deformations. Dover Publications.

Ogston, A. G., Preston, B. N., Wells, J. D., Ogston, A. G., Preston, B. N., Snowden, J. M., Wells, J. D., 1973. Transport of compact particles through solutions of chain-polymers. P Roy Soc Lond A Mat 333 (1594), 297–316.

Ohashi, T., Sato, M., Jul. 2005. Remodeling of vascular endothelial cells exposed to fluid shear stress: experimental and numerical approach rid a-5424-2012. Fluid Dyn Res 37 (1-2), 40–59.

Olgac, U., Kurtcuoglu, V., Poulikakos, D., Feb. 2008. Computational modeling of coupled blood-wall mass transport of ldl: effects of local wall shear stress. Am J Physiol-Heart C 294 (2), H909–H919.

Orgel, J. P. R. O., Antonio, J. D. S., Antipova, O., Feb. 2011. Molecular and structural mapping of collagen fibril interactions. Connect Tissue Res 52 (1), 2–17.

Orgel, J. P. R. O., Irving, T. C., Miller, A., Wess, T. J., Jun. 2006. Microfibrillar structure of type i collagen in situ. P Natl Acad Sci USA 103 (24), 9001–9005.

Orgel, J. P. R. O., Miller, A., Irving, T. C., Fischetti, R. F., Hammersley, A. P., Wess, T. J., Nov. 2001. The in situ supermolecular structure of type i collagen. Structure 9 (11), 1061–1069.

Osol, G., 1995. Mechanotransduction by vascular smooth muscle. J Vasc Res 32, 275–292.

Owens, G. K., Dec. 1989. Control of hypertrophic versus hyperplastic growth of vascular smooth-muscle cells. Am J Physiol 257 (6), H1755–H1765.

Owens, G. K., Jul. 1995. Regulation of differentiation of vascular smooth-muscle cells. Physiol Rev 75 (3), 487–517.

Owens, G. K., Rabinovitch, P. S., Schwartz, S. M., 1981. Smooth-muscle cell hypertrophy versus hyperplasia in hypertension. P Natl Acad Sci-biol 78 (12), 7759–7763.

Owens, G. K., Schwartz, S. M., 1983. Vascular smooth-muscle cell hypertrophy and hyperploidy in the goldblatt hypertensive rat. Circ Res 53 (4), 491–501.

Pandolfi, A., Manganiello, F., Nov. 2006. A model for the human cornea: constitutive formulation and numerical analysis. Biomech Model Mechan 5 (4), 237–246.

PDBe, 2013. The protein data bank in europe.
URL `http://www.ebi.ac.uk/pdbe/`

Peña, E., Calvo, B., Martinez, M. A., Doblare, M., 2006. A three-dimensional finite element analysis of the combined behavior of ligaments and menisci in the healthy human knee joint. J Biomech 39 (9), 1686–1701.

Perktold, K., Rappitsch, G., 1995. Computer simulation of local blood flow and vessel mechanics in a compliant carotid artery bifurcation model. J Biomech 28 (7), 845 – 856.

Philibert, J., 2006. One and a half century of diffusion : Fick , einstein , before and beyond. Mat Sci+ 4 (6), 1–19.

Porreca, E., DiFebbo, O., Mincione, G., Reale, M., Baccante, G., Guglielmi, M. D., Cuccurullo, F., Colletta, G., Jul. 1997. Increased transforming growth factor-beta production and gene expression by peripheral blood monocytes of hypertensive patients. Hypertension 30 (1), 134–139.

Rachev, A., Greenwald, S. E., May 2003. Residual strains in conduit arteries. J Biomech 36 (5), 661–670.

Raines, E. W., Aug. 2004. Pdgf and cardiovascular disease. Cytokine Growth F R 15 (4), 237–254.

Rapaport, D. C. (Ed.), 2002. The Art of Molecular Dynamics Simulation. Cambridge University Press.

Rausch, M., Dam, A., Göktepe, S., Abilez, O., Kuhl, E., 2011. Computational modeling of growth: Systemic and pulmonary hypertension in the heart. Biomech Model Mechanobiol 10, 799–811.

Rhodin, J. A. G., 1980. Handbook of Physiology, The Cardiovascular System. Vol. 2. American Physiological Society, Bethesda, Maryland, Ch. Architecture of the vessel wall, pp. 1–31.

Rice, J. C., COWIN, S. C., BOWMAN, J. A., 1988. On the dependence of the elasticity and strength of cancellous bone on apparent density. J Biomech 21 (2), 155–168.

Roberts, A. B., Sporn, M. B., Assoian, R. K., Smith, J. M., Roche, N. S., Wakefield, L. M., Heine, U. I., Liotta, L. A., Falanga, V., Kehrl, J. H., Fauci, A. S., Jun. 1986. Transforming growth-factor type-beta - rapid induction of fibrosis and angiogenesis invivo and stimulation of collagen formation invitro. P Natl Acad Sci USA 83 (12), 4167–4171.

Rodriguez, E. K., Hoger, A., McCulloch, A. D., Apr. 1994. Stress-dependent finite growth in soft elastic tissues. J Biomech 27 (4), 455–467.

Rodriguez, J., Goicolea, J. M., Gabaldon, F., 2007. A volumetric model for growth of arterial walls with arbitrary geometry and loads. J Biomech 40 (5), 961–971.

Rogers, J. M., McCulloch, A. D., Aug. 1994. A collocation-galerkin finite-element model of cardiac action-potential propagation. IEEE T Bio-Med Eng 41 (8), 743–757.

Rosenbloom, J., Abrams, W., Mecham, R., Oct. 1993. Extracellular matrix 4: the elastic fiber. FASEB J. 7 (13), 1208–1218.

Rubbens, M. P., Driessen-Mol, A., Boerboom, R. A., Koppert, M. M. J., van Assen, H. C., Romeny, B. M. T., Baaijens, F. P. T., Bouten, C. V. C., Jul. 2009.

Quantification of the temporal evolution of collagen orientation in mechanically conditioned engineered cardiovascular tissues. Ann Biomed Eng 37 (7), 1263–1272.

Runanyi, G. M., Freay, A. D., Kauser, K., Johns, A., Harder, D. R., Mar. 1990. Mechanoreception by the endothelium - mediators and mechanisms of pressure-induced and flow-induced vascular-responses. Blood Vessels 27 (2-5), 246–257.

Saez, A., Buguin, A., Silberzan, P., Ladoux, B., Dec. 2005. Is the mechanical activity of epithelial cells controlled by deformations or forces? Biophys J 89 (6), L52–L54.

Safar, M. E., London, G. M., Aug. 1987. Arterial and venous compliance in sustained essential-hypertension. Hypertension 10 (2), 133–139.

Sander, E. A., Stylianopoulos, T., Tranquillo, R. T., Barocas, V. H., Oct. 2009. Image-based multiscale modeling predicts tissue-level and network-level fiber reorganization in stretched cell-compacted collagen gels. PNAS 106 (42), 17675–17680.

Sarzani, R., Brecher, P., Chobanian, A. V., Apr. 1989. Growth-factor expression in aorta of normotensive and hypertensive rats. J Clin Invest 83 (4), 1404–1408.

Sasaki, N., Odajima, S., Sep. 1996. Elongation mechanism of collagen fibrils and force-strain relations of tendon at each level of structural hierarchy. J Biomech 29 (9), 1131–1136.

Schaan, B. D., Quadros, A. S., Sarmento-Leite, R., De Lucca, G., Bender, A., Bertoluci, M., Jul. 2007. 'correction:' serum transforming growth factor beta-1 (tgf-beta-1) levels in diabetic patients are not associated with pre-existent coronary artery disease. Cardiovasc Diabetol 6, 19.

Schauer, K., 2013. B. goud lab, institut curie.

Schiffrin, E. L., Park, J. B., Intengan, H. D., Touyz, R. M., Apr. 2000. Correction of arterial structure and endothelial dysfunction in human essential hyper-

tension by the angiotensin receptor antagonist losartan. Circulation 101 (14), 1653–1659.

Schofield, I., Malik, R., Izzard, A., Austin, C., Heagerty, A., Dec. 2002. Vascular structural and functional changes in type 2 diabetes mellitus - evidence for the roles of abnormal myogenic responsiveness and dyslipidemia. Circulation 106 (24), 3037–3043.

Schubert, R., Mulvany, M. J., Apr. 1999. The myogenic response: established facts and attractive hypotheses. Clinical Science 96 (4), 313–326.

SCIENCEphotoLIBRARY, 2013.
URL `http://www.sciencephoto.com`

Sherebrin, M. H., 1983. Mechanical anisotropy of purified elastin from the thoracic aorta of dog and sheep. Can J Physiol Pharma 61 (6), 539–545.

Sherratt, M. J., Baldock, C., Haston, J. L., Holmes, D. F., Jones, C. J. P., Shuttleworth, C. A., Wess, T. J., Kielty, C. M., Sep. 2003. Fibrillin microfibrils are stiff reinforcing fibres in compliant tissues. J Mol Bio 332 (1), 183–193.

Silver, F. H., Freeman, J. W., Seehra, G. P., Oct. 2003. Collagen self-assembly and the development of tendon mechanical properties. J Biomech 36 (10), 1529–1553.

Skalak, R., Dasgupta, G., Moss, M., Otten, E., Dullemeijer, P., Vilmann, H., Feb. 1982. Analytical description of growth. J Theor Biol 94 (3), 555–577.

Sommer, G., Holzapfel, G. A., Jan. 2012. 3d constitutive modeling of the biaxial mechanical response of intact and layer-dissected human carotid arteries. J Mech Behav Biomed 5 (1), 116–128.

Sommer, G., Regitnig, P., Koltringer, L., Holzapfel, G. A., Mar. 2010. Biaxial mechanical properties of intact and layer-dissected human carotid arteries at physiological and supraphysiological loadings. Am J Physiol-Heart C 298 (3), H898–H912.

Spencer, A. J. M., 1971. Theory of invariants. In: Continuum Physiscs. Academic Press, New York, pp. 239–253.

Stalhand, J., Klarbring, A., Holzapfel, G. A., Jan. 2011. A mechanochemical 3d continuum model for smooth muscle contraction under finite strains. J Theor Biol 268 (1), 120–130.

Stein, E., de Borst, R., Hughes, T. J. R., 2004. Encyclopedia of Computational Mechanics. Vol. 1 Fundamentals. John Wiley & Sons, Ltd.

Steinman, D., Thomas, J., Ladak, H., Milner, J., Rutt, B., Spence, J., 2002. Reconstruction of carotid bifurcation hemodynamics and wall thickness using computational fluid dynamics and mri. Magn. Reson. Med. 47, 149–159.

Stopak, D., Harris, A. K., 1982. Connective-tissue morphogenesis by fibroblast traction .1. tissue-culture observations. Dev Biol 90 (2), 383–398.

Strauss, B. H., Rabinovitch, M., Jan. 2000. Adventitial fibroblasts - defining a role in vessel wall remodeling. Am J Resp Cell Mol 22 (1), 1–3.

Sukumar, N., Moran, B., Belytschko, T., Nov. 1998. The natural element method in solid mechanics. Int J Numer Meth Eng 43 (5), 839–.

Sumpio, B. E., Banes, A. J., Link, W. G., Johnson, G., Oct. 1988. Enhanced collagen production by smooth-muscle cells during repetitive mechanical stretching. AArch Surg 123 (10), 1233–1236.

Taber, L. A., 1995. Biomechanics of growth, remodeling, and morphogenesis. Appl. Mech. Rev. 48, 487–545.

Taber, L. A., Jun. 1998. A model for aortic growth based on fluid shear and fiber stresses. J Biomech Eng-T ASME 120 (3), 348–354.

Taber, L. A., Sep. 2009. Towards a unified theory for morphomechanics. Phil Trans R Soc A 367 (1902), 3555–3583.

Tada, S., Tarbell, J. M., Feb. 2002. Flow through internal elastic lamina affects shear stress on smooth muscle cells (3d simulations). Am J Physiol-Heart C 282 (2), H576–H584.

Tang, D., Yang, C., Kobayashi, S., Ku, D., 2001. Steady flow and wall compression in stenotic arteries: a 3-d thick-wall model with fluid-wall interactions. J Biomech 123, 548–557.

Tang, D., Yang, C., Kobayashi, S., Ku, D., 2004. Effect of a lipid pool on stress/strain distributions in stenotic arteries: 3d fsi models. J Biomech 126, 363–370.

Tang, D., Yang, C., Kobayashi, S., Zheng, J., Vito, R., 2003. Effect of stenosis asymmetry on blood flow and artery compression: a 3-d fsi model. Ann Biomed Eng 31, 1182–1193.

Tang, D., Yang, C., Kobayashi, S., Zheng, J., Woodard, P., Sicard, G., Saffitz, J., C., Y., 2005. 3d mri-based multi-component fsi models for atherosclerotic plaques, a 3-d fsi model. Ann Biomed Eng 32 (7), 947–960.

Tang, D., Yang, C., Mondal, S., Liu, F., Canton, G., Hatsukami, T., Yuan, C., 2008. A negative correlation between human carotid atherosclerosis plaque progression and plaque wall stress:in vivo mri-based 2d/3d fsi models. J Biomech 41, 727–736.

Tarbell, J. M., 2003a. Mass transport in arteries and the localization of atherosclerosis. Annu Rev Biomed Eng 5, 79–118.

Tarbell, J. M., 2003b. Mass transport in arteries and the localization of atherosclerosis. Annu Rev Biomed Eng 5, 79–118.

Tarbell, J. M., Shi, Z. D., 2012. Effect of the glycocalyx layer on transmission of interstitial flow shear stress to embedded cells. Biomech Model Mechan.

Tarbell, J. M., Weinbaum, S., Kamm, R. D., Dec. 2005. Cellular fluid mechanics and mechanotransduction. Ann Biomed Eng 33 (12), 1719–1723.

Thakar, R. G., Cheng, Q., Patel, S., Chu, J., Nasir, M., Liepmann, D., Komvopoulos, K., Li, S., Apr. 2009. Cell-shape regulation of smooth muscle cell proliferation. Biophys J 96 (8), 3423–3432.

Tian, L., Lammers, S. R., Kao, P. H., Reusser, M., Stenmark, K. R., Hunter, K. S., Qi, H. J., Shandas, R., Nov. 2011. Linked opening angle and histological and mechanical aspects of the proximal pulmonary arteries of healthy and pulmonary hypertensive rats and calves. Am J Physiol-Heart C 301 (5), H1810–H1818.

Topol, J. T., Califf, R. M., N., P. E., D., T. J., D., T. P., 2006. Textbook of Cardiovascular Medicine. Lippincott Williams & Wilkins.

Tropea, J. A., 2011.
URL `http://lacienciaconhumor.blogspot.com.es/`

Truesdell, C., Noll, W., 2004. The Non-Linear Field Theories of Mechanics, 3rd Edition. Springer-Verlag.

van der Rijt, J., 2004. Micromechanical testing of single collagen type i fibrils. Ph.D. thesis, University of Twente.

van der Rijt, J. A. J., van der Werf, K. O., Bennink, M. L., Dijkstra, P. J., Feijen, J., Sep. 2006. Micromechanical testing of individual collagen fibrils. Macromol Biosci 6 (9), 697–702.

Vianello, M., Sep. 1996. Optimization of the stored energy and coaxiality of strain and stress in finite elasticity. J Elasticity 44 (3), 193–202.

Visse, R., Nagase, H., May 2003. Matrix metalloproteinases and tissue inhibitors of metalloproteinases - structure, function, and biochemistry. Circ Res 92 (8), 827–839.

Waffenschmidt, T., Menzel, A., Kuhl, E., Jul. 2012. Anisotropic density growth of bone-a computational micro-sphere approach. Int J Solids Struct 49 (14), 1928–1946.

Wang, D. M., Tarbell, J. M., Aug. 1995. Modeling interstitial flow in an artery wall allows estimation of wall shear-stress on smooth-muscle cells. J Biomech Eng-T ASME 117 (3), 358–363.

Weinbaum, S., Cowin, S. C., Zeng, Y., Mar. 1994. A model for the excitation of osteocytes by mechanical loading-induced bone fluid shear stresses. J Biomech 27 (3), 339–360.

Weinbaum, S., Tarbell, J. M., Damiano, E. R., 2007. The structure and function of the endothelial glycocalyx layer.

Welty, J., Wicks, C. E., Rorrer, G. L., Wilson, R. E., 2008. Fundamentals of Momentum, Heat and Mass Transfer. John Wiley & Sons.

Wenger, M. P. E., Bozec, L., Horton, M. A., Mesquida, P., Aug. 2007. Mechanical properties of collagen fibrils. Biophys J 93 (4), 1255–1263.

WHO, 2009. Disease and injury country estimates. Tech. rep., World Health Organization.

Wiener, J., Loud, A. V., GiacomelliI, F., Anversa, P., 1977. Morphometric analysis of hypertension-induced hypertrophy of rat thoracic aorta. Am J Pathol 88 (3), 619–633.

WojtowiczPraga, S. M., Dickson, R. B., Hawkins, M. J., 1997. Matrix metalloproteinase inhibitors. Invest New Drug 15 (1), 61–75.

Wolgemuth, L., 2009.
URL `http://money.usnews.com/money/careers/articles/2009/12/28/the-50-best-careers-`

Wolinsky, H., 1971. Effects of hypertension and its reversal on the thoracic aorta of male and female rats: Morphological and chemical studies. Circ Res 28 (6), 622–637.

Wong, J., Goktepe, S., Kuhl, E., 2011. Computational modeling of electrochemical coupling: A novel finite element approach towards ionic models for cardiac electrophysiology. Comput Method Appl M 200 (45-46), 3139–3158.

Wrana, J. L., Attisano, L., Wieser, R., Ventura, F., Massague, J., Aug. 1994. Mechanism of activation of the tgf-beta receptor. Nature 370 (6488), 341–347.

Yang, L., 2008. Mechanical properties of collagen fibrils and elastic fibers explored by afm. Ph.D. thesis, Universityof Twente.

Zou, Y., Zhang, Y. H., Aug. 2009. An experimental and theoretical study on the anisotropy of elastin network. Ann Biomed Eng 37 (8), 1572–1583.

Zulliger, M. A., Rachev, A., Stergiopulos, N., 2004. A constitutive formulation of arterial mechanics including vascular smooth muscle tone. Am J Physiol Heart Circ Physiol 287 (3), H1335–1343.

Zygote Media Group, I., 2011.